THE EFFECT OF THERMAL CYCLES ON THE MICROSTRUCTURE AND TOUGHNESS OF SUPERDUPLEX STAINLESS STEELS

R. N. GUNN

PH.D. 1998

THE EFFECT OF THERMAL CYCLES ON THE MICROSTRUCTURE AND TOUGHNESS OF SUPERDUPLEX STAINLESS STEELS

December 1998

Robert Neil Gunn, BSc (Hons), CEng, MIM, SenMWeldI, MICorr

Submitted in partial fulfilment of the requirements for the degree of PhD
Sponsoring establishment: TWI, Cambridge
Collaborating establishment: Imperial College of Science, Technology and Medicine, London

The thesis is concerned with the effects of weld thermal cycles on phase transformations in superduplex stainless steels, and, in particular, with precipitation of intermetallic phases. Contained within is an introduction to superduplex stainless steels followed by a literature review. The review contains three main topics, namely: i) stainless steels; ii) duplex stainless steels, covering production routes for wrought materials and the resultant mechanical and corrosion properties; and iii) the effects of welding these two phase alloys, including susceptibility to intermetallic phase formation and their effect on properties. After a description of the experimental procedures employed, which included impact and fracture toughness tests, corrosion assessment, optical, scanning and transmission electron microscopy, the results are presented.

The results are separated under two headings. The preliminary studies examined the formation of intermetallic phases in production welds, thermal cycle measurement and prediction, and isothermal heat treatments. The main body of results covers weld thermal cycle simulation studies modeled from production welds and the influence of intermetallic phases on fracture toughness. The results are discussed and conclusions drawn on experimental techniques and the significance of intermetallic phases on the toughness and pitting corrosion resistance of duplex stainless steels in the welding context. Finally, recommendations are made on areas of future work relating to this topic.

Abstract i

Contents ii

List of Tables vi

List of Figures vii

CHAPTER 1 INTRODUCTION

1.1. HISTORICAL BACKGROUND 1-1

1.2. PRESENT STUDY 1-4

CHAPTER 2 LITERATURE REVIEW

2.1. STAINLESS STEELS 2-1

2.1.1. Background 2-1

2.1.2. Martensitic Stainless Steels 2-3

2.1.3. Ferritic Stainless Steels 2-5

2.1.4. Austenitic Stainless Steels 2-8

2.1.5. Ferritic-Austenitic Duplex Stainless Steels . . . 2-12

2.2. DUPLEX STAINLESS STEELS 2-15

2.2.1. History and Development 2-15

2.2.2. Alloying Additions 2-20

2.2.3. Process Routes and Heat Treatments 2-29

2.2.4. Solution Annealed Microstructure 2-30

2.2.5. Tensile Properties 2-31

2.2.6. Fracture Toughness 2-34

2.2.7. Localised Corrosion Resistance 2-38

2.2.8. Stress Corrosion Cracking 2-41

2.3. WELDING DUPLEX ALLOYS 2-43
2.3.1. General Welding Characteristics 2-43
2.3.2. Fabrication Cracks 2-47
2.3.3. Duplex Welding Consumables 2-49
2.3.4. Decomposition of Ferrite to Primary Austenite . . 2-51
2.3.5. Element Partitioning 2-52
2.3.6. Phase Balance Measurement and Prediction . . . 2-56
2.3.7. Second Phase Particles 2-58
2.3.8. Corrosion Resistance of Weldments 2-65
2.3.9. Effect of Precipitation on Fracture Behaviour . . . 2-68

CHAPTER 3 EXPERIMENTAL PROCEDURES

3.1. APPROACH 3-1
3.2. STANDARD TECHNIQUES. 3-4
3.2.1. Chemical Analysis 3-4
3.2.2. Metallography 3-4
3.2.3. Toughness Tests and Assessment 3-5
3.2.4. Pitting Tests and Assessment 3-6
3.3. MATERIALS 3-7
3.3.1. Thin walled pipes 3-7
3.3.2. Thick walled products 3-8
3.3.3. Composition 3-9
3.3.4. Phase Balance 3-11
3.3.5. Mechanical Properties 3-11

3.4. PRODUCTION WELD INVESTIGATIONS (STUDY I) . . 3-13
3.5. THERMAL CYCLE MEASUREMENT (STUDY II) . . 3-15
3.6. FINITE ELEMENT ANALYSIS (STUDY III) . . . 3-16
3.7. ISOTHERMAL HEAT TREATEMENT (STUDY IV) . . 3-18
3.8. THERMAL CYCLE SIMULATION (STUDY V) . . . 3-19
3.9. HEAT TREATMENT TRIALS (STUDY VI) . . . 3-24
3.9.1. Laboratory Heat Treatments 3-24
3.9.2. Production Heat Treatments 3-25
3.10. FRACTURE BEHAVIOUR (STUDY VII) 3-25

CHAPTER 4 PRELIMINARY STUDY RESULTS

4.1. PROUCTION WELD INVESTIGATIONS (STUDY I) . . 4-1
4.2. THERMAL CYCLE MEASUREMENT (STUDY II) . . 4-2
4.3. FINITE ELEMENT ANALYSIS (STUDY III) . . . 4-4
4.4. ISOTHERMAL HEAT TREATMENT (STUDY IV) . . 4-7
4.4.1. Metallography 4-7
4.4.2. Effect of Intermetallic Formation on Toughness . . 4-13
4.4.3. Effect of Heat Treatment on Pitting Resistance . . 4-15

CHAPTER 5 MAIN RESULTS

5.1. THERMAL CYCLE SIMULATION (STUDY V) . . . 5-1
5.1.1. Metallography 5-1
5.1.2. Impact Tests 5-3
5.1.3. Fractography 5-4
5.1.4. Pitting Test 5-6
5.2. HEAT TREATMENT TRIALS (STUDY VI) . . . 5-7
5.2.1. Laboratory Heat Treatments 5-7
5.2.2. Production Heat Treatments 5-8

5.3. FRACTURE BEHAVIOUR (STUDY VII) 5-10
5.3.1. Metallography 5-10
5.3.2. Charpy and CTOD Toughness 5-12
5.3.3. Fracture Face and Crack Propagation Path Examination . 5-15

CHAPTER 6 DISCUSSION

6.1. EXPERIMENTAL TECHNIQUES 6-1
6.2. PREDICTION OF WELD THERMAL CYCLES . . . 6-2
6.3. INTERMETALLIC PRECIPITATION IN PRODUCTION WELDS 6-5
6.4. EFFECT OF INTERMETALLIC PHASES ON TOUGHNESS . 6-8
6.5. OTHER FACTORS THAT INFLUENCE TOUGHNESS . . 6-12
6.6. CORRELATION BETWEEN IMPACT AND FRACTURE TOUGHNESS 6-14
6.7. EFFECT OF INTERMETALLIC PHASES ON PITTING RESISTANCE 6-17

CHAPTER 7 SUMMARY AND CONCLUSIONS . 7-1

CHAPTER 8 FURTHER RESEARCH . . . 8-1

REFERENCES 9-1
BIBLIOGRAPHY 10-1
ABBREVIATIONS AND EQUATIONS . . 11-1

2-1 Composition and mechanical properties of martensitic stainless steels 2-4

2-2 Composition and mechanical properties of ferritic stainless steels . 2-7

2-3 Composition and mechanical properties of austenitic stainless steels . 2-9

2-4 Composition and mechanical properties of modern duplex stainless grades 2-12

2-5 Summary of stainless steel properties by class . . . 2-14

2-6 Influence of alloying additions on corrosion resistance . . 2-21

2-7 Crystallographic characteristics of particles 2-60

3-1 Pipes and plates employed for different studies . . . 3-8

3-2 Chemical compositions of materials examined . . . 3-10

3-3 Phase balance and lamellar spacing 3-11

3-4 Mechanical properties of plates/pipes 3-12

3-5 Summary of GTA weld parameters and procedures examined. . 3-14

3-6 Matrix of isothermal heat treatment (Study IV) . . . 3-19

3-7 Summary of thermal cycle simulations undertaken (Study V) . . 3-23

3-8 Summary of Study VI pipes and welds 3-24

3-9 Matrix of heat treatment, test type and temperature for Study VII . 3-26

4-1 Peak temperatures and Δt times from the fusion boundary . . 4-5

4-2 Effect of isothermal heat treatment on properties (Study IV) . . 4-7

5-1 Results of semi-quantitative SEM/EDX analysis . . . 5-9

5-2 Composition of phases determined by semi-quantitative EDX analysis 5-11

6-1 Comparison of measured and predicted thermal cycle data . . 6-3

6-2 Summary of results for specimen pairs subject to detailed fractography 6-9

6-3 Calculated diffusion distances for Cr and Mo in ferrite and austenite . 6-18

6-4 Calculated diffusion distances for Mo in ferrite and austenite in the HAZ 6-21

2-1 Effect of alloying elements on the microstructures of stainless steels . 2-2

2-2 Effect of carbon on the gamma loop in Fe-Cr alloys . . . 2-3

2-3 Pseudo-phase diagram for 70% Fe Cr-Ni alloys . . . 2-10

2-4 Ternary 70% Fe Cr-Ni diagram with N-effect 2-18

2-5 Effect of alloying elements on the anodic polarisation curve . . 2-20

2-6 Effect of alloying elements on the formation of various precipitates . 2-22

2-7 Effect of nitrogen on the increase in HAZ ferrite content . . 2-25

2-8 Effect of alloying elements on N-solubility at 1600°C . . 2-26

2-9 Typical microstructure of a wrought duplex stainless steel . . 2-31

2-10 Effect of nitrogen on tensile properties 2-32

2-11 Proof stress in rolling and transverse directions . . . 2-33

2-12 Petch plot relating proof stress and lamellar spacing . . . 2-33

2-13 Temperature dependence of mechanical properties . . . 2-33

2-14 Tensile strength as a function of cold work 2-34

2-15 Charpy energy versus temperature 2-35

2-16 Relation between grain size and transition temperature . . 2-35

2-17 Mechanical properties as a function of sigma phase . . . 2-35

2-18 Impact energy curves for alloys aged at 300°C or 325°C . . 2-37

2-19 CPT data for wrought stainless steels in sea water . . . 2-38

2-20 Pitting potentials for stainless steels in 3%NaCl . . . 2-39

2-21 CPTs and CCTs in ferric chloride solution 2-40

2-22 Compilation of data in NaCl environments 2-41

2-23 The effect of temperature, %NaCl and pH_2S on SSCC resistance . 2-42

2-24 Comparison of duplex stainless steel HAZ microstructures . . 2-44

2-25 Nomogram for prediction of Δt_{12-8} for duplex stainless steels . 2-45

2-26 TTT diagram for duplex stainless steels 2-47

2-27 Variation of weld metal toughness with welding process . . 2-50

2-28 Temperature dependence of element partitioning coefficients . 2-53

2-29 Typical partition coefficients 2-53

2-30 Nitrogen content of ferrite and austenite 2-54

2-31 Temperature dependence of nitrogen partition coefficients . . 2-54

2-32 Partition ratios for weld metal as a function of temperature . . 2-56

2-33 WRC-1992 diagram 2-58

2-34 TTT diagram for alloy S32404 2-59
2-35 C-curves for the beginning of sigma phase formation . . 2-62
2-36 CPT data for superduplex base metals and weldments . . 2-65
2-37 Cr-depletion in ferrite adjacent to sigma 2-66
2-38 Correlation between CTOD and Charpy impact tests. . . 2-70
2-39 CTOD versus measured sigma level 2-71

3-1 Overview of studies undertaken 3-1
3-2 Isothermal matrix undertaken in Study IV 3-3
3-3 Assembly for thermal cycle measurement 3-15
3-4 Variation in physical properties with temperature . . . 3-17
3-5 Thermal cycle set 1 3-20
3-6 Thermal cycle set 2 3-21
3-7 Thermal cycle set 3 (code 3R) 3-22

4-1 Intermetallic phases recorded in the HAZ of real superduplex welds 4-1
4-2 Attack of HAZ after exposure to ferric chloride solution . . 4-2
4-3 Section taken adjacent to thermocouple 4-2
4-4 Thermal cycles in weld II: Measured and Predicted . . . 4-3
4-5 Precipitation distribution map in the HAZ 4-4
4-6 2D finite element mesh of weld II 4-5
4-7 Comparison of predicted thermal cycles for two cases . . 4-6
4-8 Bright field TEM micrograph of α' phase 4-8
4-9 Optical micrograph of Cr_2N at δ/δ sub-grain boundaries . . 4-8
4-10 Bright field TEM micrograph of σ phase 4-9
4-11 Back scattered SEM images of steels heat treated at 900°C . . 4-10
4-12 Steel S32750/1 after heat treatment at 900°C. 4-11
4-13 Back scattered SEM images of steel S32750/1 heat treated at 1000°C 4-12
4-14 Bright field TEM micrograph of Cr_2N forming along the δ/δ boundaries 4-12
4-15 Effect of heat treatment on impact properties. . . . 4-13
4-16 Effect of intermetallic precipitates on fracture mode . . . 4-14
4-17 Sites of preferential attack after exposure to ferric chloride solution. 4-15

4-18 Effect of heat treatment on CPT in ferric chloride solution . 4-16
4-19 Relationship between intermetallic content and reduction in CPT . 4-17

5-1 SEM back scattered image of steel S32760/7 after thermal cycle code 3R 5-1
5-2 Greatest density of intermetallic phases in all thermal simulated samples 5-2
5-3 Bright field TEM micrograph of steel S32760/7 after thermal cycle 1T5 5-2
5-4 Effect of exposure time (Δt) on the absorbed energy . . . 5-3
5-5 Fracture faces of steel after thermal cycle 3R. . . . 5-5
5-6 Steel S32760/7 after thermal cycle 3R 5-5
5-7 Attack of phase boundaries after thermal cycle code 3R . . 5-6
5-8 HAZ of pipe in as-received and re-solution annealed condition . 5-7
5-9 SEM back scattered micrographs of HAZs in thin walled pipes . 5-8
5-10 Appearance of root weldments after exposure to ferric chloride . 5-9
5-11 Back scattered SEM images of different heat treated microstructures 5-10
5-12 Transition curves for different heat treatments . . . 5-12
5-13 Load-displacement traces for selected samples . . . 5-14
5-14 Optical micrographs illustrating the fracture path beneath the notch 5-15
5-15 Charpy fracture face on as-received sample . . . 5-16
5-16 Charpy fracture face on sigmatised sample . . . 5-16
5-17 CTOD fracture face on as-received sample . . . 5-17
5-18 Splits on CTOD fracture face of as-received sample . . 5-18
5-19 Splits on fracture face of sigmatised sample . . . 5-18
5-20 CTOD fracture face on sigmatised sample . . . 5-19

6-1 Schematic illustration of the variation of heat flow . . . 6-4
6-2 Charpy toughness versus intermetallic content . . . 6-9
6-3 Fracture toughness versus intermetallic content . . . 6-10
6-4 Comparison of Charpy energy and CTOD results . . . 6-15
6-5 Comparison of present data with previous results . . . 6-16
6-6 Simplified Mo concentration profiles across austenite/sigma/ferrite 6-19
6-7 Effect of intermetallic content on the drop in CPT . . 6-20

CHAPTER 1

INTRODUCTION

1.1. HISTORICAL BACKGROUND

During the 1980s, the ferritic:austenitic duplex stainless steels increased in popularity, mainly for use in chloride-containing environments, such as those experienced in the offshore oil and gas, petrochemical and pulp and paper industries. The 22%Cr variety, meeting UNS S31803, has proven to be the most heavily produced wrought grade and has found applications where the 300-series austenitic grades are susceptible to chloride stress corrosion cracking (SCC) whilst the use of Ni-base materials is considered too expensive. The duplex stainless steels also offer good general and pitting corrosion resistance, matching and often exceeding austenitic grades such as 316L. Further, the presence of about 50% ferrite in the two phase microstructure imparts to these steels about twice the proof stress of austenitic materials, allowing for substantial weight savings to be made.

It is well established that weldments made in duplex grades from the early 1980s tended to contain coarse, highly ferritic heat affected zones (HAZs) with poor impact toughness and impaired resistance to intergranular corrosion [Goo82]. For this reason it was recommended to weld at relatively high heat inputs to prolong the thermal cycle and to allow for austenite reformation. However this solution was not always acceptable and so, over the following decade, more stable microstructures were developed by balancing the ferrite-stabilising elements (e.g. Cr and Mo) with the austenitisers (e.g. Ni and N). The single most important development in this area was the increasing level of nitrogen up to 0.2% [Lil86]. Such levels not only stabilised the HAZ microstructure, as nitrogen narrows the temperature range over which austenite is unstable [Cha91], but also enhanced the pitting resistance of these steels [Tsu86].

Towards the end of the 1980s, the oil and gas industry began exploiting more aggressive environmental conditions, with increased chloride levels, elevated temperatures, lower pH and in the presence of *sour* hydrogen sulphide (H_2S). To meet this demand, more highly alloyed duplex stainless steel plate, tube, pipe and ancillary components were developed. These so-called *superduplex* steels are 25%Cr alloys, containing about 7%Ni and up to 4%Mo, 2%W and 0.3%N, with a pitting resistance equivalent number (PRE_N) [Ple82] greater than 40, where:

$$PRE_N = \%Cr + 3.3x\%Mo + 16x\%N \qquad \text{-- Eqn \{1-1\}}$$

Superduplex alloys are particularly resistant to pitting and stress corrosion cracking and provide good toughness at sub-zero temperatures (down to -40°C as-welded). Several grades are available to different UNS specifications, which vary with respect to their composition. The most notable variations are in the Mo and W contents: one grade contains 4%Mo and no W (UNS S32750), another 3.5%Mo and 0.6%W (S32760) and a third 3%Mo and 2%W (S39274). Both Mo and W are known to increase the pitting resistance of stainless steels in chloride–bearing media, but unfortunately these elements also stabilise deleterious intermetallic compounds, when exposed to elevated temperatures. For this reason, there has been discussion about the optimum composition of superduplex stainless steels, which combines the high corrosion resistance with minimal microstructural change during welding.

Several workers have studied intermetallic precipitation through isothermal heat treatment followed by metallography, impact tests and/or pitting corrosion tests [Cha91] [Jos91] [Cha94] [Her94] [Huh94] [Oka94] [Gun95]. The formation of hard, Mo-rich intermetallic phases, such as sigma (σ) and chi (χ), occurs between 600 and 1100°C, peaking at around 900°C. The reported time to form the phases varies between 10 and 600 seconds at the peak temperature, depending on the sensitivity of the measurement technique, the composition of the steel and its thermal history. However, most isothermal heat treatment studies have shown that sufficient intermetallic phases are formed after about 100 seconds at 850 to 950°C to cause a drop in the pitting corrosion and/or impact properties. Another phase called alpha prime (α') forms at lower temperatures around 500 °C, but is not considered significant in the welding context, due to its slow formation rate.

There are several differences between isothermal heat treatment and weld thermal cycles. In the first case, the material is normally subject to rapid heating, a hold at the exposure temperature, and a subsequent rapid quench. In the latter case, there are a number of rises and falls in temperature, with the rates and peak temperatures dependent on the welding conditions, material thickness and the distance from the heat source or fusion boundary.

For superduplex steel product forms of say 10 to 20mm thickness, and under normal welding conditions, it is unlikely that a region of the weld would experience a cumulative exposure in the 850 to 950°C range for more than 100 seconds, due to the quenching effect of the surrounding material. Nevertheless, during the early 1990s, intermetallic phases were found to form in superduplex production weldments and, in particular, in the heat affected zones (HAZs) of thin walled tubes (less than 5mm thick), several millimetres from the fusion boundary. In such cases, the welds had been made under controlled welding conditions with low heat inputs and interpass temperatures, and still the content of intermetallic phases could be sufficiently high to cause a significant reduction in toughness and corrosion resistance [Wie93]. Such observations question the assumption that intermetallic phase formation can be predicted based on isothermal heat treatment, and further, whether the intrinsic differences in thermal history between weld thermal cycles and an isothermal heat treatment are significant.

1.2. PRESENT RESEARCH

The present research begins with a literature review. In the first part, the different types of stainless steel are described, with the grades and applications listed, ending with a discussion on the problems associated with each stainless steel type. The second part reviews the literature on duplex stainless steels, starting with its history and development and the effect of different alloy additions, before moving on to the process routes and heat treatments employed to optimise properties. This part ends with a summary of the mechanical, corrosion and stress corrosion properties of wrought products.

The final part of the literature review covers the effect of weld thermal cycles on the HAZ microstructure and properties of superduplex alloys. This encompasses ferrite decomposition to austenite and the formation of second phase precipitates. The influence of these precipitates on corrosion properties and fracture behaviour is considered.

The present research comprised seven studies, which are described together with the experimental procedures in Chapter 3. The first four studies are entitled 'Preliminary Studies' as they cover an investigation into production welds that formed intermetallic phases in the early 1990s; techniques for measuring and modelling thermal cycles in these welds and finally isothermal heat treatments on different superduplex grades in order to gain an understanding of the precipitates that form over the 300 to 1300°C temperature range. Inspection involved optical, scanning and transmission electron microscopy (SEM and TEM), together with Charpy impact tests, fractography and some pitting corrosion tests.

The main investigation covered the final three studies, which examined samples in different heat treatment conditions and subject to a variety of weld thermal cycles. The heat treatments involved both laboratory and industrial techniques, while the thermal cycles employed simulated production welds that were known to induce intermetallic formation. The extent of intermetallic formation was assessed using optical, SEM and TEM techniques. Charpy impact and crack tip opening displacement (CTOD) tests were carried out, with commensurate fractography, to examine the effect of any intermetallic formation induced by the simulated weld thermal cycles. In addition, some corrosion tests were undertaken.

The remainder of this thesis presents the results of the work, discusses the findings and draws conclusions. The main questions addressed are:

i) What was the cause of intermetallic formation in production welds during the early 1990s?

ii) Can finite element models accurately predict the thermal cycles in production welds?

iii) Can isothermal heat treatment data be used to predict intermetallic formation in weldments?

iv) How can small volume fractions of intermetallic phase significantly reduce fracture toughness?

v) Do intermetallic phases affect fracture initiation or propagation?

vi) What is the influence of intermetallic content and morphology on pitting corrosion resistance?

CHAPTER 2
LITERATURE REVIEW

2.1. STAINLESS STEELS

2.1.1. Background

The generic name *stainless steel* applies to a group of Fe-Cr alloys that are resistant to general corrosion in the atmosphere. This corrosion resistance is due to the presence of an impervious film which builds-up on the surface, consisting of Cr-rich oxy-hydroxide [Has79]. Even though the *passive film* is less than 3.0nm thick [Uhl67], it protects the base metal from dissolution and is self-healing in a wide variety of aqueous environments.

At the 12-13%*Cr level, passive film stability is achieved and the stainless steel is capable of resisting corrosion and oxidation in the atmosphere [Bin46]. However, there are many industrial applications where aggressive aqueous solutions need to be contained, in particular acids/alkalis and chlorides, combined with extremes of temperature and pressure. Under these circumstances, 12-13%Cr stainless steels would be unsuitable, as the passive film would possess insufficient stability to prevent gross pitting or general corrosion, and so other grades containing up to 30%Cr are available. Other elements are added to ease fabrication and achieve specific properties. For example, Cr and Mo are alloyed for corrosion resistance; Mo, Cu and C for strength and Ni for formability and toughness. Depending on the final chemistry of the alloy, a range of stainless steel properties emerge, which allow for such diverse applications as domestic cutlery, oil production, cryogenic and high temperature containment and power generation.

---

* Throughout this report, % refers to weight %. NB: Weight % is almost equivalent to atomic % for stainless steels.

Stainless steels can be subdivided into several classes dependent on the microstructure and more particularly by the major phase present, i.e. *martensitic*, *ferritic* or *austenitic* stainless steels. The last class, which obtain their properties by virtue of a two phase microstructure, are the *ferritic-austenitic duplex* stainless steels.

The primary phase present and its proportion depend on the alloy chemistry and the heat treatment. Each element has a varying effect on stabilising either ferrite or austenite, although the primary elements are Cr and Ni, respectively. The simplest way of illustrating the conjoint effects of Cr, Ni and other elements is shown in Fig.2-1, first developed by Schaeffler for predicting the microstructures of weld metals [Sch49].

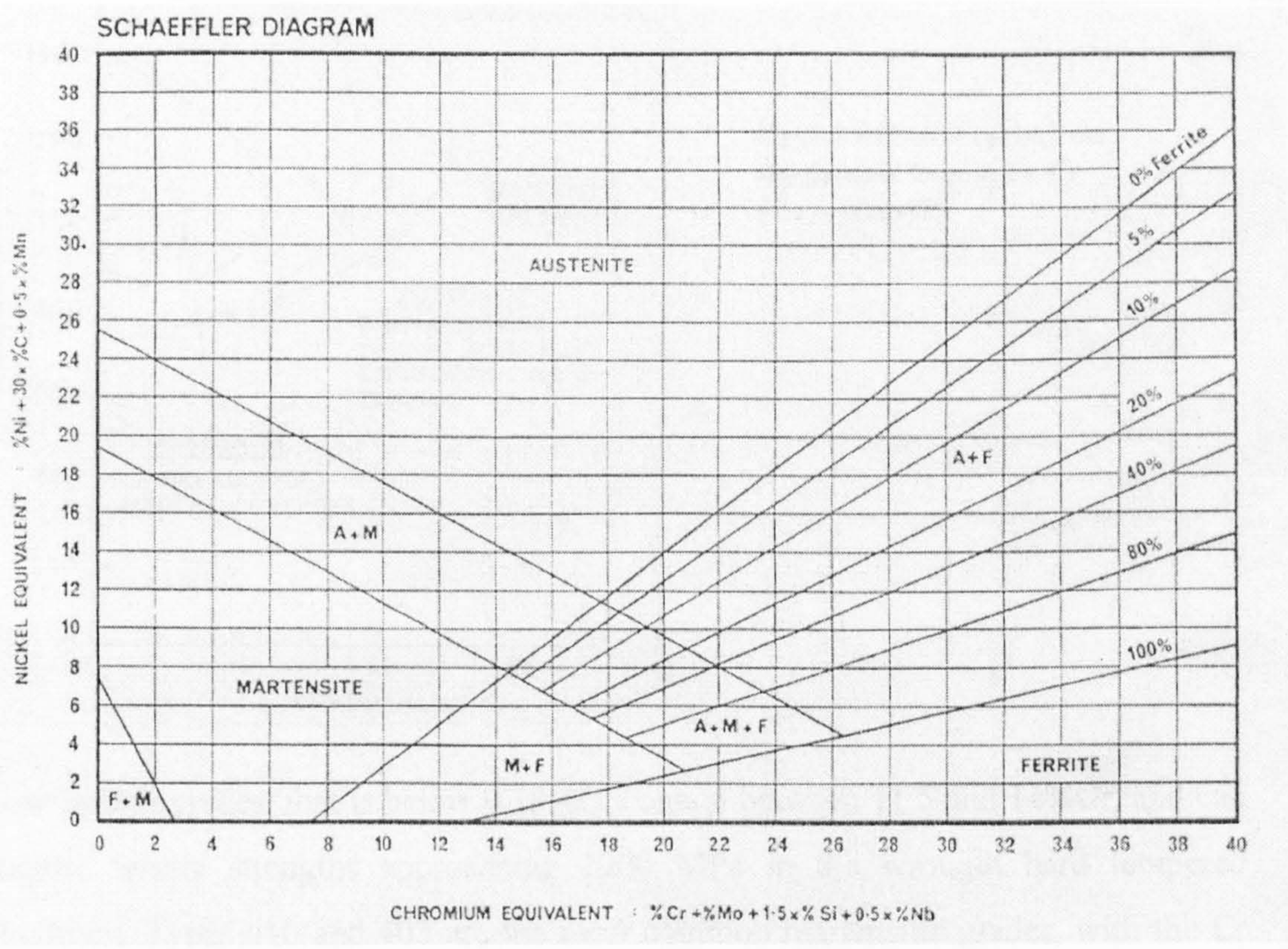


Fig.2-1 Effect of alloying elements on the microstructures of stainless steels [Sch49]. A: austenite, F: ferrite, M: martensite.

2.1.2. Martensitic Stainless Steels

An addition of between 12 and 18%Cr covers the composition range for the martensitic stainless steels (Table 2-1). They can be distinguished from the ferritic stainless steels, which also incorporate grades with less than 18%Cr, as they nominally have higher carbon contents. This increased level of carbon, an austenite stabiliser, gives complete ferrite transformation to austenite at elevated temperature, Fig.2-2, which subsequently changes to non-equilibrium martensite on rapid cooling, and allows for martensitic grades to achieve high strength and hardness by heat treatment.

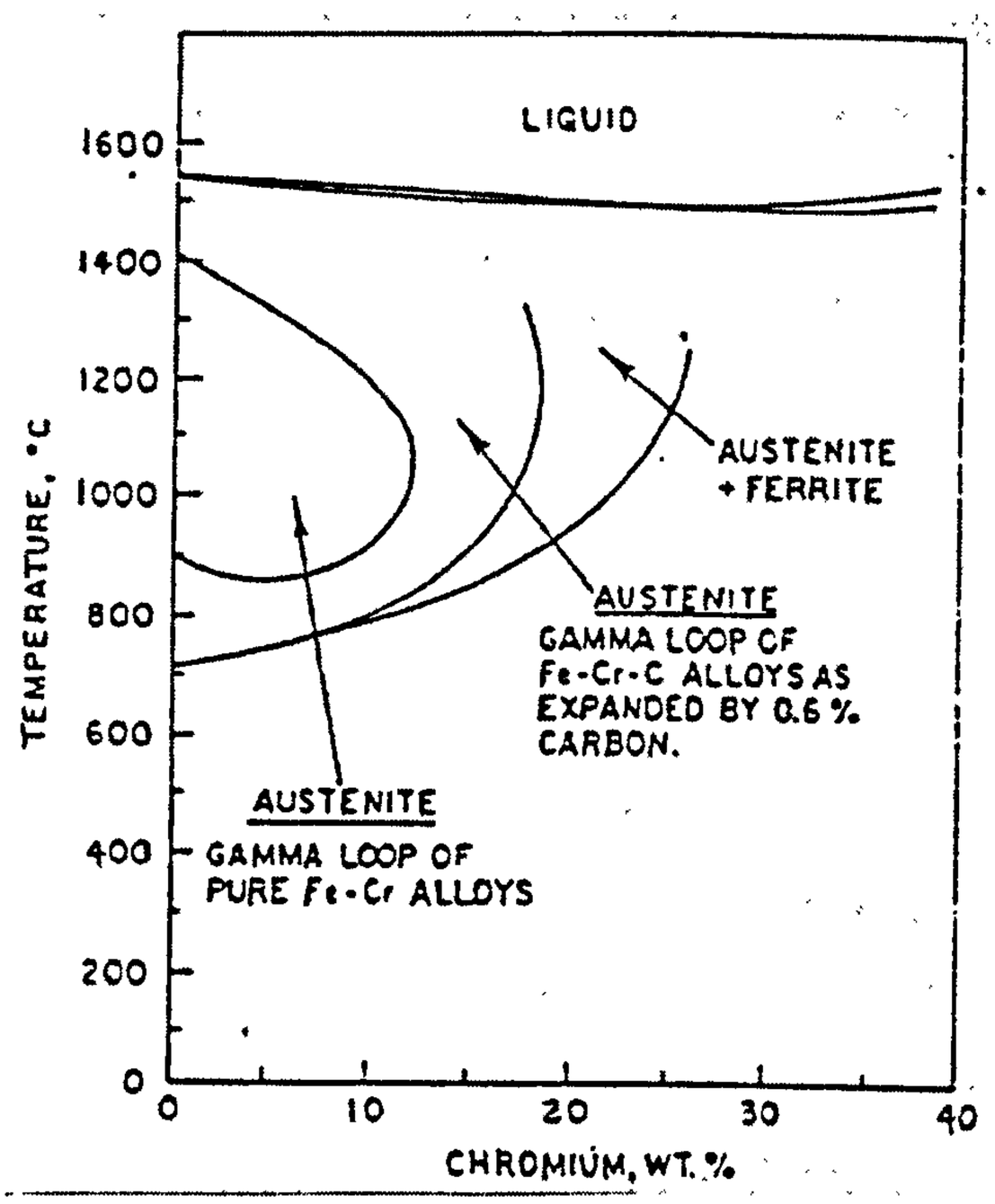


Fig.2-2 Effect of carbon on the gamma loop in Fe-Cr alloys [Zap49].

Low carbon grades, that is below 0.15%C, contain between 11.5 and 14%Cr, and can acquire tensile strengths approaching 1200 MPa in the wrought hard tempered condition. Types 410 and 403 are the most common martensitic grades, with the Cr content of 403 being more restricted than for 410 (13.0% max. compared to 13.5%) to prevent ferrite formation and, in general, 403 also contains lower levels of residual elements. These grades find uses in structural and general engineering applications and, in particular, are employed as turbine blades, valves and fittings, which involve extended service at elevated temperature. Other additions have been made to the lower carbon grades, such as Mo, W, V and Nb, which improve tempering resistance and so provide good high temperature creep strength for power generation, gas turbine and aerospace applications.

Table 2-1 Composition and mechanical properties of martensitic stainless steels

Grade		Nominal composition, wt%			Tensile properties (min.)		
Type	UNS	C*	Cr	Other	Condition	Rm, MPa	$Rp_{0.2}$, MPa
403	S40300	0.15	12	<0.50Si	A,AC	485	275
					TC	825	620
410	S41000	0.15	12	-	A,AC	485	275
					TC	825	620
414	S41400	0.15	13	1.9Ni	C	<1030	-
420	S42000	0.35	13	-	AC	<860	-
431	S43100	0.20	16	1.9Ni	AC	<965	-
F6NM	S41500	0.05	14	4Ni, 0.7Mo	T	790	620
Supermartensitic #		0.02	12	5.6Ni, 2Mo	T (AC)	845	585 (700)
440A	S44002	0.6-0.75					
440B	S44003	0.75-0.95	17	<0.75Mo	AC	<965	-
440C	S44004	0.95-1.20					

* Carbon levels are maxima, unless stated otherwise. Si and Mn are generally 1.0% max.
\# Example. Not yet standardised.
Steels are in the wrought condition with the following finish codes:
A - Annealed; C - Cold finish; T - Tempered
Elongation typically 20% minimum (annealed)

Grade 420 also contains about 13%Cr, but at higher carbon levels than 403 or 410. It can be tempered without substantial loss in corrosion resistance, which provides the grade with high hardness and reasonable ductility, suitable for cutlery manufacture.

The higher carbon martensitic grades (>0.6%C), designated 440, are divided into three sub-grades, dependent on carbon content, and are available in either the quenched and tempered or stress relieved conditions. They are utilised where high hardness and wear resistance are required, combined with moderate corrosion resistance. However, due to the high carbon level, their use is limited to applications where toughness is not an issue.

Other martensitic grades contain small additions of Ni to increase strength, but at an insufficient level to produce a fully austenitic structure at room temperature. At the 1.25 to 2.50%Ni level, two grades exist, designated 414 and 431, which retain some austenite after quenching. Other grades contain up to 6%Ni at low carbon levels producing a "soft" martensite with high strength and toughness. These grades are readily weldable and are produced as forgings (e.g. F6NM) and castings for turbines, pumps and valves for hydroelectric and offshore industries.

Martensitic grades with carbon levels above 0.12% are particularly sensitive to hydrogen cracking when welded, due to the high as-transformed hardness in the HAZ and, when using matching consumables, in the weld metal [Cas74]. Low carbon grades are less susceptible [How77], and, over recent years, a range of such materials have been developed with 0.02%C and improved weldability [Kob88] [Oka93] [Sug91] [Ish92] [Sco93]. Some of these steels have additions of Ni and Mo (also Cu and N) to improve resistance to CO_2 and chloride ions, and are produced in tubular forms for process pipework and pipelines, where good weldability is required. These so-called *supermartensitic* materials are considered low cost alternatives to duplex stainless steels, for applications where the uninhibited corrosion rate of carbon steel is unacceptable.

To produce a combination of strength, ductility and toughness, martensitic stainless steels are often air hardened and tempered. Nevertheless, this must be carried out outside the 450 to 540°C temperature range, as otherwise carbides precipitate at the grain boundaries causing *temper embrittlement* and a reduction in the notch ductility. Another form of embrittlement that may arise during melting, welding, heat treatment, or pickling and electrochemical processing, is due to hydrogen. While temper embrittlement typically is shown by a sharp drop in impact values, *hydrogen embrittlement* can take several days and even weeks to develop.

2.1.3. Ferritic Stainless Steels

The ferritic stainless steels tend to sustain their ferritic microstructure at all temperatures and, in general, cannot be strengthened by second phase formation during heat treatment. As illustrated in Table 2-2, there are a number of ferritic alloys which can be grouped dependent on their chromium content.

Grades 405 and 409 lie at the lower end of the range (11-14%Cr) and are primarily used as structural steels, although, as type 405 can easily be formed, it is utilised also in more demanding applications such as steam turbines and oil refinery components. Further, grade 405 offers good *weldability* as austenite formation at temperature restricts grain growth in the HAZ. Conversely, as type 409 was designed specifically for use as sheet and strip, it remains ferritic at all temperatures and so, on welding, grain growth takes place in the HAZ with a commensurate drop in toughness. Despite this limitation, grade 409 is produced in large tonnages, finding major applications in the automotive industry, especially in exhaust systems. Modified grades exist also, with 0.75%Nb for improved high temperature strength and 1%Al for oxidation resistance, to meet the increasing temperature and corrosion resistance requirements of present day automotive exhausts. Further, very low carbon 12%Cr grades (<0.03%C) have been developed for improved weldability. This last type of ferritic stainless steel is commonly referred to as "3CR12" and forms a soft low carbon martensite in the HAZ with moderate as-welded toughness.

Types 430, 434, and 436 (17-19%Cr) find decorative and functional applications, such as automotive trim, as well as household appliances and cookware. Type 430 was initially used on automobiles, but, as a result of corrosion from the salt used on icy roads, type 434 with 1%Mo was developed with increased corrosion resistance. However, where severe stretching in the formation of a component is required, 436 with Nb additions is preferred to 434. All these 17%Cr ferritic alloys form some austenite at temperature, which transforms to martensite on cooling. Grade 439 also contains 17-19%Cr, but is stabilised by Ti for intergranular corrosion resistance, and, as Ti is a ferrite stabiliser, remains ferritic at all temperatures.

Table 2-2 Composition and mechanical properties of ferritic stainless steels

Grade		Nominal composition, wt%					Tensile properties (min)	
Type	UNS	C*	Cr	Ni	Mo	Others	Rm, MPa	$Rp_{0.2}$, MPa
Low Cr grades								
405	S40500	0.08	12	-	-	0.2Al	480	275
409	S40900	0.08	11	-	-	Ti>6xC	415	205
"3CR12"		0.03	12	-	-	-	415	205
Medium Cr grades								
430	S43000	0.12	17	-	-	-	480	275
434	S43400	0.12	17	-	1	-	530	365
436	S43600	0.12	17	-	1	Nb+Ta >5xC	530	365
439	S43900	0.7	18	<0.5	-	<1.1Ti	-	-
High Cr grades								
442	S44200	0.20	20	-	-	-	515	275
446	S44600	0.20	25	-	-	-	480	275
26-1	S44625	0.1	26	<0.5	0.85	<0.4Mn,<0.2Cu <0.4Si, <0.015N	450	275
29-4-2	S44800	0.1	29	2.2	4.0	<0.3Mn,<0.2Si	550	415

* Carbon levels are maxima. Si 1%max, Mn 1.0-1.5
Elongation typically 20% minimum (annealed)

Although ferritic grades with between 22 and 30%Cr, like 442 and 446, have been used for many years, they have inherently low toughness due to the presence of interstitial and residual elements, such as C, N, S, P and O. Since the development of modern refining processes, such as argon and vacuum oxygen decarburisation (AOD and VOD), these elements have been reduced and new grades have emerged which can be fabricated into useful industrial products, provided they are properly annealed, welded and formed. Examples are 26-1 and 29-4-2, both of which contain Mo, and exhibit superior pitting and *stress corrosion cracking* (SCC) resistance in chloride media compared to the standard austenitic grades. They are used in the chemical industry and in power generation plants, where sea water is present for cooling purposes.

)

There are a number of problems associated with ferritic stainless steels. For instance, where the ferritic microstructure is present at all temperatures, grain growth is displayed in heavy sections and in the HAZ during welding, with a consequent loss in notch ductility. As cold work and recrystallisation is often impractical, this factor limits the application of the ferritic stainless steels.

Other problems associated with ferritic stainless steels involve precipitation of deleterious phases during exposure to elevated temperatures. Between 340 and 520°C, or slowly cooling through this temperature range, an increase in hardness results with a drop in ductility. This is primarily due to the precipitation of the Cr-rich *alpha prime* phase [Fis53] [Wil58], often referred to as *475 embrittlement*. This phenomenon is of more concern with the higher chromium steels, as 13%Cr grades are considered immune. Another deleterious precipitate is known as *sigma* phase, which forms between 540 and 870°C at grain boundaries. However, sigma phase formation is uncommon below the 14 to 15% Cr level, unless the steel is cold worked or alloyed with Mo, Ti, Nb or other elements which enhance its formation [Hus79].

2.1.4. Austenitic Stainless Steels

The austenitic stainless steels, or Fe-Cr-Ni alloys, are the most common class of stainless steel and account for about 70% of total stainless steel production. They obtain their austenitic microstructure by the addition of Ni, a strong austenite stabiliser. In most cases, the austenitic structure remains at elevated and cryogenic temperatures and, like some of the ferritic alloys, they cannot be hardened to form martensite by cooling. Furthermore, the grain size cannot be controlled except by cold rolling and recrystallisation. However, the austenitic grades can be work hardened, while some of the less stable members of the class can undergo transformation to martensite, leading to a substantial increase in strength. Even so, the austenitic stainless steels are more easily formed and welded than the ferritic grades, explaining their increased popularity.

The most heavily produced austenitic grade nominally contains 19%Cr and 9%Ni, and is commonly referred to as 304. It is available in all product forms, finding uses where resistance to mildly corrosive aqueous environments is required. However, for more demanding service, particularly in the presence of chloride ions, higher alloy grades exist producing an overall composition range of 16-26%Cr and 8-30%Ni (Table 2-3).

Table 2-3 Composition and mechanical properties of austenitic stainless steels

Grade		Nominal composition, wt%					Tensile properties (min)	
Type	UNS	C*	Cr	Ni	Mo	Others	Rm, MPa	$Rp_{0.2}$, MPa
300-series grades								
304	S30400	0.08	19	9	-	-	515	205
							1030#	690#
304L	S30403	0.03	19	10	-	-	480	170
304H	S30409	0.04-0.10	19	9.2	-	-	515	205
308	S30800	0.08	20	11	-	-	515	205
309	S30900	0.20	23	13.5	-	-	515	205
310	S31000	0.25	25	20.5	-	-	515	205
316	S31600	0.08	17	12	2.5	-	515	205
317	S31700	0.08	19	13	3.5	-	480	205
321	S32100	0.08	18	10.5	-	Ti>5xC	515	205
347	S34700	0.08	18	11	-	Nb+Ta >10xC	515	205
High alloy and superaustenitic grades								
904L	N08904	0.02	21	25.5	4.5	1.5Cu	490	220
1925hMo	N08926	0.03	21	25	6.5	0.2N, 0.9Cu	650	300
254SMO	S31254	0.02	20	18	6.2	0.75Cu, 0.2N	650	300
654SMO	S32654	0.01	24	22	7.3	0.5N, 3Mn, 0.5Cu	750	430

* Carbon maxima, unless range given.
# Cold worked.
Elongation typically 35-40% minimum (annealed).

Depending on the composition of the alloy, a mixed solidification mode can result, as illustrated in Fig.2-3. In the lower alloy grades, commonly referred to as the 300-series, primary solidification to ferrite takes place, which is followed by a solid state transformation to austenite. Small amounts of retained ferrite are deemed beneficial, as it increases weldability by reducing the risk of *solidification cracking*. However, the presence of ferrite can be detrimental in some service environments and so, for the more highly alloyed grades, the composition is balanced to ensure direct solidification to austenite.

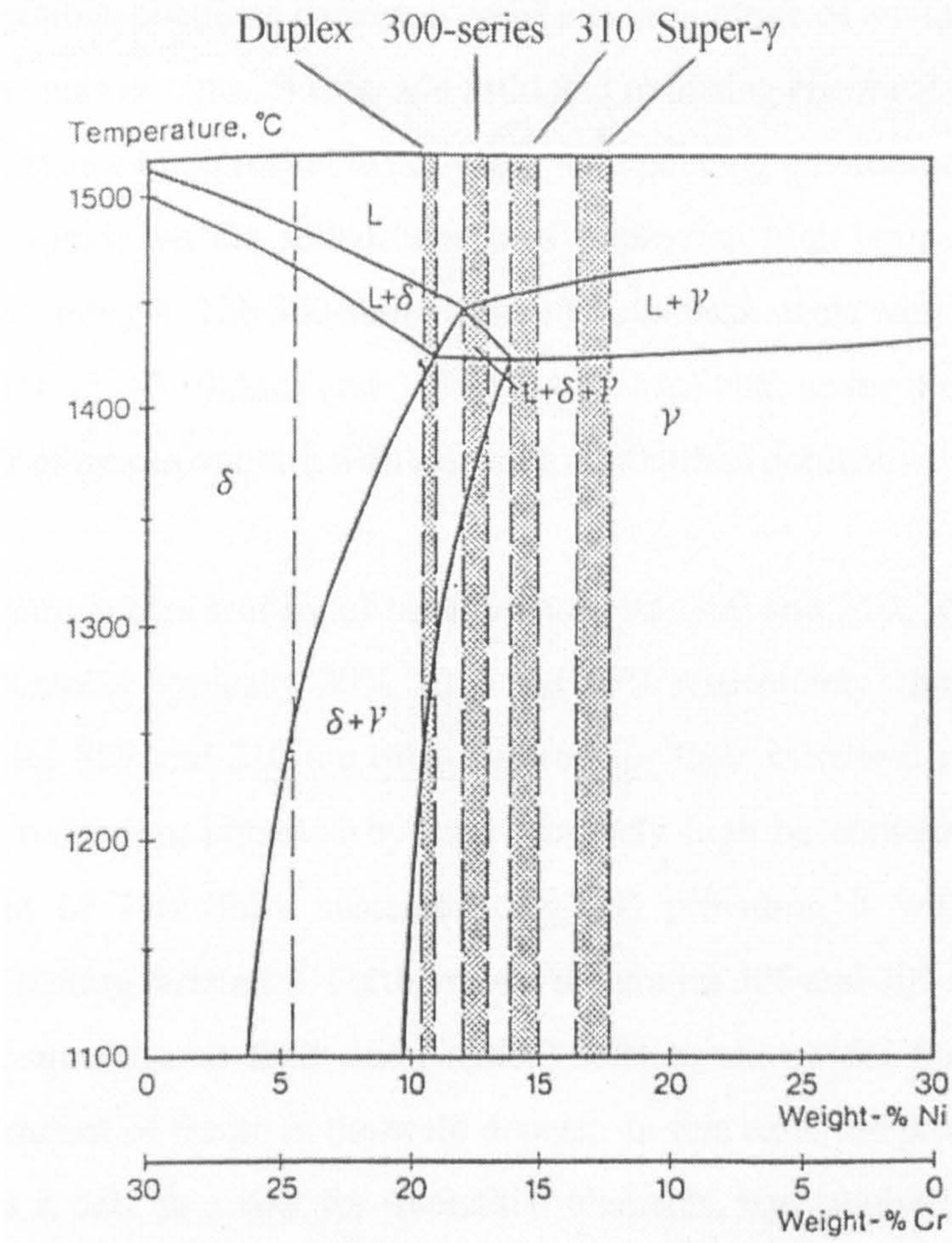


Fig.2-3 Pseudo-phase diagram for 70%Fe-Cr-Ni alloys.
L-liquid; δ-ferrite; γ-austenite

Type 304H is the high carbon version of 304, containing between 0.04-0.10%C, which enhances its strength and creep resistance. Nevertheless, if type 304H is exposed to temperatures in the range 425-815°C the carbide $M_{23}C_6$ forms at the grain boundaries (where M=Cr), whilst the adjacent region is chromium depleted. If the steel is subsequently solution annealed or exposed to high service temperatures, chromium is able to diffuse back into the denuded region ("healing") negating any problems. However, if the steel remains *sensitised* and is exposed to a corrosive environment, the denuded regions are preferentially attacked. This form of attack is called *intergranular corrosion* which is restricted by reducing the carbon content to below 0.03%C, as in the low carbon variant 304L, or by stabilising the steel using Ti and Nb additions, as in grades 321 and 347, respectively. In these latter two grades, Ti and Nb have a stronger affinity for carbon than chromium and so preferentially form carbides. Inevitably this reduces the formation of chromium carbides and denuded zones.

Grade 304 exhibits adequate corrosion resistance in a range of environments, such as industrial and marine atmospheres, and mild and oxidising chemical media. However, to ensure resistance to corrosion in sea water and reducing environments, Mo is added to the steel, which has the added benefit of improving high temperature creep and stress-rupture strength. The 300-series austenitic stainless steels with Mo additions are designated 316 (2.0-3.0%Mo) and 317 (3.0-4.0%Mo) and, as for the 304 types, there are a number of grades varying with respect to the carbon content.

Other austenitic grades worthy of mention are 308, 309 and 310, which have higher chromium contents (typically 20%, 23% and 25% respectively) than the 304 or 316 grades. Grades 309 and 310 are often utilised for their increased resistance to high temperature oxidation, imparted by their relatively high Ni content, with the higher alloy content of 310 (fully austenitic, Fig.2-3) providing it with excellent high temperature scaling resistance. Furthermore, the grades 308 and 309 are often used for welding consumables as their composition balance allows for the formation of a controlled amount of ferrite in the weld deposit. In this case, the presence of ferrite is beneficial as it acts as a sink for interstitial elements, e.g. sulphur, which form low melting point films and cause solidification cracking [Goo90].

The use of *superaustenitic* stainless steels, with around 6%Mo, is becoming more widespread as the demand for plant reliability in aggressive process environments increases. They have been directly developed from the 300-series austenitic steels with increased additions of Cr, Mo, Cu and N (Table 2-3) to improve pitting resistance to reducing acids and chloride containing media. Higher Ni levels are required, than in the 300-series grades, to balance the steel and to produce a fully austenitic microstructure at ambient temperature, Fig.2-3. It is not uncommon to find nitrogen alloyed into these steels (up to 0.5%), which increases strength and pitting resistance and also stabilises austenite. These steels are now commonplace in the pulp and paper industry and for oil and gas process pipework and equipment.

The 300-series austenitic stainless steels are easily welded by virtue of a stable microstructure at elevated temperatures. Some susceptibility to solidification cracking should be noted [Goo90], but this can be overcome by selection of consumables which retain some ferrite on cooling. However, the high alloy content of the superaustenitic grades enhances the formation of sigma phase in the HAZ during welding. Nevertheless, as these hard particles form in a ductile austenitic matrix, they are not considered to have a significant effect on mechanical properties.

2.1.5. Ferritic-Austenitic Duplex Stainless Steels

The major distinguishing feature between the ferritic-austenitic duplex stainless steels, and the other classes is their two phase microstructure. Typically, a wrought product will contain between 40 and 60% ferrite, balance austenite, which can be adjusted to obtain specific material properties. The composition of the standard duplex alloys falls in the δ-ferrite + γ-austenite phase field (Fig.2-3), but as the δ/δ+γ and δ+γ/γ boundaries are not vertical, the proportions of ferrite and austenite vary with temperature, with the structure becoming more ferritic at higher temperatures. It is for this reason that the duplex structure of wrought alloys is produced by hot working and annealing at elevated temperatures and quenching from between 1020 and 1100°C.

Table 2-4 Composition and mechanical properties of modern duplex grades

Grade		Nominal composition, wt%						Tensile properties (min)	
Type	UNS	Cr	Ni	Mo	Cu	W	N	Rm, MPa	$Rp_{0.2}$, MPa
2205	S31803	22	5	3	-	-	0.14	620	450
	S32205	22.5	5	3.2	-	-	0.16		
2304	S32304	23	4	-	-	-	0.1	600	400
Alloy 255	S32550	25	5.5	3	2	0.16	0.18	760	550
Superduplex grades									
2507	S32750	25	7.5	4	-	-	0.28	795	550
Zeron 100	S32760	25	7	3.7	0.6	0.6	0.24	750	550
DP3W	S39274	25	7	3.2	0.5	2	0.3	780	550

Carbon less than 0.03%.
Elongation range between 15 and 30%

Duplex stainless steels have found increasing popularity, as they offer an attractive combination of properties. They compete with the martensitic and ferritic grades for corrosive applications, as they are more easily welded (Table 2-5). Further, duplex alloys offer much higher strength-to-weight ratios than the austenitic grades, combined with superior resistance to chloride SCC.

The present range of alloys originated from cast compositions of 25Cr/5.5Ni/3Mo with additions of N and Cu (Alloy 255 in Table 2-4), designed for use in sulphuric acid plant. Subsequently, these castings were used extensively for pumps and valves in the oil and gas industry, but, more recently, the wrought form, i.e. S31803, based around a lower chromium content (22Cr/5Ni/3Mo/0.16N), has found increasing use in process plant and pipework.

As a result of the susceptibility of duplex alloys to the precipitation of embrittling intermetallic phases, such as sigma phase, high temperature use is limited to about 300°C, whilst cryogenic service is prohibited due to poor weld metal toughness below, say, -40°C. The corrosion resistance, as for other stainless steels, mainly depends on the Cr, Mo and N contents. For this reason, the cast 25Cr/5.5Ni/3Mo/0.18N alloys have superior corrosion properties compared to the wrought 22Cr/5Ni/3Mo/0.16N form.

As many applications require the versatility of plate and pipe, wrought grades have been developed with 25%Cr. These *superduplex* alloys contain 7%Ni to maintain a 50:50 ferrite:austenite phase balance, with up to 4%Mo to improve pitting resistance (Table 2-4). Other additions include nitrogen, up to 0.3%, for strength, pitting resistance and to maintain the HAZ phase balance. Cu and W are added also for corrosion performance in specific media. A summary of the effects of each alloying element on the properties of duplex stainless steels is given in Table 2-5 and described further in the next section.

Table 2-5 Summary of stainless steel properties by class

Property	Stainless steel class			
	Martensitic	**Ferritic**	**Austenitic**	**Duplex**
Strength	High by heat treatment	Good, non-hardenable	Good, if cold worked	Good, improved by cold work
Physical property	Magnetic	Magnetic	Non-magnetic	Semi-magnetic
Corrosion resistance	Moderate	Moderate to good, improves with Cr. Good wet abrasion. Superferritic grades offer improved pitting and chloride SCC	Good, improves with Mo, ie superaustenitic grades. Good wet abrasion. 300-series grades susceptible to chloride SCC, superaustenitic grades resistant.	Good pitting resistance, especially superduplex grades; high SCC resistance
Temperature	Brittle below 0°C	Brittle below 0°C	Cryogenic and elevated service (scaling resistant) to 925°C.	-100°C (-40°C if welded) to +300°C
Weldability	Poor	Moderate to poor. Newer 12%Cr grades are better.	Excellent, all processes. Also good formability.	Good, most processes. Also good formability.
Typical applications	Knife blades, shafts, spindles, nozzles, springs, fasteners	Sinks, kitchen utensils, conveyors and liners, transport equipment, automotive exhausts and trim	Cleanability and hygiene: food & drink, hospital & pharmaceutical. Cryogenic: Storage of liquefied gases. High temperatures: heat exchangers, furnace components (up to 925°C), fume extraction. Grade 310 can operate at 950 to 1100°C. Corrosion: tanks, pipework, vessels, valves (for chemical, petrochemical, pulp & paper, mineral extraction)	Oil and gas, sea water, desalination, heat exchanger panels and tubes, materials handling equipment, tanks and vessels
Product forms	Bar, strip	Sheet and coil, welded tube.	Plate, sheet, coil, strip, tube, pipe, bar, rod, wire.	Plate, sheet, tube and pipe

2.2. DUPLEX STAINLESS STEELS

2.2.1. History and Development

A duplex alloy is defined as one that contains a two-phase structure and is more often a description of an alloy where both phases are present in significant quantities. In the context of this thesis, the term duplex stainless steel covers ferritic/austenitic Fe-Cr-Ni alloys with between 30 and 70% ferrite. The first reference to such alloys appears in 1927, when Bain and Griffith published data on ferritic:austenitic structures [Bai27]. Within the next few years, several foundries in France, Germany, Sweden and the USA explored such steels, initially in the cast form.

Possibly the first commercial product dates to 1929 [Lef97] when Avesta Jernverk produced a grade called 453E with approximate composition 25%Cr-5%Ni. Soon after in 1932 and 1933 a modified grade with 25%Cr-5%Ni-1%Mo (grade 453S) was marketed. Applications included coolers of the Brobeck type (plate and forgings), autoclaves for gunpowder production (castings) and valves for sulphite pulp (castings).

Another record of early duplex products dates back to 1933, when an error during the melting of an 18%Cr-9%Ni-2.5%Mo grade at the Firminy works of the J. Holtzer Company, France, lead to a 20%Cr-8%Ni-2.5%Mo steel. Subsequent analysis of the casting found it had a high volume fraction of ferrite in an austenitic matrix and was not sensitive to intergranular corrosion (IGC) in various corrosive media [Hoc50]. This was a significant discovery, as the high carbon austenitic grades of the time tended to form a continuous chromium carbide network, leading to rapid corrosion in the surrounding chromium depleted zones [Sch38] [Pay32] [Col55] [Hoc73]. This observation, combined with the superior strength over the austenitic grades [Tru65], encouraged French patents to be issued in 1935 and 1937 [Pat35] [Pat37]. The latter patent covered a grade with copper additions to further enhance the corrosion resistance in the most aggressive media. Research was undertaken at several laboratories [Ros86], so that, by the late 1940s, a new family of stainless steel was available which was patented and marketed simultaneously in France, Sweden and the USA.

The Korean war (1950-1) encouraged a nickel shortage, which led to further research into the relatively low nickel-content duplex alloys. It became apparent that a balance of ferrite and austenite had better resistance to chloride SCC than a fully austenitic microstructure. Ever since, this has been one of the main exploited advantages of duplex over austenitic stainless steels. In France the UR50 grade with 20-35% ferrite (UNS S32404) was marketed in various product forms, including forgings, for such industries as oil refining, food processing, pulp and paper, and pharmaceuticals. These steels were produced in high frequency induction furnaces using precisely weighed alloying additions. A partial vacuum ensured carbon removal, rudimentary deoxidation and restricted nitrogen ingress [Cha91]. Nevertheless, plate products remained sensitive to expensive edge cracks [Sou90].

Towards the end of the 1950s, the cast alloy CD4-MCu, originally with about 70% ferrite, was marketed (UNS J93370), but had relatively poor toughness and ductility. Improvements were made [Fon64] [Fon65] by lowering the chromium content to 22-23% and the introduction of a quench-annealing treatment to increase ductility. And yet, the understanding of physical metallurgy still had not progressed sufficiently to offer a material that was easy to manufacture and fabricate. These factors gave the duplex a reputation for crack sensitivity and left them in a niche market until the 1960s.

During the late 1960s and early 1970s, there were two main factors which progressed the development and use of duplex alloys. First, there was another nickel shortage that pushed up the price of austenitic alloys, combined with increased activity in the offshore oil industry which demanded a stainless material to handle aggressive environments. Second, steel production process techniques improved dramatically with the introduction of the vacuum and argon oxygen decarburisation (VOD and AOD) practices. These techniques lead to steels with simultaneously low carbon, sulphur and oxygen contents whilst allowing for greater control of composition, especially nitrogen.

One example of such a steel was UNS S31500 (e.g. 3RE60) which had a maximum carbon content of 0.03% and was designed for enhanced SCC resistance [PatUSa]. In particular, the chemical composition was more carefully controlled to optimise the ferrite:austenite phase balance and nitrogen was added to improve corrosion resistance and high temperature microstructure stability, e.g. the HAZ by stabilising the austenite. The hot workability and rolling experience was greatly improved [Tsu91] [Kom91], making possible the production of wide sheets and coils.

Another approach taken in the Soviet Union was to add titanium to the steel (about 0.4%Ti), in a similar manner to stabilised 300-series austenitic grades. The titanium formed carbides in preference to chromium and reduced the frequency of IGC. Further, the titanium carbides helped to pin the grain boundaries and restricted excessive ferrite grain growth in the HAZ [Yus93].

Even though grades such as S31500 were a breakthrough in alloy design and can be described as the second generation of duplex stainless steel, they were still susceptible to IGC under certain conditions [Hen75] [Ols86] [Ols94]. This was believed [Hof81] to be due to a high Cr/Ni equivalent ratio which lead to an almost fully ferritic HAZ after welding with associated grain growth. As the solubility of carbon and nitrogen is very low in ferrite, carbides and nitrides precipitated along grain boundaries and caused local chromium depletion of the matrix, i.e. sensitisation. To overcome this problem, higher levels of nickel and nitrogen were added and IGC resistance was greatly improved.

In the early 1970s, the 22%Cr duplex grade was developed in Germany and Sweden, i.e. DIN 1.4462 or UNS S31803 (Table 2-4). One patent [Pat72] claimed that this new steel was not sensitive to IGC upon welding due to a balanced chemistry (i.e. Cr/Ni equivalent ratio), including the addition of nitrogen [Cha91], Fig.2-4. And yet, as the permitted compositional ranges were too wide, highly ferritic HAZs formed with an associated reduction in corrosion resistance [Qui94].

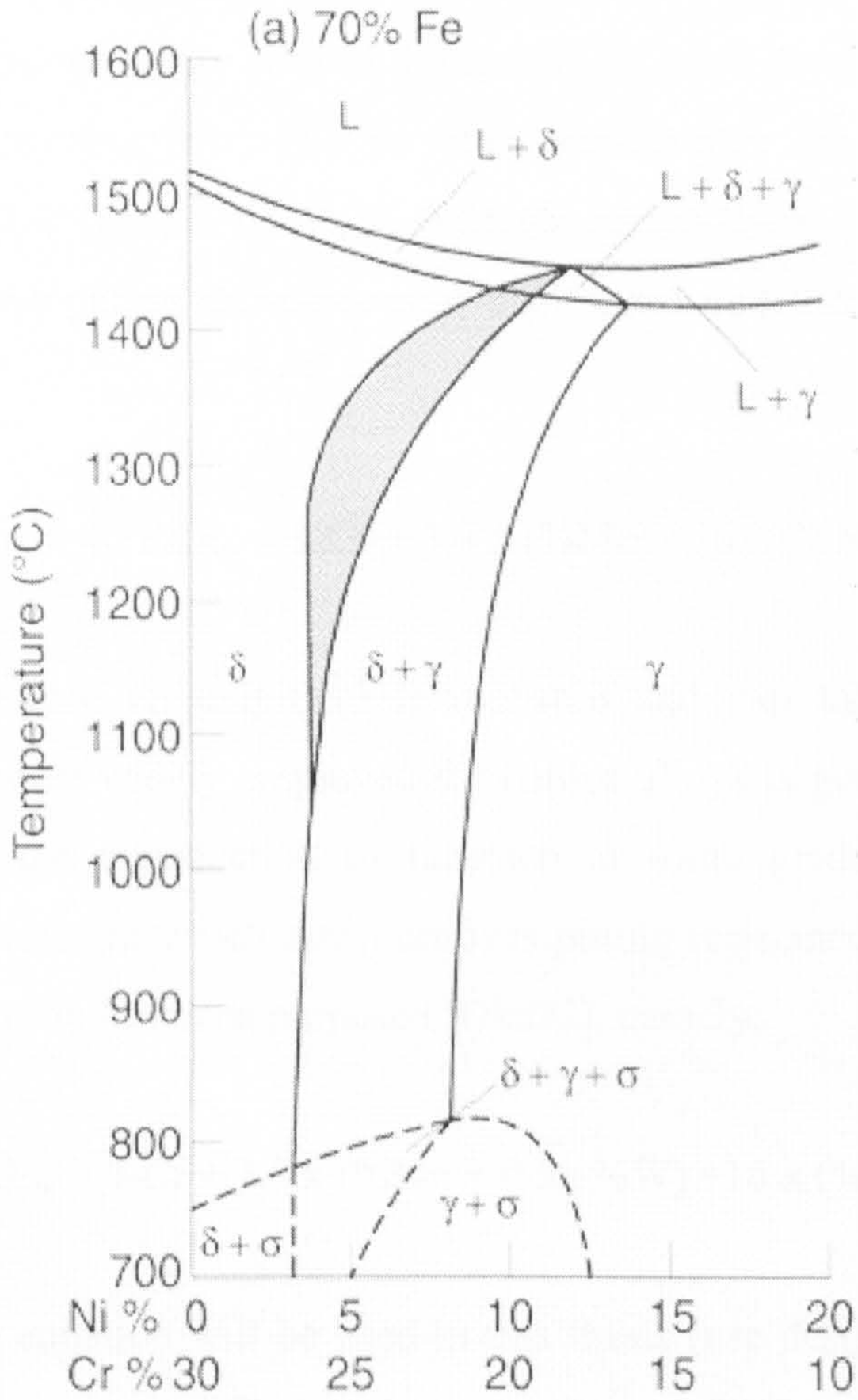


Fig.2-4 Section through **the ternary Fe-Cr-Ni constitution diagram at 70%Fe. The schematic effect of nitrogen is shown by the shaded area [Cha91].**

Such wide compositional ranges persist in national and international specifications (e.g. S31803), even though most producers and end users commonly specify closer limits to control the weldability. In particular, it is has proved important to keep the nitrogen content towards the upper end of the range, e.g. the limits specified for S32205 (Table 2-4). This latest development has marked the introduction of the third generation of duplex alloys, signalling that the production and welding metallurgy have become established.

More highly alloyed grades with 25%Cr have existed for sometime, typified by the S32550 alloys (e.g. Ferralium 255) which also contain up to 2%Cu. These alloys were originally developed as castings, such as pumps and valves, and have been used extensively in the offshore industry and for sulphuric acid service.

During the 1980s, more highly alloyed duplex grades were developed to withstand more aggressive environments. The so-called superduplex grades contain about 25%Cr, 6-7%Ni, 3-4%Mo, 0.2-0.3%N, 0-2%Cu and 0-2%W (Table 2-4). These grades typically have pitting resistance equivalent numbers (PRE_N) greater than 40, where:

$$PRE_N = \%Cr + 3.3 \times (\%Mo) + 16 \times (\%N) \quad \text{--Eqn \{1-1\}}$$

PRE_N is derived from an empirical relationship and can take several forms. Nevertheless, the most widely employed for duplex alloys is given above [Ple82]. However, due to the introduction of tungsten to some grades of superduplex stainless steel, an element which also improves pitting resistance, a modified form of the PRE relationship has been proposed [Oka92], namely:

$$PRE_W = \%Cr + 3.3 \times (\%Mo + 0.5 \times \%W) + 16 \times (\%N) \quad \text{--Eqn \{2-1\}}$$

Both forms of the equation will be used in this thesis (use designated by N or W sub-fix). Clearly there is no difference between the two PRE forms for those steels with only residual tungsten contents.

In the making of superduplex alloys, the steel makers took care to balance the Cr and Ni-forming elements, and added higher levels of nitrogen (Fig.2-4). These two factors provided the steels with thermal stability during welding and high strength. On the down side, the higher alloy content promotes intermetallic precipitation (leading to a reduction in properties). But this deleterious phenomenon can be avoided by good process control and solution annealing practice, and by limiting arc energies and interpass temperatures during welding.

Another development during the 1980s was a lean alloy grade exemplified by S32304. The lower alloy content, in particular Mo, than the standard grade S31803 means that it is cheaper to produce, but has lower pitting resistance. In this respect, it competes with the high volume production austenitic grades, such as 304L and 316L, on the grounds of its higher strength, similar pitting resistance in chloride media and better resistance to chloride SCC.

2.2.2. Alloying Additions

Chromium

The main advantage of adding chromium to steel is to improve the localised corrosion resistance, by the formation of a passive chromium-rich oxy-hydroxide film [Has79]. Electrochemically this is achieved by extending the passive range (refer to Fig.2-5) and reducing the rate of general corrosion (i_{pass}). However, there is a limit to the level of chromium that can be added to such a steel, as the beneficial effect of ever higher levels is negated by the enhanced precipitation of intermetallic phases, Table 2-6 and Fig.2-6, such as sigma. These phases often lead to reduction in ductility, toughness and corrosion properties.

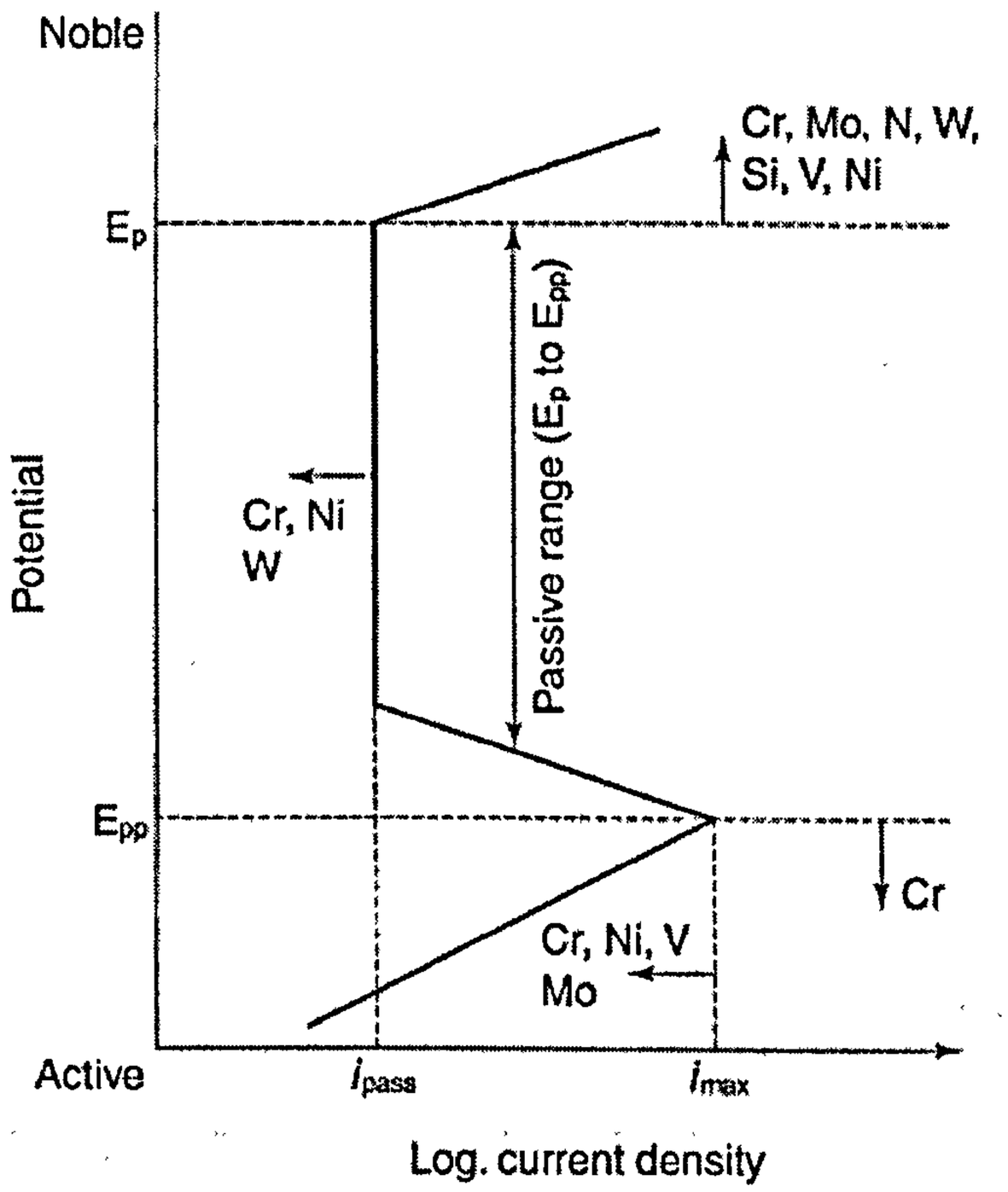


Fig.2-5 Schematic summary of the effects of alloying elements on the anodic polarisation curve [Sed84].

Chromium and other elements stabilise ferrite, although the effect of different elements vary. Equations have been derived to quantify these effects (the so-called chromium equivalents, Cr_{eq}) of which the most favoured is [Kot92]:

$$Cr_{eq} = \%Cr + \%Mo + 0.7x\ \%Nb \quad \text{-- Eqn \{2-2\}}$$

Table 2-6 Influence of different alloying additions and microstructure on the pitting and crevice corrosion resistance of duplex stainless steels. Based on ref [Ber91].

Alloying elements	Effect	Reason	Practical limitation
C	Negative	Causes precipitation of chromium carbides with accompanying chromium depleted zones	About 0.03% maximum
Si	Positive	Si stabilises the passive film	About 2% maximum, due to its effect on structural stability and on nitrogen solubility
Mn	Negative	Mn-rich sulphides act as initiation sites for pitting. Mn may also destabilise the passive film.	About 2%. Higher levels might also increase the risk of intermetallic precipitation
S	Negative	Sulphides, if not Cr-, Ti- or Ce-rich, tend to initiate pitting attack	About 0.003%, if maximum pitting resistance required. For reasonable machinability, up to 0.020% allowed.
Cr	Positive	Cr stabilises the passive film	Between 25-28% maximum depending on the Mo-content. Higher Cr-content increases the risk of intermetallic precipitation.
Ni	Negative	Increased Ni, other elements constant, dilutes the γ-phase with regard to N, which in turn decreases the PRE of the γ-phase. If the alloy is very sensitive to precipitation of chromium nitrides, Ni can have a positive effect.	Ni should primarily be used to give the alloy the desired austenite content.
Mo	Positive	Mo stabilises the passive film, either directly or through enrichment beneath the film.	About 4-5% maximum depending on the Cr-content. Mo enhances the risk of intermetallic precipitation.
N	Positive	N increases the PRE of the γ-phase dramatically, not only by increasing the N-content, but also by increasing the Cr and Mo contents through their partitioning coefficients.	About 0.15% in Mo-free grades. About 0.3% in superduplex grades and some 0.4% in 25%Cr, high Mo, high Mn alloys.
Cu	Disputed	Marginal positive or negative effects	About 2.5% maximum. Higher levels reduces hot workability and undesirable hardenability
W	Positive	Probably the same as for Mo	Increases the tendency for intermetallic precipitation. 1%W max in 4%Mo steel & 2%W max in 3%Mo steel
Ferrite	Positive	Increased ferrite content increases the N, Cr and Mo contents of the γ-phase	Too high ferrite can enhance chromium carbide/nitride precipitation in a coarse microstructure
Sigma phase	Negative	Precipitates with accompanying depletion of alloying elements (Cr, Mo)	If steel manufacturers recommendations are followed, intermetallic precipitation should not occur during heat treatment or welding.
Chromium carbides and nitrides	Negative in oxidising & corrosive Cl^- containing media	Precipitation of carbides/nitrides causes Cr-depleted zones which are selectively attacked in certain corrosive media	In older generations of duplex alloys, nitrides were frequently present in welded joints and in base metal with a coarse microstructure. This has rarely been the reason for a corrosion failure

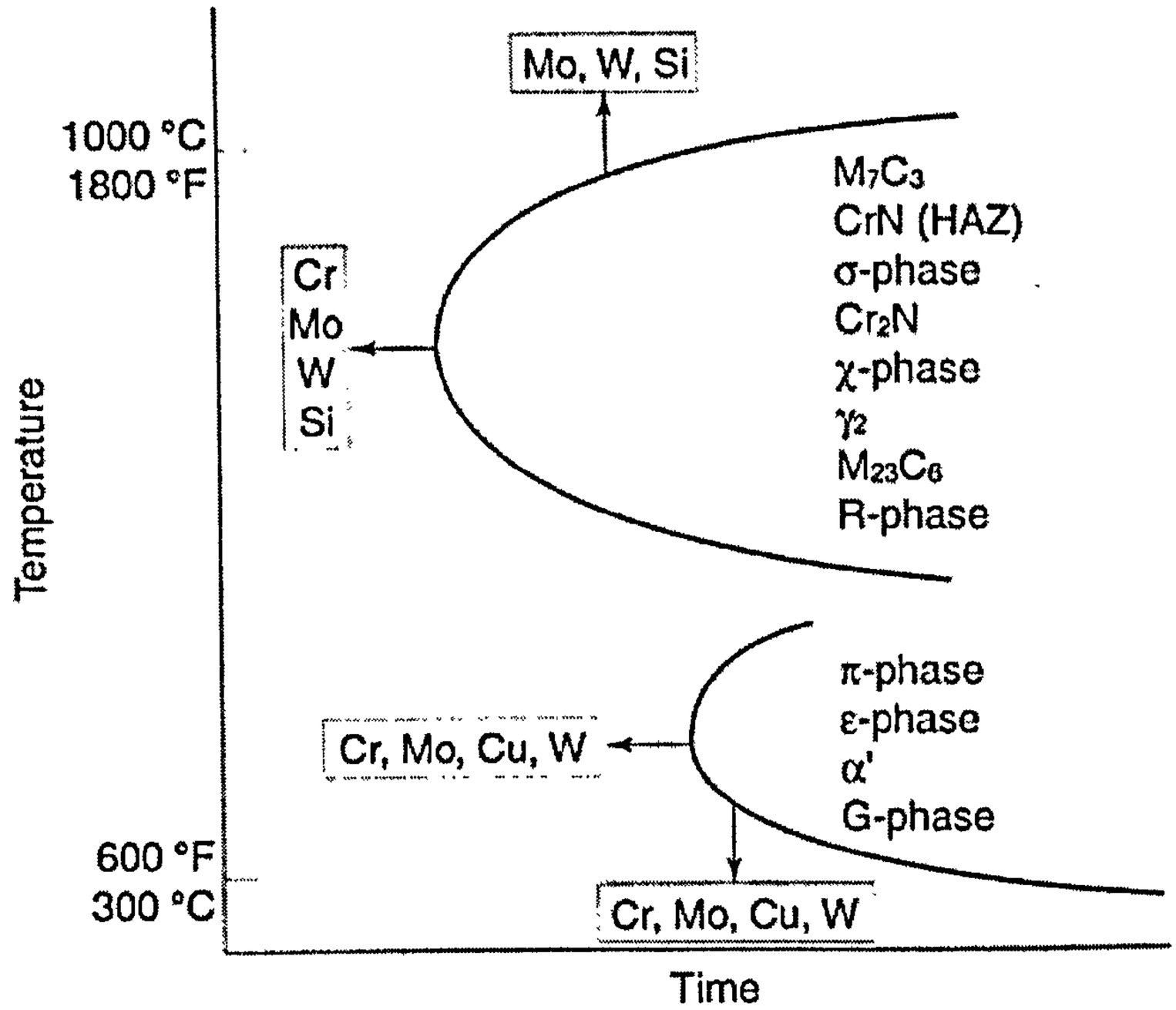


Fig.2-6 Schematic summary of the effects of alloying elements on the formation of various precipitates [Cha91].

Molybdenum

The beneficial influence of molybdenum on the pitting and crevice corrosion resistance of an alloy in chloride solutions has been recognised for many years (Fig.2-5). As for chromium, molybdenum extends the passive potential range and reduces the corrosion current density (i_{max}) in the active range. Molybdenum is included in both PRE relationships, Eqns {1-1} & {2-1}, and is given a coefficient of 3.3 times that of chromium, whilst it has a similar effect on ferrite stability as chromium, Eqn {2-2}. The mechanism by which molybdenum increases the pitting resistance of an alloy has been examined by a number of workers [Sed79] [New84] [Ole84] [Ann84], and has been found to suppress active sites via formation of an oxy-hydroxide or molybdate ion [Hal95].

In high temperature sea water, the addition of at least 3%Mo is recommended [Nag81] to prevent crevice corrosion, while an upper limit of about 4%Mo has been quoted [Ros86]. This limit stems [Gol51] from the enhanced sigma forming tendency in the hot working temperature range, i.e. above 1000°C, Fig.2-6.

Nickel

Counter to the ferrite-stabilising effect of chromium (Mo and Nb), there is another group of elements which stabilise austenite [Kot92]:

$$Ni_{eq} = \%Ni + 35x\ \%C + 20x\ \%N + 0.25x\ \%Cu \quad \text{-- Eqn \{2-3\}}$$

In order to maintain about 40 to 60% ferrite, balance austenite, the ferrite stabilising elements, Eqn {2-2}, need to be balanced with the austenite stabilisers, Eqn {2-3}. For this reason, the level of nickel addition to a given duplex alloy will depend primarily on the chromium content.

At excessive Ni contents, the austenite level increases to well above 50%, with the consequence that Cr and Mo are enriched in the remaining ferrite. As a result, ferrite transformation to intermetallic phases may be enhanced [Gol51] when the alloy is exposed to temperatures in the range 650 to 950°C. Further, high Ni-contents accelerate alpha prime formation [Sol78], an embrittling intermetallic phase, in the ferrite. In summary, nickel does have some direct effect on corrosion properties, for instance moving E_p in the noble direction and reducing i_{pass} (Fig.2-5), and yet it appears that the main role of nickel is to control phase balance and element partitioning.

Nitrogen

Nitrogen has a multiple effect on stainless steels by increasing pitting resistance, austenite content and strength. It has a similar influence on pitting as Cr and Mo, moving E_p in the noble direction and thus increasing the passive potential range, Fig.2-5. This effect is enhanced in the presence of Mo and it has been suggested [Tru77] [Gar82] [Oga82] that Mo and N have a synergistic influence on pitting characteristics. The proposed factor for nitrogen in the PRE_N relationship varies between 13 and 30, but the most widely used value for duplex alloys is 16, Eqn {1-1}.

Nitrogen partitions preferentially to the austenite due to the increased solubility in the phase [Kol83] and also concentrates at the metal-passive film interface [Lu83]. During prolonged passivation of stainless steels in acid solutions, surface nitrogen enrichment has been witnessed [New84], which explains how nitrogen can influence repassivation. However, to breakdown the passive film the anodic current density must be high, in the order of several A/cm^2. For nitrogen-bearing 316L type stainless steel in 4M HCl, nitrogen reversibly impedes active dissolution from reaching these high values, possibly by surface enrichment of nitrogen atoms [New87]. The inhibitive nature of nitrogen was postulated to result from its dissolution, whereby nitrogen combines with hydrogen ions to form ammonium ions. This is a cathodic reaction, which becomes too slow at high potentials to balance the anodic dissolution of the metal and allows for surface enrichment of nitrogen, leading to the blocking effect observed.

Nitrogen has also been noted to increase the crevice corrosion resistance. Workers have proposed [Oso86] [Cla89] [Fuk80] that this is due to nitrogen altering the crevice solution chemistry or by segregating to the surface, which is in keeping with the mechanism for enhanced pitting resistance [New87].

Another important property of nitrogen is its ability to stabilise duplex alloys against the precipitation of intermetallic phases [Cha90], such as sigma and chi, by reducing Cr-partitioning [Liz81]. It is also reported [Lil86] that increasing the nitrogen level actually reduces the risk of nitride formation. This may appear contradictory, but is due to an increase in austenite content and so a reduction in the distance between austenite islands.

The addition of C and N strengthens both ferrite and austenite by dissolving at interstitial sites in the solid solution [Irv61] [Irv63]. And yet, as carbon is undesirable in stainless steel, due to the risk of sensitisation, the addition of nitrogen is preferred. Further, as nitrogen is a strong austenite stabiliser its addition to duplex stainless steel suppresses austenite dissolution and encourages austenite reformation in the HAZ (Fig.2-7).

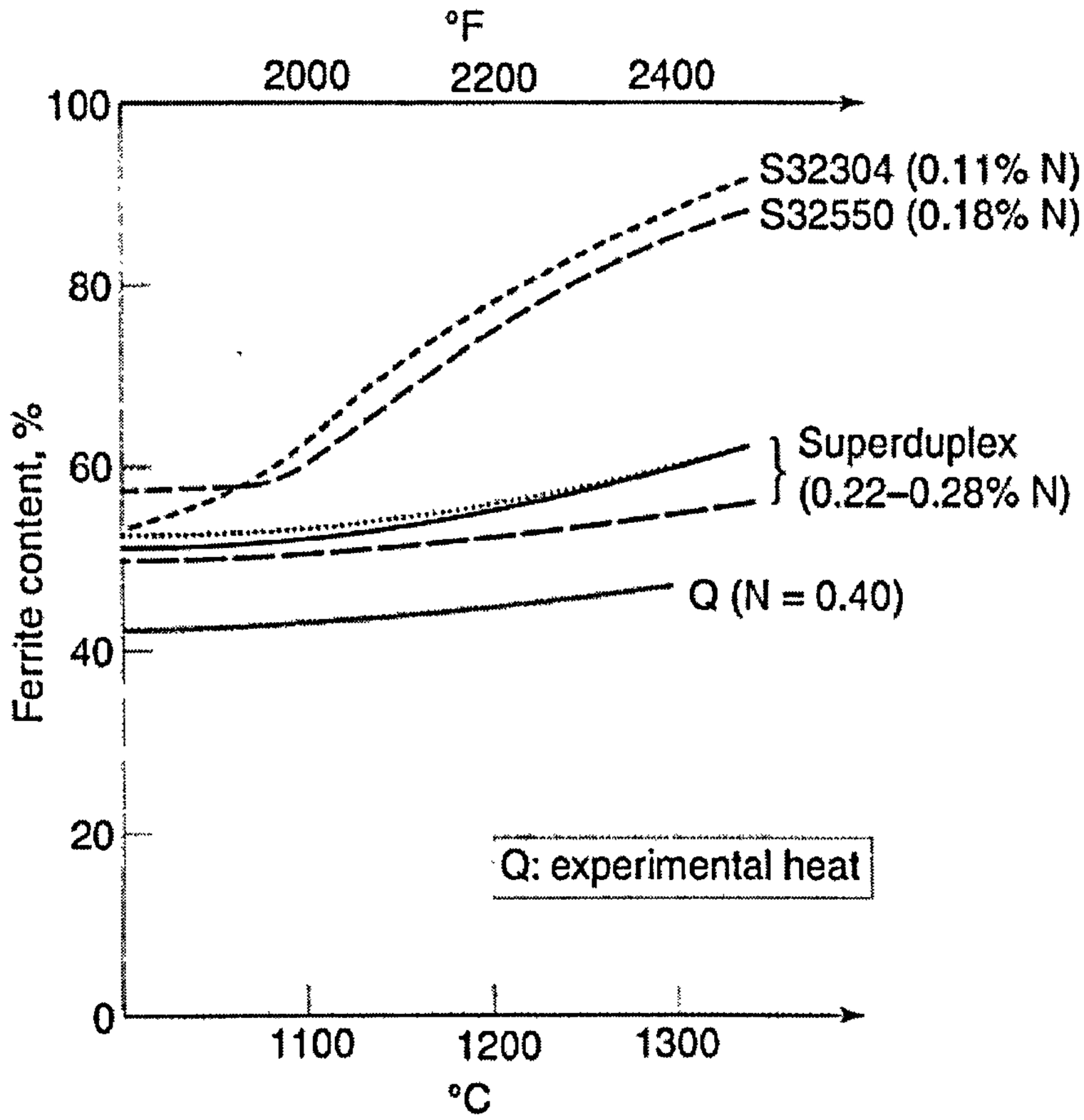


Fig.2-7 Effect of nitrogen on the increase in HAZ ferrite content [Cha90].

Comparison of the nitrogen contents of different duplex stainless steels, Table 2-4, shows that the superduplex grades contain higher levels than the lower alloyed variants. This enhanced level of nitrogen is possible due to the higher alloy content of these steels and, in particular, enhanced chromium contents, Fig.2-8 [Sma68]. In this regard, the beneficial influence of manganese should also be noted. In other grades, with lower Cr and Mn contents, the nitrogen solubility limit can be reached, leading to severe out-gassing or porosity during solidification.

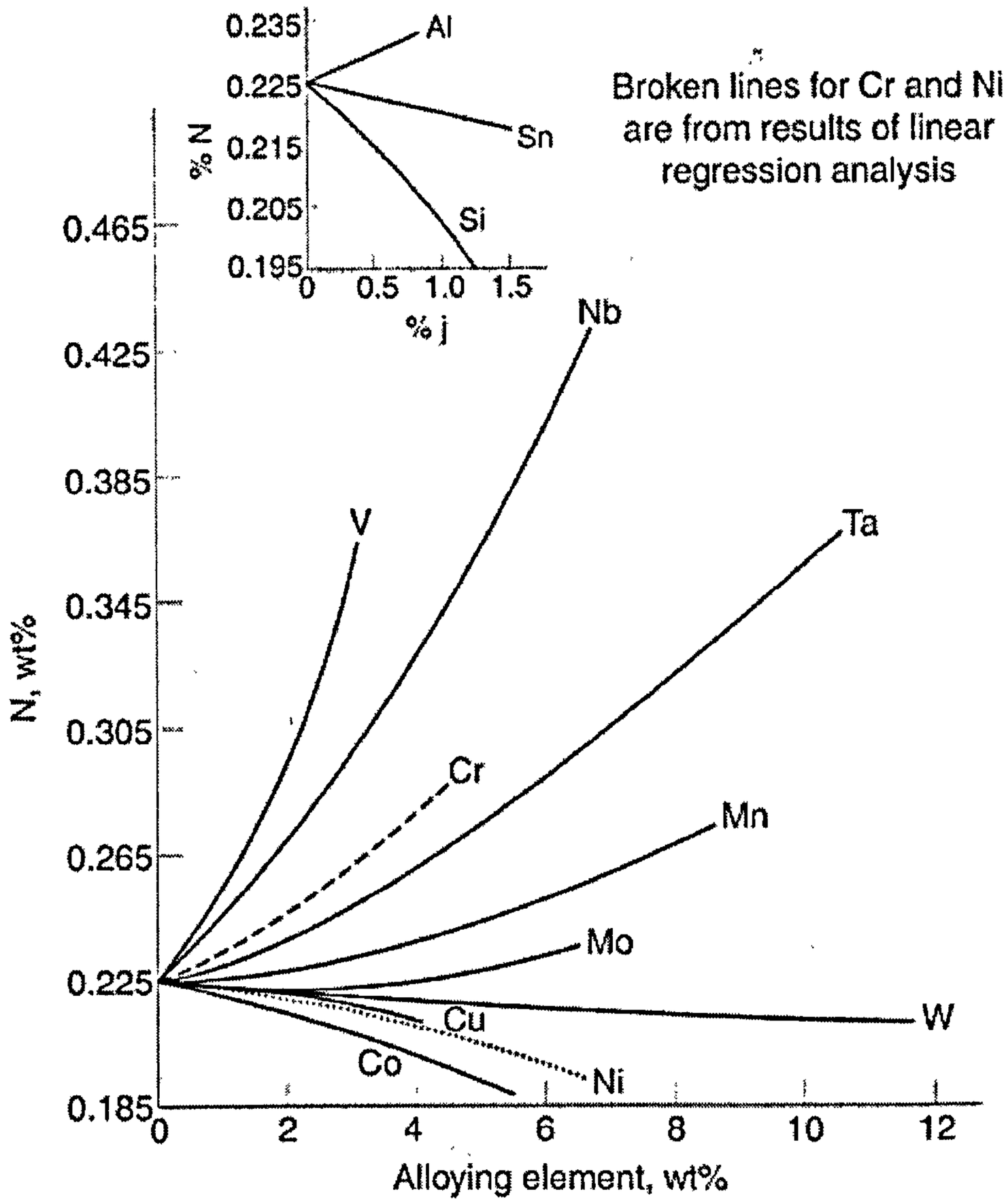


Fig.2-8 Effect of alloying elements on the solubility of nitrogen in liquid Fe-18%Cr-8%Ni alloys at 1600°C and 1 atm N_2 [Sma68].

Manganese

Manganese has been quoted [Sch49] [DeL56] as an austenite stabiliser for 'austenitic' steels and yet, for duplex alloys, mixed results have been obtained [Cha82] [Gui67]. The current understanding is that manganese has little effect on duplex phase balance, especially at the levels normally encountered, and is excluded from the Cr_{eq} and Ni_{eq} equations quoted above [Kot92], ie Eqns {2-2} and {2-3}. Nevertheless, it would appear [Ros84] that Mn can increase the temperature range and formation rate of detrimental sigma phase.

Manganese additions to stainless steel increase abrasion and wear resistance [Sou90] and tensile properties without loss of ductility [Ros86]. Further, Mn increases the solid solubility of nitrogen (Fig.2-8) and thus allows for increased nitrogen contents to be achieved without risk of out-gassing. However, Mn-additions in excess of 3% and 6%, for nitrogen levels of 0.1% and 0.23% respectively, significantly decrease the critical pitting temperature (CPT), probably due to the increased likelihood of MnS inclusions which can act as initiation sites for pits [Guh82]. Nevertheless, the combined addition of Mn and N in modern duplex alloys improves the pitting resistance and counteracts the singular problems associated with Mn [Cha82].

Copper

Copper additions to high alloy austenitic stainless steel are recognised to reduce the corrosion rate in non-oxidising environments, such as sulphuric acid. In some 25%Cr duplex alloys, 1.5%Cu is added to obtain the optimum corrosion resistance in 70% H_2SO_4 at 60°C [Guh82], whilst, for boiling HCl, an addition of 0.5%Cu decreases both the active dissolution and crevice corrosion rates. In general, the addition of Cu to duplex stainless steels is limited to about 2%, since higher levels reduce hot ductility and can lead to precipitation hardening.

Under high velocity conditions where cavitation erosion in H_2S-contaminated sea water prevail, Cu appears [Pin79] to be beneficial, due to the formation of a Cu-rich layer on the surface during active dissolution [Heu83]. Unfortunately, no data from the field supports this mechanism [Ros86]. Further, copper has been found to improve machinability in low oxygen and sulphur materials and can lead to hardening after exposure to the 300-600°C temperature range, Fig.2-6. This is apparently due to the precipitation of tiny Cu-rich precipitates [Sou90]. These precipitates (epsilon phase in Table 2-7) do not significantly reduce corrosion resistance or toughness and have been exploited for improving abrasion-corrosion resistance in duplex pump castings [Nie91].

Tungsten

Tungsten additions of up to 2% have been made [Ros86] [Oka92] to duplex steels to improve pitting resistance, i.e. extend the passive potential range and reduce i_{pass}, Fig.2-5. Similarly, tungsten increases crevice corrosion resistance in heated chloride solutions [Nag81]. This is thought to be due to the adsorption of tungsten into the passive layer without modification of its oxide state [Bui83]. However, in acid chloride solutions tungsten appears to pass from the substrate into the passive film by interaction with water to form insoluble WO_3. In neutral chloride solutions, WO_3 interacts with other oxides increasing their stability and bonding to the substrate.

Tungsten is known to encourage intermetallic formation in the 700 to 1000°C temperature range, Fig.2-6, and encourages secondary austenite formation in weld metal [Nil94]. It is believed [Ued93] to be thermodynamically equivalent, but kinetically non-equivalent, to molybdenum with respect to sigma formation. However, levels between 1 and 3% have been shown to restrict the formation of sigma at the phase boundaries and, instead, precipitation occurs at intragranular sites. This is thought to be due to the large tungsten atom influencing the diffusion of Mo and W at the phase boundaries and thus nucleation of sigma. Notwithstanding this, tungsten alloyed weld metal has been shown to form chi phase more rapidly than otherwise similar deposits without the addition [Her94] [Huh94]. Nevertheless, a tungsten content of 1% is usually not exceeded in a 4%Mo duplex steel [Ros86], with 2%W added to steels with about 3%Mo (S39274 in Table 2-4).

Silicon

Silicon is beneficial for concentrated nitric acid service and also enhances the high temperature oxidation resistance [Sou90]. High silicon (3.5-5.5%) bearing duplex stainless steels have been developed with increased pitting resistance, Fig.2-5, and a claimed [Ros86] immunity to SCC. Nevertheless, as Si is generally considered to enhance sigma formation, Fig.2-5, it is generally preferred to limit its addition to the 1% level.

Carbon, sulphur and phosphorus

The carbon content of most wrought duplex stainless steels is limited to 0.02% or 0.03%, primarily to suppress the precipitation of Cr-rich carbides which can act as initiation sites for pitting corrosion and intergranular attack. Similarly, S and P contents are controlled, although not eliminated as the presence of some sulphur is important for weld bead penetration [Sou90]. Nowadays, levels of C and S can be controlled by the modern steel making processes, such as AOD and VOD, whilst phosphorus contents can be reduced using good melting practice.

2.2.3. Process Routes and Heat Treatments

As composition varies between the duplex alloys, inevitably there are differences in the solution annealing temperature and cooling rates required to produce the optimum phase balance and microstructure. Nevertheless, a typical process route for duplex alloys involves production of a melt using either high purity material in a conventional induction furnace, or high alloyed scrap in an electric arc furnace (EAF) followed by AOD, VOD or VARP converters [Neu94]. Although both these methods produce high quality materials, the latter method favours lower sulphur contents. But the converters do not naturally reduce phosphorus, unless careful scrap selection and good base mix practice are undertaken. Overall, the aim is to reduce sulphur and phosphorus, as far as possible, in order to increase the ultimate corrosion resistance [Chr91].

The next stage of refinement involves deoxidation and inoculation by adding a combination of the following agents: SiCaMn, SiCaCe, REM, Al, Ti, Mg, Nb, Zr etc. These additions lead to the precipitation of microscopic oxides which act as multiple nucleation sites for ferrite crystals and provide grain refinement. The precise combination of agents employed depends on the (previous) oxygen and carbon contents, and is selected in view of the final corrosion and mechanical properties [Neu94]. Besides the deoxidants, the cooling rate has a significant effect on grain size, which, in the case of castings, remains essentially unchanged during subsequent solution heat treatment and water quenching.

Hot rolling takes place in a number of stages, at a temperature which corresponds to 50-60% ferrite content, i.e. 1000-1300°C. At the higher end of this range, favoured for the more highly alloyed superduplex grades, the small grain size present can lead to superplastic behaviour, which can aid hot workablility [Mae87]. Shot-blasting and grinding is undertaken between each stage with the final solution anneal taking place between 1050°C to 1100°C. A water quench is employed to avoid intermetallic precipitation [Cha90], although this can prove difficult in heavy section products [Coz94]. Higher solution heat treatment temperatures have been examined, up to 1300°C [Ros84], which produced an increase in tensile properties, although toughness and ductility dropped on account of the structure becoming fully ferritic at temperature. Final processing involves descaling the steel either by mechanical means or by pickling in a HNO_3/HF acid mixture.

2.2.4. Solution Annealed Microstructure

As the proportion of ferrite present at the solution annealing temperature is greater (up to 100%) than the equilibrium amount at room temperature, Fig.2-4, on quenching from such temperatures the ferrite becomes unstable and decomposes to austenite in the solid state. As described above, the steel maker carefully controls the chemical composition and thermomechanical treatment to give a final ferrite volume fraction of between 40 and 45%. The morphology of austenite can take various forms dependent on the degree of hot work, solution annealing temperature and cooling rate. However, a typical wrought parent material microstructure will consist of elongated islands (or lamellae) of austenite in a ferrite matrix, Fig.2-9, with a degree of directionality reflecting the hot working characteristics. Typically, the coarseness of such directional microstructures is described by the lamellar spacing. This is defined as the average distance between the middle of austenite islands, measured in the through thickness direction.

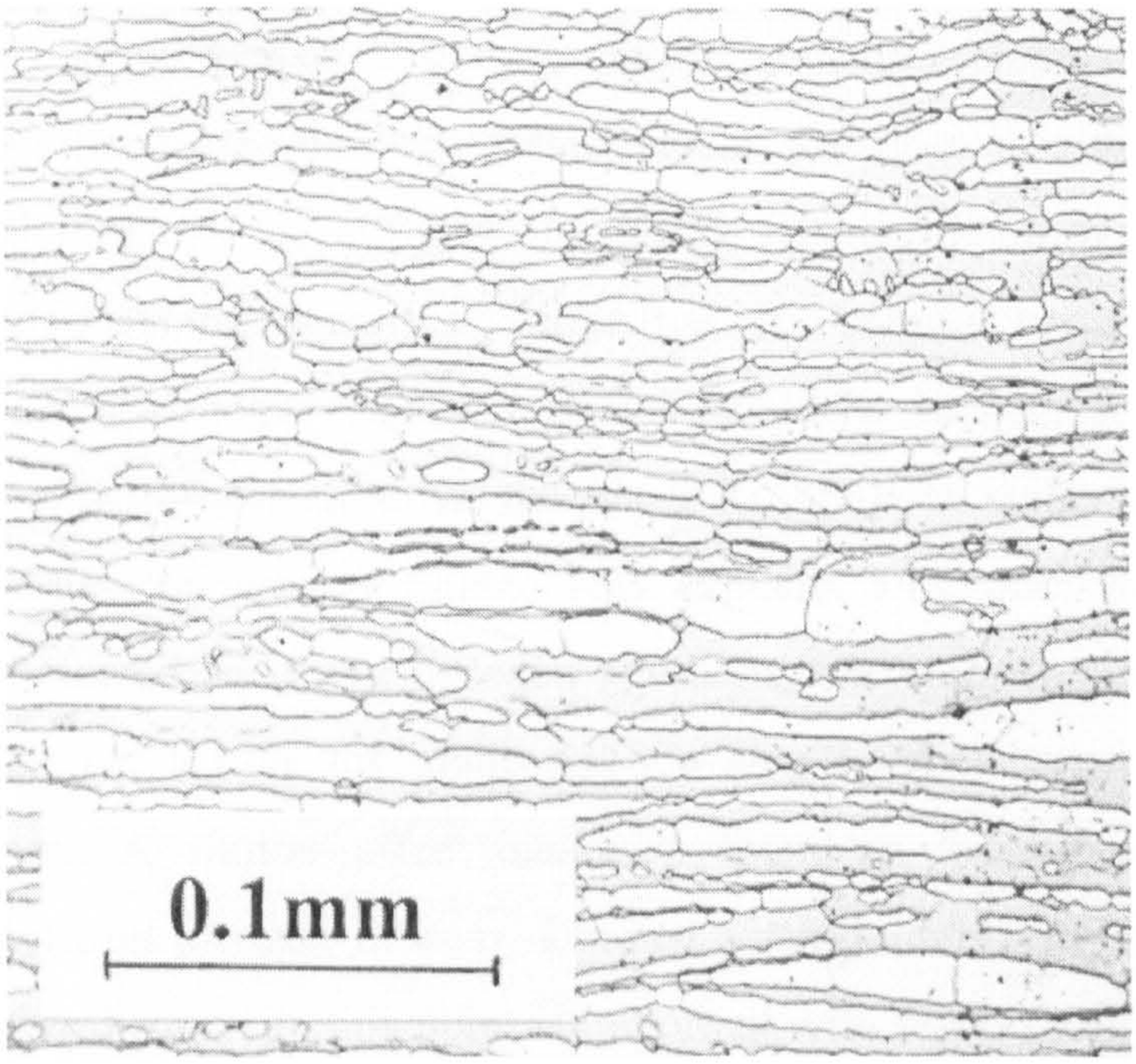


Fig.2-9 Typical microstructure of a wrought duplex stainless steel, x250 (AB1937).

2.2.5. Tensile Properties

The minimum tensile properties for a range of modern duplex alloys are given in Table 2-4. Even though there are variations between the grades, it can be seen that solution annealed wrought duplex stainless steels exhibit high strength and ductility. The minimum 0.2% proof stress (R_p) varies between specifications, but is typically about 500 MPa, compared to 200-250 MPa for austenitic grade 304 (Table 2-3), whilst tensile strengths above 700 MPa are not uncommon. The room temperature ductility is illustrated by typical minimum elongation values of 25%. Vickers hardness values range from 230 to 290 VHN for solution annealed products without cold work.

The high proof and tensile strengths are the result of several simultaneous mechanisms:

- interstitial solid solution hardening (C, N)
- substitutional solid solution hardening (Cr, Mo, Ni, etc.)
- strengthening by grain refinement due to the presence of two phases
- possible hardening due to the formation of γ_2 phase
- strengthening due to ferrite, since, for a similar composition, this phase is harder than the austenitic structure
- strain induced by differential contraction of the two phases on cooling from annealing temperatures

The combination of these different mechanisms explains the remarkable mechanical properties of the duplex stainless steels. However, it is important to emphasise the particular role of nitrogen. In effect, raising the nitrogen content preferentially strengthens the austenite by interstitial solid solution hardening, to the point where it becomes stronger than the ferrite [Wah87]. Indeed, for low nitrogen contents (<0.1%), the austenite has the lower R_p, while at higher levels (>0.2%) the ferrite becomes the weaker phase. This explains why macroscopic hardening is most pronounced for small nitrogen additions, becoming less marked beyond a certain level, i.e. 0.12% for grade S31803 (Fig.2-10), where only moderate hardening occurs. A similar effect has been found in the superaustenitic grades, as no significant increase in R_p is obtained when the nitrogen content raises from 0.20 to 0.28%. Moreover, this point is important with respect to the SCC resistance and the fatigue strength, since, depending on the compositional balance, either the austenite or the ferrite can be the first to yield.

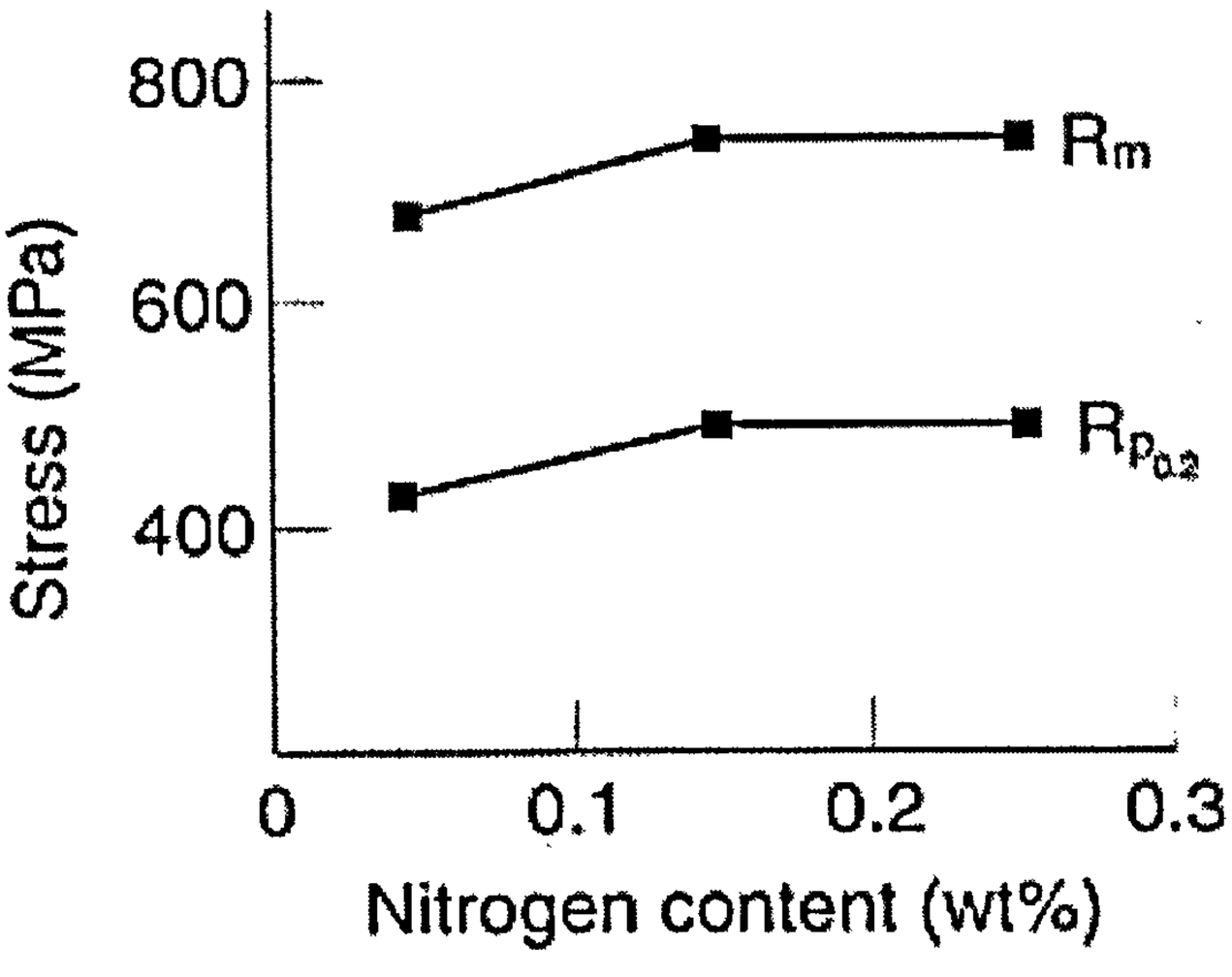


Fig.2-10 Effect of nitrogen on the 0.2% proof ($R_{p0.2}$) and ultimate tensile (R_m) strength of S31803-type alloys [Wah87].

The tensile properties of duplex grades are influenced by plate thickness, becoming increasingly anisotropic with reduction in thickness, Fig.2-11. The anisotropy, and concomitant strengthening, are due to refinement of the structure, with the ferrite/austenite structure being elongated parallel to the principal strain axis, Fig.2-12. There is no "fibre-strengthening" effect, since the two phases have similar hardness levels. However, a marked and unusual texture is observed for the two phases, with a major orientation of the type (100)[011] to (211)[011] for the ferrite fibres and (110)[223] for the austenite fibres.

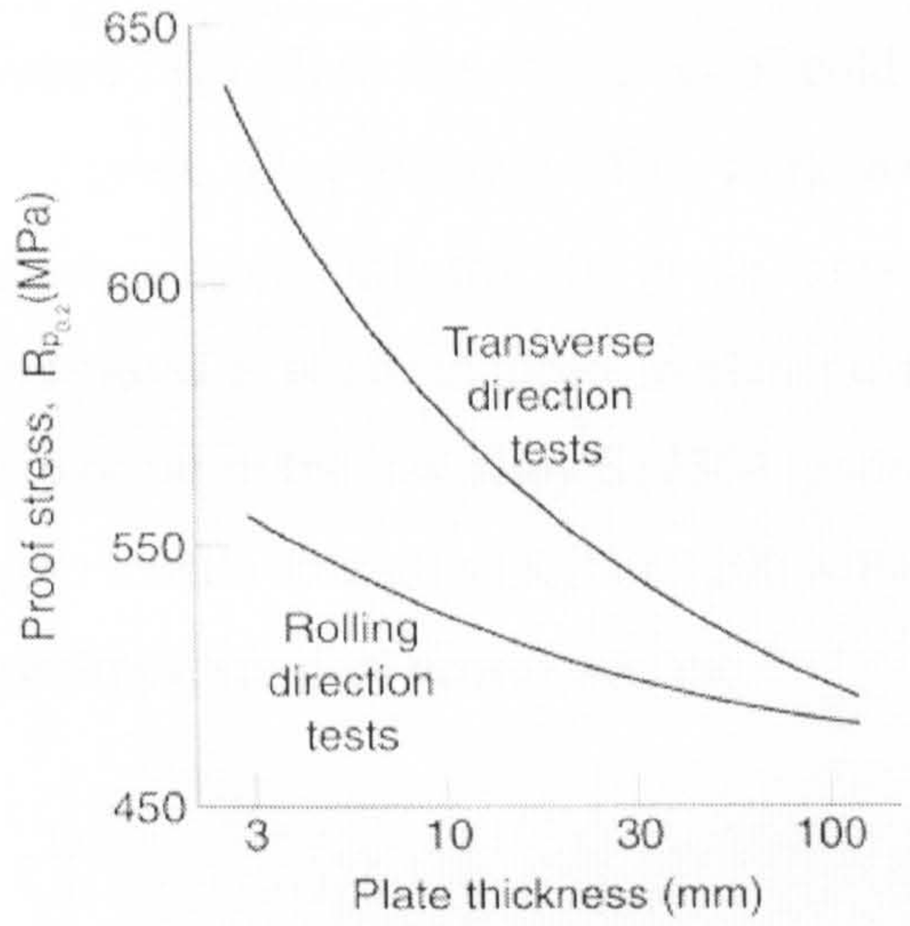


Fig.2-11Representative proof stress in the rolling direction and transverse directions, as a function of plate thickness [Hut86].

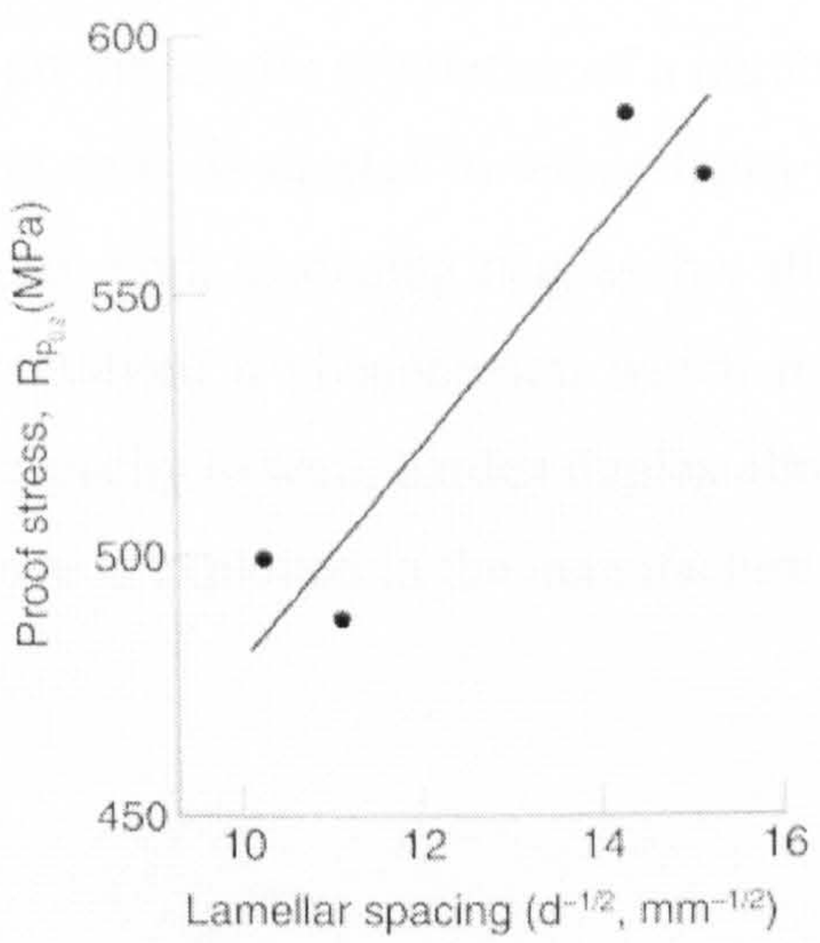


Fig.2-12 Petch plot relating proof stress (average of 0° and 90° tests) to lamellar spacing (d) [Hut86].

The influence of temperature on the tensile properties of various duplex grades is shown in Fig.2-13, together with austenitic and ferritic alloys with similar composition. The variation in mechanical strength for duplex alloys can be seen to be controlled essentially by the ferrite. Strengthening is accentuated at low temperatures, with some drop over the temperature range 20 to 300°C. This drop can be significant, as an increase in wall thickness may prove necessary when operating at 100°C, as compared to 20°C.

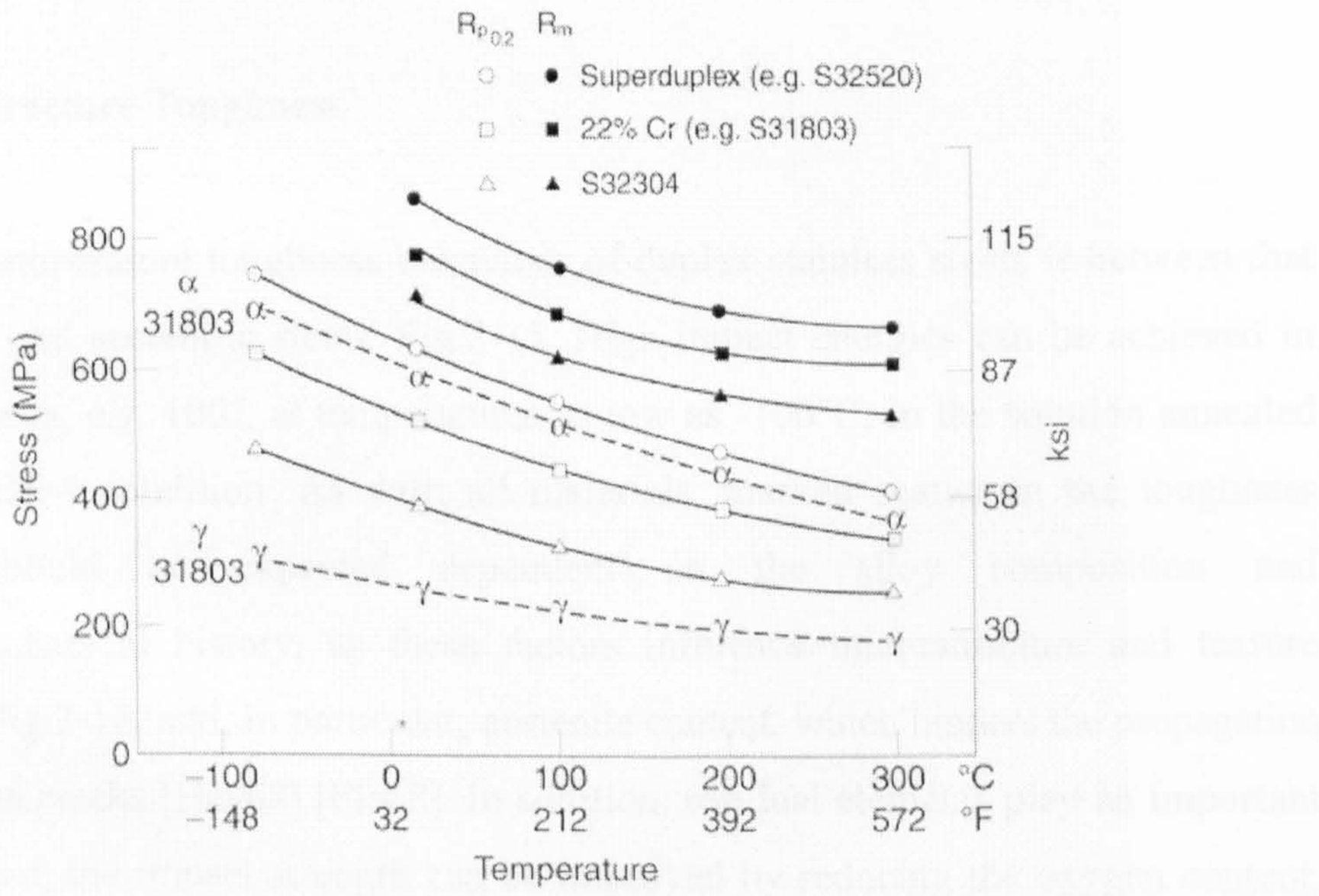


Fig.2-13 Temperature dependence of mechanical properties of several stainless steels [Cha91].

Figure 2-14 illustrates the effect of cold work on the tensile properties of a number of duplex alloy [Cig91]. The work hardening rate is similar to other types of stainless steel. Only the 304 grade shows a higher work hardening rate, as this alloy undergoes a strain-induced martensite transformation: a phenomenon which may also occur in the low alloy S32304 grade. The capacity to work harden duplex alloys up to tensile strengths (R_m) of 1200 MPa or above is exploited in the manufacture of wirelines, surgical prostheses, etc.

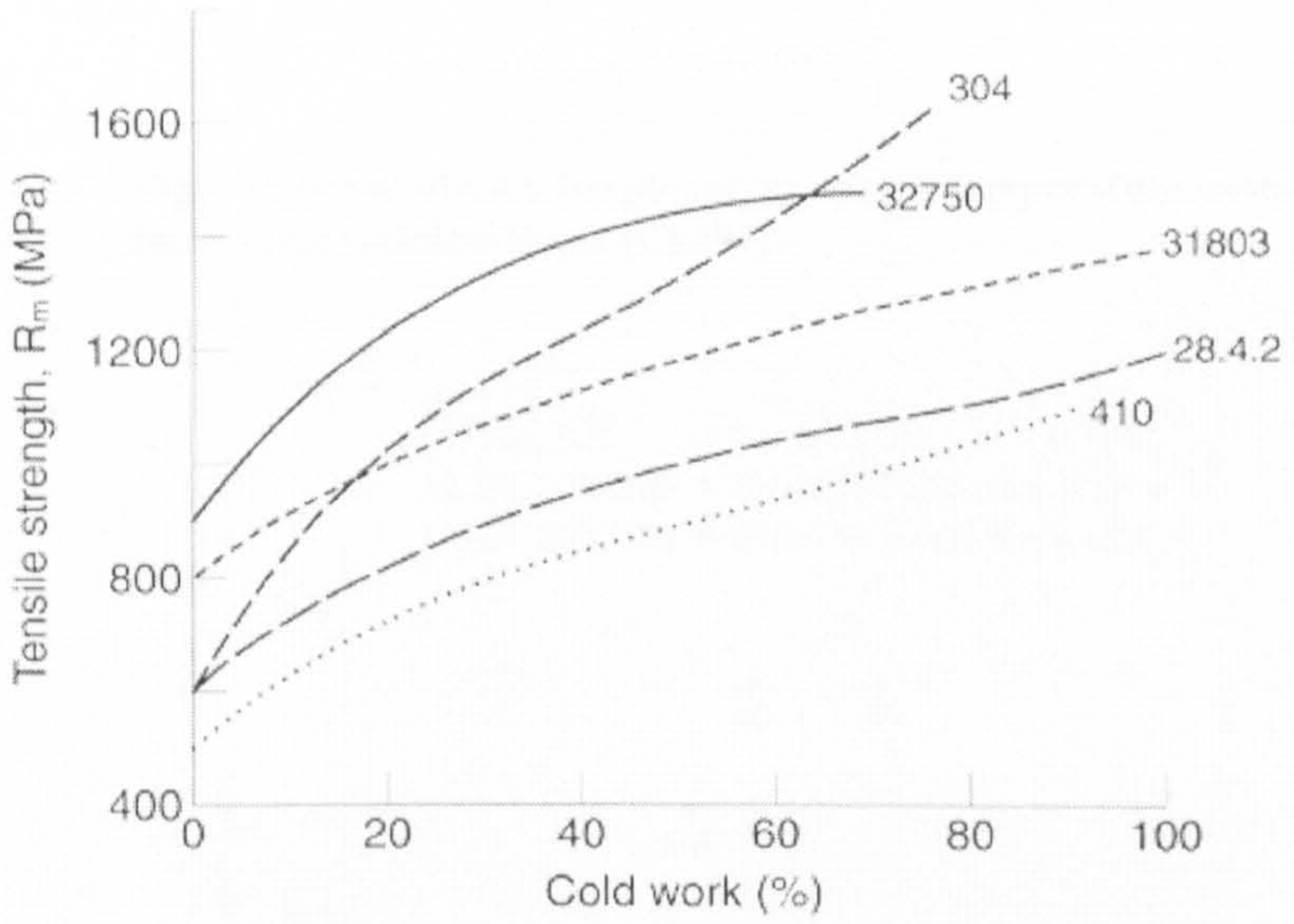


Fig.2-14 Tensile strength of different stainless steels as a function of cold work by wire drawing [Cig91] [Gru88]

2.2.6. Fracture Toughness

The low temperature toughness behaviour of duplex stainless steels is between that of ferritic and austenitic steels, Fig.2-15. High impact energies can be achieved in duplex alloys, e.g. 100J, at temperatures as low as -100°C, in the solution annealed and unwelded condition. As with all materials, marked scatter in the toughness values should be expected dependent on the alloy composition and thermomechanical history, as these factors influence microstructure and texture [Lin91], Fig.2-16, and, in particular, austenite content, which hinders the propagation of cleavage cracks [Hay68] [Flo68]. In addition, residual elements play an important role. Indeed, the impact strength can be improved by reducing the oxygen content, and by controlling the aluminium level [Cha90] [Bon91a] [Nis87] to avoid the formation of AlN.

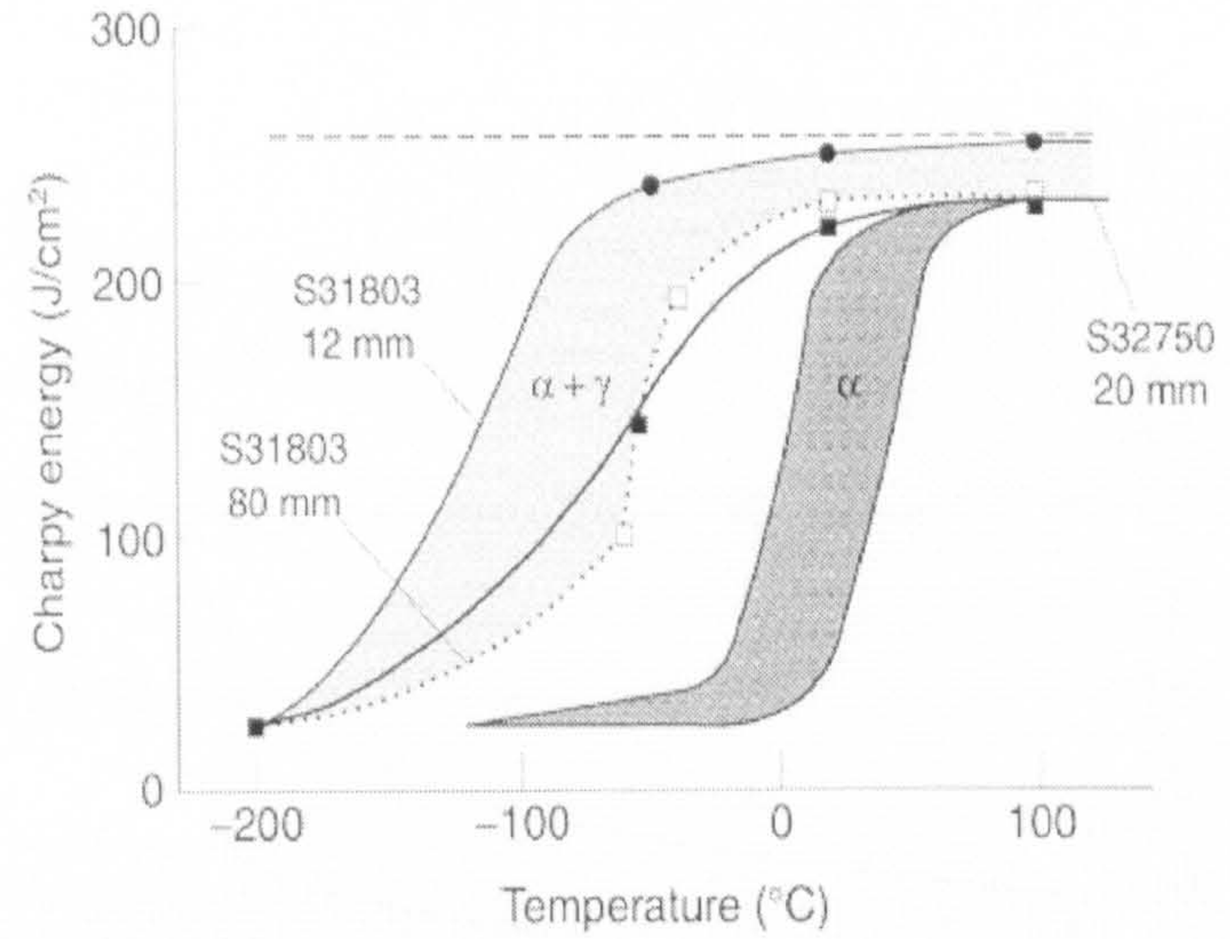


Fig.2-15 Normalised Charpy energy versus temperature measured for several stainless steels [Cha91].

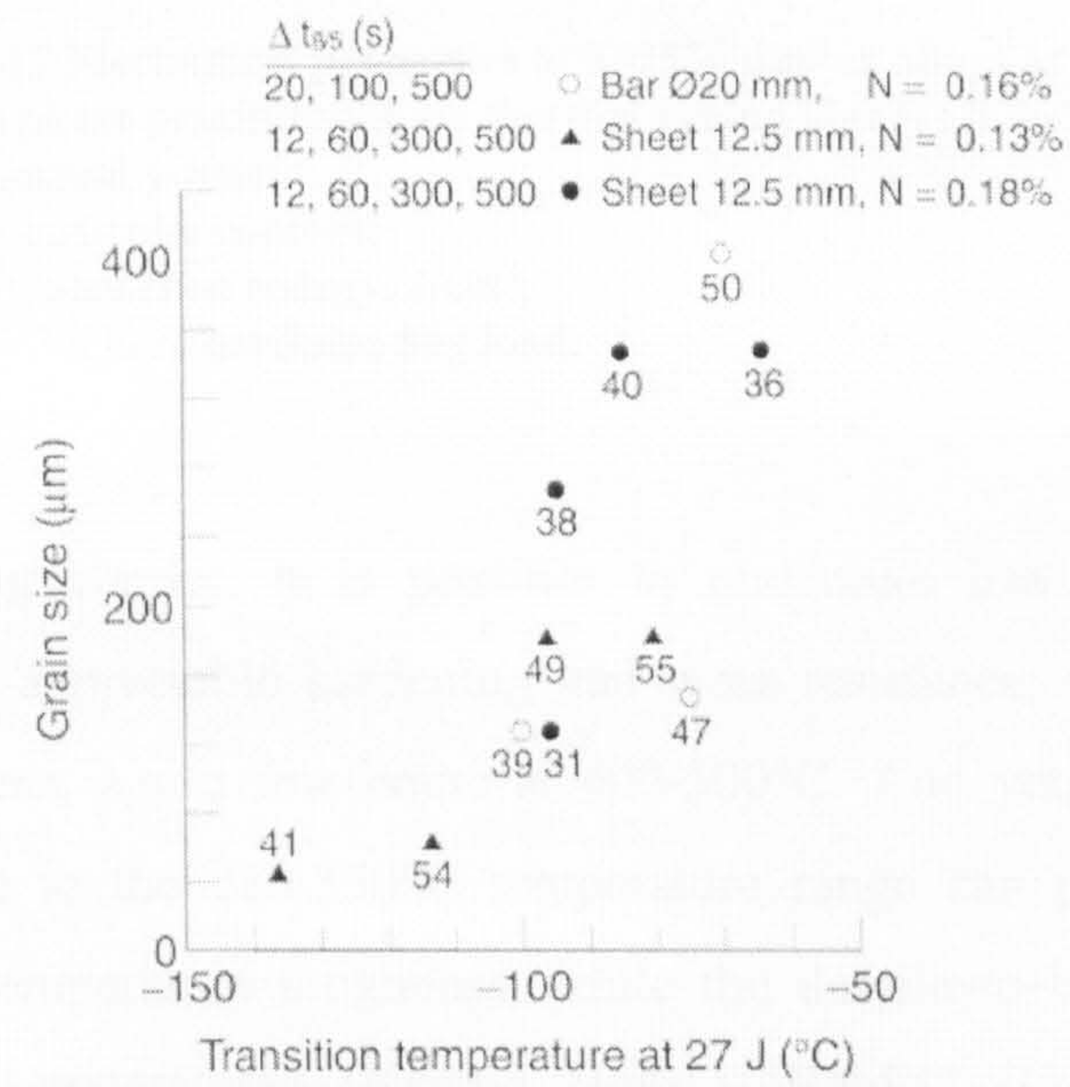


Fig.2-16 Relation between grain size (HAZ) and impact transition temperature (27J) for S31803 with austenite content given in the graph [Lin91].

There are a number of other factors that affect the toughness of wrought duplex alloys [Nys91] [Itu91] [Rob91] [Com82]. Any precipitation of intermetallic phases, such as sigma, chi etc., leads to a sharp decrease in toughness, e.g. Fig.2-17. This phenomenon is particularly important in the superduplex grades, in which the transformations are the most rapid. Care should be taken throughout the total thermomechanical process, including the correct solution anneal, with attention paid [Hil87] to the thickness of the component and quench rate.

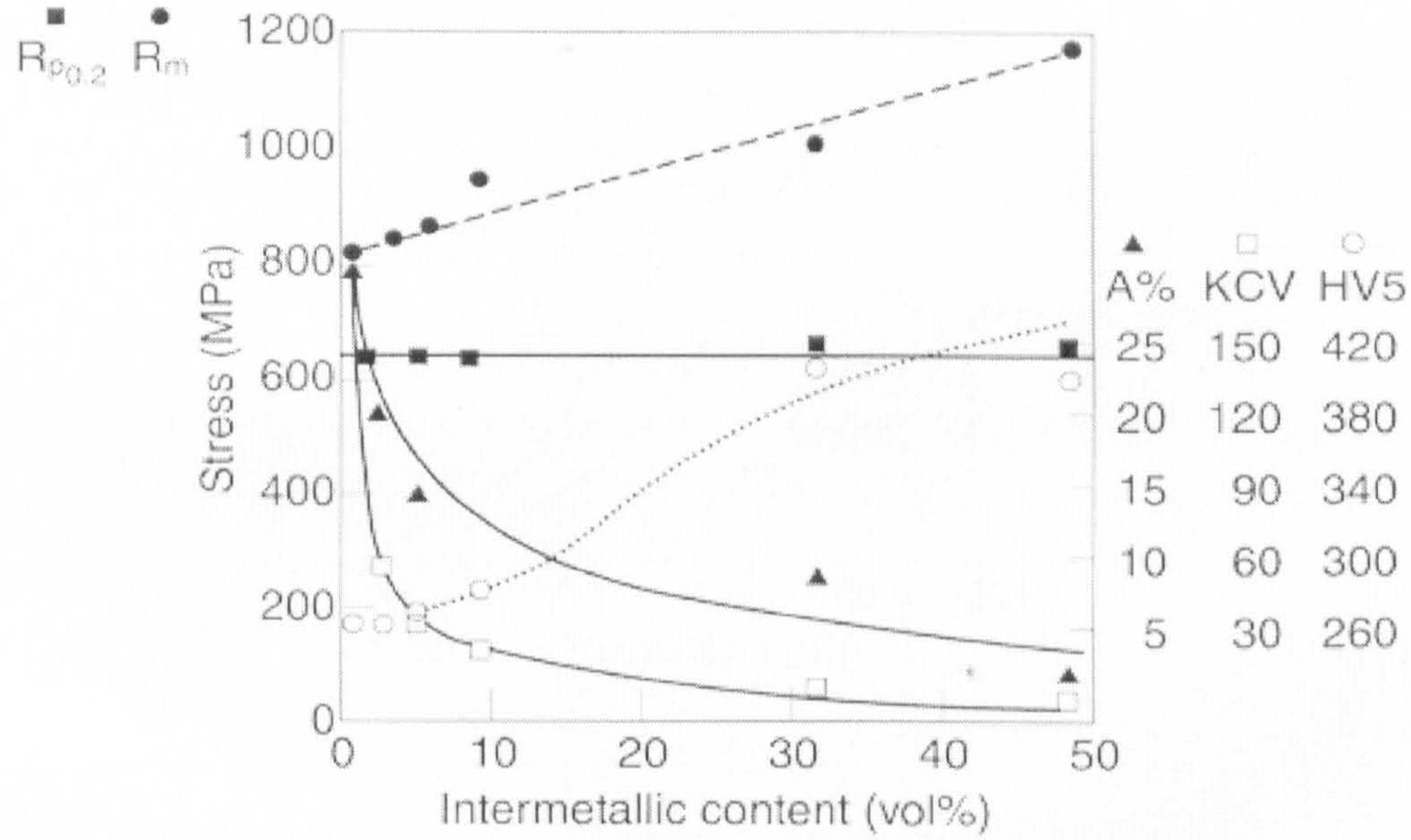


Fig.2-17 Mechanical properties of S32550 duplex alloys as a function of sigma phase precipitation by thermal ageing [Jac91] [Cha91].
Note second y-axis:
A% = austenite content;
KCV = absorbed energy, J/cm^2;
HV5 = Vickers hardness 5kg load.

In alloys containing copper, it is possible to undertake low temperature heat treatment to obtain appreciable hardening and wear resistance, while maintaining satisfactory toughness, e.g. a few hours at 400-500°C. And yet, for most grades, prolonged exposure in the 280-350°C temperature range can produce a marked decrease in room temperature toughness, while the ductile-to-brittle transition is shifted to higher temperatures [Nys91] [Itu91] [Rob91] [Com82], Fig.2-18a. Nevertheless, even in superduplex alloys, respectable impact toughness may remain after such exposures.

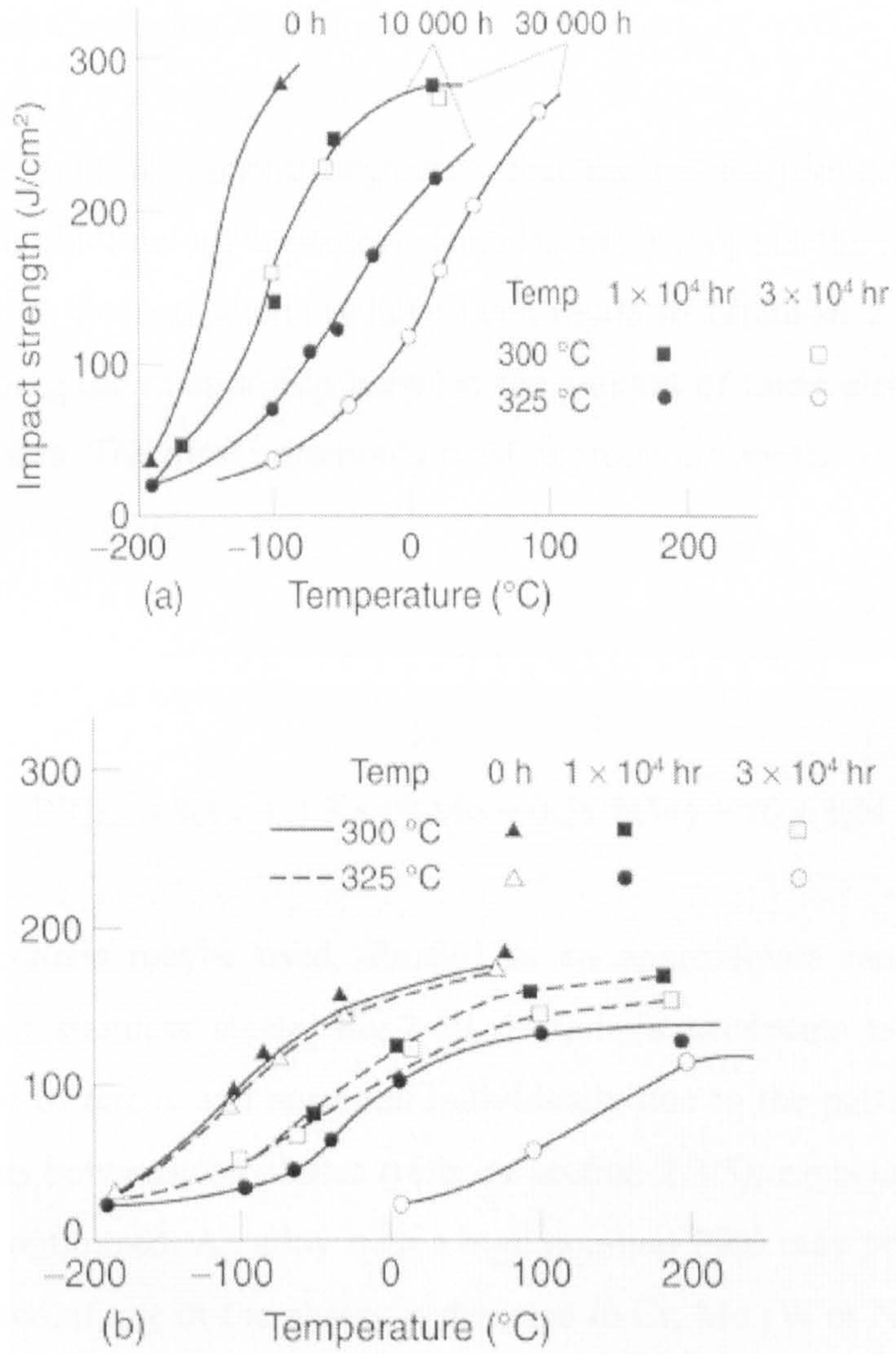


Fig.2-18 Impact energy curves for alloys aged at 300°C or 325°C: (a) quench annealed S32750; (b) cold worked S31803 [Cha91].

Cold work reduces the room temperature impact strength of the duplex steels and increases the ductile-to-brittle transition temperature (DBTT). The combination of cold work and ageing in the range 300-400°C leads to an even greater drop in the room temperature impact strength, and in some batches of grade S31803, it has been reported [Cha91] that the ductile-to-brittle transition can be raised above ambient temperature, Fig.2-18b.

Given the current understanding, duplex steels should not be used beyond 300°C, unless specific toughness evaluations are made. Furthermore, particular attention must be paid to welds, where the initial impact strength should be sufficiently high to accommodate the drop which occurs after service ageing. Indeed, a limit of 250°C has been propounded for welded structures [Nas91] [Ste91].

2.2.7. Localised Corrosion Resistance

All alloying elements, to varying degrees, affect the pitting resistance of duplex stainless steels in chloride environments [Ber91], Table 2-6, but the main elements are Cr, Mo and N. Several attempts have been made to establish a mathematical formulae describing the relationship between the amount of these elements and the corrosion properties. The most commonly used expressions are the so called pitting resistance equivalents (PRE):

$$PRE_N = \%Cr + 3.3 \times \%Mo + 16 \times \%N \qquad \text{--Eqn \{1-1\}}$$

or

$$PRE_W = \%Cr + 3.3 \times (\%Mo + 0.5 \times \%W) + 16 \times \%N \qquad \text{--Eqn \{2-1\}}$$

The PRE expressions maybe used [Ros86] as an approximate ranking between different wrought stainless steels, Fig.2-19. But, it is necessary to consider the pitting resistance of ferrite and austenite individually due to the partitioning of the alloying elements between the phases (refer to section 2.3.5), especially if the heat treatment is not optimised. An alloy with a high nominal PRE may produce a lower CPT than expected, if one of the phases is depleted in Cr, Mo (W or N) compared to the other phase. In other words it has a lower localised PRE_N-value. In particular, the effect of partitioning on corrosion resistance should be considered in relation to weldments, which is addressed separately in Section 2.3.8.

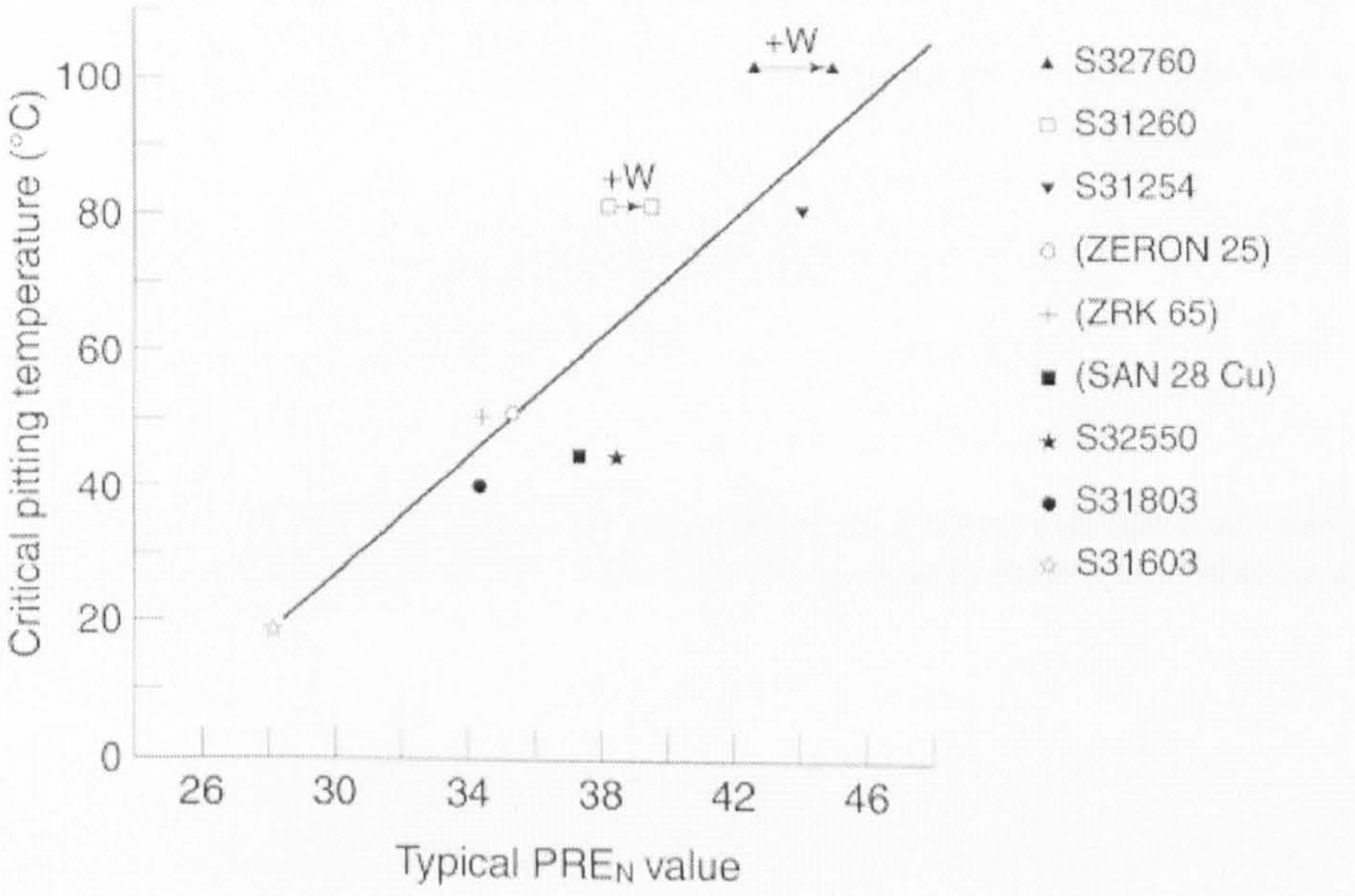


Fig.2-19 CPT data for wrought stainless steels in seawater using potentiostatic polarisation techniques and plotted against PRE_N [Ros86].

Initiation of pitting comprises local breakdown of the surface passive layer and, for duplex steels as well as for austenitic steels, the condition of the surface, e.g. grinding, pickling, cold work, dirt etc., has a more marked influence in chloride environments than in environments where general corrosion takes place. The pitting resistance is further influenced by factors such as grain size, inclusion distribution and possible precipitation of intermetallic phases. For these reasons, some degree of conservatism should be introduced when extrapolating laboratory results to site fabrication, as, in the latter case, it is difficult to control conditions.

From Fig.2-20 it can be inferred that the application range of a particular alloy (and welding conditions) may vary considerably depending on the conditions [Dru90] [Fra97]. In oxygen-free water with chlorides (low potential), S32205/S31803 can be used at very high temperatures, while in chlorinated sea water (around +600 mV SCE) only superduplex or superaustenitic steels can be applied. There is only a small effect of pH on pitting resistance with lower pH conditions being more aggressive [Ber90].

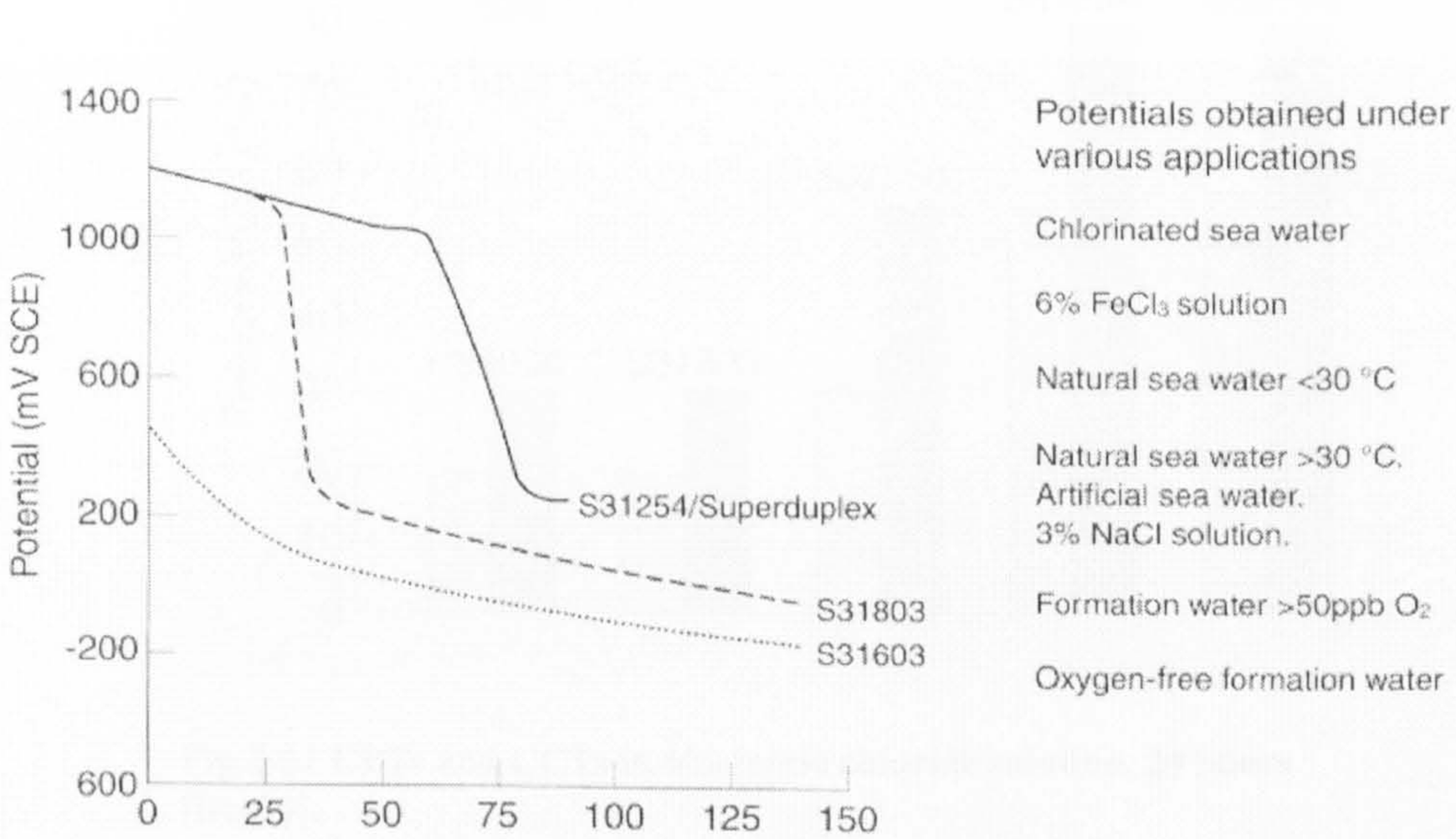


Fig.2-20 Critical pitting potentials determined for different stainless steels in 3%NaCl and 2.5bar CO_2. Also included are potentials of various industrial and laboratory media [Dru90] [Fra97].

One laboratory test medium, which is of interest when studying the pitting resistance of stainless steels, is ferric chloride solution. This test solution allows for a quick assessment of a materials performance in chloride media, as it is extremely aggressive (around pH1) and can give results in 24 or 72 hours. It has been reported that ferric chloride gives a similar potential to chlorinated sea water, Fig.2-20, even though pH values are markedly different [Ren86]. It is often used as a quality control test for welded joints and, for this purpose, a specific recommended practice for duplex weldments has been developed [TWI93a].

CPT and CCT data generated in ferric chloride solution are shown [Ber90] for several unwelded grades in Fig.2-21. As expected, improved resistance is obtained with the higher alloy grades (S32750 compared to S31803). Further, grade S31803 has similar resistance to the austenitic steel N08904, while superduplex alloys, e.g. S32750, are comparable to the 6%Mo austenitic grades, e.g. S31254.

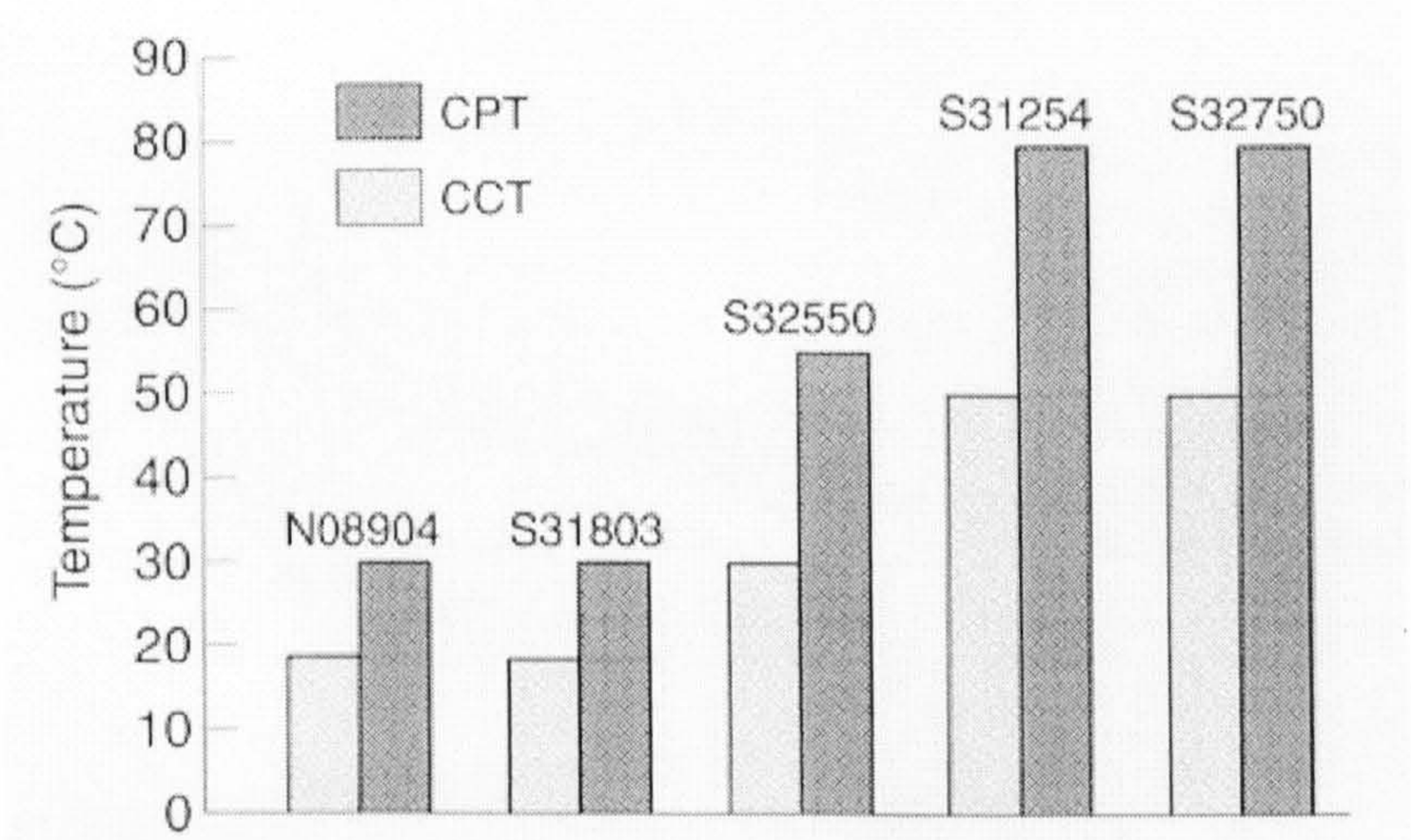


Fig.2-21 CPTs and CCTs in 6% ferric chloride solution, 24 hours [Ber90].

Crevices can be formed at flanged joints, beneath weld spatter etc. and, as a rule, the tighter the gap the more likely that crevice corrosion will occur for a given bulk environment. The crevice corrosion resistance of stainless steels can be related to the pitting corrosion resistance, as the critical crevice temperatures (CCTs) are roughly proportional to the CPTs, although considerably lower [Ber90], Fig.2-21. As the modern grades of duplex stainless steel have low carbon contents (typically below 0.03%), intergranular corrosion (IGC) of solution annealed material is generally not a practical problem.

2.2.8. Stress Corrosion Cracking

One of the most common failure mechanisms in stainless steels is chloride induced stress corrosion cracking (SCC). In particular, the conventional austenitic grades are susceptible to this failure mode. Duplex stainless steels offer much greater resistance to this form of cracking [Car70] [Ono82] [Hoc73], Fig.2-22, attributable to the presence of ferrite [Sak82] [Ber82], with all grades being superior to 316L and the superduplex grades apparently immune [Ber91] in 3%NaCl up to 250°C. Nevertheless, duplex alloys do suffer from SCC given concentrated chloride solutions. And, at least for austenitic alloys, this will also be dependent on the cation present, i.e. Mg>Ca>Na in order of increasing aggressivity [Old91]. In addition, high applied stress to tensile strength ratios, with elevated temperatures and high oxygen contents enhance susceptibility, combined with the presence of a crevice/deposit [Des84] [Sou90].

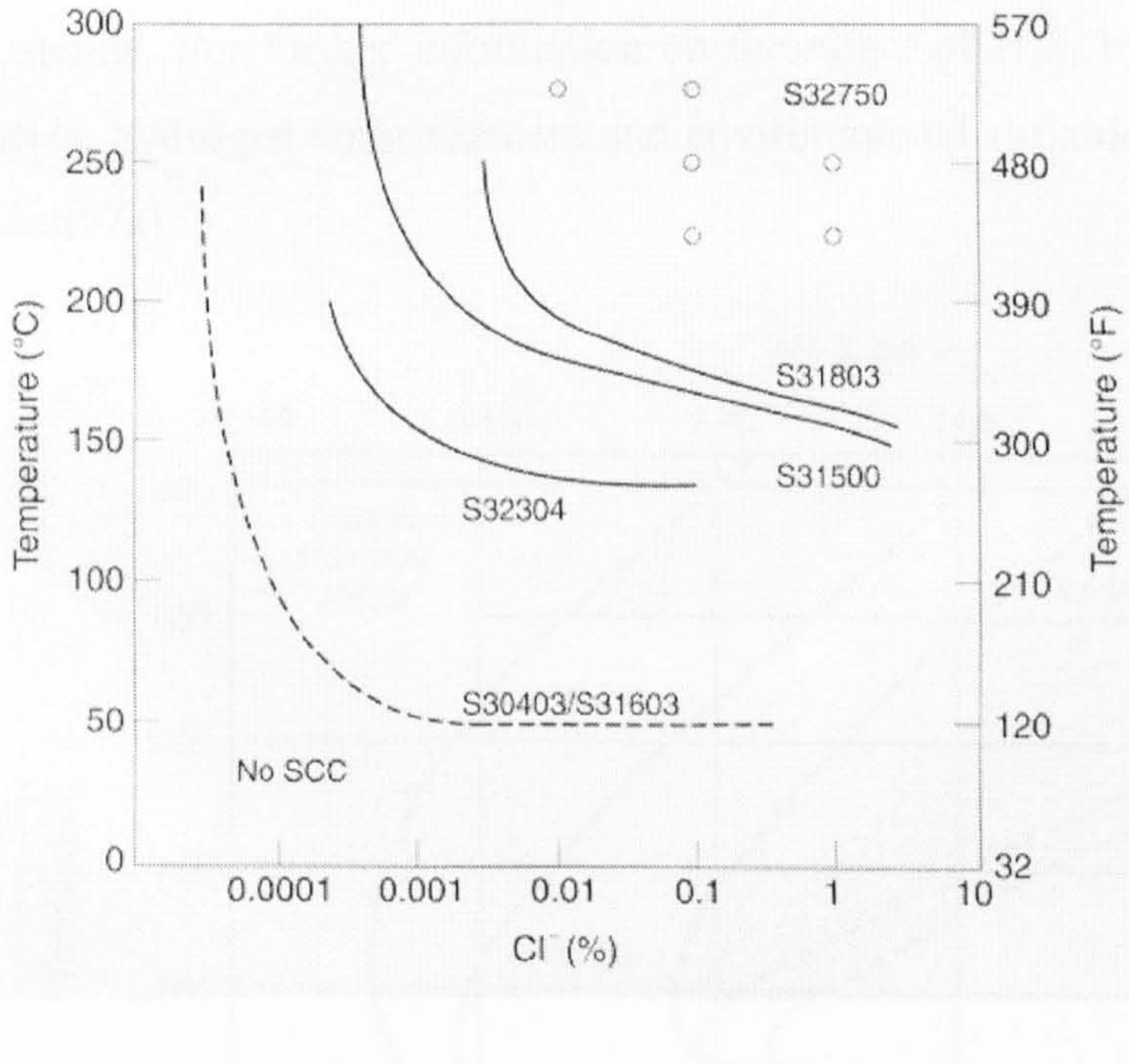


Fig.2-22 Compilation of practical experience and laboratory test data in neutral aerated (~8ppm) aqueous NaCl environments. Testing time 1000 hours. Load > R_p at test temperature [Ber91]

The beneficial effect of a two phase, austenite and ferrite, microstructure has been known since the early days of duplex stainless steels. Work [Ede53] [Roc84] in the 1950s and 1960s on austenite-rich microstructures concluded that the ferrite protects the austenite against SCC, as the ferrite has a lower corrosion potential in an acidified (hydrolysed) crack solution, such that, once a crack in the austenite reaches ferrite, the mixed potential inside the crack is depressed and the austenite is protected.

Another environmental cracking mechanism of concern for duplex alloys is sulphide induced SCC, defined here as SSCC. The SSCC behaviour of duplex steels has been examined extensively, but there is still uncertainty as to the maximum H_2S level which can be tolerated for a given temperature, due to the conjoint effects of H_2S and CO_2 partial pressures; chloride concentration; pH, temperature and material condition, e.g. Fig.2-23. Laboratory failures have been induced at ambient temperatures [Sak82] [Ono82] [Ber80] [Her80] [Kol81] [Ore82], thought to be hydrogen-assisted. At temperatures above 50°C, the presence of H_2S in chloride-containing media increases the risk of SCC, probably involving a combination of chloride and hydrogen cracking mechanisms, although cracking tends to be concentrated in the ferrite [Gun93a]. Duplex steels appear to reach a plateau of susceptibility at around 100°C [Rho82], Fig.2-23, as such temperatures are high enough to encourage passive film breakdown, corrosion and acidification and thus hydrogen ingress, but not so high that sensitivity to hydrogen embrittlement of ferrite becomes negligible. Nonetheless, at temperatures above 100°C, the risk of cracking reduces with attack being more prevalent in the austenite. For further information on the effect of H_2S, hydrogen entry into duplex steels, hydrogen embrittlement and environmental variables, the reader is referred to [Gun97a].

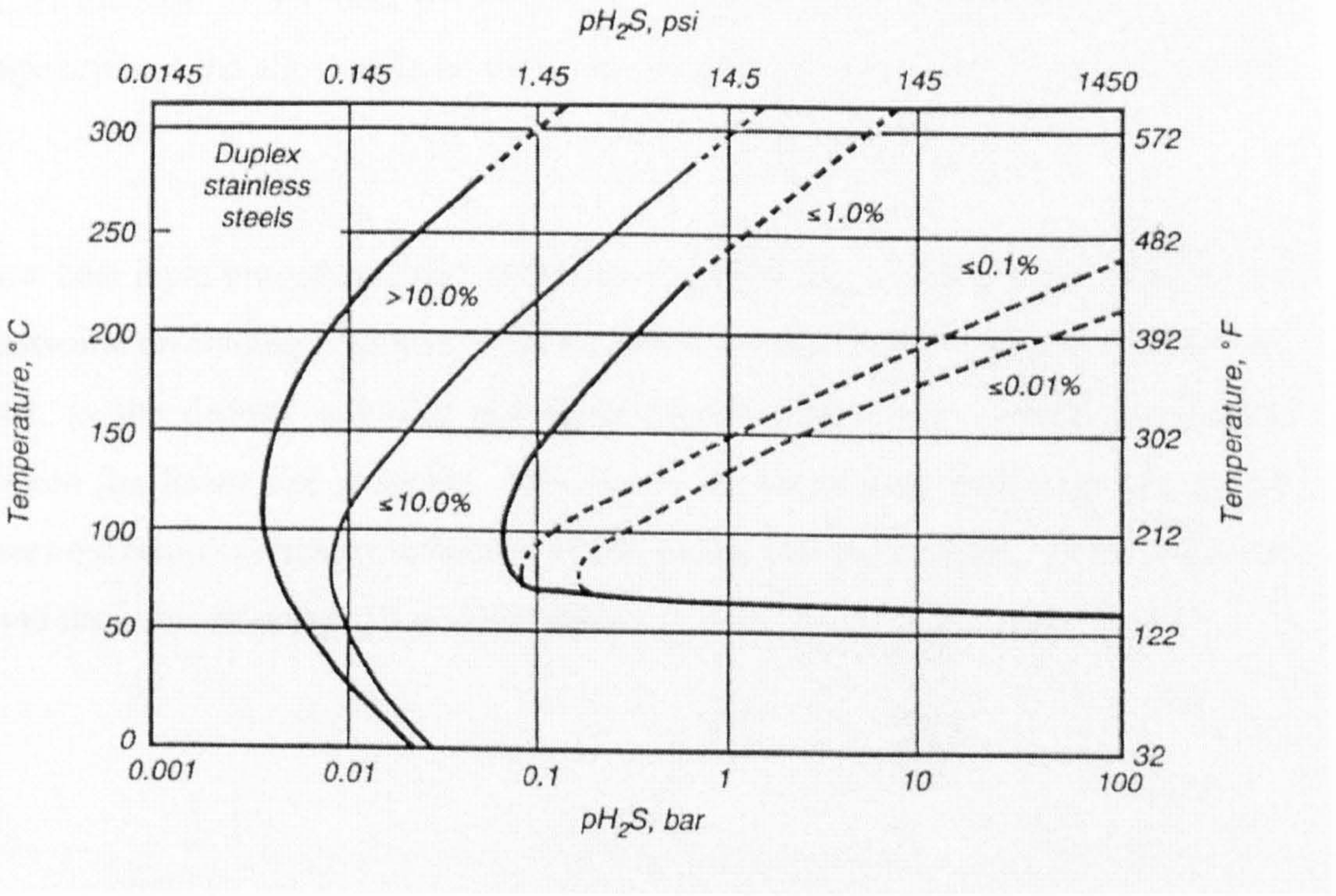


Fig.2-23 The effect of temperature, % NaCl and H_2S partial pressure on the SSCC of duplex stainless steels [Goo92].

2.3. WELDING DUPLEX ALLOYS

2.3.1. General Welding Characteristics

Duplex stainless steels exhibit similar fusion and penetration characteristics to the austenitic steels and so joint preparations and welding procedures for austenitic grades are often applicable to duplex alloys [Hon76] [Hon79]. All conventional processes can be employed, including the gas shielded (GTA and GMA) and flux shielded (SMA, FCA, SA) welding [Nob92]. To this end, a range of welding consumables are available, specifically developed for the different wrought grades and for the required weld metal properties.

The steel maker goes to great lengths to achieve the correct alloy content and phase balance in the wrought product. However, during welding, temperatures approaching the melting point are reached in the high temperature HAZ, which allows for some austenite to transform to ferrite with subsequent grain growth. Further, as the weldment is subject to the stresses induced by expansion and contraction of the weld pool, some degree of cold work is induced in the HAZ austenite, evidenced by twins and an increase in hardness [Bax93]. The extent of these changes depends on the composition of the alloy, material thickness, number of passes and the overall cooling rate.

If low heat input procedures, and so fast cooling rates, are adopted, then the reversion to austenite on cooling is limited. Further, low arc energy is not beneficial for the weld metal, as the deposit solidifies and cools quickly minimising element partitioning between the ferrite and austenite. This leaves the ferrite lean in Cr and Mo, which lowers the pitting corrosion resistance of this phase. For these reasons, there is a lower bound limit for arc energy [Nas82] [Hof82].

On the other hand, the use of a high heat input, with its slow cooling rate, encourages element partitioning and austenite formation, which increases HAZ and weld metal toughness. Nevertheless, high heat inputs also lead to a wider region of the HAZ that is exposed to temperatures above that for austenite dissolution, leading to enhanced grain growth [Goo82]. Further, the slower cooling through the 400 to 1050°C temperature range can lead to the precipitation of deleterious intermetallic phases.

The earlier grades of duplex alloys were especially susceptible to forming highly ferritic HAZs (Fig.2-24a) with commensurate low impact properties, but, through the addition of nitrogen which expands the austenite phase field to higher temperatures, Fig.2-4, modern grades are always expected to contain between 30 and 70% austenite with minimal grain growth, Fig.2-24b. This austenite range ensures that there is little effect of phase balance on the weld metal and HAZ impact properties [Lil86].

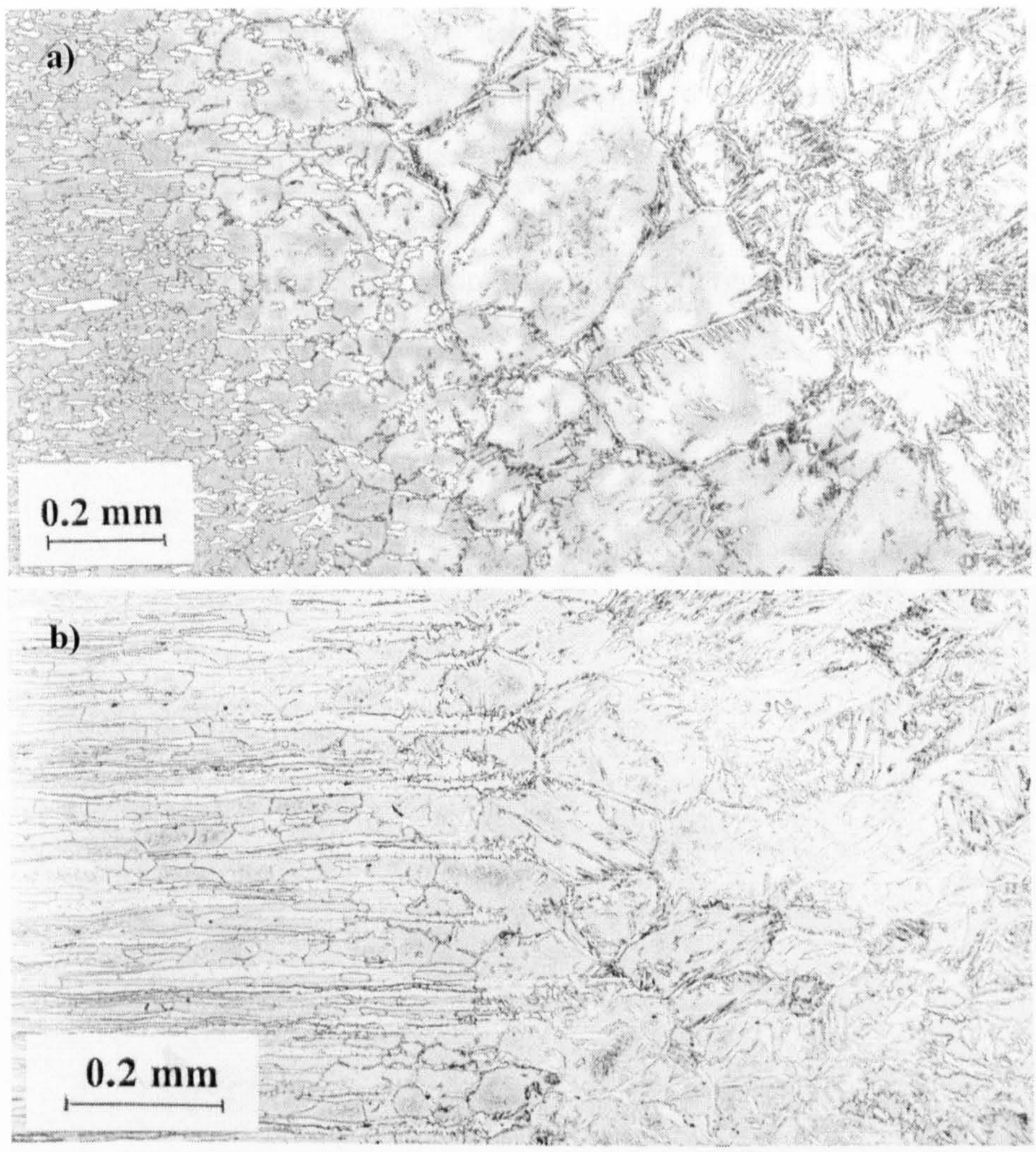


Fig.2-24 Comparison of duplex stainless steel HAZ microstructures:
a) old steel with low nitrogen and coarse HAZ [AC234, x80]
b) modern steel with higher nitrogen and limited HAZ grain growth [AE2135, x100]
Note: Parent metal on left, weld metal on right, HAZ in between.

Given the above, to keep the phase balance within the 30 to 70% range, the welding parameters need to be kept within a "window". However, as welding parameters are interlinked, it is often preferred to describe this window in terms of cooling rates over a given temperature range, which is independent of material thickness etc. Initially, cooling times between 800 and 500°C ($\Delta t_{8/5}$) were used to describe the window, as this term was established for ferritic steels. In these terms, $\Delta t_{8/5}$ of 8 to 30 seconds was proposed for the alloy lean 22%Cr alloy meeting UNS S31803, in order to give a high austenite content with limited carbide formation [Nas82]. Even though, the $\Delta t_{8/5}$ temperature range does not take into account the higher temperatures at which austenite formation is most rapid [Goo82] [Koh78], these cooling times are roughly incorporate the normal welding practice employed for other grades of stainless steel.

In terms of austenite formation and precipitation reactions, the time spent between 1200 and 800°C (Δt_{12-8}) was seen as a better descriptor of duplex behaviour. For instance, a Δt_{12-8} of less than 4 seconds was proposed [Gun94a], based on practical experience when welding superduplex stainless steels. This equates to an arc energy limit of 1.2 kJ/mm for wrought products between 15 and 20mm thick [Gun93b]. This cooling rate can be converted to approximate arc energies for a range of material

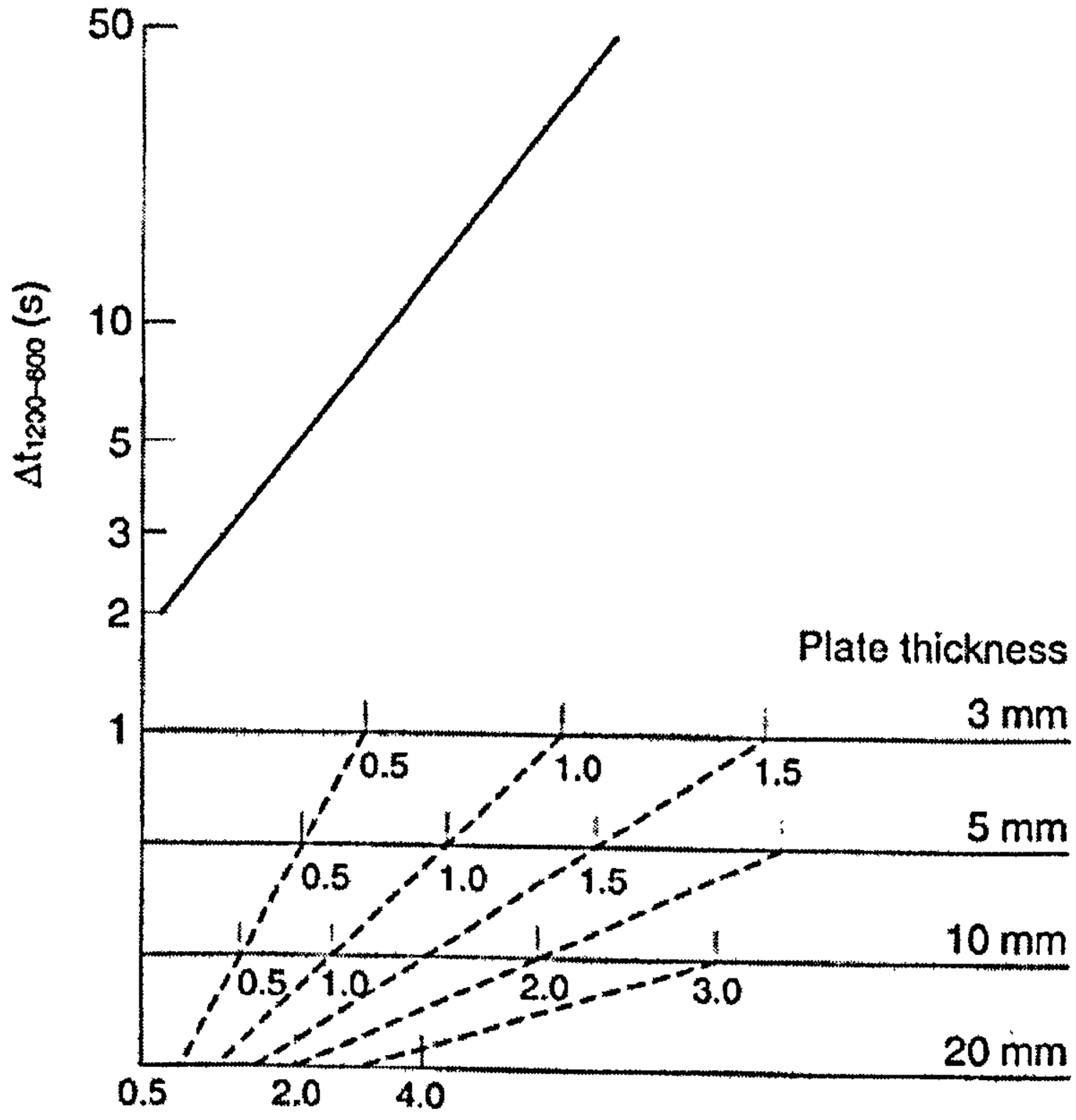


Fig.2-25 Nomogram for prediction of Δt_{12-8} for duplex stainless steels [Nob86].
Note: for guidance only.

As duplex alloys are susceptible to the precipitation of intermetallic phases during prolonged exposure to elevated temperatures, a maximum interpass temperature of 150 or 225°C is recommended for 22%Cr grades [Wal90], which is reduced to as low as 70°C for thin walled superduplex products [Ste92]

As duplex stainless steels contain a high level of nitrogen, it has been noticed that gas shielded processes lead to a loss of nitrogen in the deposited weld metal [Bon91b] [Jon91]. This is due to the common use of pure argon for the GTA deposition of the root run. However, to counteract the nitrogen loss, nitrogen-containing backing and shielding gases have been recommended [Cha90] [Gun92] [Gun94b], with the effect being more marked for the shielding gas, as the arc passes through the shield, which also shrouds the weld pool.

It is generally accepted that duplex stainless steels can be employed in the as-welded condition [Goo94], without the need for PWHT. Nevertheless, there are a number of situations where PWHT can be applied, for instance:

i) thick section welds with high restraint,
ii) joints in thin materials, where high ferrite levels are recorded,
iii) when specific properties are required, e.g. high toughness.

The temperature, time at temperature and cooling rate should be selected with caution. Solution heat treatment at 1050°C has been used on heavy section weldments, primarily to improve toughness, while the reformation of austenite and reduction in partitioning should also increase corrosion resistance. A second temperature range is available between 500 and 550°C [Sol82], which is above the temperature for alpha prime formation, but below that for sigma, Fig.2-26. This 'window' in the TTT diagram allows for stress relief of a component, although the exact temperature should be selected bearing in mind the particular alloy chemistry, with care taken over the holding time and quenching conditions. Finally, a degree of stress relief is achieved by heating the component below the temperature for alpha prime formation, for instance two hours at 350°C has been recommended for alloy S32550 [Guh82].

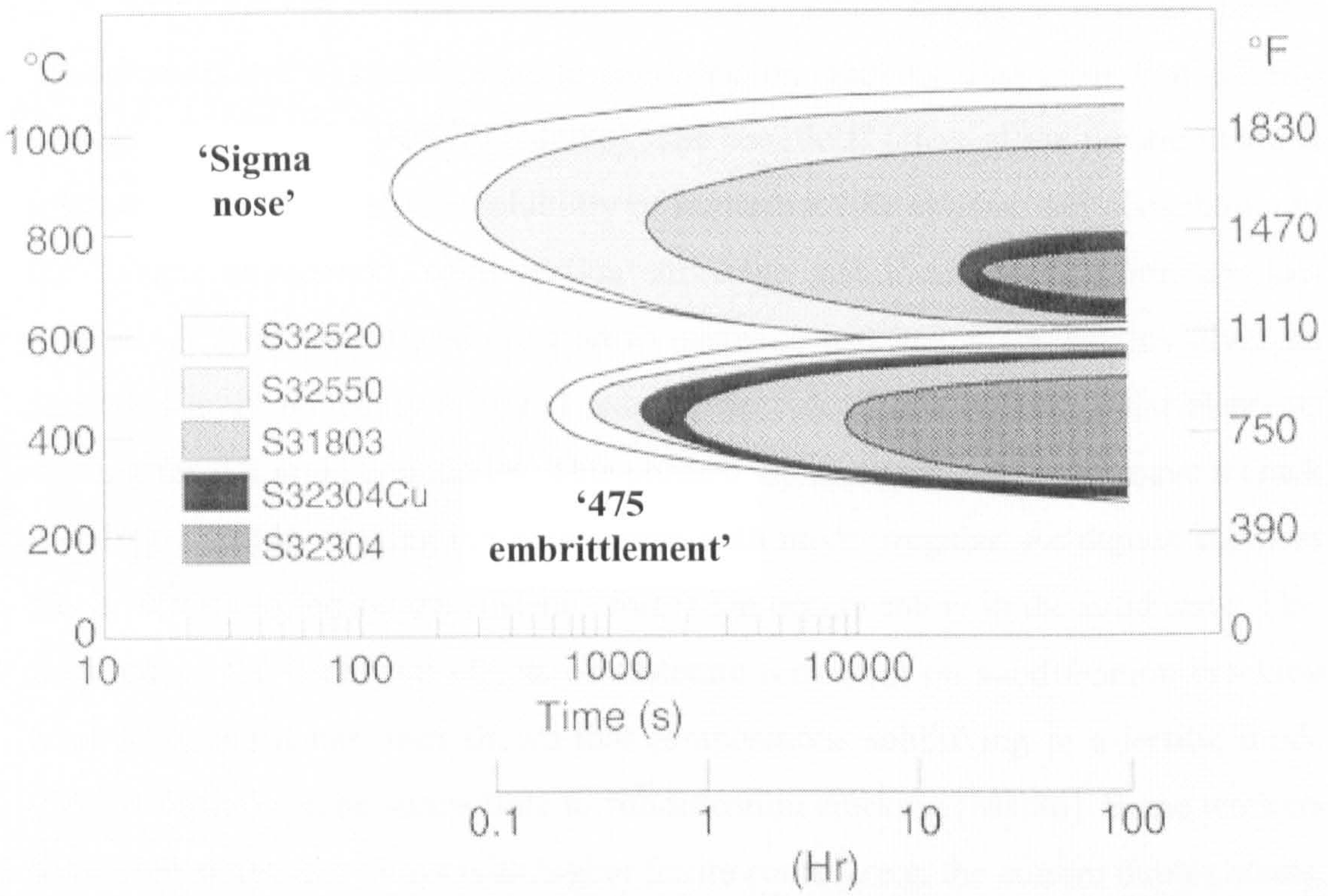


Fig.2-26 Time-Temperature-Transformation diagram for duplex stainless steels [Cha91].

2.3.2. Fabrication Cracks

Varestraint tests show that commercial duplex stainless steels are less susceptible to weld metal solidification cracking than austenitic alloys with primary austenitic solidification. However, austenitic stainless steels that solidify as primary ferrite have higher resistance to solidification cracking than the duplex stainless steels [Lip91] [Nel87]. The general practical experience is that solidification cracking is not a significant problem for the duplex stainless steels, albeit that, in highly restrained constructions, hot cracking may occur, e.g. heavy section submerged arc welds.

It is well established that austenitic stainless steels having a primary ferritic solidification are less susceptible to solidification cracking than those that solidify primarily as austenite [Kuj79] [Mat86]. The beneficial effect of the ferritic mode is often ascribed to the greater solubility of impurities like sulphur and phosphorus in the ferrite. In addition, solidification shrinkage and thermal expansion are less marked. A solid state transformation to austenite just below the solidus gives an increased grain boundary area and reduces the risk of low melting point elements wetting the δ/δ grain boundaries. This phase transformation might also have a crack arresting effect by making the propagation path more irregular. As duplex stainless steels solidify to ferrite, the austenite formation occurs solely in the solid state. This may reduce the beneficial effects of austenite formation on solidification cracking hindrance, and it has been shown that compositions solidifying in a ferritic mode (5-20% ferrite) can be susceptible to solidification cracking [Mat86]. Some workers have even stated that alloys with higher ferrite content, e.g. the current duplex steels, have a coarser columnar structure and are more likely to exhibit solidification cracks [Nel87] [Per86].

A second form of cracking involves transgranular cleavage facets [Cla81], typical of a low temperature mechanism. These hydrogen cracks have been noted in heavy section deposits (50mm thick) of low austenite content, which exhibit coarse grained ferrite with low notch toughness. Hydrogen can be absorbed in the weld pool due to:

i) contamination of the weld joint,

ii) the presence of hydrogenous material in electrode coatings or submerged arc flux,

iii) the use of hydrogen addition to the shielding gas.

High weld metal hydrogen contents can be avoided by baking SMAW electrodes at appropriate temperatures, but inadequate drying can result [Lun92] in sufficient diffusible hydrogen to cause weld metal cracking in high ferrite welds.

The diffusivity of hydrogen in the ferrite is much higher than in the austenite and the solubility of hydrogen in the austenite is thirty times higher than in the ferrite [Jar91]. The ferritic matrix provides a rapid transport of hydrogen to the austenite islands, which act as a barrier to hydrogen escape, with cracking occurring predominantly in the ferrite. If hydrogen pick-up during welding cannot be precluded, it may be possible to avoid cracking by preheating to 200°C, by soaking for about 100 hours at 200°C after welding, or by PWHT immediately after welding [Lun92] [Fek86] [Jar91]. Nevertheless, hydrogen cracking only seems to be of practical concern where high ferrite (>70%) and hydrogen contents are present [Cha90], probably combined with high restraint in thick section joints [Gun96].

2.3.3. Duplex Welding Consumables

In a weld produced either autogenously or using a matching filler, there is a tendency towards high ferrite levels, due to the fast cooling rates experienced. In extreme cases, such as electron beam or laser welding, this can lead to a fully ferritic microstructure [Hon78]. High ferrite contents are generally not desirable, due to the associated low toughness, and so a weld metal austenite content of between 30 and 70% is often recommended. To keep the weld metal phase balance within these limits, it is common practice to overalloy the consumable with an austenite stabiliser. This is generally achieved by the extra addition, over the parent composition, of 2-4% Ni and/or by nitrogen [Bow86] [Ple84] [Goo82] [Kot82].

Nickel can have a minor adverse effect on corrosion resistance by changing the partitioning of certain elements [Wal91]. Another consequence of increased nickel contents, compared to parent steel, is that a postweld heat treatment may result in low ferrite contents. Further, if the dilution from parent steel is small, as in large welded sections, ferrite levels as low as around 20-25% have been measured [Lil86] [Gre87], which might affect the weld metal properties [Kot89]. It has been shown [Kom91] that this ferrite has higher Cr and Mo contents than solution annealed parent steel which makes it more prone to formation of intermetallic phase. Thus, to avoid such precipitation, a higher solution heat treatment temperature is necessary, or, if welded components are to be subjected to a postweld heat treatment, consumables with the same composition as the parent steel have been recommended [Ste91]: the latter situation may arise with repairs of castings, for example.

Even when consumables overalloyed with nickel are employed, weld metal toughness is consistently inferior to that of base metal. The main factor is welding process and thus oxygen content [Cha90], Fig.2-27, with weld metals deposited by gas shielded processes (GTAW better than GMAW) providing higher toughness than flux shielded processes (SAW, SMAW) with basic flux systems preferred to rutile [Lil86]. For this reason, when low temperature toughness is required, it is advised that either GTA welding is used, or if thick joints are to be completed, then basic type coatings/fluxes are employed.

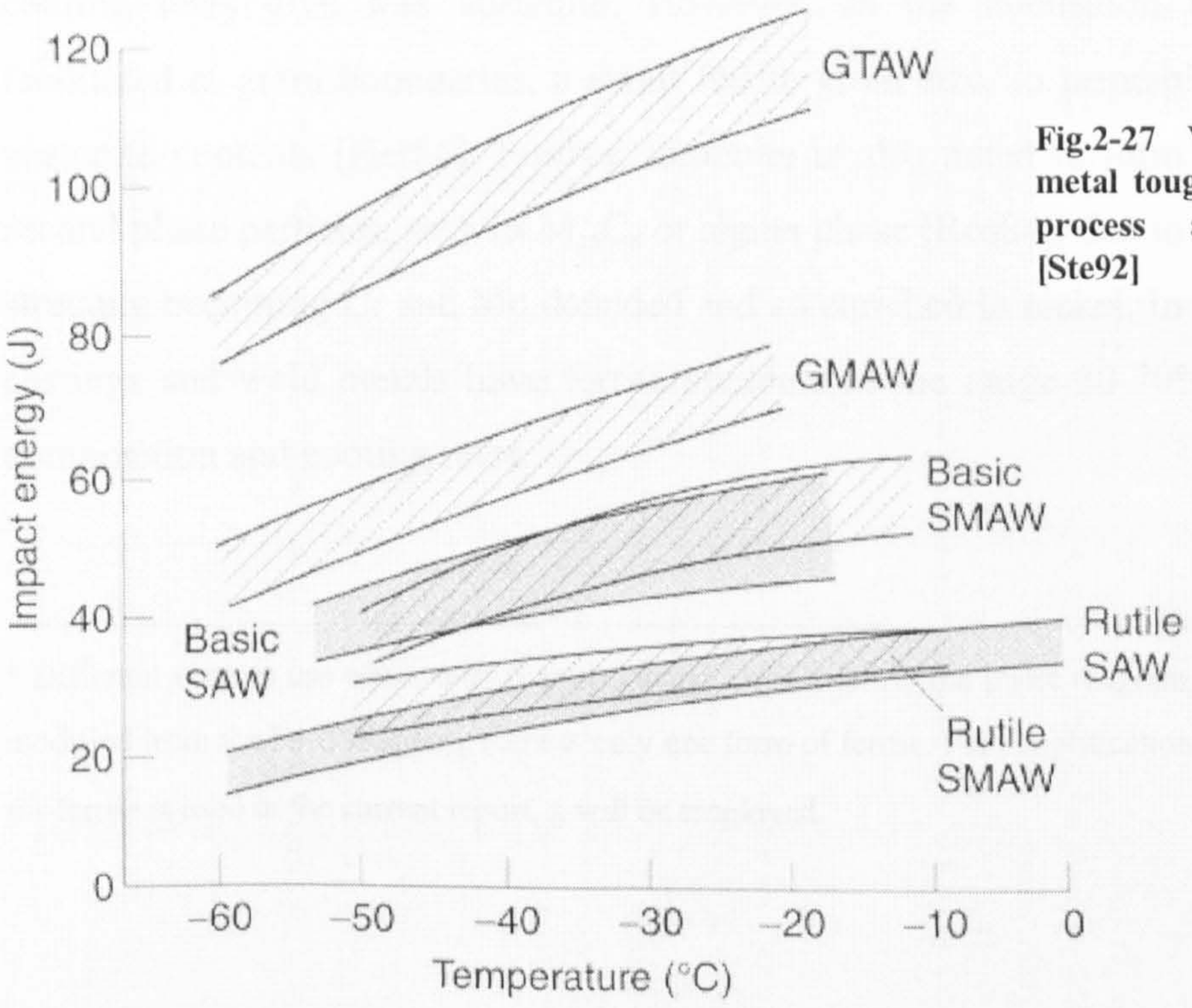


Fig.2-27 Variation of weld metal toughness with welding process and flux system [Ste92]

As explained in section 2.3.5, nitrogen content has been measured to be about 10 times higher in the austenite than in the ferrite at room temperature [Lil86]. As Cr, Mo and N are primarily responsible for the pitting resistance, see Eqn.{1-1}, the ferrite becomes susceptible to attack in borderline service conditions. Thus, it is recommended, when duplex stainless steels are selected for critical applications, that the Cr, Mo and N contents of the consumable be above that of the parent material, e.g. for alloy S31803 with a PRE_N-value of 35, a consumable with a PRE_N of 38 to 40 is employed [Wal91].

2.3.4. Decomposition of Ferrite to Primary Austenite

Duplex stainless steels are fully ferritic at elevated temperatures, Fig.2-4, with solid state austenite formation on cooling. Austenite precipitation starts below the A4 or δ-ferrite* solvus temperature, which is dependent on composition. Initial formation occurs intergranularly, followed by Widmanstätten side plates or intragranular plates depending on the ferrite grain size and cooling rate [Sou80]. Austenite precipitation is a diffusion controlled nucleation and growth process [Mun85] [Her86] [Mun83] [Ata91a] and, at least, during fast cooling, the austenite reformation is controlled by a para-equilibrium transformation mechanism whereby the diffusion of interstitial elements (carbon and nitrogen) is the controlling process [Her86] [Her93] [Her91]. Thus, the cooling rate is of major importance in determining the extent of transformation. Slow cooling rates result in more austenite formation, while fast cooling rates give less austenite. However, as the nucleation of austenite is facilitated at grain boundaries, a small ferrite grain size, in principle, favours high austenite contents [Her86]. Further, austenite is also noted to form next to Cr-rich second phase particles, such as $M_{23}C_6$ or sigma phase [Ros84], due to the surrounding structure becoming Cr and Mo denuded and so enriched in nickel. In general, duplex castings and weld metals have ferrite contents in the range 30-70% depending on composition and cooling rates.

---

* Different sources use either α or δ as shorthand for ferrite. As the phase diagram for duplex steels is modified from the Fe-C diagram, there is only one form of ferrite. For simplification, where a shorthand for ferrite is used in the current report, δ will be employed.

Once the equilibrium austenite volume fraction has been reached, selective coarsening of the phase takes place. This is reportedly encouraged by sub-boundaries, which aid diffusion. Throughout both the growth and coarsening stages, the austenite and ferrite are related by the Kurdjumov-Sachs orientation relationship [Kur30] and, during the growth stage, the austenite precipitates exhibit at least one interface that can be indexed, namely:

$$(111)\,\gamma \,//\, (110)\,\delta \;\} \qquad \text{--Eqn \{2-4\}}$$
$$[101]\,\gamma \,//\, [111]\,\delta \;\}$$

In the weld metal, ferrite solidification involves epitaxial growth from the parent material at the fusion boundary [Ata91b], i.e. the HTHAZ. The initial dendrite growth is oriented in relation to the thermal gradient [Nas91], and produces a columnar ferritic structure. This provides the starting conditions for further solid state transformations upon cooling and will dominate the final weld metal structure. The ferrite grain size and orientation, together with ferrite content and morphology, influence weld metal properties. For example, the morphology affects the weld metal Charpy impact toughness [Lil86].

2.3.5. Element Partitioning

The phase diagram shown in Fig.2-4 illustrates that the ferrite and austenite will have different compositions depending on the temperature, further illustrated by experimental data in Fig.2-28. Several workers have studied the composition of the phases and resultant partition coefficients in solution annealed product. They have demonstrated that, with the exception of nitrogen, the partition coefficients for a given element do not vary significantly between alloys [Str86] [Her82] [Sol82] [Miy82] [Lar87] [Ish86], in spite of the wide range of compositions investigated. This is due to the solubility limits for these elements not being exceeded, for the concentrations and annealing temperatures concerned. All agree that the ferrite is enriched in P, W, Mo, Si and Cr and the austenite in N, Ni, Cu and Mn, Fig.2-29. However, for the most highly alloyed grades (superduplex steels), it has been proposed that the partition coefficients tend more towards unity [Cha94], apparently due to the use of higher solution annealing temperatures, Fig.2-28.

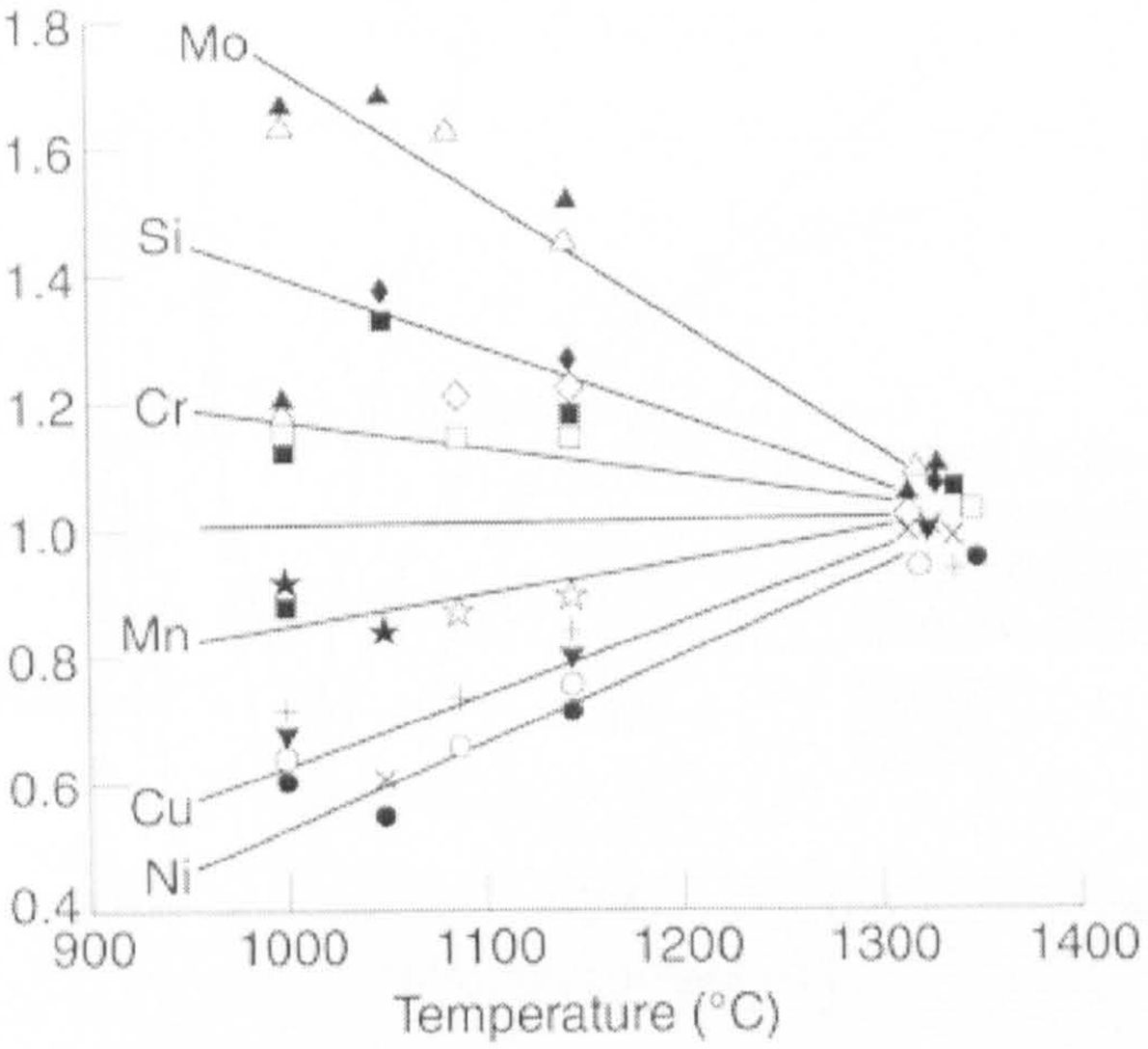


Fig.2-28 Temperature dependence of element partitioning coefficients (K = ferrite/austenite) for a range of duplex steels [Cha94]

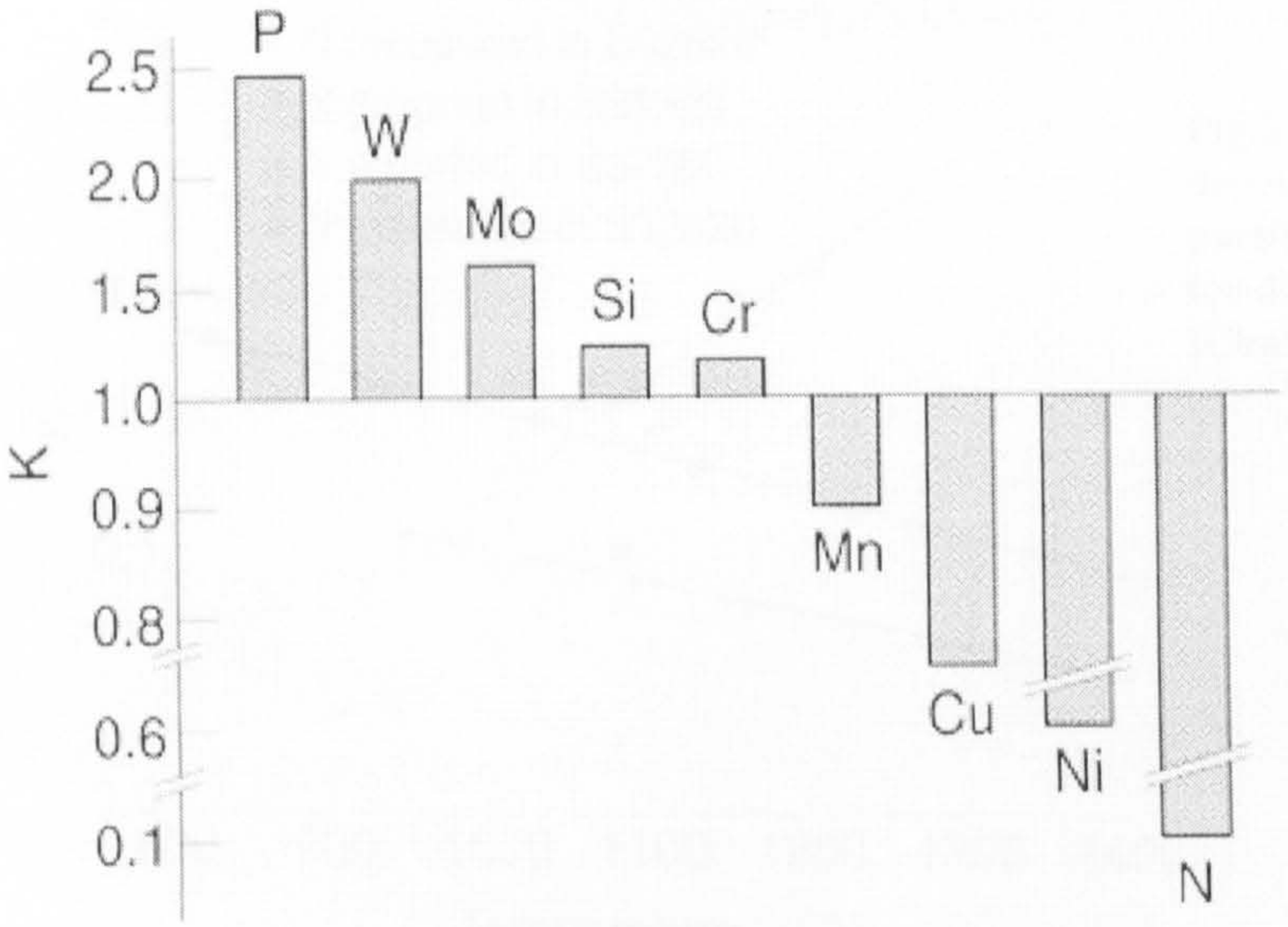


Fig.2-29 Typical partition coefficients, K, for solution annealed and water quenched products [Cha94]

The partition coefficient for nitrogen is seen to vary markedly between alloys and is highly dependent on composition. In particular, Cr and Mn increase nitrogen solubility, Fig.2-8, which explains why the superduplex grades can contain higher nitrogen contents than the lower chromium variants, Table 2-4. Nevertheless, the nitrogen partition coefficient is governed also by temperature. During a solution anneal, even though the solubility of nitrogen in ferrite may increase a little, the volume fraction of austenite decreases markedly. This leads to enrichment of nitrogen in the remaining austenite [Cha94], Fig.2-30, and so nitrogen partitioning is increased, i.e. K tends away from unity [Cha94] [Ono92] [Her92], Fig.2-31.

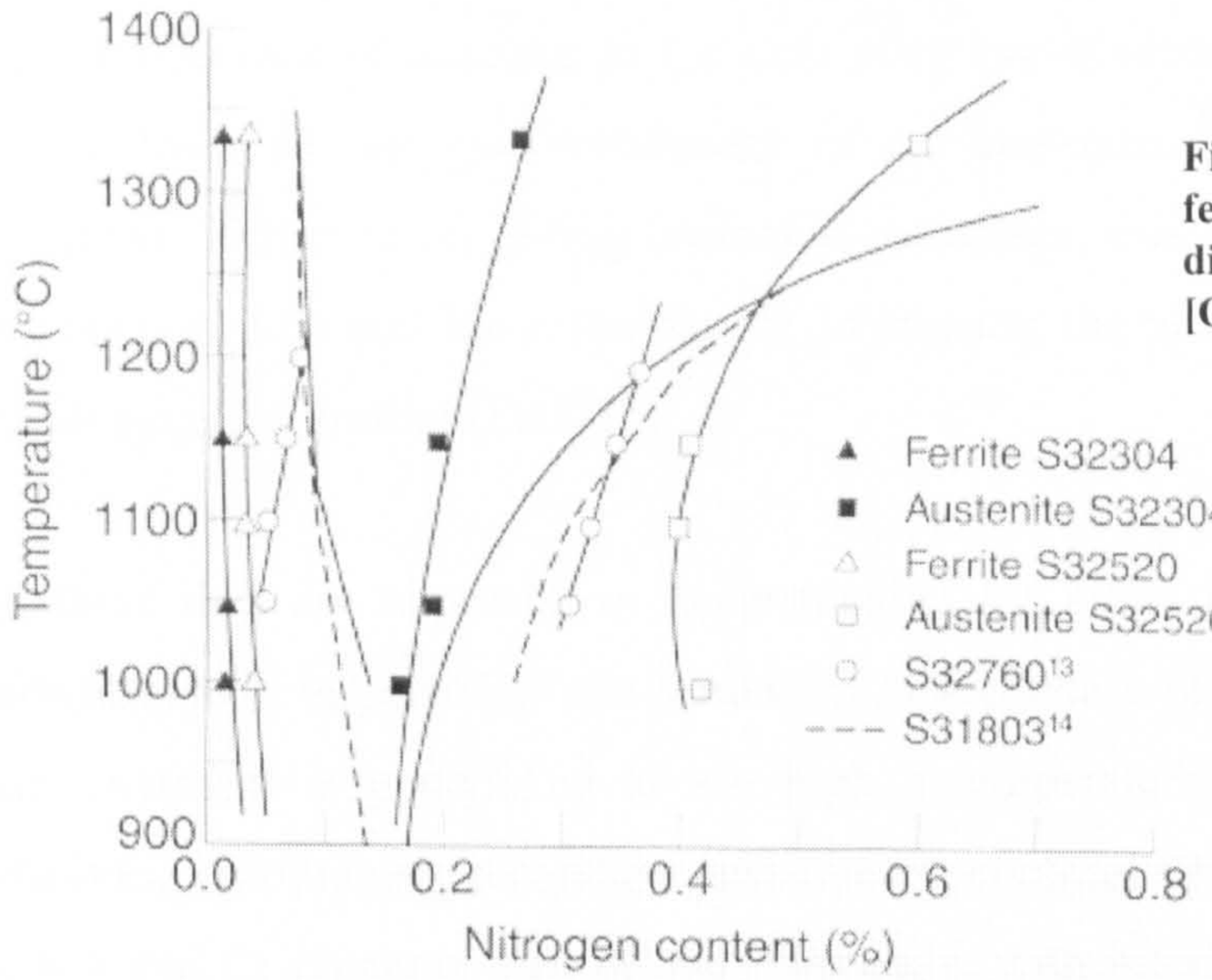


Fig.2-30 Nitrogen content of ferrite and austenite for different alloys [Cha94] [Ono92] [Her92]

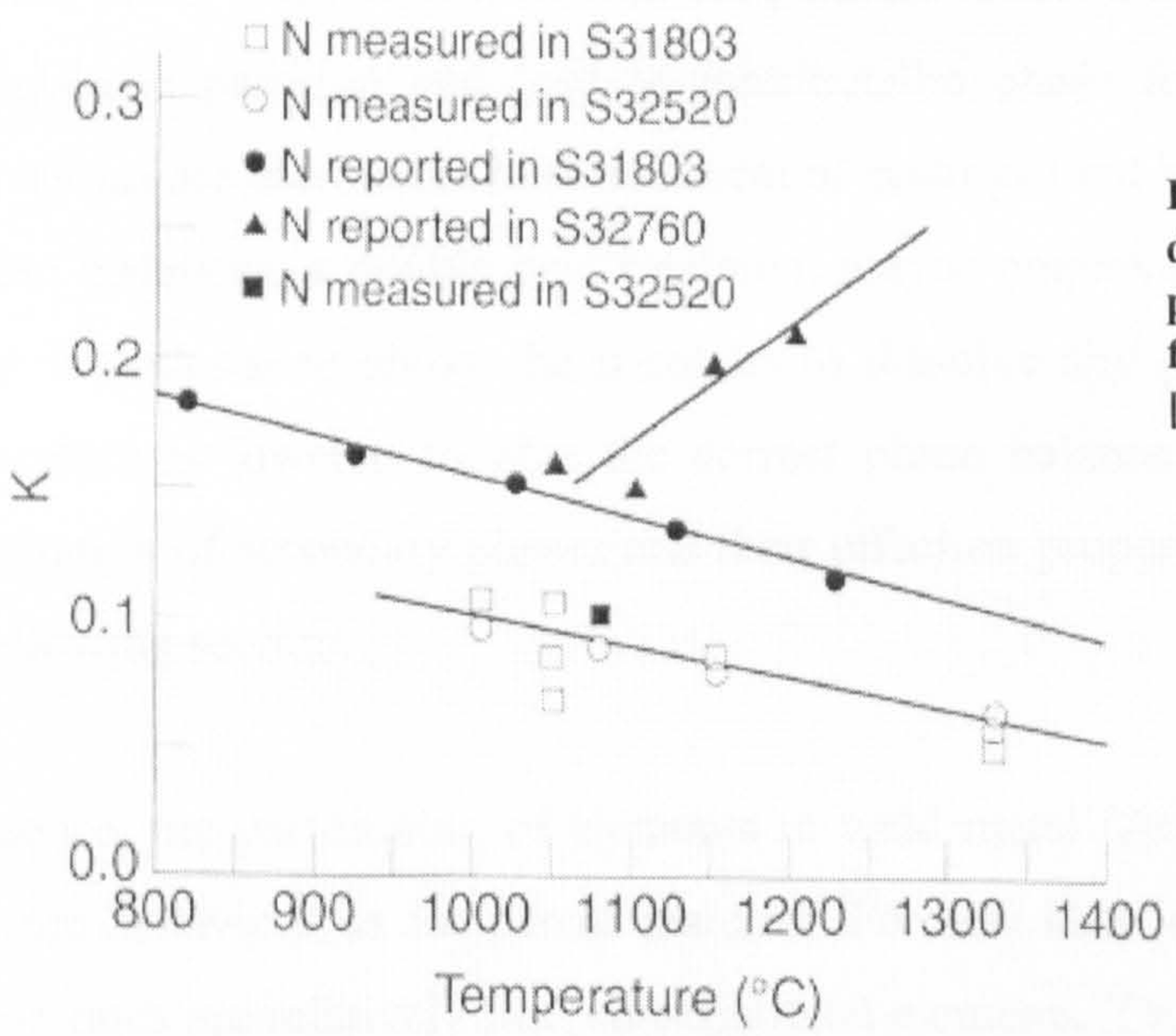


Fig.2-31 Temperature dependence of nitrogen partition coefficients (K) for different grades [Cha94] [Ono92] [Her92]

Figures 2-30 and 2-31 also show that results generated [Her92] by Thermocalc™ are in good agreement with the experimental data. Moreover, it has been observed [Cha94] that the nitrogen content is highest next to the ferrite:austenite interface, just within the austenite, due to phase boundary displacement. However, on cooling, austenite formation occurs and the ferrite becomes rapidly saturated with nitrogen, with the excess nitrogen diffusing into the austenite, with 0.03-0.05%N being the equilibrium solubility limit in ferrite at ambient temperatures [Lil86].

Further additions of nitrogen to the bulk alloy composition, as in the superduplex grades, leads to nitrogen enrichment in the austenite. And, as nitrogen has a significant influence on pitting corrosion resistance, this balances the preferential partitioning of Cr and Mo to the ferrite. In essence, the pitting resistance of the two phases becomes similar [PatUSb].

All these data are important in understanding the effect of heat treatment on the microstructure, in particular the formation of secondary phases. For instance, if the heat treatment is undertaken at too high a temperature, then primary austenite dissolves, encouraging secondary austenite on cooling, which has inherently lower N, Mo and Cr contents than primary austenite, with inferior pitting resistance. On the other hand, if the heat treatment temperature is too low, then the substitutional elements can partition and lead to intermetallic phase formation. In fact, these observations are used in the heat treatment of castings (and heavy forgings) [Hoc91]. In these instances, a double heat treatment maybe employed where first a solution anneal is undertaken above the σ-solvus to dissolve any precipitates. Second, the temperature is lowered to give the correct phase balance before quenching. The precipitation of secondary phases and their effect on properties will be addressed in the following section.

In essence, the partitioning of elements in weld metal [Ata91b], Fig.2-32, follows the same behaviour as for parent material. For low heat input welding, where the cooling rates are relatively fast, substitutional elements (Cr, Ni, Mo etc.) are almost equal in both phases whereas the interstitial elements controlling the reaction are heavily concentrated in the austenite. On the other hand, if higher heat inputs are employed, slower cooling rates result, and austenite transformation is mainly diffusion controlled with subsequent partitioning of the substitutional elements [Lip91] [Ata91b]. Multipass welding has a similar effect on partitioning as slow cooling [Oga90].

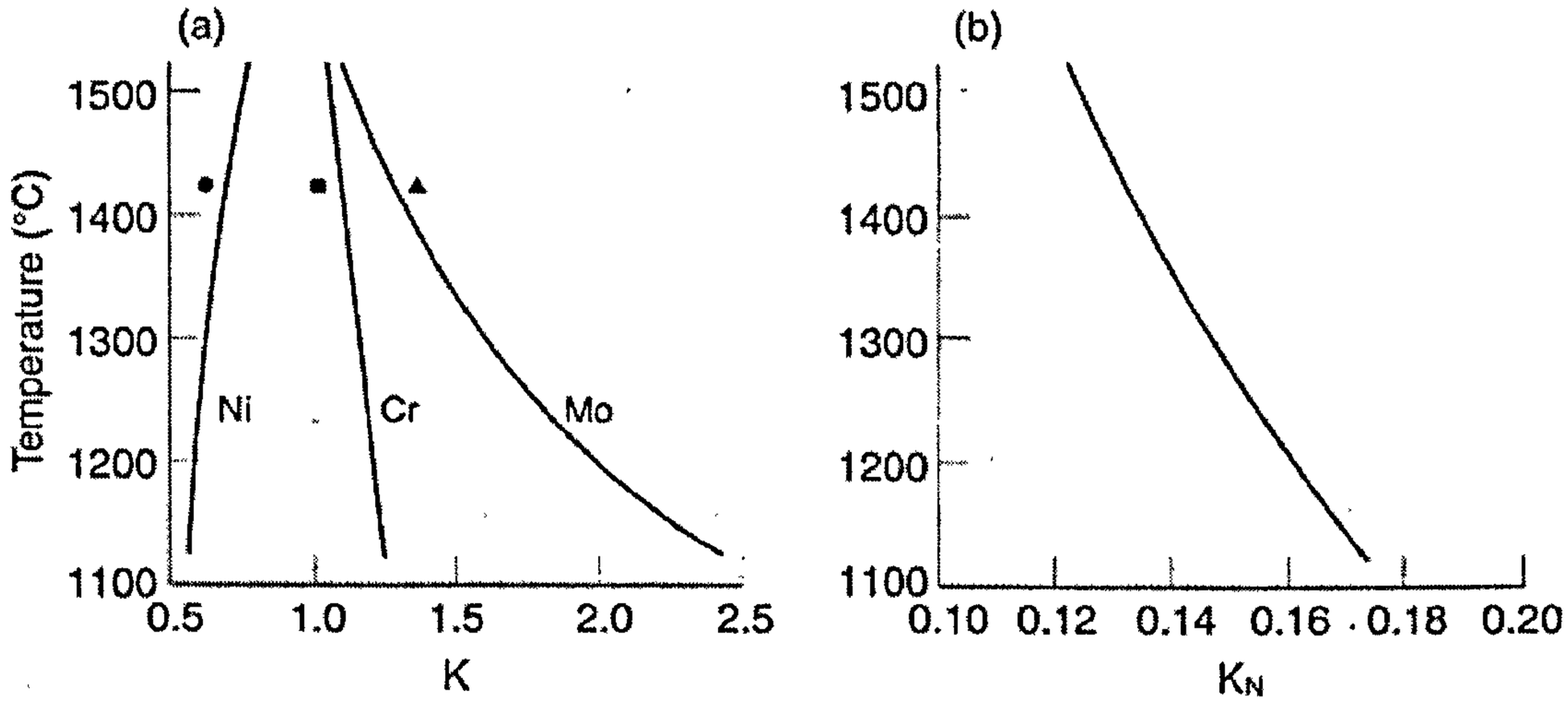


Fig.2-32 Partition ratios (K) for S31803 weld metal as a function of temperature. (a) Cr, Ni and Mo (b) N. [Ata91b]

2.3.6. Phase Balance Measurement and Prediction

Essentially there are two methods for measuring the ferrite content of weld metals and parent materials, both of which have advantages and disadvantages. The first requires careful metallographic preparation to a 1μm finish, followed by an etch in 40% KOH solution at 7-8V [TWI93b]. The ferrite phase becomes a brown/orange colour in contrast to the white austenite and so the volume content of ferrite can be measured using a point count procedure, following the essence of ASTM standard E562-95. Image analysis systems can be employed for parent material assessment, but it is not advised for weld metal due to the more variable etching response. The advantage of point counting is that it can be applied to all microstructures, including the narrow HAZ, but is difficult to undertake in-situ (i.e. generally considered a destructive technique) and is relatively slow and expensive. The accuracy of this method, in terms of the 95% confidence interval, is at best ±5% ferrite at the 50% ferrite level [Gla60].

The second measurement technique takes advantage of the different magnetic properties of the two phases: ferrite is ferro-magnetic while austenite is not. In this case an arbitrary 'Ferrite Number' (FN) is assigned to a given level of magnetic attraction, defined from primary standards (based on coating thickness) and a magnetic beam balance known commercially as a MagneGage instrument. At low ferrite levels, typical of those found in nominally austenitic weld metals, FN-values were once considered to be approximately the same as ferrite percent [DeL74] (say up to 6% or 6FN), while higher FN-values overstated the ferrite percent. It now seems that FN overstates ferrite percent at all levels [Kot97]. As the FN of a particular weld metal depends not only upon the amount of ferrite, but also upon the composition of the ferrite (in particular iron content), no simple correlation between the two scales can be drawn [Kot97]. A correlation made for one alloy is not likely to carry over to another alloy.

The prediction of Fe-Cr-Ni microstructures can be traced to work by Bain and Griffith in 1927 [Bai27]. More recently, the Schaeffler diagram (Fig.2-1) was used, which is an empirical description of weld metal microstructures [Sch49]. This type of diagram has been employed for many years to predict cast or weld metal microstructures in conventional austenitic and other stainless steels and to some extent to optimise base metal and filler compositions.

It became apparent that the Schaeffler diagram did not predict duplex microstructures very well [Hof78] and so other diagrams and relationships were proposed [Nob86] [Sku78], culminating in the WRC-1992 diagram [Kot92], Fig.2-33. The WRC diagram provides reasonable agreement in many practical applications [Nas82], although for relatively low and high nitrogen contents (<0.19%N and >0.26%N), FN values are over- and under-estimated respectively [Zha96]. This may imply that a variable factor for nitrogen is required, as proposed by DeLong in 1956 [DeL56] or that cooling rate should be considered [Yas94]. Nevertheless, the WRC-1992 diagram is still recommended for first approximation of weld metal content.

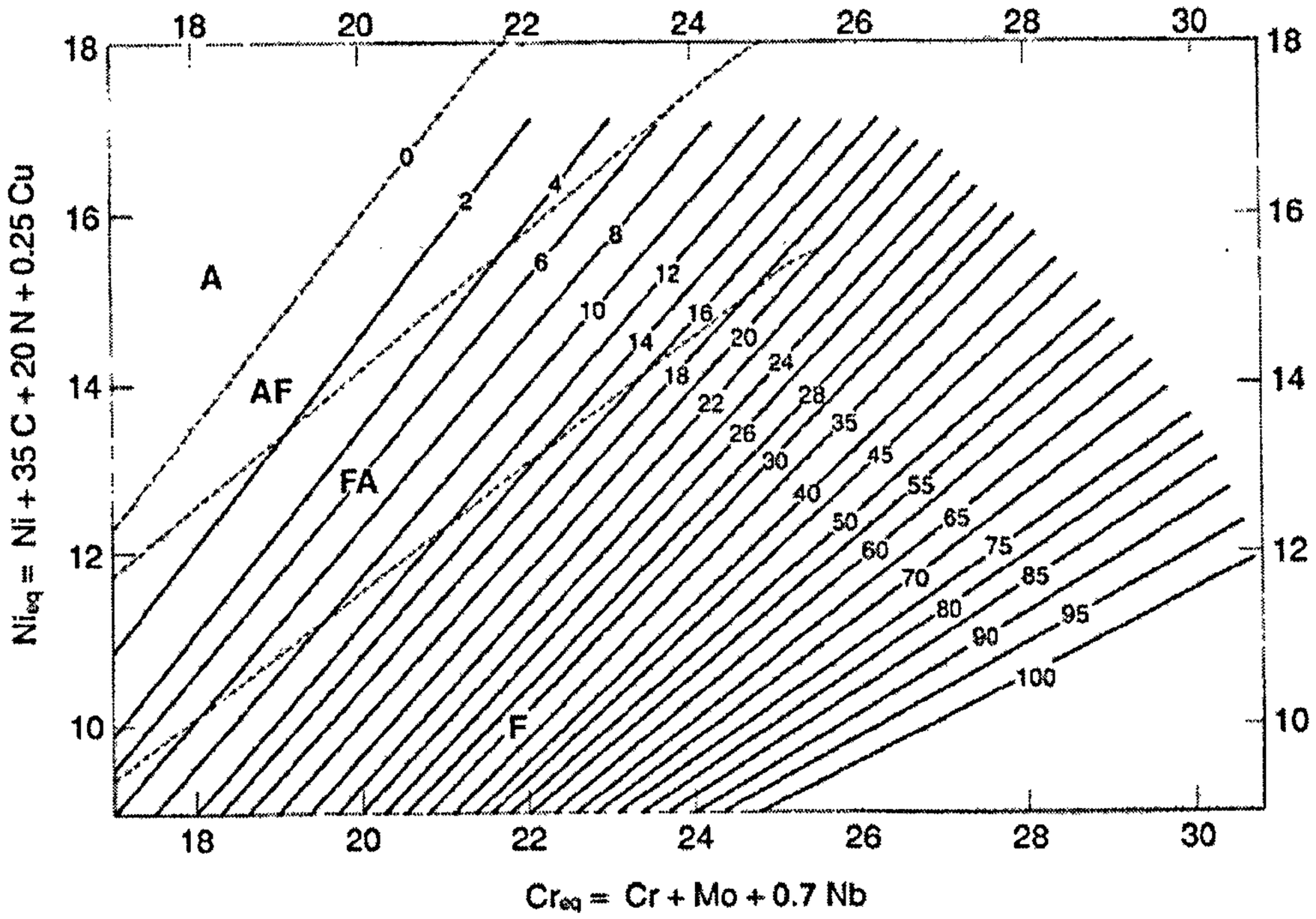


Fig.2-33 WRC-1992 diagram [Kot92]. The FN prediction is only accurate for weld compositions that fall within the bounds of the iso-FN lines that are drawn on the diagram.

2.3.7. Second Phase Particles

Alpha prime (α') and G-phase

The lowest temperature decomposition within a duplex steel is that of alpha prime (α'), which occurs between 300 and 525°C (Fig.2-34). It is the main cause of '475' embrittlement in ferritic stainless steels [Fis53] [Mar64] [Bla64], commensurate with an increase in hardness. Further, it is suggested that α'-formation is a consequence of the miscibility gap in the Fe-Cr system [Wil58], whereby ferrite undergoes spinodal decomposition into Fe-rich δ-ferrite (Table 2-7) and a Cr-rich α' [Sol79] [Lag67] or, just outside the spinodal but still within the gap, classical nucleation and growth of α' occurs [Hil61] [Cah68]. Alpha prime is often associated with the co-precipitation of Cr_2N in the form of subgrain networks of Cr_2N needles interspersed within a film of α'. As a result, there has been conflicting evidence in the past as to the nature of 475 embrittlement [Sol79] [Hos78].

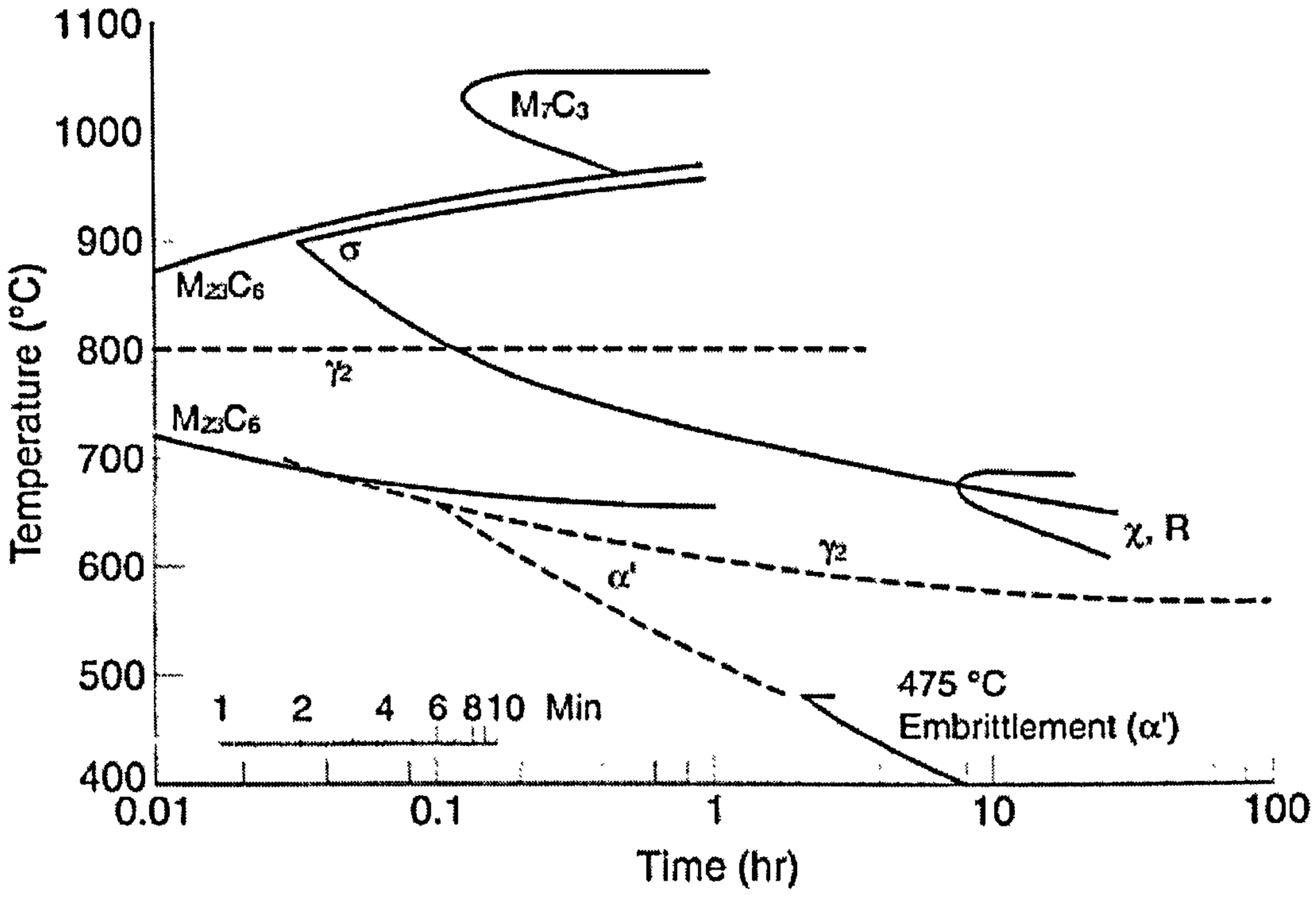


Fig.2-34 Time-Temperature-Transformation (TTT) diagram for alloy S32304 [Sol82]

At temperatures below 400°C, the Arrhenius equation is often employed to describe the kinetics of embrittlement. The activation energy characteristic of 475 embrittlement is similar to Cr-diffusion in ferrite, although other factors influence α' formation, such as Cr, Mo and Cu contents and high ferrite levels [Sol82] [Com82]. This is illustrated in Fig.2-26, in which the tendency to α' formation is compared for several duplex stainless steels. Further, G-phase develops at α/α' interfaces between 300 and 400°C, due the enrichment of Ni and Si at these locations [Aug90], Table 2-7.

Secondary austenite (γ_2)

Secondary austenite or γ_2 can form by different mechanisms depending on the temperature (Table 2-7). Below about 650°C, γ_2 has a similar composition to the surrounding ferrite, suggesting a diffusionless transformation, with characteristics similar to martensite formation [Sou80].

At temperatures between 650 and 800°C where diffusion is more rapid, Widmanstätten austenite can precipitate [Sol79]. This form of γ_2 obeys the Kurdjumov-Sachs relationship [Kur30] and appears diffusion assisted, as it is enriched in Ni compared to the ferrite matrix [Jos91], Table 2-7. Even though there is some enrichment of nitrogen in γ_2 compared to the ferrite matrix, both Cr and N contents of γ_2 are substantially below that of primary austenite [Nil94].

Table 2-7 Crystallographic characteristics of particles observed in duplex stainless steels

Particle	Chemical formula	Cr	Ni	Mo	Formation range, °C	Lattice type	Space group	Lattice parameter (A)	Orientation relationship	Preferred location	Reference
ferrite (δ)*	-	27.4	8.7	4.0	-	BCC	Im3m	a=2.86-2.88		Matrix	-
alpha prime (α′)	-~	65	2.5	13	300-525	BCC	Im3m	a=2.86-2.88	(001)α′ // (001) δ [100]α′ // [100]δ	Intra- δ	-
G-phase	≥14%Si $	25	25	4	300-400					Inter α/α′	[Aug90]
primary austenite (γ)*	-	26.6	9.6	3.3	<1250	FCC	Fm3m	a=3.58-3.62	K-S: (111)γ // (110)δ [101]γ // [111]δ	Intra- δ	-
secondary austenite (γ_2)	Type 1	same as ferrite			<650	FCC			<133> δ N-W	Intra- δ	[Sou80]
	Type 2	24.3	11	3.4	650-800				K-S	δ/γ and δ	[Jos91] [Nil94]
	Type 3				700-900					with σ	[Nil92b]
sigma (σ) #	Fe-Cr-Mo	30	4	7	600-1000	tetragonal	$P4_2/mnm$	a=8.79, c=4.54	(111)γ // (001)σ [110]γ // [110]σ	Inter δ/γ	[Hal66]
chi (χ) #	$Fe_{36}Cr_{12}Mo_{10}$	25	3	14	700-900	BCC-αMn	I43m	a=8.92		Inter δ/γ	[Kas54] [Tho84]
R or Laves ^	Fe_2Mo	25	6	35	550-650	trigonal	R3	a=10.903, c=19.34	$<0001>_R$ <111>δ	δ/γ and δ	[Red91] [Rid51]
chromium nitrides	Cr_2N ~	72	6	15	700-950		P31m	a=4.795, c=4.469	<0001>Cr_2N <011>δ	Intra- δ	[Eri34]
	CrN					cubic	Fm3m	a=4.13-4.47			[Nil92a]
Pi (π) ^	$Fe_7Mo_{13}N_4$	35	3	34	550-600	cubic	$P4_132$	a=6.47	<001>π <012>δ	Intra- δ	[Nil91a] [Eva57]
Epsilon (ε)	Cu-rich				not defined					Intra- δ	[Her86]
Tau (τ)					550-650	orthorhombic	Fmmm	a=4.05, b=4.84, c=2.86			[Cah82]
Carbides	M_7C_3				950-1050		Pnma	a=4.52, b=6.99, c=12.11	{111}δ <111>δ	Inter δ/γ	[Rou70]
	$M_{23}C_6$ ~	58	2.5	12	650-950	FCC	Fm3m	a=10.56-10.65		Inter δ/γ	[Bow72]

Composition refs: * = [Kas54]; # = [Cha91]; ^ = [Kol83]; ~ = [Cha82]; $ = [Aug90].

K-S = Kurdjumov-Sachs; N-W = Nishiyama-Wasserman

In the 700-900°C temperature range [Jos91], a eutectoid of γ_2 + σ can form, as γ_2 absorbs Ni and, to some extent, rejects Cr and Mo (Table 2-7), encouraging Cr, Mo-rich precipitates, such as sigma phase. Similarly, one form of γ_2 which forms at δ/γ boundaries, is found to be depleted in Cr, especially if it has co-precipitated with Cr_2N [Nil92b]. Either of these diffusion controlled reactions can render the area susceptible to pitting corrosion.

Sigma (σ)

The deleterious Cr, Mo rich σ-phase is a hard brittle precipitate, which forms between 650 and 1000°C, Fig.2-34, reducing both impact properties and corrosion resistance. At the peak temperature of around 900°C, ferrite decomposition to sigma takes about two minutes. The nucleation of σ-phase has been discussed in the literature with some controversy, mainly concerned with the requirement for pre-existing $M_{23}C_6$ particles [Gol67] [Ble67] [Wei72]. Certainly, σ-phase has been found to nucleate at temperatures above 750°C on such particles [Red91] [Wan91], with the following order of preference: δ/γ phase boundaries, austenitised δ/δ sub-grain boundaries and high energy δ/δ grain boundaries (Table 2-7). These nuclei can grow into coarse plates, lamellar eutectoid σ+γ [Cha82] [Str86] [Ohm84] or σ+δ aggregates [Red91]. In the last case, the interlamellar ferritic region has a high dislocation density probably attributed to the volumetric expansion from δ to σ. Further, in the case of phase boundaries, e.g. when δ transforms to γ or γ_2, the remaining δ becomes enriched in Cr and Mo, and denuded in Ni, enhancing σ-formation and, for the same reason, growth progresses into the destabilised ferrite.

The elements Cr, Mo, Si and Mn have been noted to encourage σ-formation [Cha82] [Ros84] [Str86], Fig.2-6, whilst nitrogen is reported to stabilise austenite against σ-formation [Cha90]. On the other hand, Ni has been found to enhance σ-formation, but reduce the equilibrium volume fraction [Mae83a], as it enhances γ-formation and so concentrates the σ-promoting elements in the remaining ferrite. Finally, deformation decreases the time required to form sigma by one magnitude [Mae83b] and higher solution annealing temperatures increase δ-content, reduces the concentration of σ-promoting elements, and so retards formation [Jos91].

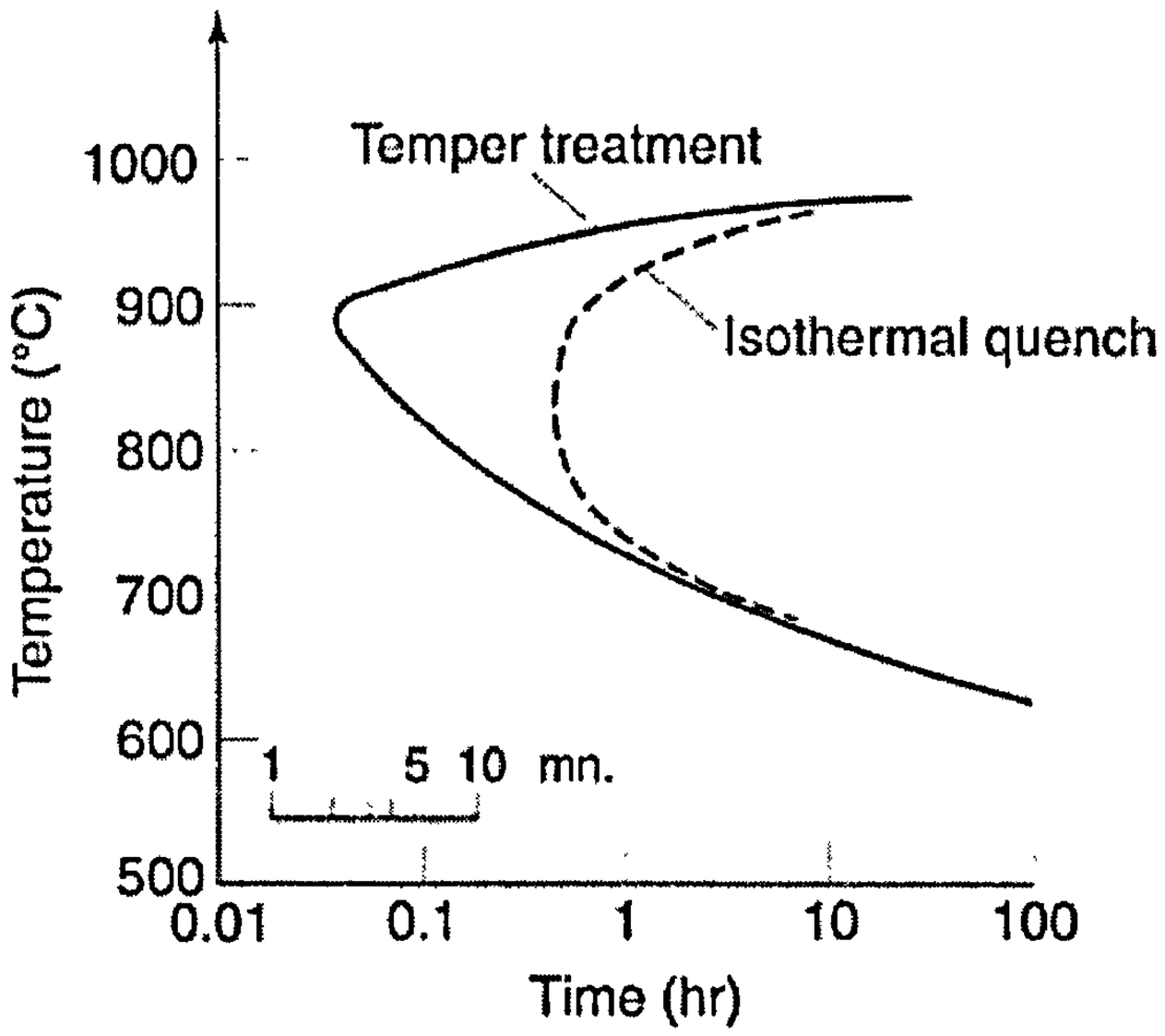


Fig.2-35 C-curves for the beginning of sigma phase formation by a temper treatment or by an isothermal quench [Hoc73]. Results from an old steel with nominal composition: 20Cr/8Ni/2.5Mo/1.5Cu

Comparison of σ formation rates for tempering (reheating from room temperature) and isothermal quenching (cooled from higher temperature) tests, have shown that the rate is faster when tempering the metal [Hoc73], Fig.2-35. It is known that the nucleation rate of a precipitate is low, near its decomposition temperature plateau [Cot75], which for σ-phase is about 900°C. However, as nuclei form by a diffusion mechanism, formation is enhanced at higher temperatures. Thus, as the temperature drops to just below the decomposition plateau during an isothermal quench, the structure is devoid of sigma nuclei and formation is governed by the nucleation rate, which is relatively slow. However, in tempering tests, the alloy is brought up through a temperature range where sigma nucleation is rapid. As the temperature is further increased these nuclei are able to grow quickly.

Chi (χ) phase

Like σ-phase, χ-phase forms between 700 and 900°C, although in much smaller quantities [Nil92a]. However, enrichment of ferrite with intermetallic forming elements during a long exposure to relatively low temperatures, i.e. 700°C, favours the precipitation of χ-phase (Fig.2-34). Like sigma, χ-phase often forms on the δ/γ interface and grows into the ferrite and has three times the lattice parameter of ferrite [Red91]. However, the cube-cube orientation relationship (Table 2-7) ensures continuity between χ and the δ-matrix. χ–phase has a similar influence on corrosion and toughness properties as σ-phase, but as the two phases often co-exist, it is difficult to study their effects individually.

The original EDX analysis of χ-phase performed by Kasper [Kas54] was undertaken on low Mo-bearing steel. More recent work on modern duplex steel has shown the composition to be more Mo-rich [Tho84], and, as χ-phase contains more high atomic number elements than σ-phase, it is easily identified using back scattered electron imagery [Nil92b].

R, π, and τ phases

Laves or R phase (Fe_2Mo) precipitate in small quantities between 550 and 650°C (Table 2-7), at both intra and inter-granular sites [Nil92a], with the precipitates found at the former sites containing about 35%Mo [Nil91a]. Both forms, influence the pitting resistance, but, as the intergranular form contains slightly more molybdenum, i.e. 40%Mo, its affect is more marked.

The π-nitride precipitates at intragranular sites in duplex weld metal [Nil91a] after isothermal heat treatment at 600°C. It is Cr and Mo rich (Table 2-7) and so has been previously confused with σ-phase. Further, heat treatment in the temperature range 550 to 650°C can lead to the formation of the heavily faulted needle-like τ-phase on δ/δ boundaries [Red91], Table 2-7.

Nitrides Cr_2N and CrN

The solubility of nitrogen is considerably higher in austenite than in ferrite, and has been shown to partition to the former phase [Kol83]. Above the solution annealing temperature (about 1040°C), the volume fraction of ferrite increases, until just below the solidus a completely ferritic microstructure can be present (Figs.2-3 & 2-4); though in the higher alloy grades some austenite may remain. At these temperatures, the nitrogen solubility in ferrite is high, but on cooling the solubility drops and the ferrite becomes supersaturated in nitrogen, leading to the intragranular precipitation of needle-like Cr_2N [Nil92b]. In a similar manner, Cr_2N is more likely to form after higher solution heat treatment temperatures [Ros84] and forms rapidly even if quenched form such temperatures [Nil88]. However, welding favours the formation of another nitride in the HAZ: the cubic CrN [Kaj91] [Her86], Table 2-7.

Isothermal exposure to the 700-950°C temperature range, Fig.2-6, produces intergranular Cr_2N at δ/δ grain boundaries as thin plates on subgrain boundaries, triple points, inclusions and along dislocation arrays (Table 2-7). This latter form of Cr_2N has been stated to effect pitting corrosion [Nil92a].

Carbides $M_{23}C_6$ and M_7C_3

In duplex grades with moderately high carbon levels, the carbide $M_{23}C_6$ rapidly precipitates between 650 and 950°C (Fig.2-34), requiring less than one minute to form at 800°C [Sol79]. Precipitation predominantly occurs at δ–γ boundaries, where Cr-rich ferrite intersects with carbon rich austenite. However, $M_{23}C_6$ can also be found at the δ/δ and γ/γ boundaries and to a lesser degree inside the ferrite and austenite grains [Cha82]. Several precipitate morphologies have been recorded including cuboidal and fibrous particles, as well as a cellular form [Bec69]. A typical analysis is given in Table 2-7, illustrating a ca.60%Cr rich precipitate (with Fe, Mo and Mn) and an associated Cr depleted zone in its vicinity. This zone has been reported as a site for pit initiation [Sol82], which subsequently propagates into the Cr- and Mo-lean austenite phase.

M_7C_3 forms between 950°C and 1050°C (Fig.2-34) at the δ/γ grain boundaries [Sol82]. However, as its formation takes 10 minutes, it can be avoided by normal quenching techniques. Further, as modern duplex grades contain less than 0.02%C, carbides of either form are rarely if ever seen [Nil92a].

2.3.8. Corrosion Resistance of Weldments

The chloride pitting resistance of both phases can be optimised for the annealed parent steel by using thermodynamic databases and by adopting suitable factors for elements influencing the corrosion resistance [PatUSb] [Tsu86], Section 2.2.7. To this end, the empirical PRE_N relationship appears to predict the ranking order for base steels (Fig.2-36). However, in a duplex weldment, a number of metallurgical reactions occur that can effect the local PRE_N value or make the conditions so complex that it is impossible to predict the pitting resistance by a single expression [Gun94a], Fig.2-36.

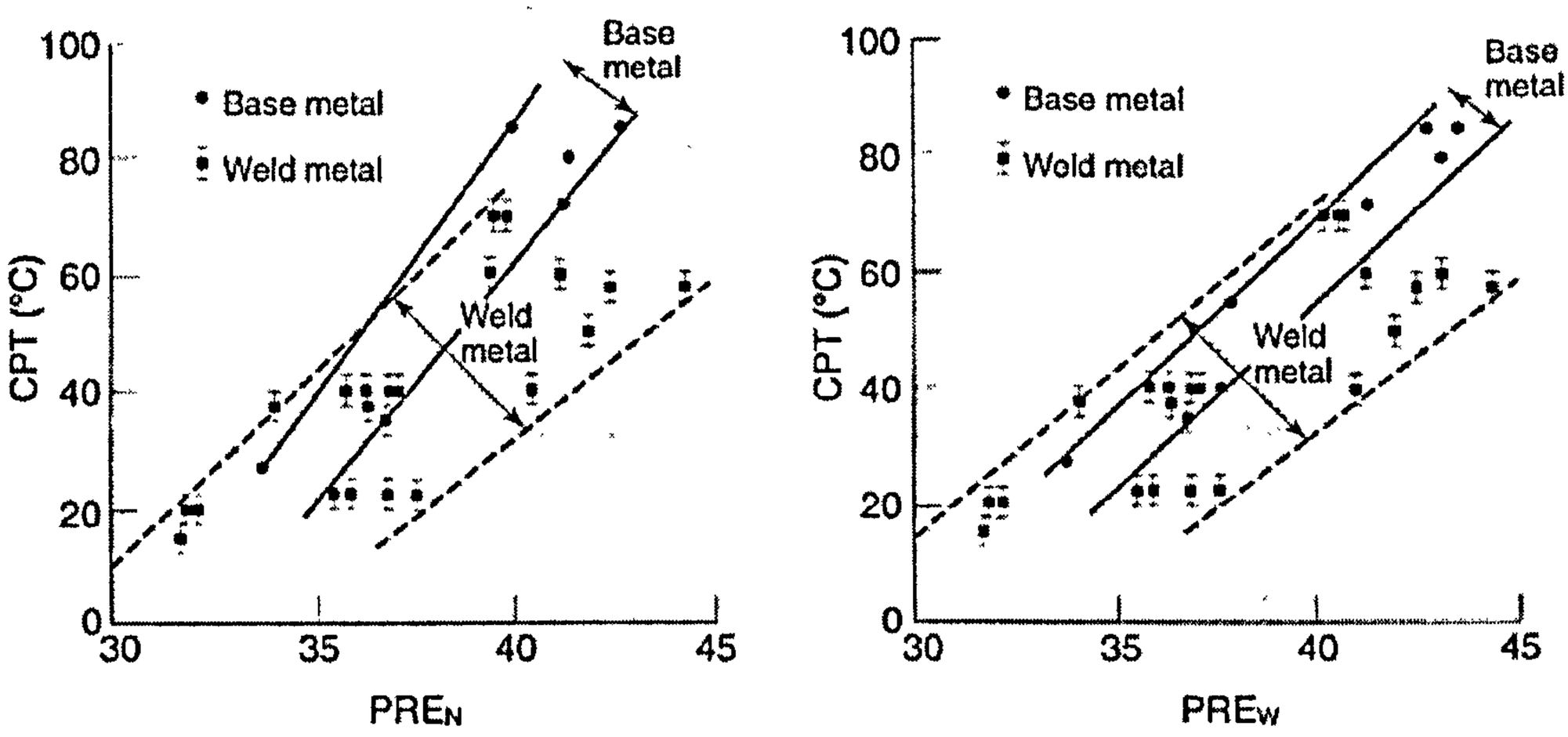


Fig.2-36 Ferric chloride critical pitting temperature (CPT) data for a range of duplex and superduplex base metals and weldments against: (a) PRE_N and (b) PRE_W [Gun94a]

Partial austenite formation in a weld creates substantial partitioning of important elements between the phases compared to the solution annealed material. Furthermore, precipitation of nitrides, intermetallic phases and secondary austenite may all contribute to a loss in pitting resistance. In particular, σ-phase in the HAZ renders ferrite susceptible to pitting corrosion [Fag91] [Fau91], as sigma progresses into the ferrite denuding the phase of Cr and Mo [Ohm84] [Tho84], e.g. Fig.2-37. In a similar manner, γ_2 can be a preferred site for attack weld metal [Pak90], presumably because it is Cr, N and, to a lesser extent, Mo depleted [Sol82] [Nil94].

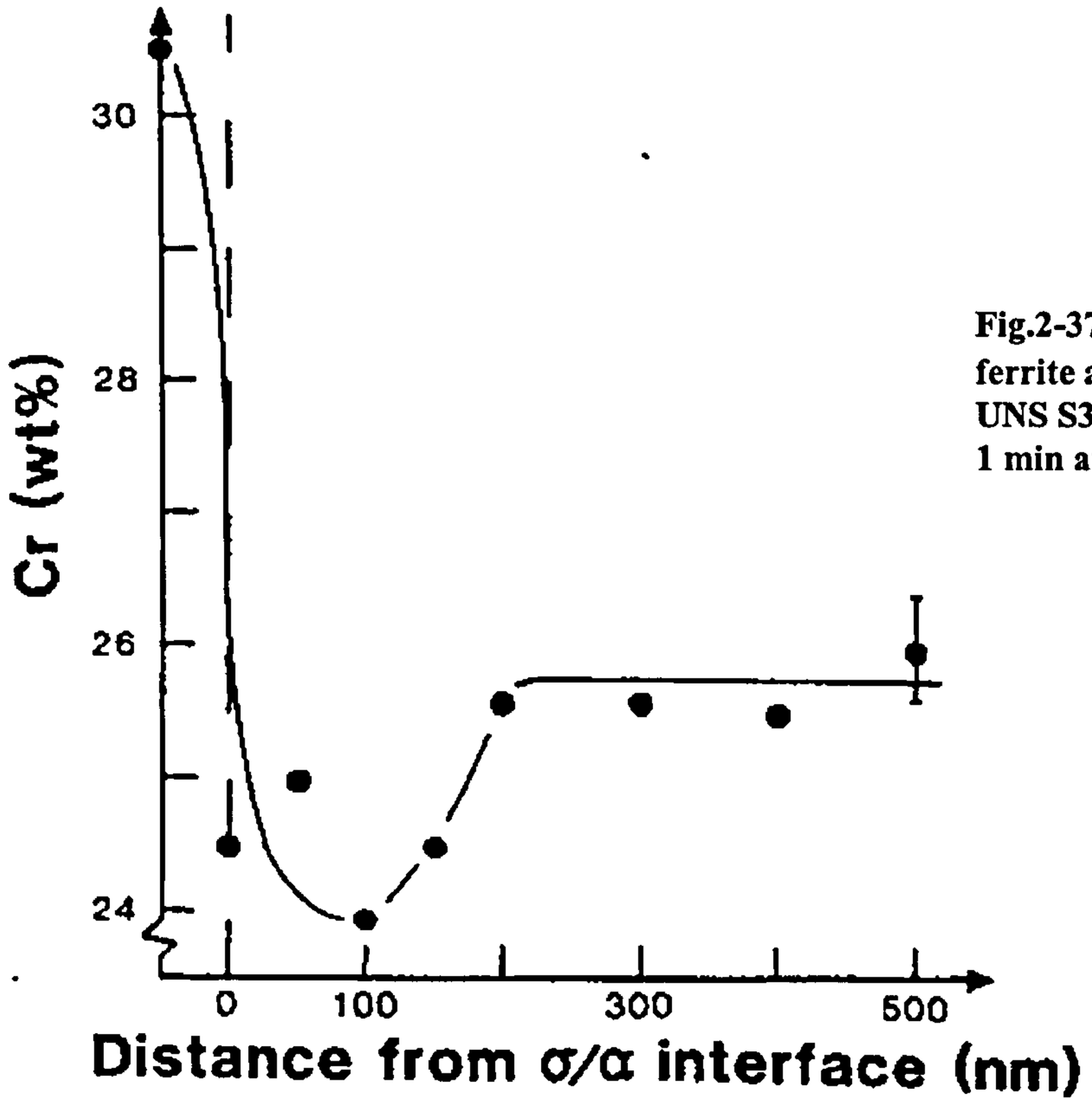


Fig.2-37 Cr-depletion in ferrite adjacent to σ in UNS S31803 steel aged for 1 min at 850°C [Tho84]

Many investigations show that the pitting corrosion rate increases [Yas86] [Ume86] [Sri84] [Kit86] and the critical pitting temperature decreases with lowered heat input [Kit86] [Goo86], i.e. fast cooling rates. Attack can occur in the HTHAZ, due to a high ferrite content that encourages nitride precipitation, causing chromium depleted zones. Alternatively, as there is little time for element partitioning between the phases in the weld metal, the austenite contains similar Cr and Mo contents as the ferrite, but virtually all of the nitrogen. This situation renders the ferrite prone to attack [Oga89] [Her91] [Kol82].

At sufficiently high arc energies (i.e. slow cooling rates), Cr_2N precipitation takes place in the remote LTHAZ and, for the superduplex grades, intermetallic phase precipitation can occur. Further, multipass welding can result in formation of secondary austenite with low contents of Cr, Mo and N and thus a lower pitting resistance [Bow86] [Nil91b], if these precipitates are exposed to the environment. A PWHT can restore the pitting resistance [Lil86] [Lun87], although this should take account of the comments made in Section 2.3.1.

At intermediate cooling rates, element partitioning between the austenite and ferrite occurs within the weld metal. This provides the two phases with similar composition to solution annealed base material (see Section 2.3.5), although nitrogen remains concentrates in the austenite [Lil86] [Her91]. Further, austenite formation in the HTHAZ occurs, reducing the likelihood of nitride precipitation in the ferrite. Both factors lead to a more balanced weldment and can be described as the optimum condition for localised corrosion resistance [Ume86] [Oga86]. In order to encourage this optimum condition, which, to some extent, can be translated into an optimum ferrite range, a more austenitic consumable is used, i.e. higher Ni-content. Nitrogen addition to the shielding gas can also have a positive effect [Gun94b].

The above findings illustrate that the parent steel pitting resistance is disturbed by fusion welding. This results in a reduction of the pitting resistance even if nickel-enhanced fillers and nitrogen-containing shielding gas are used. The greatest risk of poor performance exists in the root run where relatively high dilution from the parent steel and insufficient gas protection may prevail. To overcome this problem, welding consumables with higher pitting index could be used. It has been shown that a duplex filler with a PRE_N value 2-3 units above that of the parent material is sufficient to obtain equal pitting resistance [Wal91]. To this end, the practice of using 'superduplex' consumables to weld 22%Cr grades (S31803/S32205) has become common-place. For superduplex steels, higher alloyed fillers will have a less stable microstructure, that are more likely to precipitate intermetallic phases with an adverse effect on corrosion resistance.

Surface effects, such as slag particles which act as crevices, and weld oxidation have detrimental influence on the pitting corrosion. It is almost impossible to avoid oxidation even if proper gas protection is used. The oxygen content in the backing gas and the efficiency of the purge determines weld oxidation. The presence of only 25 ppm 0_2 in argon backing gas is sufficient to cause a significant reduction in pitting resistance of duplex steel [Ode91]. Pitting resistance can be restored by postweld treatment, i.e. brushing or pickling [Ode91] [Nic94]. Although it should be noted that powered brushes can lead to the formation of micro-crevices on the root run and produce erratic corrosion behaviour [Goo94]. Further, postweld treatment of the root run maybe impractical in many cases, e.g. root runs in pipe girth welds. In this respect, purging with pure nitrogen or 90%N_2+10%H_2 have been used to good effect [Nic94] [Jos91]. These gases produce a root region with reduced 'oxidation', a moderate increase in weld metal nitrogen content and a skin of austenite on the root run surface [Gun94b], which is about 10μm thick and presumably N-rich. But the potential problems associated with these gases should be noted [Gun97a].

2.3.9. Effect of Precipitation on Fracture Behaviour

The mode of failure in impact tests for duplex alloys depends upon phase balance and phase morphology, and the presence of second phase particles. However, in general, fracture includes a combination of microvoid coalescence in the austenite and cleavage in the ferrite phase. The brittle failure mechanism exhibited by the ferrite phase becomes more dominant as the test temperature is lowered [Hon78].

As discussed in previous sections, heat treatment above 300°C leads to the precipitation of various phases, most of which have a detrimental influence on toughness. However, this can be simplified into two main effects, Fig.2-26, namely the precipitates that form between 300 and 525 °C (475 embrittlement) and those between 600 and 1000 °C.

The presence of α′ affects the mechanical properties, leading to an increases in tensile strength, and a reduction in ductility and impact energy [Ros84] [Str86], although the proof stress may not be affected [Gut91]. These effects appear to peak at 475°C, even though α′ grows most rapidly at 600°C. This can be explained as the reduced number of α′ nuclei that form at high temperature result in fewer and more widely spaced particles; which have a reduced effect on the properties. To this end, heat treatment between 400 and 550°C can increase strength whilst still maintaining adequate ductility and toughness [Ros84], for certain duplex grades.

The main cause of embrittlement between 600 and 1000°C is sigma phase, which significantly impairs both ductility and impact properties with the effect increasing with higher volume fractions [Pic78] [Len54] [Tru82]. However, it is difficult to define a critical volume fraction of σ, as some state that 27J is reached with 4%σ [Nil92b] while others have found that 2.5% can be tolerated in thin walled pipe [Wie93]. Nevertheless, it is clear that a marked reduction in toughness is seen even below the 1% level [Gun95]. Further, the definition of a critical sigma volume fraction is complicated by the presence of other phases such as χ and Cr_2N [Nil91a].

Given that the critical cooling rates to avoid embrittlement will depend on steel composition, heat treatment type and severity of test, there is still significant variation between different workers using superduplex grades. For instance, a cooling rate of 0.4 °C/s has been proposed to form 1%σ [Jos91] and yet 0.56 °C/s has been stated to form no precipitates [Cha91]. These cooling rates equate to 180-250 seconds in the 600 to 1050°C temperature range, which would appear protracted in terms of a weld in thin walled pipe. Nevertheless, as will be shown in Chapter 4, intermetallic phases are found in such welds with a commensurate effect on toughness.

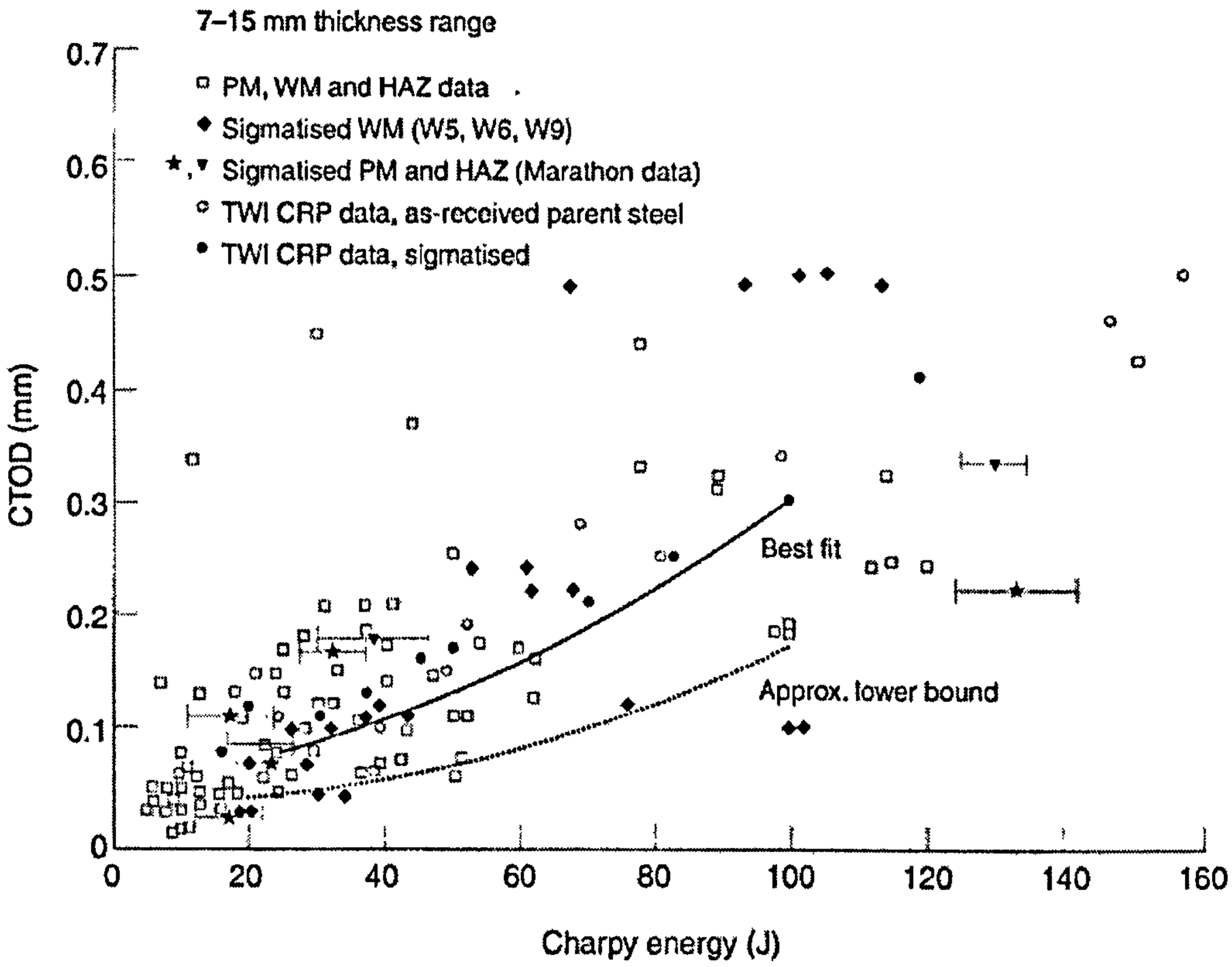


Fig.2-38 Correlation between CTOD and Charpy impact tests for different duplex weldments, intermetallic contents and test temperatures [Wie97].

CTOD results show similar trends to notch toughness data with regard to composition and phase balance [Hon78] [Den76], although low CTOD data generated on samples containing sigma phase can be obtained where impact energies in excess of 27J are recorded, Fig.2-38 [Wie97]. Presumably, this is a function of the two test types, whereby notch toughness gives a mean energy required for the crack to propagate through thickness, whilst a CTOD test is more dependant on crack initiation. This is further illustrated by Fig.2-39, where CTOD values drop below 0.1mm with less than 1%σ and yet from Fig.2-38 this would still equate to a reasonable notch toughness. These observations highlight concerns over the presence of intermetallic phases and their assessment by Charpy impact tests. As these phases would appear to effect crack initiation more than propagation, an over optimist view may be gained by the latter test method.

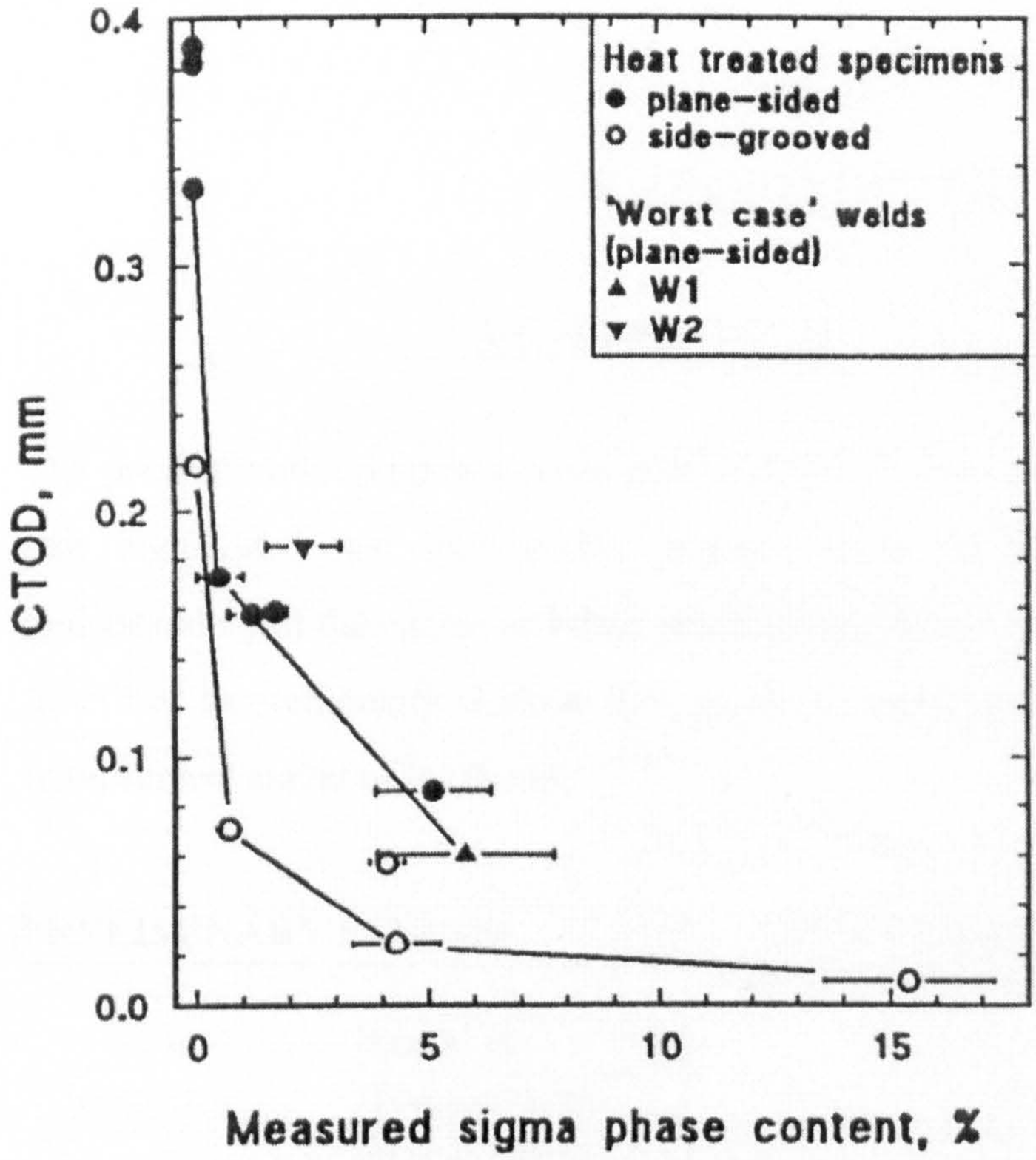


Fig.2-39 CTOD toughness versus measured sigma level in S32760 material at -20°C [Wie93].

It is well established that the drop in fracture toughness is dependent on the volume fraction of σ-phase, e.g. Fig.2-39, and that the preferred formation site is at the δ/γ phase boundaries (Table 2-7). Study of the fracture faces of samples containing σ-phase has shown that they contain splits or delaminations, which are perpendicular to the fracture face and follow the rolling direction [Rob91] [Era92]. The side walls of these splits appear brittle and are assumed to run along the precipitate decorated phase boundaries. In turn, this leads to a decrease in the degree of constraint as, effectively, two specimens of reduced thickness are produced.

CHAPTER 3

EXPERIMENTAL PROCEDURES

3.1. APPROACH

The present work comprises seven studies (Fig.3-1) from the original investigations that highlighted that intermetallic phases formed in production welds, to an understanding of the causes and their practical significance. The first four studies are described as preliminary work as they produced background data necessary for the main subject matter of the thesis.

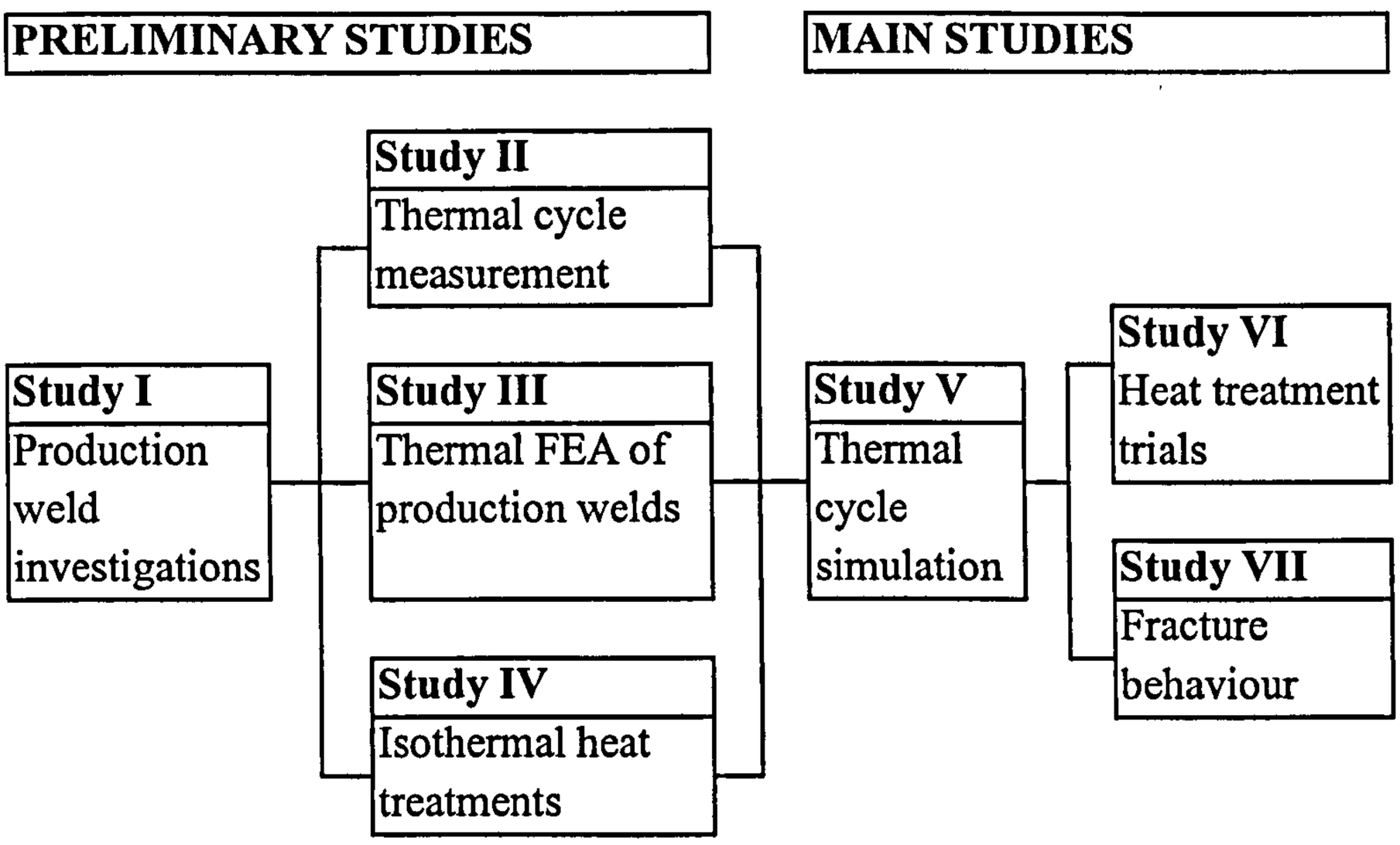


Fig.3-1 Overview of studies undertaken

Study I covers the initial investigations of production welds in superduplex thin walled tubes from the early 1990s, which were found to contain intermetallic phases in the HAZs. These investigations involved metallography, pitting corrosion and impact tests. As precipitation appeared to be a phenomenon associated with thin walled tubes, thermal cycles were recorded in simulated production welds (Study II). This study consisted of GTA welding of similar thin walled tubes with a series of thermocouples placed at a range of distances from the fusion boundary. Study III involved the production of 2D finite element meshes simulating the Study I production welds, so that the heating and cooling cycles of any point in the pipes could be predicted. This approach was also adopted to model the Study II weld, such that predicted and measured thermal cycles could be compared.

The last part of the preliminary work (Study IV) comprised a series of isothermal heat treatments on two superduplex alloys with assessment of toughness and pitting resistance. As the aim of Study IV was to evaluate the effect of various precipitates on the properties, a hold time of nominally 10 minutes was used over the 300 to 1300°C temperature range at 100°C intervals (Fig.3-2). This hold time may be considered fairly long relative to a weld thermal cycle, but ensured that precipitation occurred, particularly in the 'sigma nose'. In fact, 10 minutes allowed the intermetallic phases to coarsen and so facilitated identification. Moreover, this time can be considered to take account of repeated thermal cycling and allow for any accelerating effect of conjoint expansion/contraction strain on intermetallic formation rate.

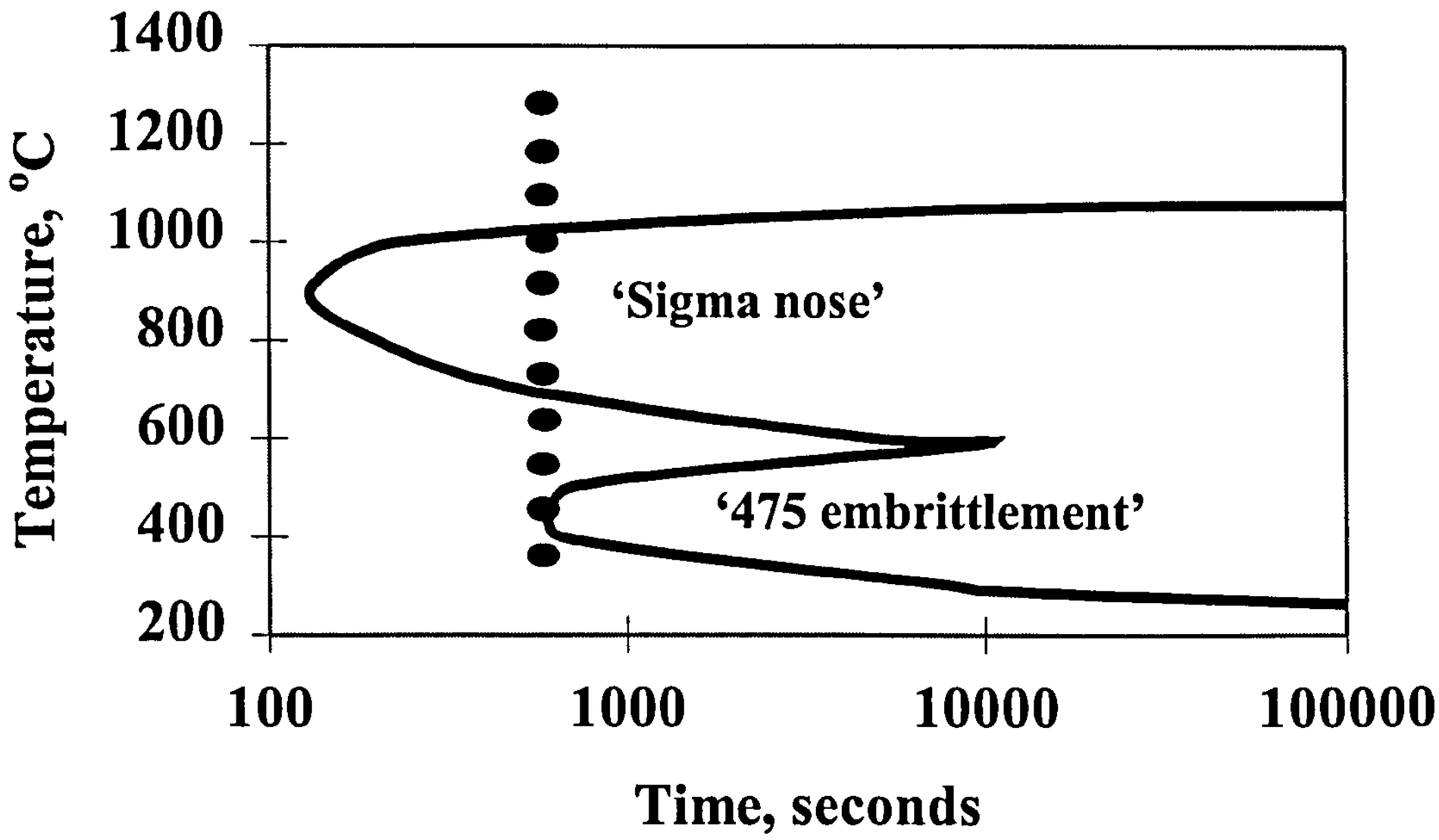


Fig.3-2 Illustration of isothermal heat treatments undertaken in Study IV superimposed on C-curves for superduplex steel S32520 (see Fig.2-26).

The background information gained from the preliminary studies (I-IV) laid the basis for the main studies (V-VIII). In order to examine the influence of time/temperature combinations more representative of weld thermal cycles, Study V comprised short exposure times to elevated temperatures. This utilised the thermal cycles developed from Study III and involved thermal simulation on three superduplex grades, covering a range of composition, product form and thickness. The thermal cycles were applied to 11mm thick samples (machined from the as-supplied thickness), with and without compressive strain during cycling to simulate the effect of joint restraint. The simulated samples underwent Charpy 'V' notch impact tests, with subsequent fractography, metallography, and some pitting tests.

The results from Study V were inconsistent with the literature and practical experience and so a series of welds were undertaken in Study VI. In this study, S32760 tubes made by both powder metallurgy and solid extrusion process routes were GTA welded either in the as-received or solution annealed conditions. The HAZ of each weld was examined for the presence of intermetallic phases and pitting corrosion tests undertaken.

The final series of tests (Study VII) was carried out on one grade of superduplex steel to compare the fracture behaviour of similar specimens tested by Charpy 'V' notch impact tests and a more conventional fracture mechanics approach, namely crack tip opening displacement (CTOD). For these tests, both fracture specimen types received a matrix of heat treatments covering as-received pipe, a solution anneal and weld thermal cycle simulation. The intermetallic contents were evaluated and the fracture faces compared.

3.2. STANDARD TECHNIQUES

For all studies, standard laboratory tests were undertaken on the different samples. This section describes these standard techniques, while deviations from these methods will be described in the Section 3.4 under Study headings.

3.2.1. Chemical Analysis

Substitutional elements were analysed by X-ray fluorescence (XRF) or optical emission spectrometry (OES), while C and S were assessed by combustion in oxygen and O and N by inert gas fusion.

3.2.2. Metallography

From all materials, metallographic samples were removed transverse to the rolling direction and ground and polished to a 1μm finish. In addition, selected broken fracture toughness specimens were sectioned perpendicular to the notch and similarly prepared. After electrolytic etching in 20% H_2SO_4 with addition of 0.1g/l NH_4CNS at 2.4V, the ferrite:austenite phase balance of each specimen was evaluated by a point count method following an adapted version [TWI93b] of ASTM standard E562-89 (3 readings of 200 counts). Further, each sample was examined for intermetallic and other precipitates by optical techniques. If such precipitates were present in sufficient quantities, then the level was measured by a similar point count procedure as for ferrite, but employing 5 readings of 200 counts. The increased number of points counted reduces the error [Gla60], reported as the 95% confidence interval (95% CI).

For identification of different intermetallic phases, a CamScan CS44 SEM was used, with a thin window energy dispersive X-ray (EDX) detector and a PGT Imix image analysis system. Often this was undertaken with back scattered electron imaging, which highlights intermetallic phases due to the enrichment of high atomic number elements, e.g. Mo, W. The volume fraction of intermetallic phases was estimated for a given region by counting the number of precipitates per screen over 20 screens at x1000, and then estimating the average precipitate cross-sectional area compared to the total area of a screen.

Transmission electron microscope (TEM) techniques were employed for positive phase identification and to resolve finer precipitation. For this purpose, thin foils were prepared from selected samples and etched in 10% glycerol, 20% perchloric acid, 70% ethyl alcohol using the following conditions: 40V, 0.5A, 1.5 flow rate, 5-7 photo sensitivity at +20°C. These foils were viewed under two JEOL microscopes, namely a JEM 100CX for Study IV and a JEM 2000FXII for Study V. For both studies, selected area diffraction patterns (SADP) were taken in order to identify the crystal structure of the phase under study.

3.2.3. Toughness Tests and Assessment

Specimens produced by both isothermal heat treatment (Study IV) and thermal simulation (Studies V and VIII) were taken perpendicular to the rolling direction and machined down to 55x10x10mm, with a notch placed through the thickness of the plate/pipe, (i.e. TL orientation). All of these specimens were subjected to Charpy impact tests following BS EN 10045-1:1990 at -40°C, as a common test temperature specified for offshore applications.

For the fracture toughness study (VIII), pairs of similar specimens were prepared from one pipe (S32750/2), taken with their axes along the pipe axis direction. One of these specimens was Charpy impact tested, as described above, while the other was prepared for CTOD tests.

For the CTOD tests, 55x10x10mm single edged notch bending fracture toughness specimens were made to BS7448: 1991: Part 1. The specimens were through thickness notched and fatigue pre-cracked to a crack depth-to-specimen ratio of nominally 0.5. Fracture mechanics toughness tests (in terms of CTOD) were carried out to BS7448: 1991 Part 1. The Charpy/CTOD pairs of similar dimensions were tested at the same temperature covering the range -100 to 0°C. Following testing, the CTOD specimens were broken open in liquid nitrogen.

For all studies, selected broken specimens were mounted for fractography. For this purpose, the fracture surfaces were viewed under both optical and scanning electron microscopes.

3.2.4. Pitting Tests and Assessment

Selected samples were subject to immersion tests in ferric chloride solution following an adapted version of ASTM standard G48-97 [TWI93a]. For the isothermal heat treatment study (IV), this involved grinding and polishing to 1μm finish followed by electropolishing to suppress edge attack on the through thickness faces before weighing. Immersion in 600ml of 10%$FeCl_3.6H_2O$ began at 15°C for 23hrs with the specimen being subsequently cleaned by nylon brushing under a running tap, dried using ethanol and reweighed. The specimens were then re-exposed in fresh solution at the next highest temperature (2.5°C increase every 23 hours), until a significant weight loss was recorded (i.e. 10mg) or visible pitting occurred. This temperature was defined as the critical pitting temperature (CPT).

Similar tests were undertaken on samples from the thermal cycle simulation study (V), although, in this case, the coupons were given a 600-grit finish with rounded edges and corners. Exposure started at 30°C and increased by 2.5°C every 23 hours. Areas of attack were sectioned and prepared for examination under SEM and optical microscopes.

3.3. MATERIALS

3.3.1. Thin Walled Pipes

Throughout the reported investigation, thin walled tubes to UNS S32760 were employed. Study I investigated production welds in superduplex tubes (S32760/1 and /2 in Table 3-1), which were established to contain intermetallic phases in the HAZ. Both of these tubes were about 3mm wall thickness and were made from a powder metallurgy process route, but had different outer diameters (26.7 and 60.3mm). The thermal cycles of these welds were modelled in Study III.

A further thin walled pipe in S32760 material was employed for Study II. Pipe S32760/3 was also made from a powder metallurgical route and was found to form intermetallic phases in production welds. This pipe was welded in the laboratory and the thermal cycles measured using thermocouples (Study II), and was also employed in the heat treatment trials in Study VI. Pipe S32760/4 was made by a solid extrusion process and was included in Study VI for comparison.

A further two thin walled pipes were forwarded by the manufacturer (S32760/5 and /6). Both pipes were originally 6″ Schedule 40 (168mm OD, 7.11mm wall), but had been machined to 165mm OD, 3.7mm wall, in order to simulate the pipe dimensions (and heat sink) that had led to intermetallic formation in production welding. Pipe S32760/6 had been re-solution annealed in an alternative continuous furnace which had become available recently to the manufacturer. The new furnace was designed to address the problems of pipe collapse, allowing for a longer soak time at temperature and rapid quench.

Table 3-1 Pipes and plates employed for different studies

Material grade	Original product form	Study						
		I	II	III	IV	V	VI	VII
Thin walled pipes								
S32760/1	26.7mm OD, 2.9mm wt	Y	-	(Y)	-	-	-	-
S32760/2	60.3mm OD, 2.8mm wt	Y	-	(Y)	-	-	-	-
S32760/3	60.3mm OD, 2.8mm wt	-	Y	Y	-	-	Y	-
S32760/4	48.3mm OD, 3.7mm wt	-	-	-	-	-	Y	-
S32760/5	168mm OD, 7.11mm wt*	-	-	-	-	-	Y	-
S32760/6	168mm OD, 7.11mm wt*	-	-	-	-	-	Y	-
Thick section products								
S32750/1	18mm thick plate	-	-	-	Y	Y	-	-
S32760/7	12mm thick plate	-	-	-	Y	Y	-	-
S39274	219mm OD, 13.4mm wt	-	-	-	-	Y	-	-
S32750/2	219mm OD, 12.7mm wt	-	-	-	-	-	-	Y

Y = Material used for particular study
(Y) = Weld procedure associated with particular pipe employed
- = Not employed
* = Machined down to 165mm OD, 3.7mm wt

3.3.2. Thick Walled Products

During the course of the heat treatment trials (Studies IV, V and VII), four heats of 'thick section' superduplex stainless steel were employed and compared, i.e. greater than 10mm thick. The isothermal heat treatments in Study IV covered two grades/heats of plate (S32750/1 and S32760/7 in Table 3-1). However, it is noted that plate S32750/1 had been REM (rare earth metal) treated to improve hot workability. Further, this plate was originally formed as pipe, before being re-rolled into plate.

The thermal simulation work (Study V) included the same plates as the preliminary work (Study IV), together with a newer grade of superduplex pipe to S39274 from Japan. For the final study (VII), which examined the fracture behaviour in the presence of intermetallic phases, one source of pipe was employed (S32750/2).

3.3.3. Composition

The chemical analysis are given in Table 3-2 and can be compared with the compositional requirements of the relevant UNS specifications in Table 2-4. Each steel can be seen to meet the compositional requirements of its respective specification.

The Cr-content of all the steels were nominally 25%, although two thick section products (S32760/7 and S32750/2) showed somewhat lower values (24.2%Cr). More notable differences can be seen in the Cu, W and Mo contents between the steels. The products coded S32760 all contain about 0.6%Cu, 0.6%W and 3.6%Mo, while steels coded S32750 contain neither Cu nor W, but have higher Mo additions (about 3.9%). The seamless pipe S39274 contains significantly higher W (2.16%) and lower Mo (3.03%) than the other steels. The composition of steel S39274 gives to a PRE_N-value just below the superduplex limit of 40 at 39.6. However, W also improves pitting resistance [Oka94], e.g.:

$$PRE_W = \%Cr + 3.3x(\%Mo + 0.5x\%W) + 16x\%N \qquad \text{--Eqn \{2-1\}}$$

Using this relationship, pipe S39274 has a PRE-value of 43.2.

Some variation is also apparent in the interstitial elements with nitrogen varying from 0.22 to 0.29% and carbon from 0.018 to 0.03%. Further variations are seen in the Si (0.18-0.54%) and Mn (0.35-0.94%) contents between the different materials.

Table 3-2 Chemical compositions of pipes and plates examined

Material grade	Study	Element weight %												PRE_N
		C	S	P	Si	Mn	Ni	Cr	Mo	Cu	W	O	N	
Thin walled pipes (Studies I-III, VI)														
S32760/1	I, (III)	0.021	0.006	0.022	0.40	0.94	7.0	25.5	3.48	0.74	0.70	-	0.23	40.7
S32760/2	I, (III)	0.022	0.006	0.017	0.43	0.77	7.0	25.6	3.62	0.69	0.82	-	0.27	41.9
S32760/3	II, VI	0.03	0.007	0.022	0.54	0.91	6.9	25.1	3.62	0.85	0.72	0.022	0.264	41.3
S32760/4	VI	0.022	0.001	0.025	0.28	0.49	6.94	25.0	3.58	0.60	0.60	-	0.22	40.4
S32760/5+	VI	0.025	<0.001	<0.03	0.52	0.70	7.0	25.7	3.51	0.68	0.71	≈0.003	0.27	41.6
S32760/6+	VI	0.026	<0.001	<0.03	0.49	0.66	7.1	25.2	3.51	0.74	0.62	≈0.003	0.22	40.3
Thick section products (Studies IV, V, VII)														
S32750/1	IV, V	0.022	≤0.001	0.014	0.40	0.35	7.6	24.6	4.04	0.16	<0.05	0.003	0.287	42.5
S32760/7	IV, V	0.027	≤0.001	0.026	0.18	0.73	6.9	24.2	3.72	0.61	0.63	0.003	0.241	40.3
S39274+	V	0.018	≤0.001	0.021	0.32	0.52	6.9	25.2	3.03	0.50	2.16	-	0.273	39.6
S32750/2	VII	0.026	0.003	0.017	0.23	0.30	7.2	24.2	3.77	0.05	-	0.001	0.276	41.1

All steels: < 0.01 Ti, ≤0.02 Nb + Product analysis; - = not determined

Analysis reference numbers: S/90/289, S/90/54, S/95/254/5, S/96/404, ON/90/122, ON/90/106, ON/95/80, ON/97/2.

3.3.4 Phase Balance

The phase balances of the steels were all statistically the same at around 50% ferrite, 50% austenite (Table 3-3). However, significant variation was recorded in the lamellae spacings of the different product forms (defined in Section 2.2.4 and illustrated in Fig.2-9). All the thin walled pipes had spacings of less than 20μm, while the thicker section products varied from 35 to 121μm.

Table 3-3 Phase balance and lamellae spacing

Material grade	Ferrite content, vol% ± 2s.d.	Lamellae spacing, μm *
Thin walled pipes		
S32760/1	50.0±3.9	18
S32760/2	46.4±1.9	17
S32760/3	47.0±3.5	16
S32760/4	49.4±4.3	17
S32760/5	50.5±2.9	14
S32760/6	56.5±4.8	11
Thick section products		
S32750/1	49.8±3.4	35
S32760/7	49.2±4.1	108
S39274	46.4±3.4	48
S32750/2	48.4±2.8	121

*Typical error ±10% of value, ie 2s.d.

3.3.5. Mechanical Properties

The mechanical properties of the steels are presented in Table 3-4, together with the requirements of ASTM specifications A790 for pipe and A240 for pressure vessel plates. All of the products meet with the minima laid down in these two standards. Moreover, some the steels have proof stress values significantly above the requirement of 550 MPa, e.g. 803MPa (S32760/3), which implies that some degree of cold work was undertaken after the final solution anneal.

Table 3-4 Mechanical properties of plates/pipes

Material grade	Reported as-received condition	Result type	$Rp_{0.2}$ (MPa)	Rm (MPa)	Elongation (%)
Thin walled pipes					
S32760/1	PM. 1100°C. Quenched into water	Test results*	700	957	33.2
S32760/2	PM. Heat at 500 to 900°C in 30 sec. Then 264 sec at 1110°C. Cool from 1130 to 600°C in 162sec.	Test results	na	na	na
S32760/3	PM. Not reported	Test results	803	964	29
S32760/4	Solid extrusion. Hot worked and solution anneal at 1110°C.	Test results*	632	851	29
S32760/5	PM. Solution annealed at >1100°C. Quenched into water	Test results*	689	856	31.5
S32760/6	PM. Solution annealed at >1100°C. Quenched into water. Then re-solution annealed in a continuous furnace.	Test results*	630/611	825/881	33.5/nr
	ASTM A790/A790M-89	*Specified min*	*550*	*750*	*25*
Thick section products					
S32750/1	1060°C for 10 mins, water quenched	Test results*	565	827	32
		Specified min.+	*550*	*795*	*15*
S32760/7	1100°C for 80 mins, water quenched	Test results*	635	831	31
		Specified min+	*550*	*750*	*25*
S39274	"Solution treated"	Test results*	627	863	43
		*Specified min^*	*550*	*750*	*25*
S32750/2	"Solution treated"	Test results	627	875	40
		*Specified min^*	*550*	*795*	*15*

* = Taken from manufacturer's mill certificate.
\+ = Taken from ASTM A240-93b.
^ = Taken from ASTM A790/A790M-89.
PM = Powder metallurgy process route.
/ = Two results: Before and after re-solution anneal.
nr = not recorded.

3.4. PRODUCTION WELD INVESTIGATIONS (STUDY I)

Between 1990 and 1992, several investigations were carried out on thin walled superduplex pipes, all of which were found to contain intermetallic precipitation. However, for the purposes of this thesis, two examples are described in detail, i.e. welds I-1 and I-2. Both involved GTA welds with two passes in pipe meeting S32760 (Table 3-5). For weld I-1, pipe S32760/1 was welded in the 6G position (i.e. fixed pipe at 45°) and the extent of intermetallic formation was determined by metallographic techniques. In addition, impact tests were performed using sub-size Charpy specimens (10x2.5mm) at -45°C.

In the second weld, I-2, pipe S32760/2 was employed although cut longitudinally and welded in the 1G position (flat). Further, once the first two passes had been completed, the second pass was ground back and a third pass applied in the form of a repair. Evaluation involved metallography and a pitting corrosion test at 35°C for 24 hours.

Table 3-5 Summary of GTA weld parameters and procedures examined (Studies I-III, VI)

Weld code	Pipe S32760	Preparation angle*, face	Root gap	Wire type, diameter	Position	Pass	Amps A	Voltage V	Travel speed mm/min	WFS mm/min	ROL mm	Arc energy kJ/mm	Interpass °C
I-1	/1	75°, 1.6mm	3mm	25.10.4L, 1.6mm	Vertical, 6G	1	60-80	11-13	35-45	Manual	ns	0.9 - 1.5	<100
						2	60-80	11-13	55-65	Manual	ns	0.6 - 1.2	<100
I-2	/2	70°, 1.0mm	2mm	Zeron 100X, 1.6mm	Flat, 1G	1	60	10	46	200	100	0.8	<100
						2	60	10	46	150	100	0.8	<100
						3R	60	10	46	205	150	0.8	<100
II	/3	75°, 1.0mm	2.4mm	Zeron 100X, 1.6mm	Horizontal & fixed,	1	40-50	10-10.5	30-60	150-250	50 x 4	0.5 - 1.0	30-60
						2	55-65	10-11	80-90	100-200	50 x 4	0.4 - 0.5	85-100
						3	60-80	10-11	60-110	100-150	50 x 4	0.5 - 0.6	90-100
VI-1	/3	75°, 1.0mm	2.4mm	Zeron 100X, 1.6mm	Horizontal & fixed	1	40-60	10-11	45-60	100-200	50 x 4	0.5 - 0.6	24-100
						2	50-60	10-11	50-100	50-150	50 x 4	0.4 - 0.7	75-100
						3	55-70	10-11	60-90	50-100	50 x 4	0.4 - 0.6	80-100
VI-2	/3	75°, 1.0mm	2.4mm	Zeron 100X, 1.6mm	Horizontal & fixed	1	50-60	10	65-75	150-250	50 x 4	0.45 - 0.5	24-90
						2	50-55	10	75-105	100	50 x 4	0.3 - 0.4	65-100
						3	55-60	10	85-90	50-100	50 x 4	0.35 - 0.4	85-100
VI-3	/4	75°, 1.0mm	2.4mm	Zeron 100X, 1.6mm	Horizontal & fixed	1	45-55	10-10.5	60-100	200-500	50 x 4	0.25 - 0.5	24-95
						2	50-55	10-10.5	100-110	100-150	50 x 4	0.3 - 0.35	85-100
						3	60-65	10-10.5	105-120	100	50 x 4	0.35 - 0.4	35-90
VI-4	/5	37°, 1.0mm	2.4mm	Zeron 100X, 1.6mm	5G	1	49-58	8.7-9.0	36-52	nr	140x4	0.59-0.75	13-36
						2	59-73	9.1-10.0	59-83	nr	140x4	0.50-0.58	59-73
						3	69-85	9.3-9.9	70-100	nr	140x4	0.51-0.59	59-71
VI-5	/6	37°, 1.0mm	2.4mm	Zeron 100X, 1.6mm	5G	1	51-59	8.9-9.7	39-69	nr	140x4	0.49-0.69	13-31
						2	66-72	9.5-9.9	79-102	nr	140x4	0.39-0.53	66-72
						3	73-82	9.2-9.6	65-73	nr	140x4	0.62-0.74	35-53

* Included angle; WFS = wire feed speed; ROL = run out length; nr = not recorded

3.5. THERMAL CYCLE MEASUREMENT (STUDY II)

From pipe S32760/3, a 100mm length was removed and a weld preparation machined. Along this face, a series of twelve holes were drilled around the pipe circumference, grouped in three out of the four quadrants to study through thickness effects. The first quadrant contained six holes placed between 2 and 10mm from the preparation edge and at the pipe mid thickness, into which Pt-Pt/Rh thermocouples were inserted and peened into position (Fig.3-3). These thermocouples were sheathed in ceramic and connected to a six pen chart recorder. The other two series of three holes were placed in two further quadrants (2 to 10mm away from the pipe edge) and were placed near the outer surface (thermocouples discharge welded into position) and near the inner surface (thermocouples peened into position) of the pipe.

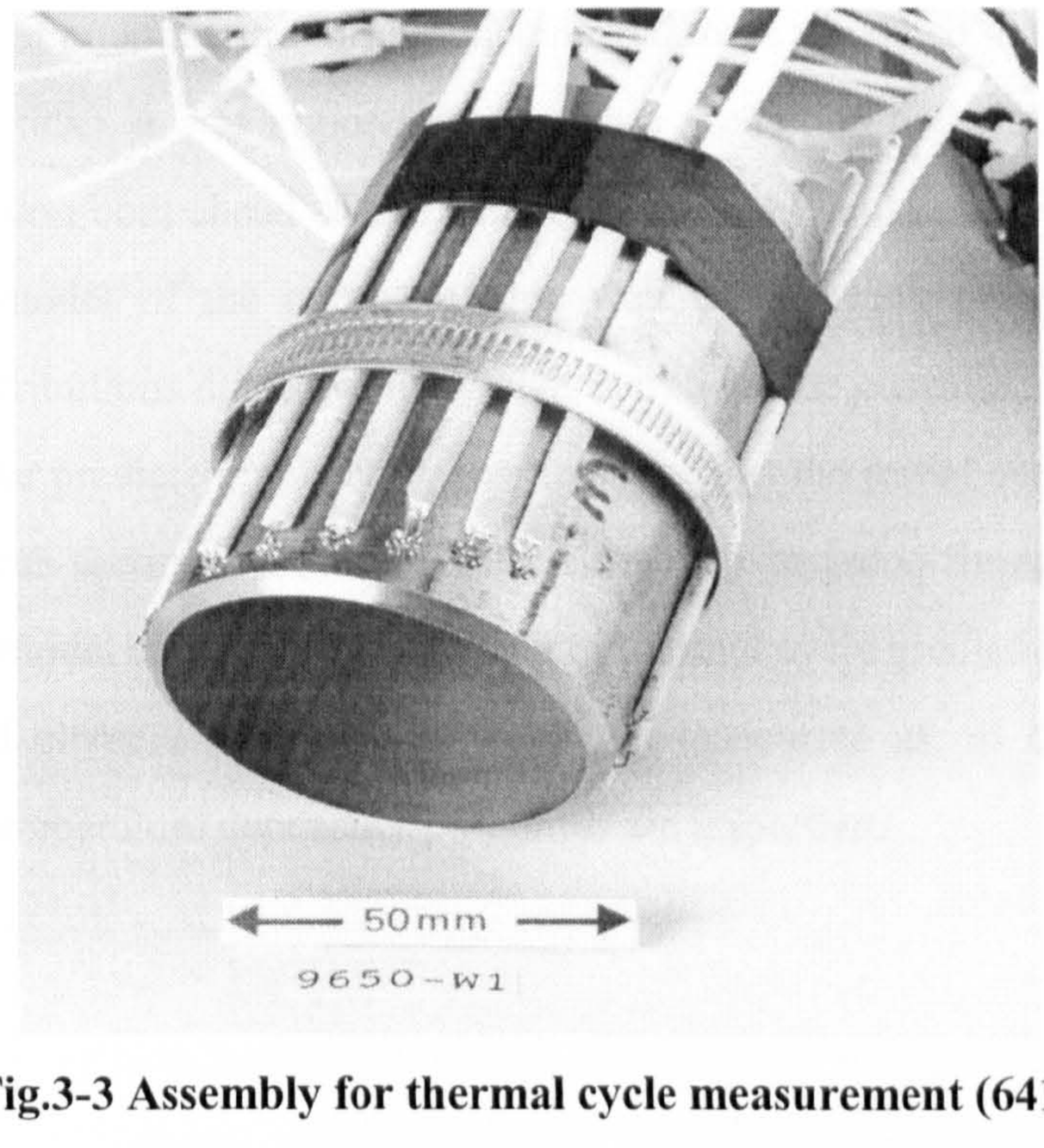


Fig.3-3 Assembly for thermal cycle measurement (64155/10)

The assembly containing the thermocouples was placed in position for welding and tacked to a further length of the same pipe. Welding followed a production procedure, established to form intermetallic phases in the HAZ. This involved the GTA process and a superduplex wire (Table 3-5), with a total of three passes. However, each pass was broken down into four quadrants which restricted a build up of temperature in the thin walled pipe and allowed the welder to re-position himself during this manual procedure. To this end, the three quadrants, in which thermocouples were positioned, were located towards the middle of a welding quadrant. The thermal cycle experienced by each Pt-Pt/Rh thermocouple was recorded on chart recorders, for which the voltage had been calibrated against temperature (0 to 1400°C).

3.6. FINITE ELEMENT ANALYSIS (STUDY III)

As the problem of intermetallic formation appeared to be restricted to thin walled pipes (i.e. small heat sink), it was important to select a prediction technique that took into account conduction both ahead of and behind the molten weld bead. For this reason, a shell element model of the complete pipe was used, which predicted the global temperature distributions during welding and, therefore, the possible level of heat flow 'preheating'. The predicted preheating was then used as the initial condition for a two dimensional cross sectional model of the weld which included the weld profile. The cross sectional model enhanced the accuracy of thermal cycle prediction near the weld, where the shell element model alone would be inaccurate as, in this region, local geometry and temperature dependent properties are important.

Non-linear boundary conditions were assumed and the heat input was time-varying. Heat losses were due to both convection and radiation, and so a convection heat loss coefficient of 10W/mK was assumed with a radiative emissivity of 0.25 [Tek87]. The heat model was a volumetric thermal energy flux into the weld reinforcement. This is a simplification of the real heat flow behaviour in the actual weld where convection flow occurs in the molten weld bead. Nevertheless, as the behaviour within the weld bead was not of primary importance, these convection currents were not modelled and heat flow was assumed to be conduction only. This meant that the heat input model involved trial and error in order to achieve a similar fusion boundary profile as witnessed in the production weld.

Figure 3-4a shows good agreement between the values for duplex alloys [Lang] and those for austenitic stainless steel up to around 400°C [Tek87]. Further, as the alloy content of austenitic and ferritic steel does not have a significant effect upon the conductivity at higher temperatures [Mye67], it was assumed with confidence that the temperature dependence of thermal conductivity for austenitic alloys are appropriate for the duplex weld model [Smi92].

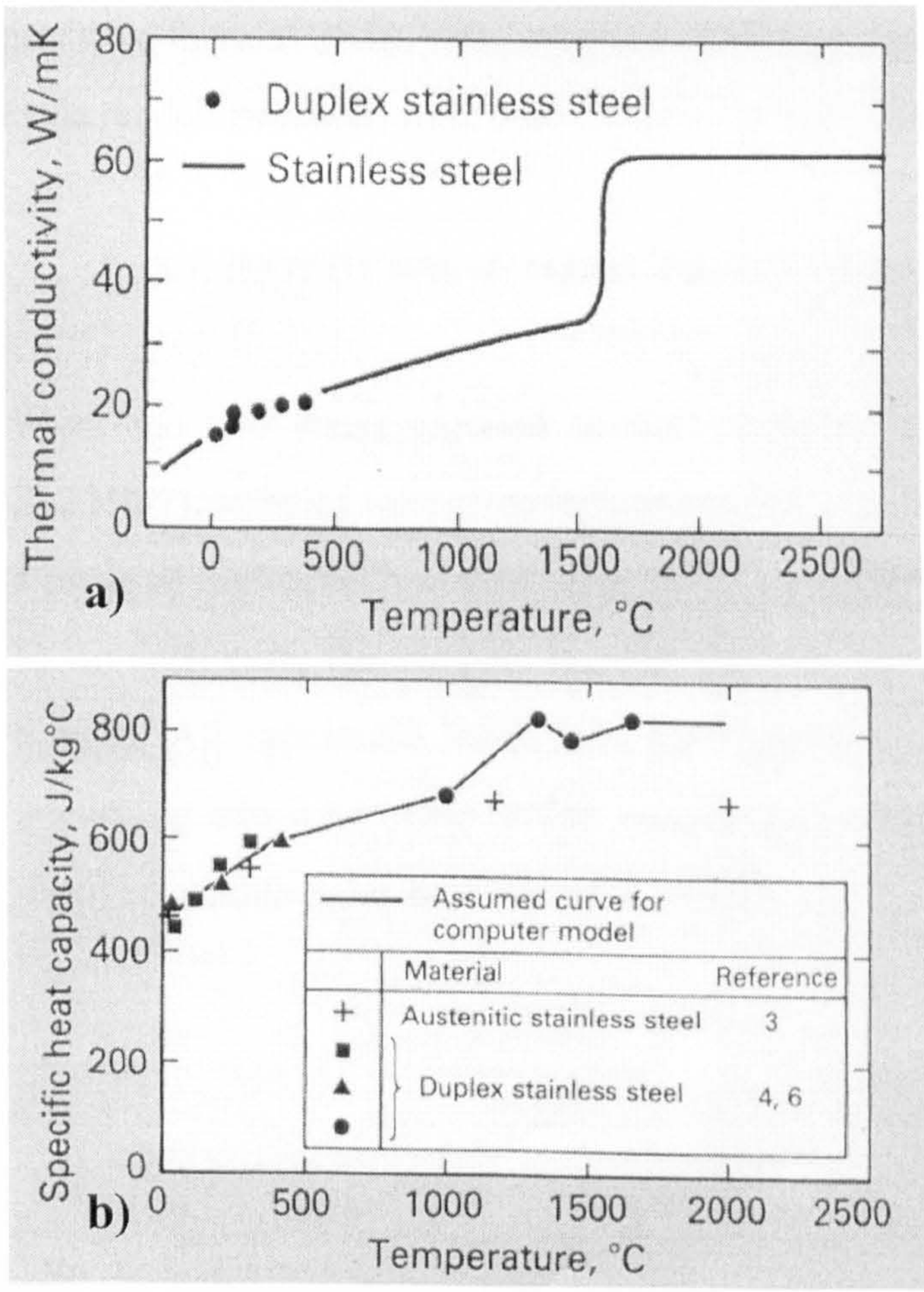


Fig.3-4 Variation in physical properties with temperature.
a) Thermal conductivity [Tek87]
b) Specific heat capacity [Tek87] [Lang] [Sand]

Specific heat capacity data for both austenitic and duplex stainless steels were collated from a number of sources and compared in Fig.3-4b. At lower temperatures both steel types give similar values, while for higher temperatures (above 1000°C) the duplex values are much higher. Consequently the duplex data were used in the model.

The latent heats for the transformations from liquid to ferrite (1440 to 1340°C) and from ferrite to austenite (1340 to 1330°C) were obtained [Sand], i.e. 414 kJ/kg and 27.15 kJ/kg respectively. However, as these transformations occur at similar temperatures, the modelling assumed a single phase transformation between 1440 to 1330°C and a release of 441 kJ/kg of latent heat over that temperature range.

The simulations were performed using the MARC/Abaqus finite element code [MARC90], which employs a backward difference step method. The solution accuracy is controlled by the specific maximum allowable temperature change per time step, which, in the present case, was taken as 50°C. This technique had been previously demonstrated for bead on plate welds on duplex plates [Smi92] and was applied to the production welds I-1 and I-2 (Study I) and weld II (Study II). In the last case, the predicted thermal cycles were compared with those measured in Study II. The thermal cycle models produced were used to make test specimens in Studies V and VII.

3.7. ISOTHERMAL HEAT TREATMENT (STUDY IV)

From the two steels reported in this phase of the work (plates S32750/1 and S32760/7), samples were removed transverse to the rolling direction and subjected to a range of isothermal heat treatments from 300 to 1300°C at 100°C intervals (Table 3-6). In each case, the samples reached the heat treatment temperature in about one minute. All specimens were held at temperature for about 10 minutes, before quenching into water. One further sample from each steel was also tested in the as-received condition, i.e. heat treated at 24°C.

The aim of this study was to generate baseline data for specific test alloys and to become familiar with different precipitates and their influence on common properties. To this end, the samples were subject to metallographic examination under optical, SEM and TEM microscopes. Charpy impact tests were conducted at -40°C and CPTs determined in ferric chloride solution (Section 3.2).

Table 3-6 Isothermal heat treatments (Study IV)

Temperature, °C	Steel grade		Δt, sec
	S32750/1	S32760/7	
24	X	X	0
300	X	X	0
400	X	X	0
500	X	X	0
600	X	X	10
700	X	X	399
800	X	X	654
900	X	X	405
1000	X	X	414
1100	X	X	960/30*
1200	X	X	30*
1300	X	X	30*

Δt = total exposure time between 600 and 1050°C
X = Specimens produced for Charpy impact tests (-40°C), pitting corrosion tests, metallography and phase balance assessment.
* = Δt only recorded on cooling cycle as peak temperature above 1050°C

3.8. THERMAL CYCLE SIMULATION (STUDY V)

From each material (i.e. S32750/1, S32760/7, S39274), specimens were removed perpendicular to the principal rolling direction (60x12x12mm), and subjected to a variety of simulated weld thermal cycles. The rationale behind each set is summarised below:

i) Set 1: The first set utilised linear rises and falls in temperature (Fig.3-5) and explored the effect of single, double and triple thermal cycles. In each case, the first cycle comprised heating at 150°C/s to 1000°C followed by cooling at 25°C/s to simulate the thermal cycle experienced by a point in the parent material which was a few millimetres from the fusion boundary. In particular, a peak temperature of 1000°C was expected to match the location where intermetallic precipitation should be most rapid. Different second and third thermal cycles were examined, which involved heating at 10°C/s to 700°C and then cooling at either 5°C/s (Fig.3-5a) or 10°C/s (Fig.3-5b), to simulate the effect of subsequent passes.

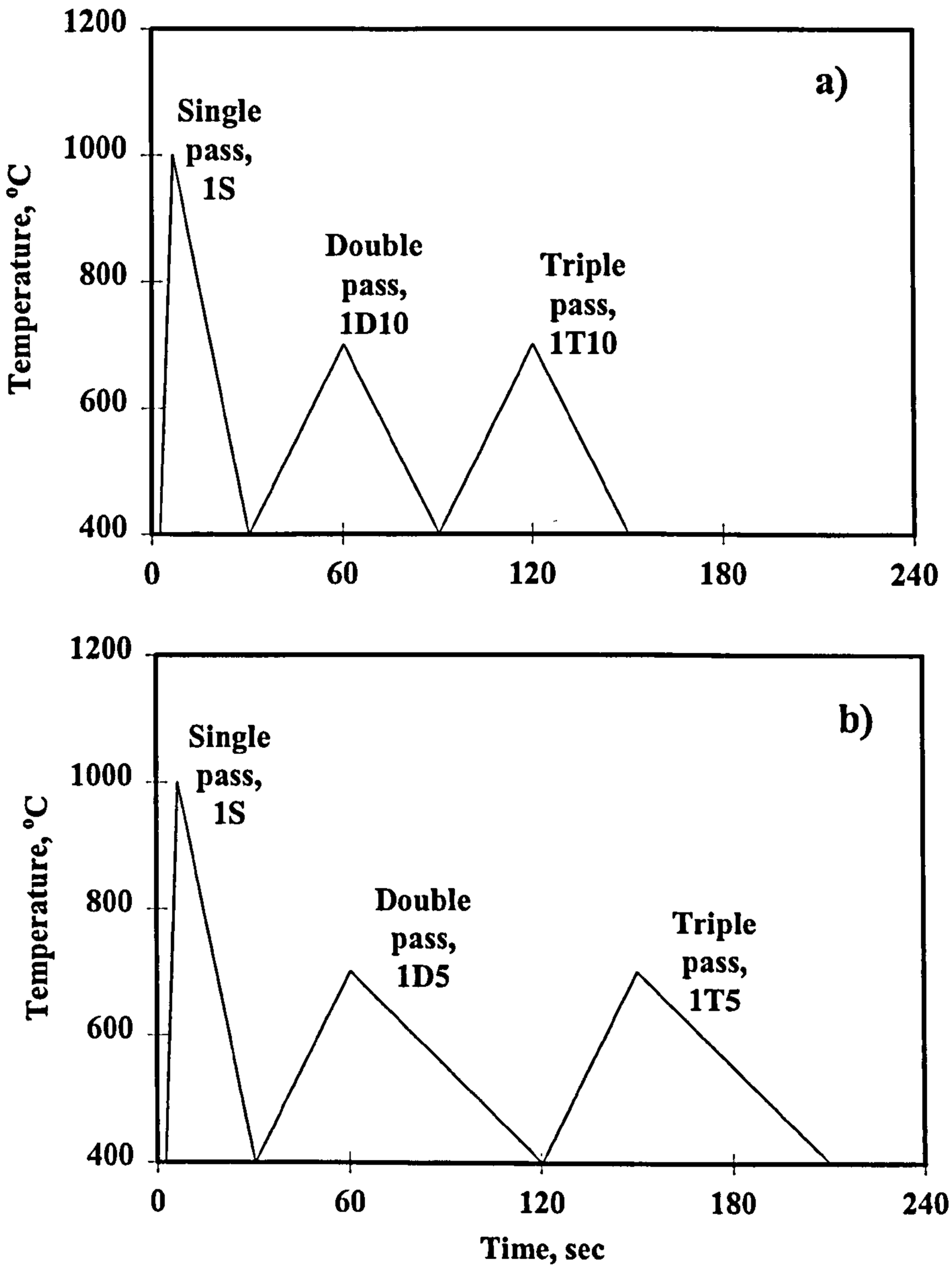


Fig.3-5 Thermal cycle set 1. Cooling rate after each cycle of a) 10°C/s and b) 5°C/s

ii) Set 2: Set 2 used the thermal cycles developed in Study III on the weld I-1 in S32760/1 pipe (Table 3-5). To study the effect of a second welding pass, specimens were subject to both single and double cycles, Fig.3-6. Further specimens were put through the double cycle of Set 2 (i.e. 2D), but, in addition, 3.1% tensile strain was applied to the full length of the specimens (i.e. 2D+), in order to simulate the effect of welding strains. The strain was applied incrementally, starting at about 800°C on the heating cycles, reaching a maximum strain at the peak temperatures, and finishing at about 850°C on the cooling cycles.

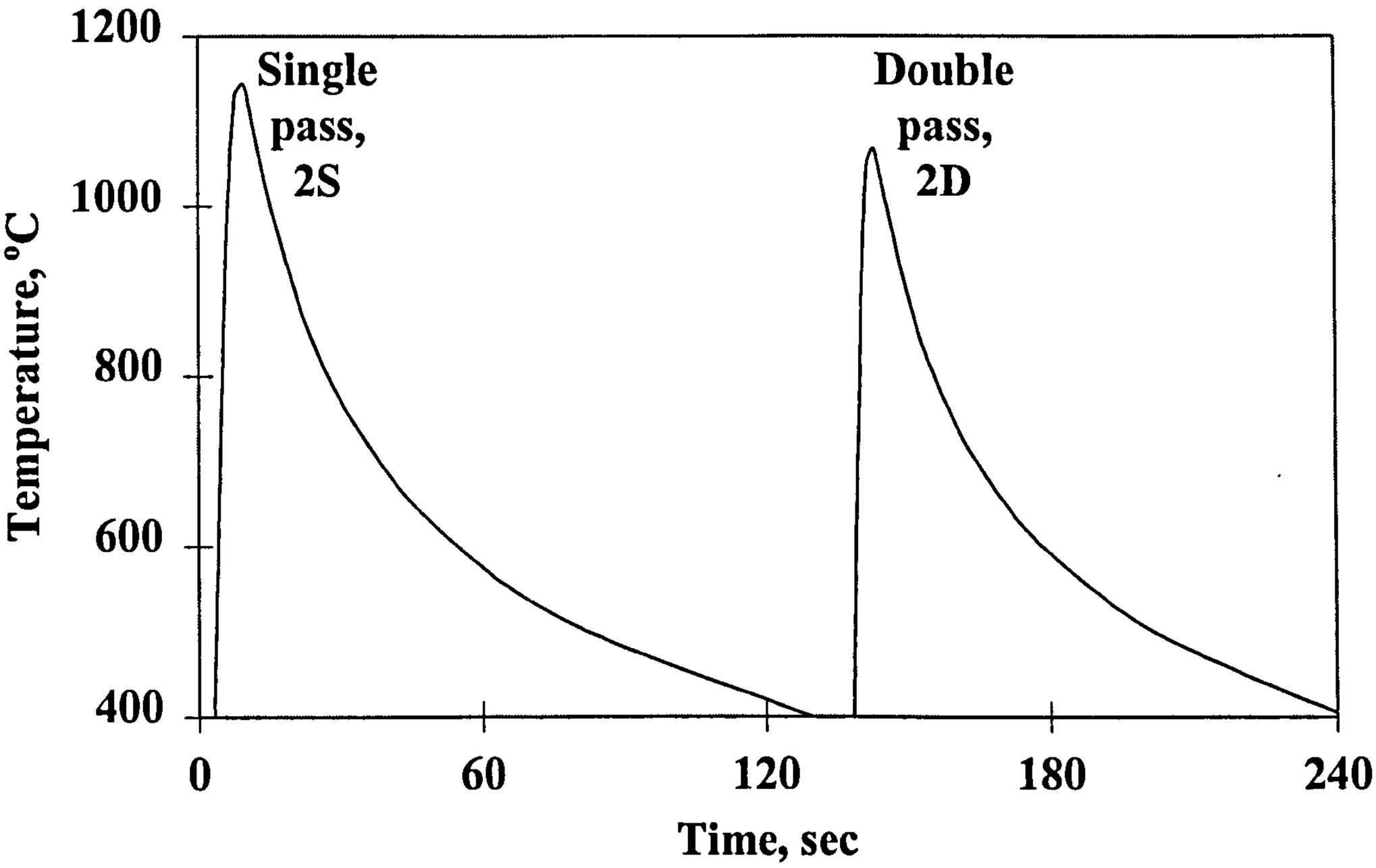


Fig.3-6 Thermal cycle set 2 generated by finite element analysis of production weld I-1.

iv) Set 3: The final set (Fig.3-7) was produced using the finite element mesh of Study III which modelled a repair procedure (weld I-2 in pipe S32760/2) and had induced precipitation and a reduction in the pitting resistance measured in a ferric chloride test.

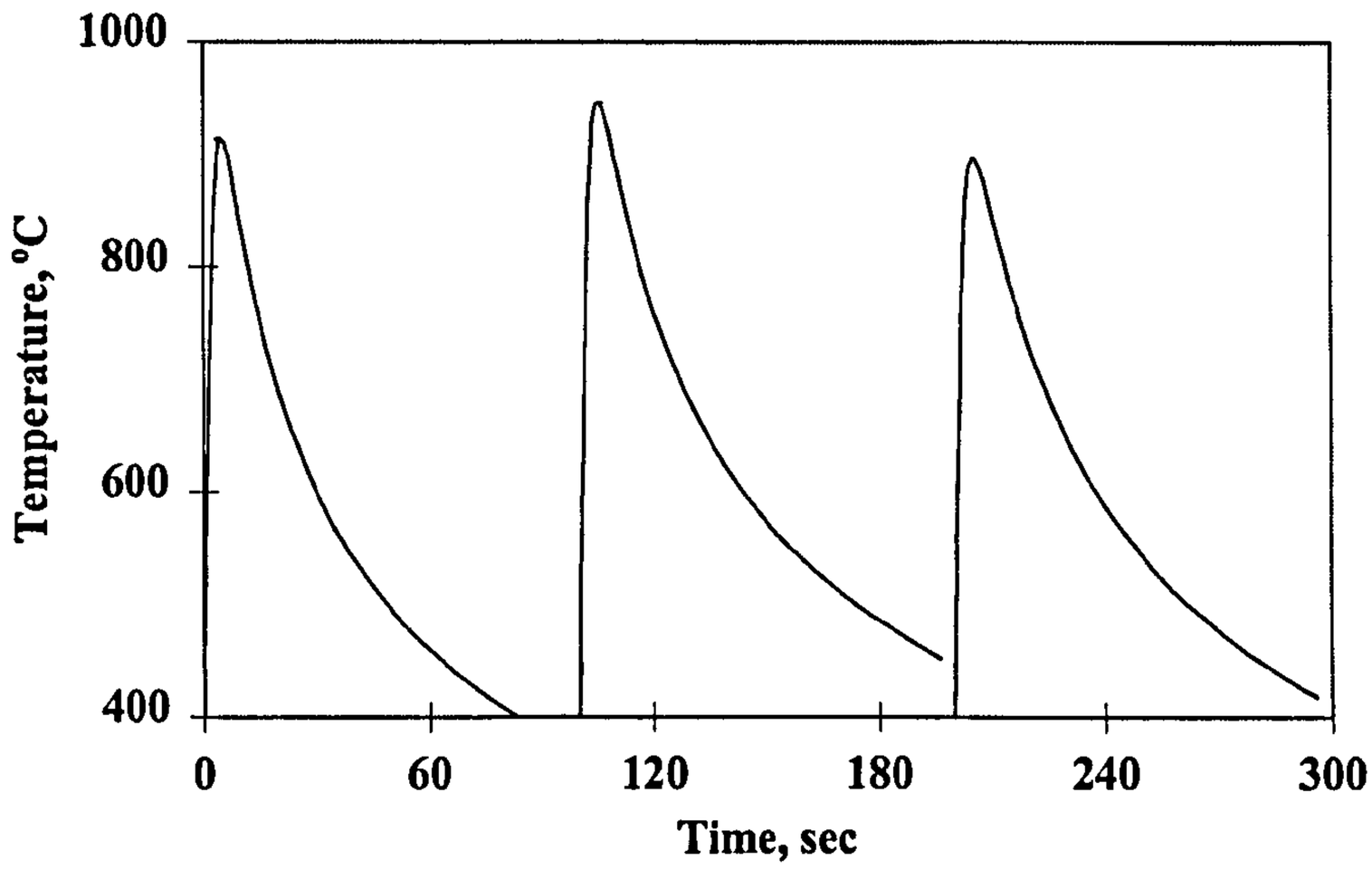


Fig.3-7 Thermal cycle Set 3 (code 3R) generated by finite element analysis of repair weld I-2.

A parameter Δt is introduced in Table 3-7 for comparison of the different thermal cycles, where Δt is defined as the total time exposed, both on the heating and cooling cycles, to temperatures in the range 600 to 1050°C; i.e. the temperature range for intermetallic phase precipitation in superduplex grades, Fig.3-2. Moreover, the upper temperature limit for intermetallic stability in the alloys under study can be taken from the manufacturers solution anneal given in Table 3-4, i.e. 1060 to 1110°C. This definition of Δt was selected in preference to cooling curve parameters (described in Section 2.3.1), such as $\Delta t_{12\text{-}8}$ (1200 to 800°C) or $\Delta t_{8\text{-}5}$ (800 to 500°C), as being more appropriate to intermetallic formation in duplex stainless steel. Further, if the temperature peaked above 1050°C then only the cooling time was considered. This definition takes account of intermetallic dissolution at such elevated temperatures, so that the currently used Δt accounts for new precipitates that form on the cooling and subsequent cycles.

Each of the thermally simulated samples underwent standard metallographic preparation and were examined under optical, SEM and TEM microscopes. Selected samples were subject to Charpy impact tests and CPT determination (Section 3.2).

Table 3-7 Summary of thermal cycle simulations undertaken (Study V)

Thermal cycle Set	Description	Code	First cycle			Second cycle			Third cycle			Δt, sec
			Heating rate*, °C/s	Peak temp, °C	Cooling rate*, °C/s	Heating rate*, °C/s	Peak temp, °C	Cooling rate*, °C/s	Heating rate*, °C/s	Peak temp, °C	Cooling rate*, °C/s	
0	As-received plate	**AR**	-	-	-	-	-	-	-	-	-	0
1	Single pass	**1S**	150	1000	25	-	-	-	-	-	-	19
	Double pass 10°C/s	**1D10**	150	1000	25	10	700	10	-	-	-	39
	Triple pass 10°C/s	**1T10**	150	1000	25	10	700	10	10	700	10	59
	Double pass 5°C/s	**1D5**	150	1000	25	10	700	5	-	-	-	49
	Triple pass 5°C/s	**1T5**	150	1000	25	10	700	5	10	700	5	79
2	Single pass	**2S**	150	1145	17	-	-	-	-	-	-	52
	Double pass	**2D(+)**	150	1145	17	145	1070	13	-	-	-	91
3	Two passes and Repair	**3R**	110	915	13	90	945	12	100	900	8.5	108

* The heating and cooling rates presented for the thermal cycle Sets 2 and 3 were taken at 600°C.
Δt = total exposure time between 600 and 1050°C.
\- = not applicable

3.9. HEAT TREATEMENT TRIALS (STUDY VI)

3.9.1 Laboratory Heat Treatments

As will be discussed in later sections, the results from Studies I to V showed some inconsistencies relating to the behaviour of thin walled production tubing available in 1990-1992. In an attempt to clarify the situation, six similar sections of pipe were prepared for investigation. This involved four pieces from pipe S32760/3 and two from S32760/4 (Table 3-8), of which two of the former were given a re-solution anneal in a laboratory furnace at 1120°C (±10°C) for 90 minutes, rapidly followed by a water quench. (Steel S32760/4 has a similar composition and wall thickness to S32760/3, but was made by solid extrusion rather than a powder metallurgy process route). This time was selected to ensure that complete solution treatment was achieved. In practice, a shorter time would be more appropriate, recognising the likelihood of component distortion/collapse etc. The two re-solution annealed pieces (S32760/3), together with the as-received pipe pieces, were welded using a production procedure employing the GTA process and three passes [Wie93], Table 3-5. The three welds (VI-1, -2 and -3) were sectioned, prepared by standard metallographic techniques and viewed under an optical microscope.

Table 3-8 Summary of Study VI pipes and welds

Weld code	Pipe	
	S32760	Condition
VI-1	/3	As-received
VI-2	/3	Laboratory solution anneal
VI-3	/4	Solid extrusion
VI-4	/5	As-received
VI-5	/6	Furnace solution anneal

3.9.2 Production Heat Treatments

Given the results of the laboratory heat treatments, the manufacturer forwarded two welds in thin walled pipe (Table 3-8). One of these pipes was welded in the as-manufactured condition (pipe S32760/7, weld VI-4), while the other had been re-solution annealed prior to welding (pipe S32760/6, weld VI-5) in an alternative continuous furnace which had become available recently. The new furnace was designed to address the problems of pipe collapse, allowing for a longer soak time at temperature and rapid quench.

The GTA welding parameters employed followed the same production procedure as employed in 3.9.1, which was known to induce HAZ intermetallic precipitation (Table 3-5). From each weld, metallographic samples were removed from both the 6 and 12 o'clock positions for assessment of the phase balance and intermetallic phases, using both optical and SEM techniques. Given these results, one pitting corrosion test sample was removed from each weld at the location of highest intermetallic content.

3.10. FRACTURE BEHAVIOUR (STUDY VII)

The final study evaluated the effect of intermetallic phase precipitates on fracture toughness behaviour. For this purpose, samples were prepared from one material, namely pipe S32750/2, for both Charpy impact and CTOD tests. All samples were removed parallel to the pipe length and given one of three heat treatments, together with a set of samples in the as-received condition (Table 3-9). The first heat treatment simulated a solution anneal and comprised exposure to 1125°C for five minutes followed rapidly by a water quench. The second involved heat treatment at 1000°C for five minutes and a water quench, in order to form significant levels of intermetallic phase (i.e. "sigmaticed"). The final heat treatment utilised thermal simulation in the Gleeble equipment and cycle 3R (Table 3-7), which was found to form low intermetallic contents.

Table 3-9 Matrix of heat treatment, test type and temperature for Study VII

Test temperature, °C	As-received pipe		Re-solution annealed		Triple thermal cycle (3R)		"Sigmatised"	
	CVN	CTOD	CVN	CTOD	CVN	CTOD	CVN	CTOD
0	X	X	X	-	X	X	X	-
-10	X	X	-	-	X	X	-	-
-20	X	X	X	-	X	X	X	X
-30	X	X	-	-	X	X	-	-
-40	X	X	X	-	X	X	X	-
-50	X	X	-	-	X	X	-	-
-60	X	X	X	-	X	X	X	X
-70	X	X	-	-	X	X	-	-
-80	X	X	X	-	X	X	X	-
-90	X	X	-	-	X	X	-	-

X = examined, - = not examined

All samples were machined to 55x10x10 and notched through thickness and tested at the temperatures shown in Table 3-9. Selected fractured samples were sectioned and prepared for optical and SEM examination, in order to establish the fracture modes.

CHAPTER 4

PRELIMINARY STUDY RESULTS

4.1. PRODUCTION WELD INVESTIGATIONS (STUDY I)

There were several common features in the production welds that formed intermetallic phases in the HAZ. First they were all GTA welds in thin walled pipe to UNS S32760 made by the powder metallurgical route. Second the intermetallic phases formed in a band from 1.5 to 4mm away from the fusion line (FL). However, in the two welds reported herein different intermetallic levels were recorded. In weld I-1 (pipe S32706/1) about 1.7% was measured reaching a peak at FL+1.7mm (Fig.4-1a), while in the repaired weld I-2 (pipe S32760/2) significantly higher levels were recorded (9.5% at FL+3.8mm in Fig.4-1b).

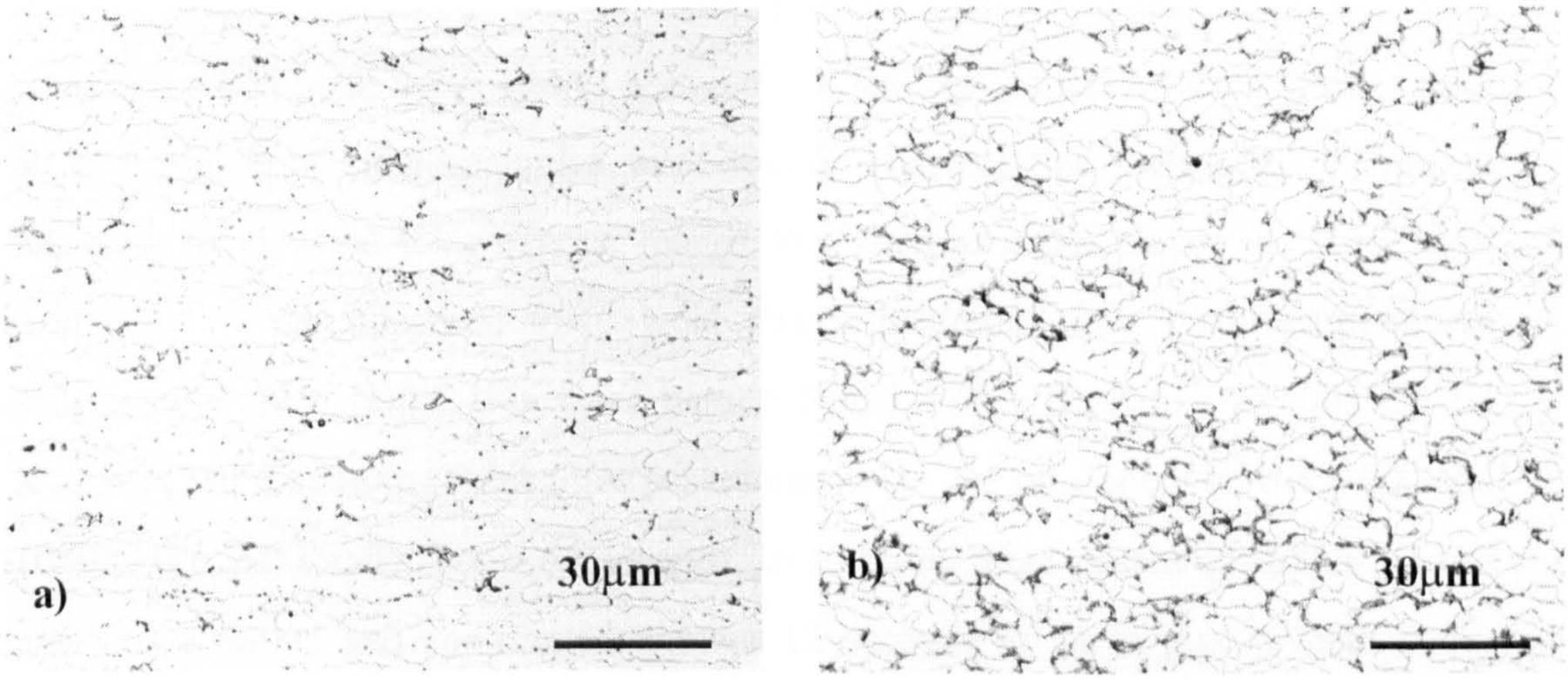


Fig.4-1 Intermetallic phases (dark precipitates) recorded in the HAZ of real superduplex welds.
a) 1.2 ± 0.3%I at FL + 1.7mm (12 o'clock position) in weld I-1 [x500, AE1449]
b) 9.5 ± 1.7%I at FL + 3.8mm in weld I-2 [x500, AD2011]

Other data were generated for the two welds. Sub-size Charpy impact specimens (10x2.5mm) were removed from weld I-1, apparently notched near the intermetallic band, and tested at -45°C. The lowest result was 10J, which was borderline for the project requirements and instigated a fuller investigation. For weld I-2, pitting corrosion tests were conducted at 35°C, which led to a weight loss of 570mg (test failure constitutes >10mg) with attack concentrated in the intermetallic band (Fig.4-2). The thermal cycles experienced by both of these were modelled in Study III.

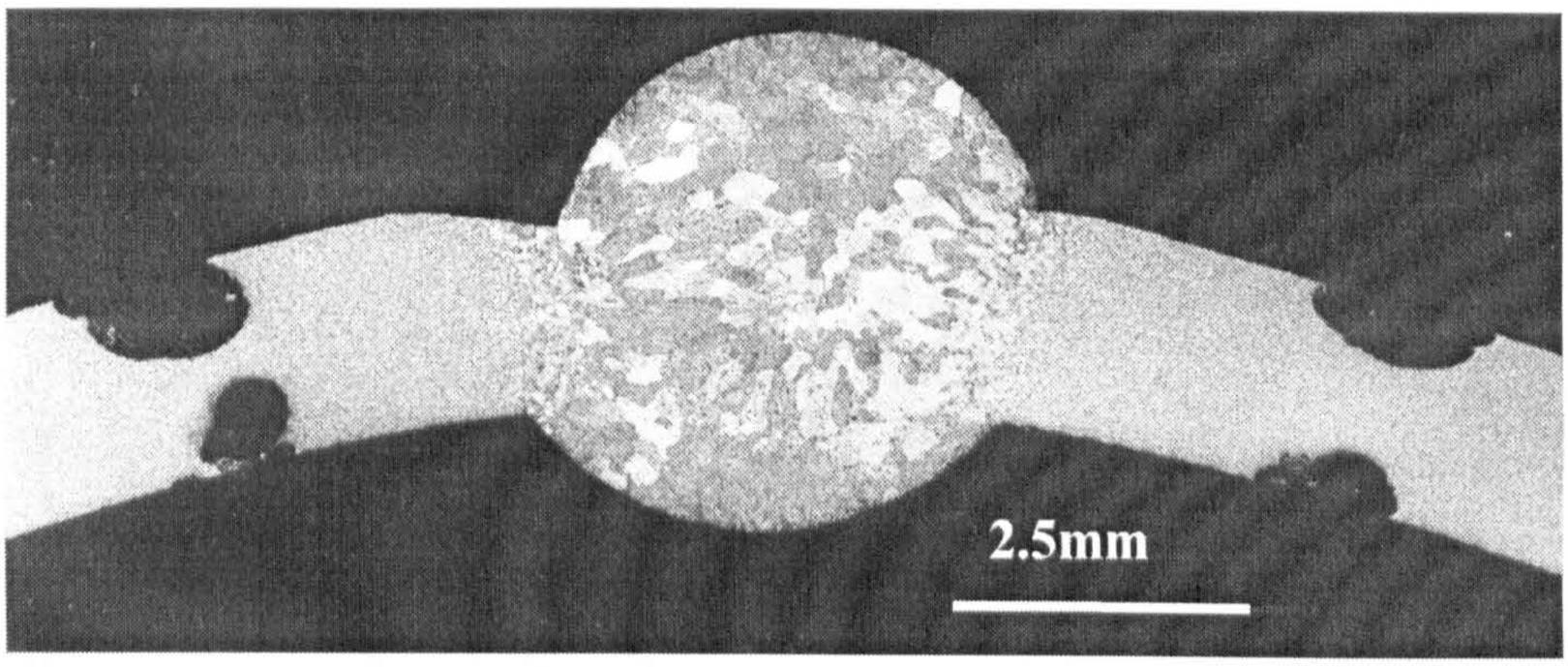


Fig.4-2 Attack of HAZ in weld I-2 (pipe S32760/2) after exposure to ferric chloride solution at 35°C [AD3253, x8]

4.2. THERMAL CYCLE MEASUREMENT (STUDY II)

The thermal cycles measured in weld II (Table 3-5) covered a range of distances from the fusion line (FL+1.3 to 6.0) confirmed by metallographic sections taken through the thermocouple locations. The most important data pertain to those thermocouples which recorded peak temperatures above 600°C and gave total Δt times greater than 40 seconds. Four such examples were found. The one that produced the longest exposure to elevated temperatures relates to a thermocouple placed at FL+1.3mm (Fig.4-3). At this location, three weld passes/quadrants gave peak temperatures significantly above 600°C (Fig.4-4a), namely Run 1-4 (825°C), Run 2-2 (1065°C) and Run 3-2 (750°C). During these three passes/quadrants, the time spent between 600 and 1050°C (i.e. Δt) totalled some 51 seconds. In addition, other passes/quadrants peaked just above 600°C and contributed another 12 seconds to Δt to give a total Δt for location FL+1.3mm of 63 seconds.

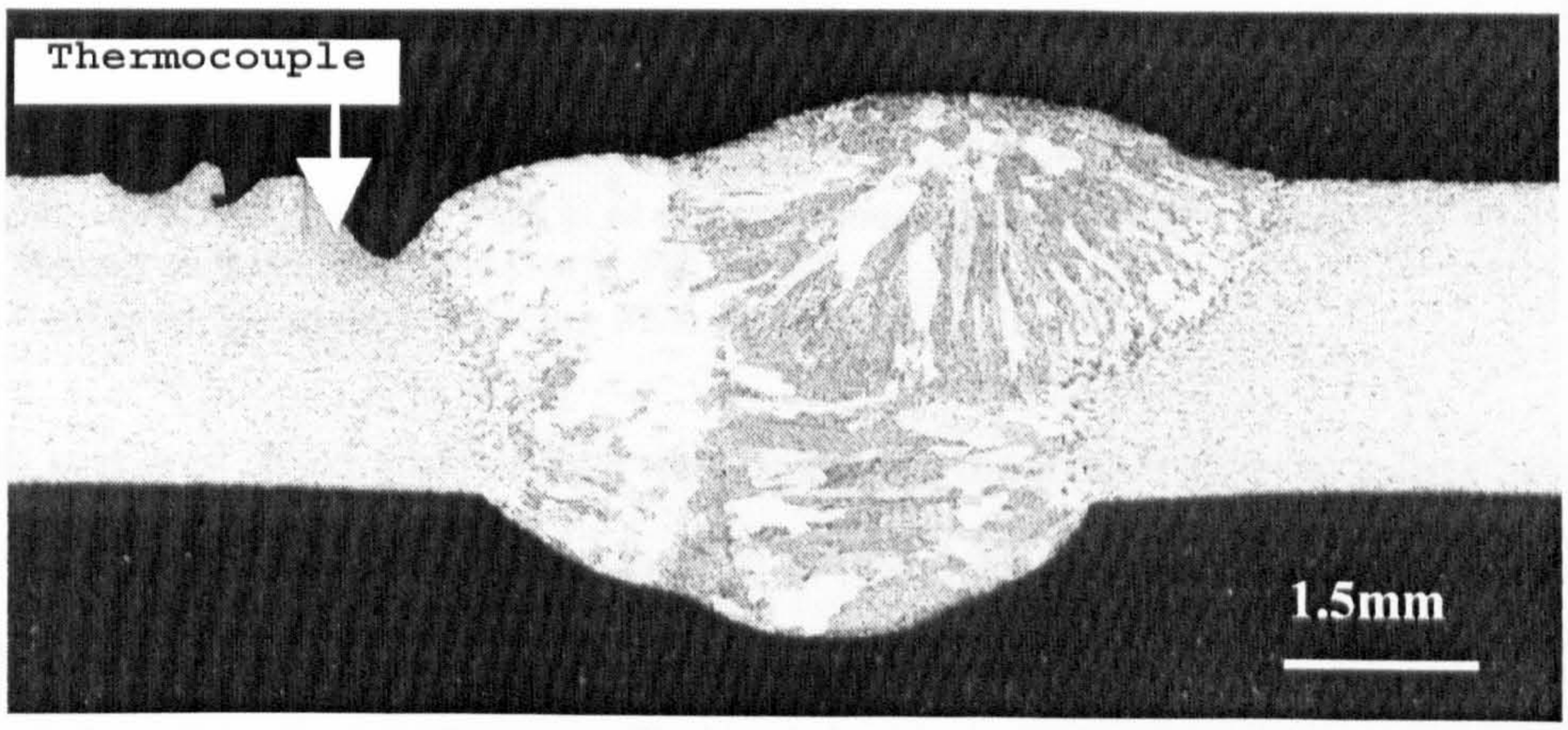


Fig.4-3 Section taken adjacent to thermocouple located at FL + 1.3mm in weld II (Study II). [x10, AK158]. Note: Compare with finite element mesh in Fig.4-6.

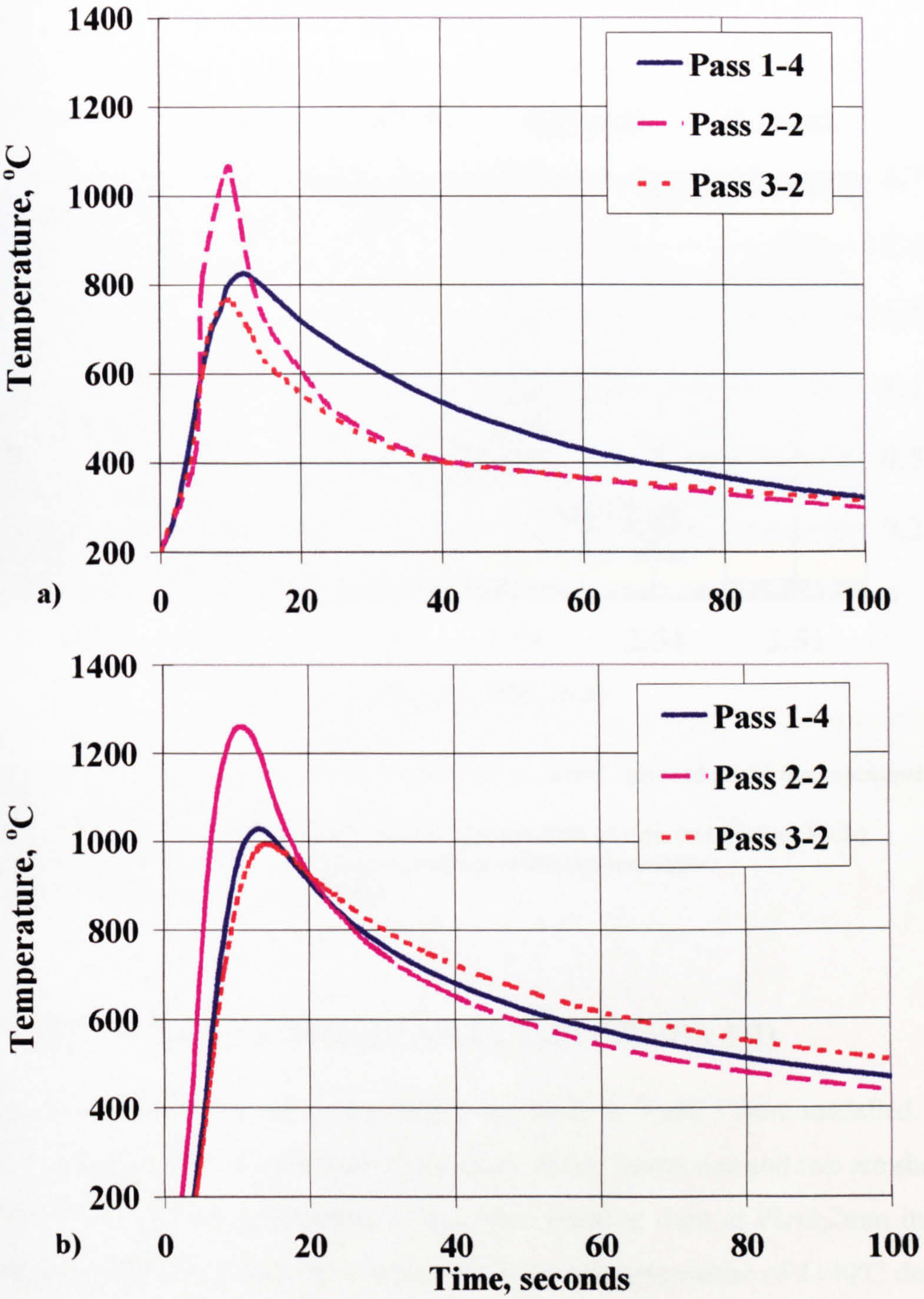


Fig.4-4 Thermal cycles in weld II at a thermocouple placed at FL+1.3mm (TC51C)
a) Measured thermal cycles (Study II)
b) Predicted thermal cycles using FEA (Study III)

Back scattered SEM analysis was undertaken on the metallographic section taken about the thermocouple at FL + 1.3mm in weld II (Fig.4-3). This involved counting the number of precipitates in each field of view on a grid basis (Fig.4-5). Given that the thermocouple is large in comparison to intermetallic band, its location can be seen to approximate to the centre of the band.

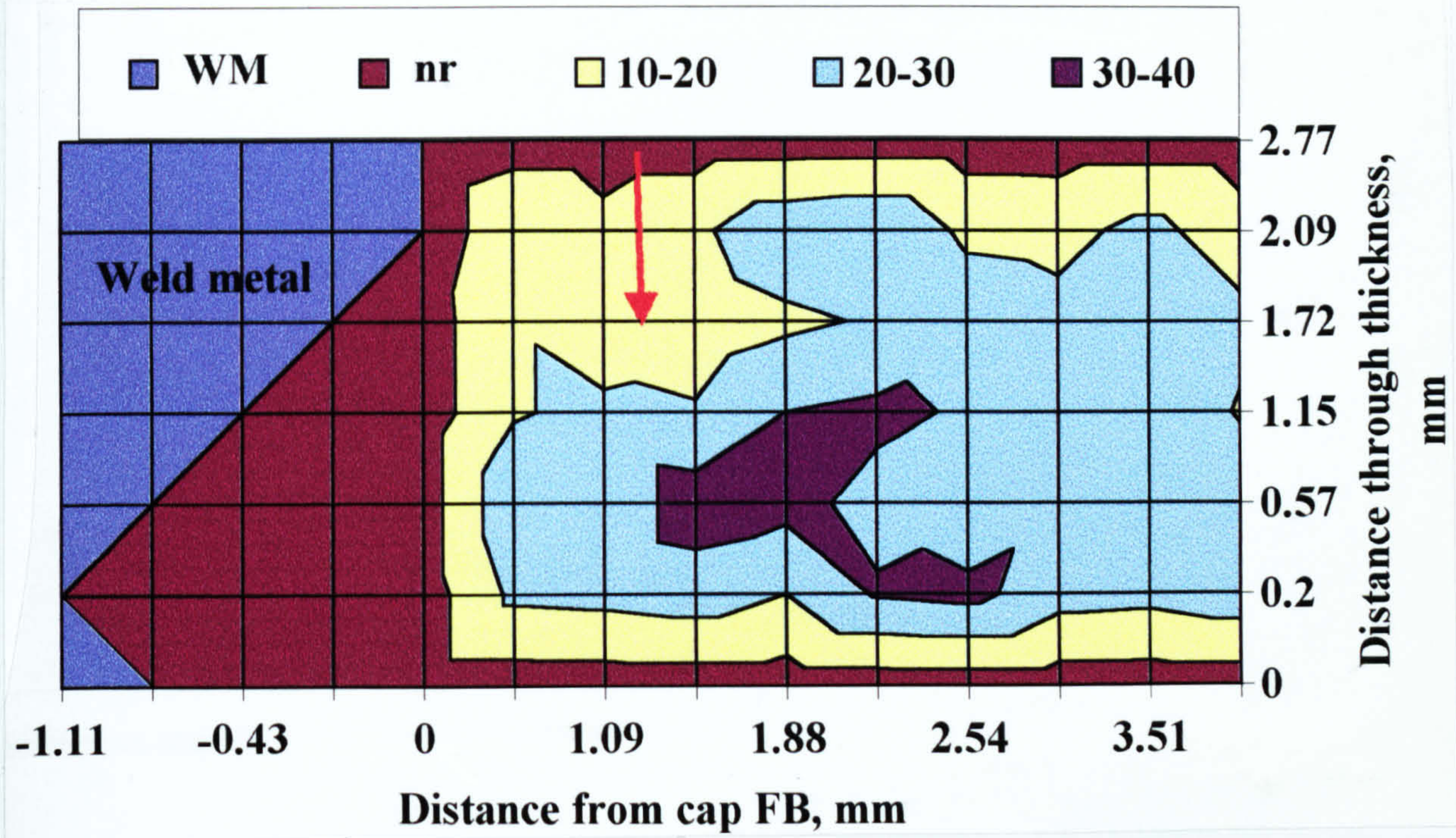


Fig.4-5 Precipitate distribution map in the HAZ of section removed about thermocouple at FL + 1.3mm in weld II.
Key: Values plotted are number of precipitates per field of view (see Section 3.2.2.)
The red arrow shows the approximate location of the thermocouple.
WM = weld metal, nr = not recorded.

4.3. FINITE ELEMENT ANALYSIS (STUDY III)

In the first part, the two production welds described in Study I were modelled. For weld I-1, the predicted temperature distributions during passes one and two are shown in Fig.3-4. Given that intermetallic phases were noted to form at FL+1.7mm in the production weld (Fig.4-1a), this corresponds to a peak temperature of 1140°C during the first pass and 1070°C during the second. Further, Δt for both passes combines to 91 seconds (Table 3-7). On the other hand, the second weld modelled, I-2 in Fig.3-5, did not reach such high peak temperatures (i.e. 915, 945 and 900°C), but, due to the repair, a longer value for Δt of 108 seconds was obtained.

The same method was applied to the location of thermocouple TC51C in weld II (Fig.4-4). The heat source was varied so that the resultant 2D mesh gave similar fusion boundaries to the real weld cross-section (Fig.4-6).

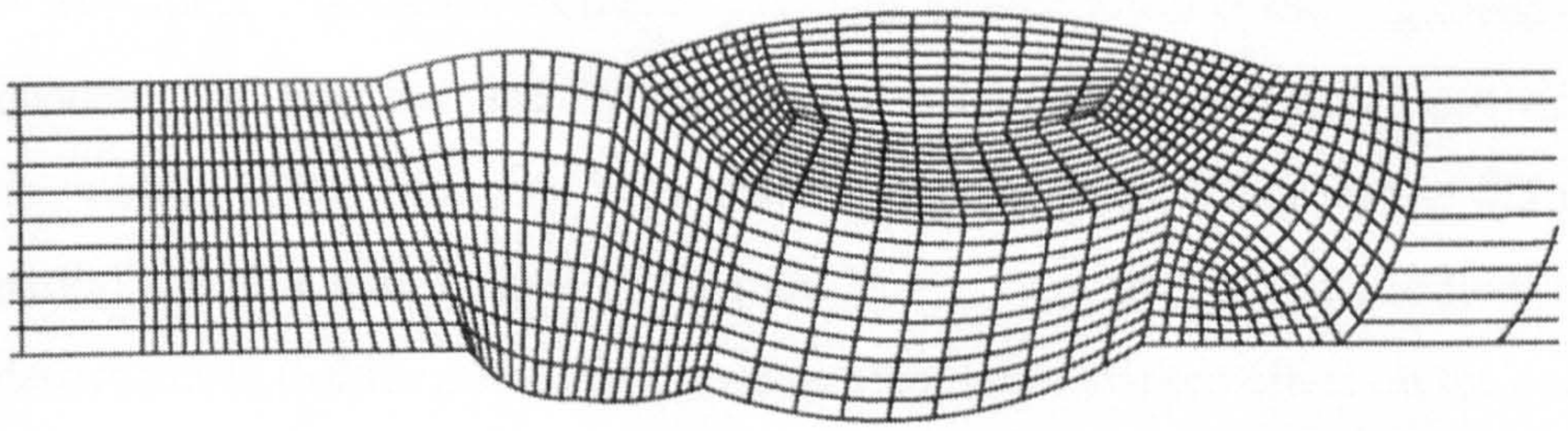


Fig.4-6 2D finite element mesh of weld II about a thermocouple placed at FL+1.3mm (TC51C). Note: Compare with macrosection in Fig.4-3.

From the mesh, thermal cycles were generated for each weld pass at the location of the thermocouple (Fig.4-4b). The FEA correctly predicted that the highest temperatures were reached during pass 2-2 (Fig.4-4a). However, the predicted peak temperatures were higher and Δt times were longer than measured. To explore the limitations with the 2D FEA model, several experiments were undertaken. First, the sensitivity of peak temperature to distance from the fusion line was considered. Table 4-1 shows that a variation of about 1mm corresponds to a difference in peak temperature of about 100°C and yet there was little difference in the cooling time from 1050 to 600°C, e.g. Δt.

Table 4-1 Peak temperatures and Δt times for different distances from the fusion boundary during Pass 2-2 in Study III)

Location	Peak temperature	Time above 600°C	Δt
FL + 1mm	1294°C	43.8 sec	31.5 sec
FL + 1.3mm	1260°C	43.5 sec	32.0 sec
FL + 1.8mm	1176°C	42.5 sec	32.4 sec
FL + 2.6mm	1116°C	41.6 sec	33.0 sec

Second, the variation of peak temperature through the pipe thickness was examined, but the 2D model employed indicated that this had virtually no effect for thin walled pipe.

It was noted that thermocouple TC51C was located towards the beginning of a weld quadrant and thus the pipe behind the pool would be cooler than comparable pipe in the middle of the weld run. This observation was tested using simple 3D models of partial and total width plates of the same thickness as the pipe in question. Figure 4-7 demonstrates that temperature of 'remote pipe' has a marked effect on the cooling rate, but not the peak temperature, and highlights a limitation of the 2D model.

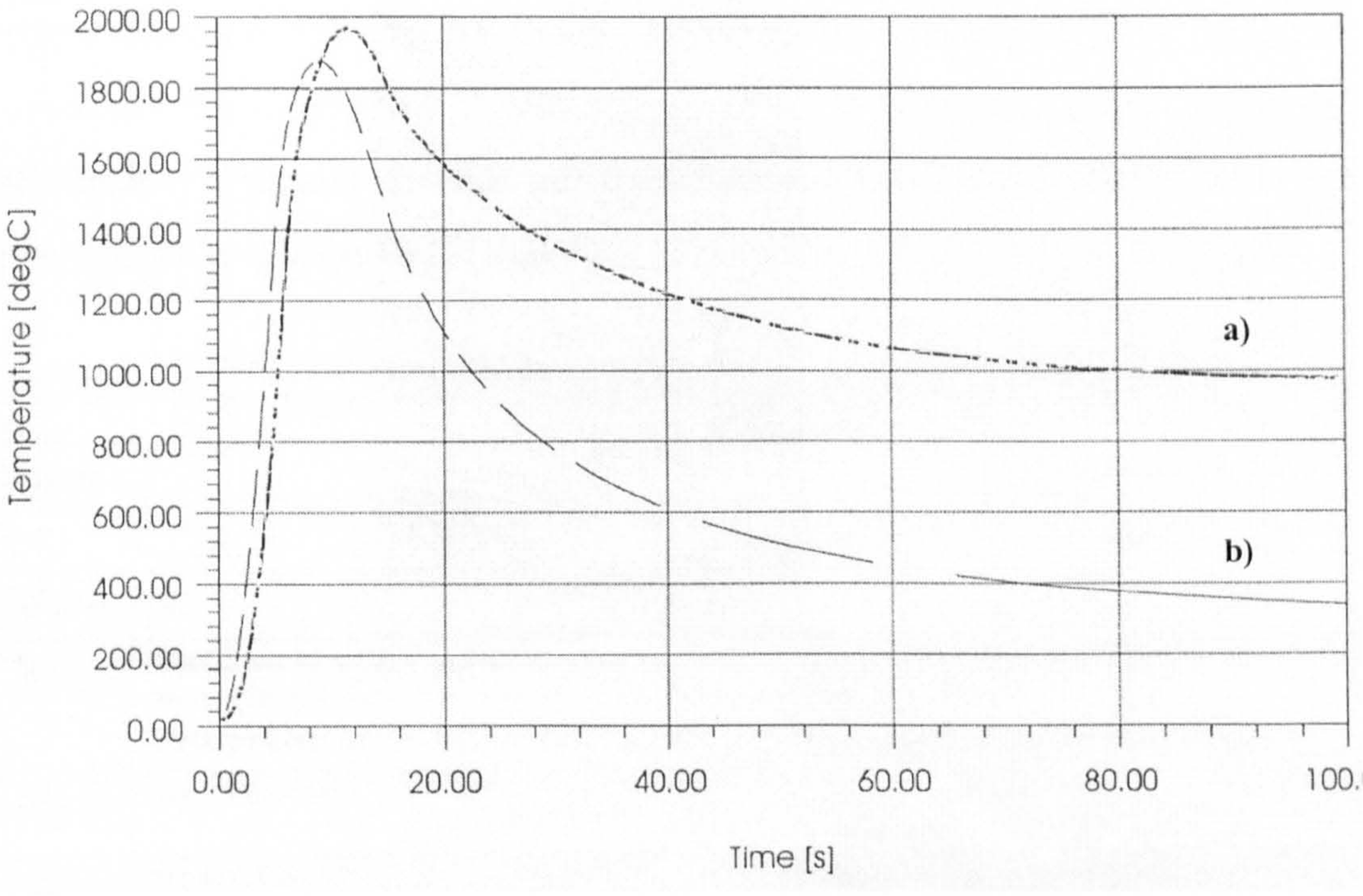


Fig.4-7 Comparison of predicted thermal cycles for two theoretical cases:

a) 'whole width of plate' case which reflects the assumptions in the 2D model

b) 'partial width of plate' case which considers the influence of 'cold' material beyond the weld pass

NB For the simple 3D models employed, the peak temperature could not be restrained

4.4. ISOTHERMAL HEAT TREATMENT (STUDY IV)

4.4.1. Metallography

At 500°C, there was an increase in hardness (Table 4-2), although no change in microstructure could be discerned from optical metallography, magnetic response methods or by back-scattered SEM imaging. Nevertheless, TEM bright field examination revealed very fine precipitates in the ferrite phase (Fig.4-8), which has previously been described as the decomposition of δ to α' [Sol82]. At 700°C, precipitates necklaced the δ/δ sub-grain boundaries (Fig.4-9), which have been previously identified as Cr_2N [Yas86].

Table 4-2 Effect of isothermal heat treatment on properties (Study IV)

Heat treatment (°C)	Plate codes	
	S32760/7	S32750/1
300&400	NC	NC
500	**Inc:** δ hardness; HV & HRC. **Red:** CVN. **Precipitates:** α'	**Inc:** δ hardness; HV & HRC. **Red:** CVN **Precipitates:** α'+ Cr_2N at δ/δ gbs.
600	**Inc:** δ hardness	**Inc:** δ hardness **Red:** CPT.
700	**Red:** CVN **Precipitates:** Cr_2N at δ/δ gbs & within δ	**Red:** CVN **Precipitates:** Cr_2N at δ/δ gbs & within δ
800	**Inc:** δ hardness; HV5 & HRC **Red:** CVN; CPT. **Precipitates:** σ+χ (0.7%I)	**Inc:** δ & γ hardness; HV5 & HRC. **Red:** CVN, CPT. **Precipitates:** σ+χ (3%I)
900	**Inc:** hardness **Red:** %δ & FN; CVN; CPT. **Precipitates:** σ+χ (4%I) + some eutectoid (σ+γ)	**Inc:** δ hardness; HV5 & HRC. **Red:** %δ & FN, CVN, CPT. **Precipitates:** σ+χ (18%I) + eutectoid
1000	**Inc:** HV5 & HRC. **Red:** CVN, CPT. **Precipitates:** σ (3.0%I)	**Red:** %δ & FN; HV5 & HRC CVN, CPT. **Precipitates:** σ (6.1%I)
1100	**Inc:** %δ & FN, δ Hardness. **Red:** CPT. **Precipitates:** Cr_2N at δ/δ gbs & within δ	**Properties:** NC **Precipitates:** Cr_2N at δ/δ gbs & within δ
1200	**Inc:** %δ & FN, δ hardness; HV5 & HRC. **Red:** CVN, CPT. **Precipitates:** Cr_2N at δ/δ gbs & within δ	**Inc:** %δ & FN; HV5 & HRC. **Red:** CPT **Precipitates:** Cr_2N at δ/δ gbs & within δ
1300	**Inc:** %δ & FN; δ hardness; HV5 & HRC. **Red:** CVN, CPT. **Precipitates:** Cr_2N within δ	**Inc:** %δ & FN; HV5 & HRC. **Red:** CVN, CPT. **Precipitates:** Cr_2N at δ/δ gbs & within δ

NC = no significant change in properties compared to solution annealed plate.
Inc = Increase; Red = Reduction; CPT = critical pitting temperature; CVN = toughness, HV = Vickers hardness; HRC Rockwell, hardness, δ = ferrite, FN = Ferrite Number, I = intermetallic, i.e. σ+χ

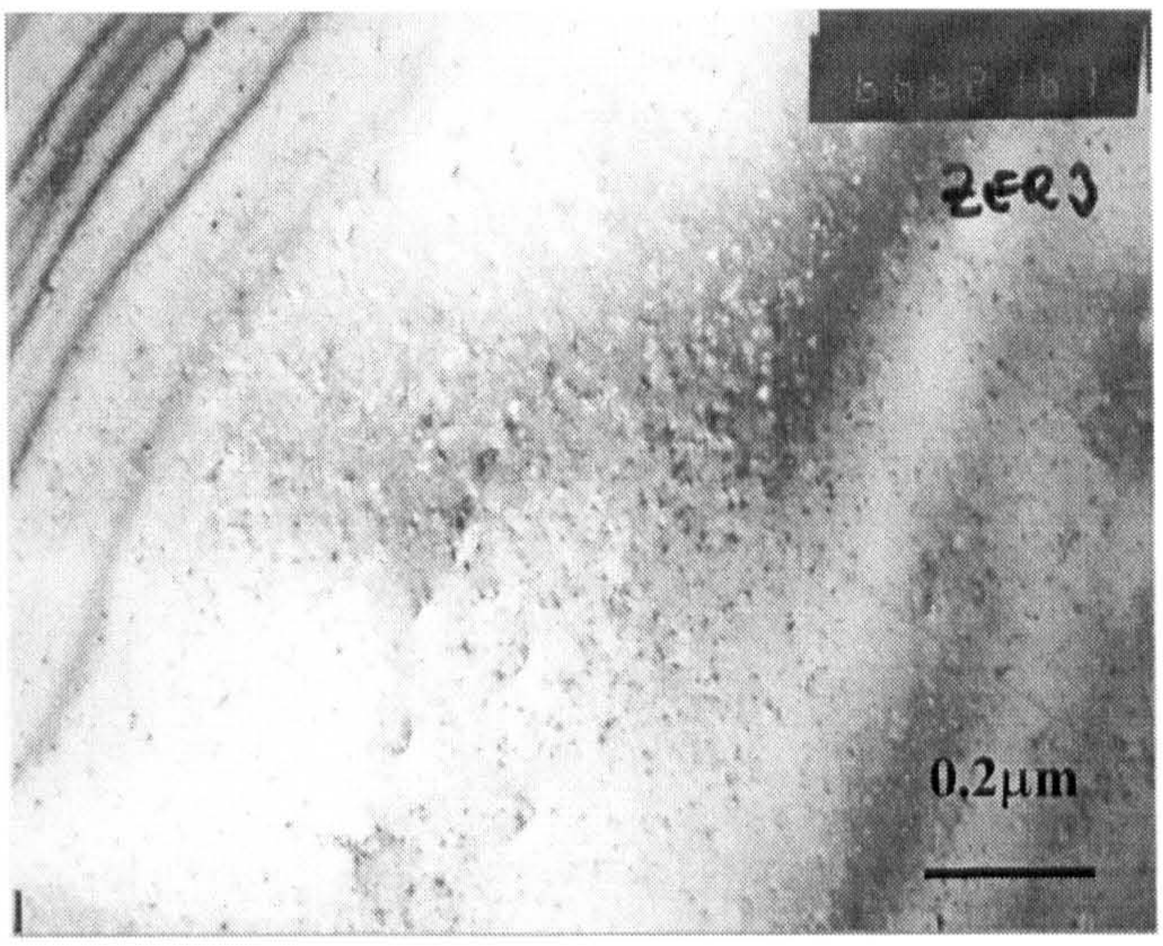
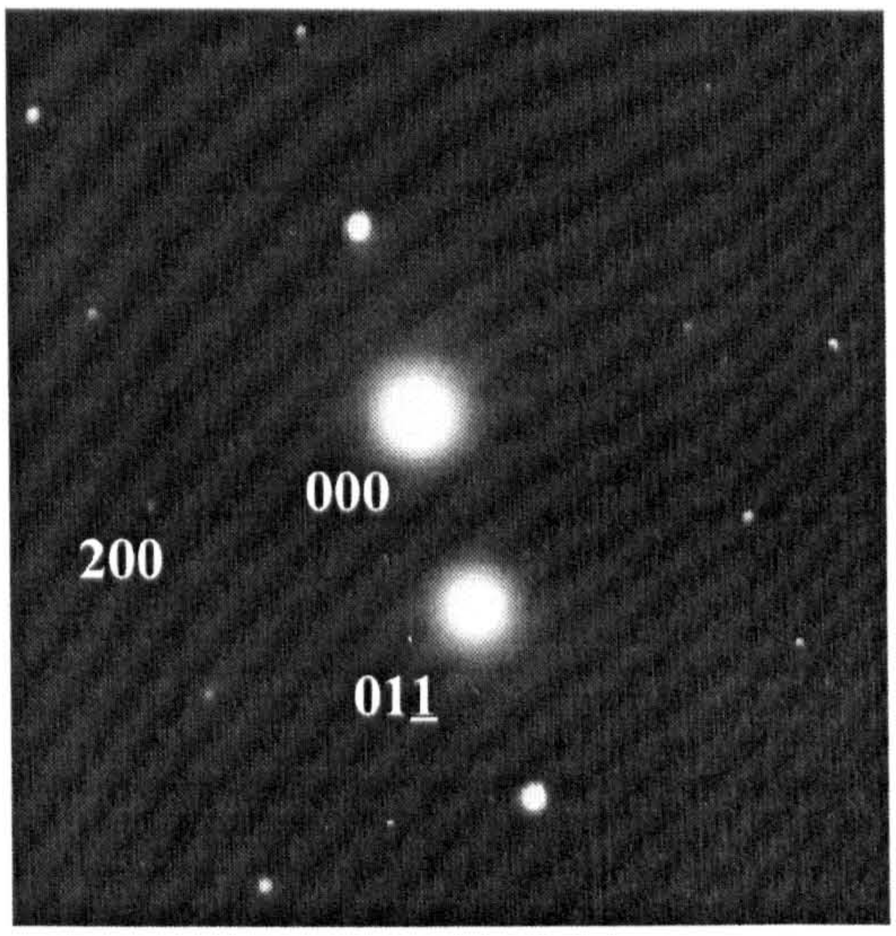


Fig.4-8 Bright field TEM micrograph of steel S32760/7 after exposure to 500°C for about 10 minutes. The fine precipitation within the ferrite is presumed to be α'-phase. [x66k, 62161]



SADP for Fig.4-8 demonstrating that 'α'-phase' is present in ferrite [011], 62160. Note: α' 'particles' were too small to produce characteristic SADP

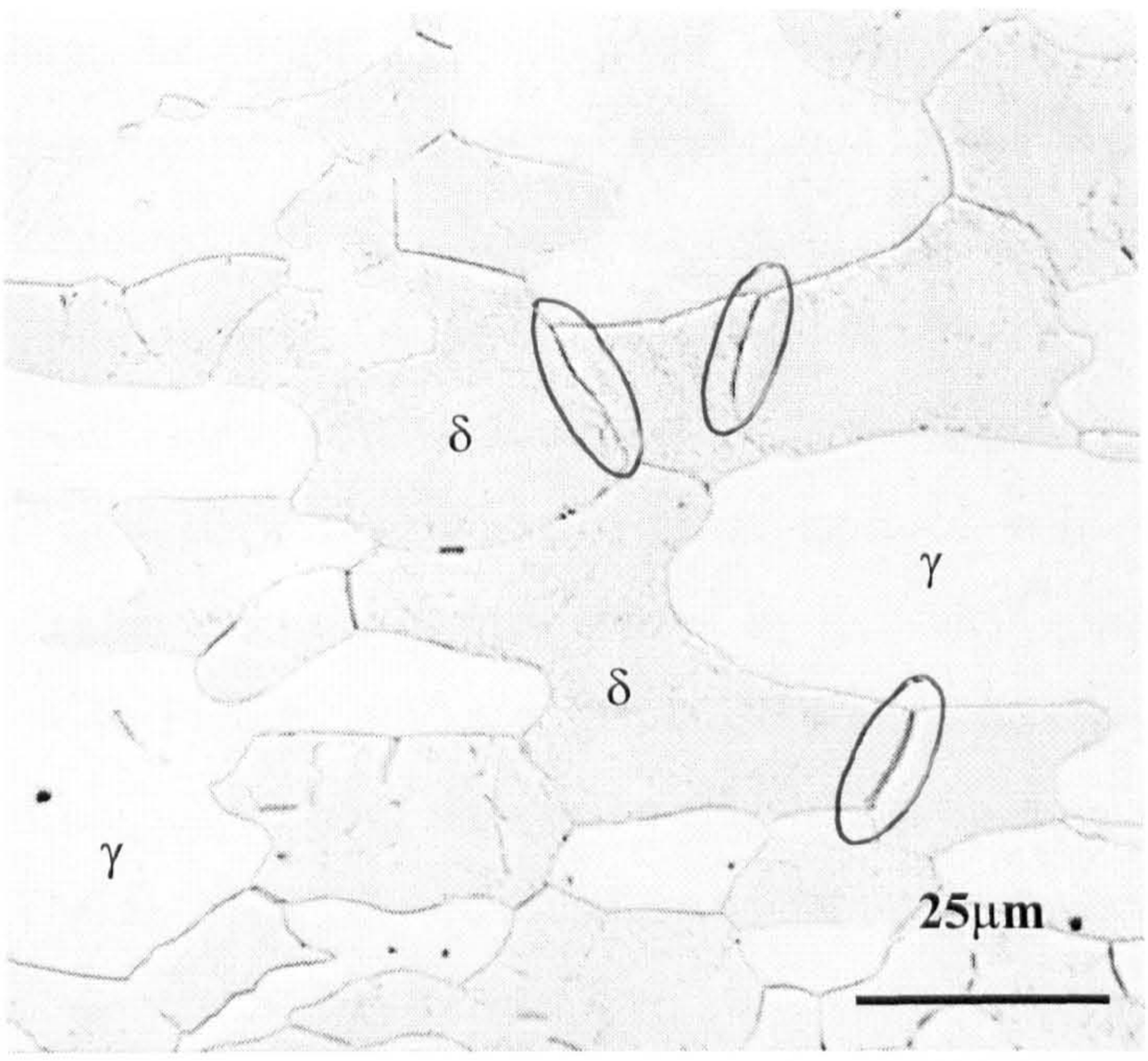


Fig.4-9 Optical micrograph of steel S32750/1 after exposure to 700°C for about 10 minutes. Austenite is white and δ–ferrite is grey. The precipitates seen necklacing (circled) the δ/δ sub-grain boundaries are presumed to be Cr_2N [x800, AG773]

Between 800 and 1000°C, all of the steels formed intermetallic phases to varying extents (Table 4-2), although, in each case, the most precipitation occurred at 900°C (i.e. 4 to 18%), growing from the δ/γ boundaries into the δ-phase. The most prevalent of these precipitates was identified as sigma (σ) phase, Fig.4-10.

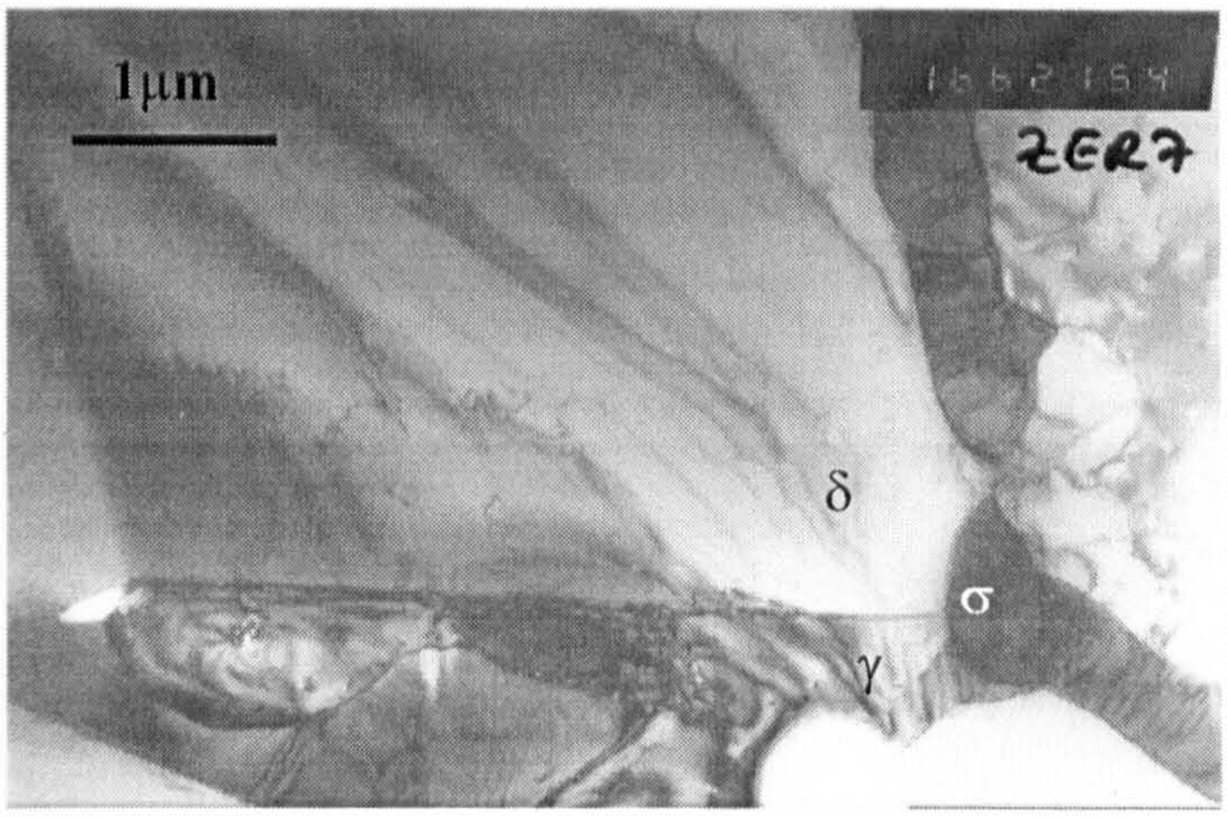
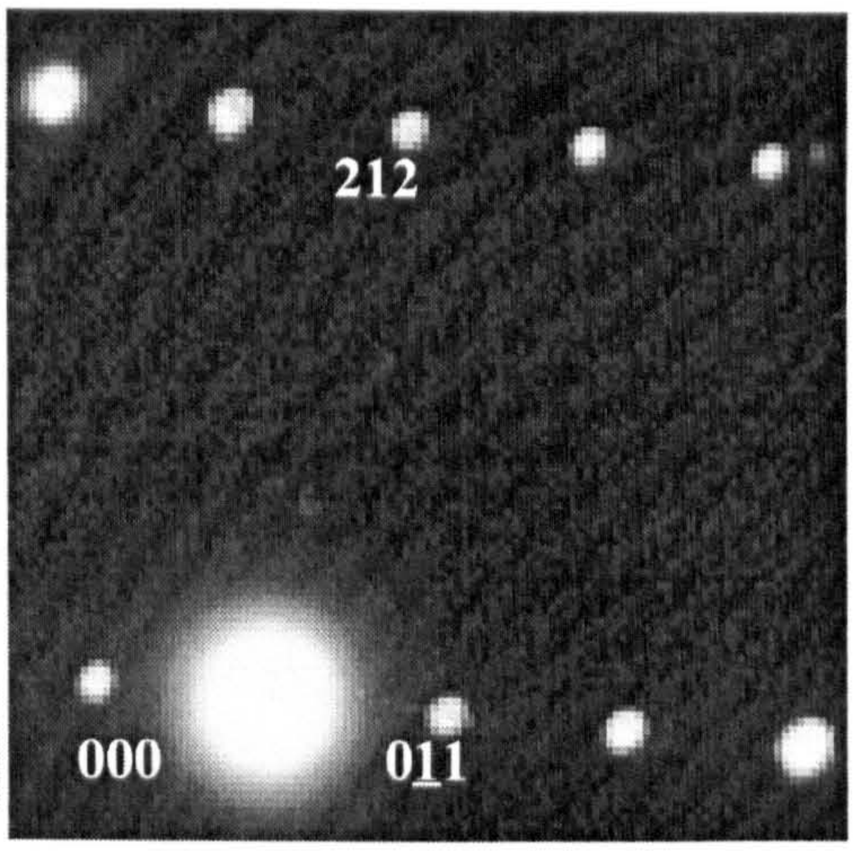
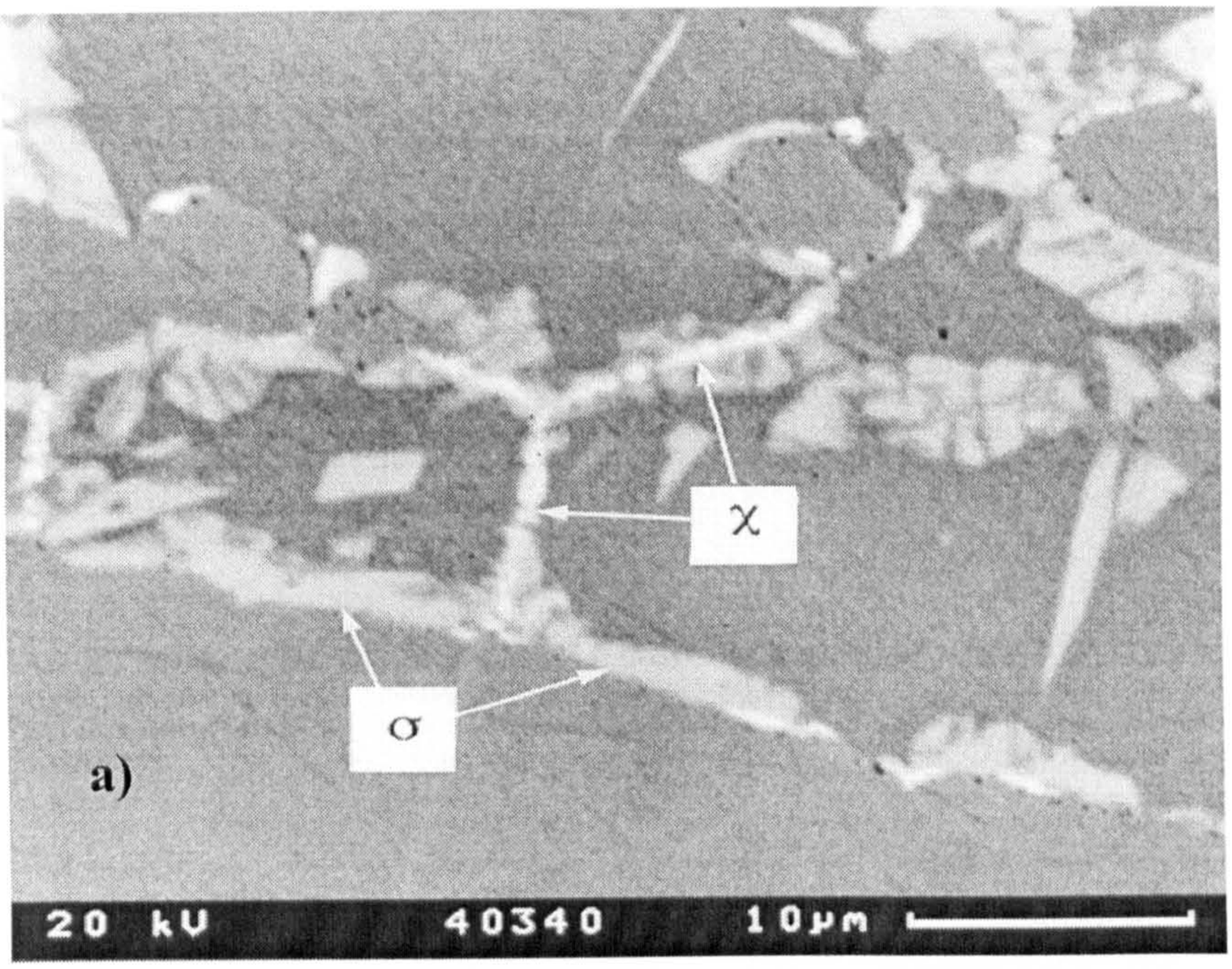


Fig.4-10 Bright field TEM micrograph of steel S32760/7 after exposure to 900°C for about 10 minutes. The precipitates on the δ/γ boundaries were identified as σ-phase [x16k, 62154]



SADP for σ-phase in Fig.4-10 [62152]

The greatest σ-precipitation was seen in steel S32750/1 (i.e. 18 ± 3.9%) comprising large lathes and discrete phase boundary particles (Fig.4-11a). In addition to σ–precipitation, two other precipitation forms were observed. The first had a laminated structure, forming in δ-ferrite and growing into this phase (Fig.4-11b). These observations are consistent with the $\sigma+\gamma_2$ eutectoid [Jos91]. Alternatively, the second precipitate was located at the δ/γ boundaries or at the centre of σ-precipitation (Figs.4-11a&b). This second phase appeared to be more enriched in high atomic number elements than σ, evident by its whiter appearance in SEM back scattered mode. Further, as shown by the EDX maps in Fig.4-12, this second phase can be distinguished from alloy-rich σ (Fig.4-12a), by its enhanced Mo-content (Fig.4-12b). These observations are consistent with the second precipitate being χ-phase [Nil92b].



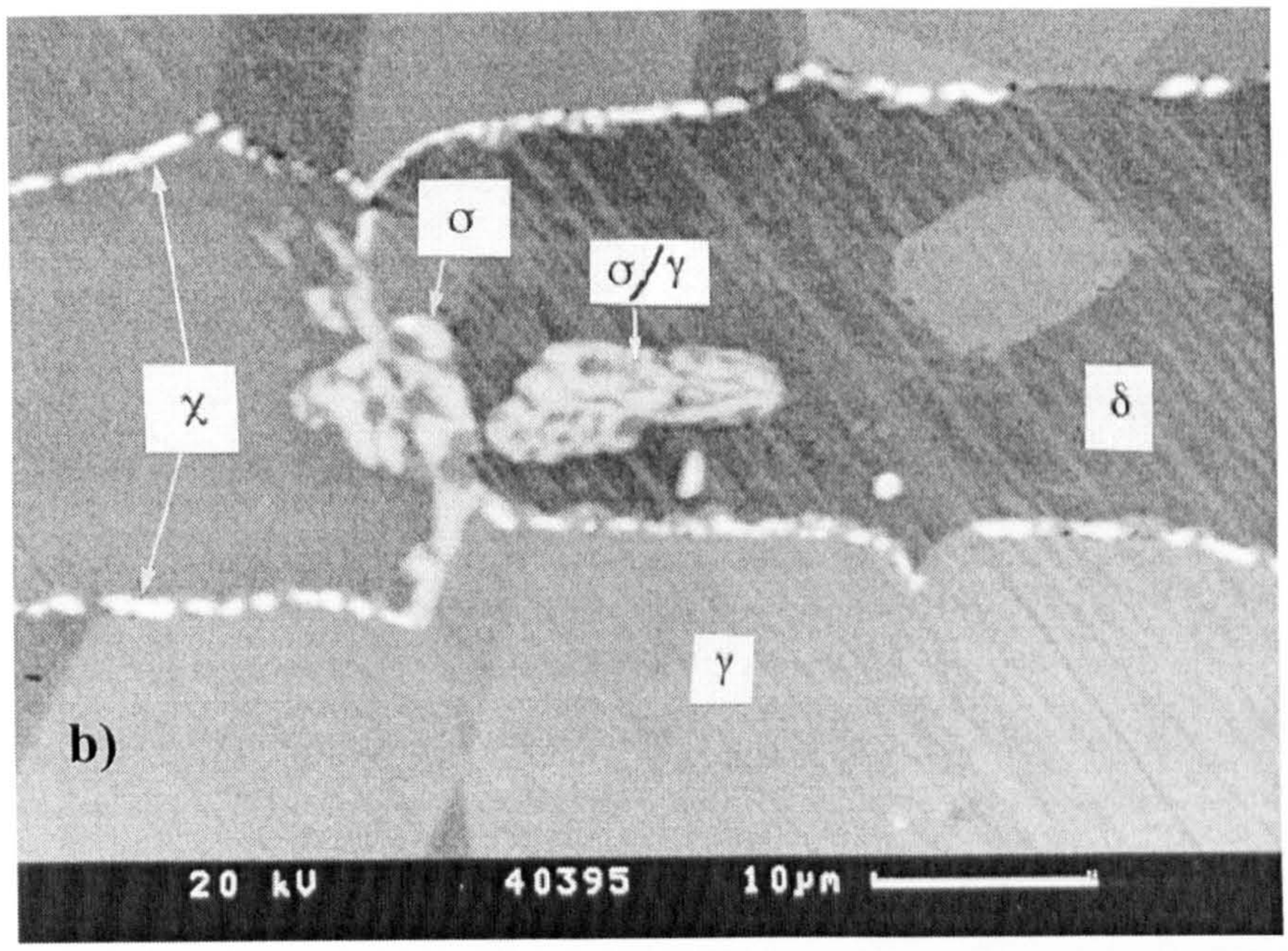


Fig.4-11 Back scattered SEM images of steels heat treated at 900°C. Nom. mag. x2000. a) Steel S32750/1 and b) Steel S32760/7.

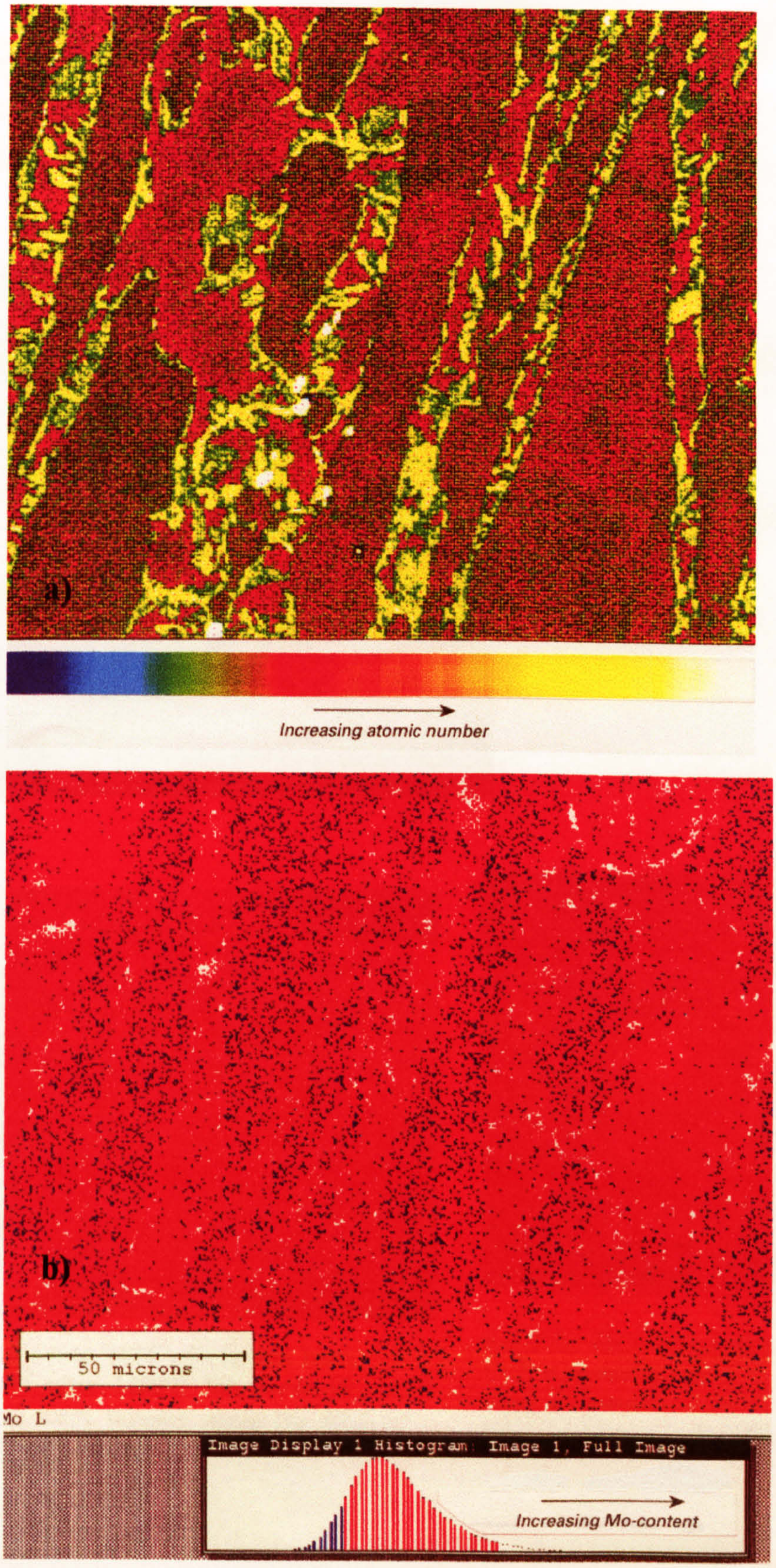


Fig.4-12 Steel S32750/1 after heat treatment at 900°C for about 10 minutes.

a) Back scattered SEM image showing contrast between elements of high and low atomic number. γ -phase is red, δ is red/green, intermetallic phases (e.g. σ, χ) are yellow.

b) EDX map for Mo. γ -phase is Mo-lean (red), δ -phase is Mo-rich (blue), and χ–phase is Mo-rich (white)

At 1000°C, relatively large precipitates of σ were observed (Fig.4-13) and at the more elevated heat treatment temperatures, both steels showed an increase in δ-level and precipitation of Cr_2N within the grains and at the ferrite sub-grain boundaries (Fig.4-14).

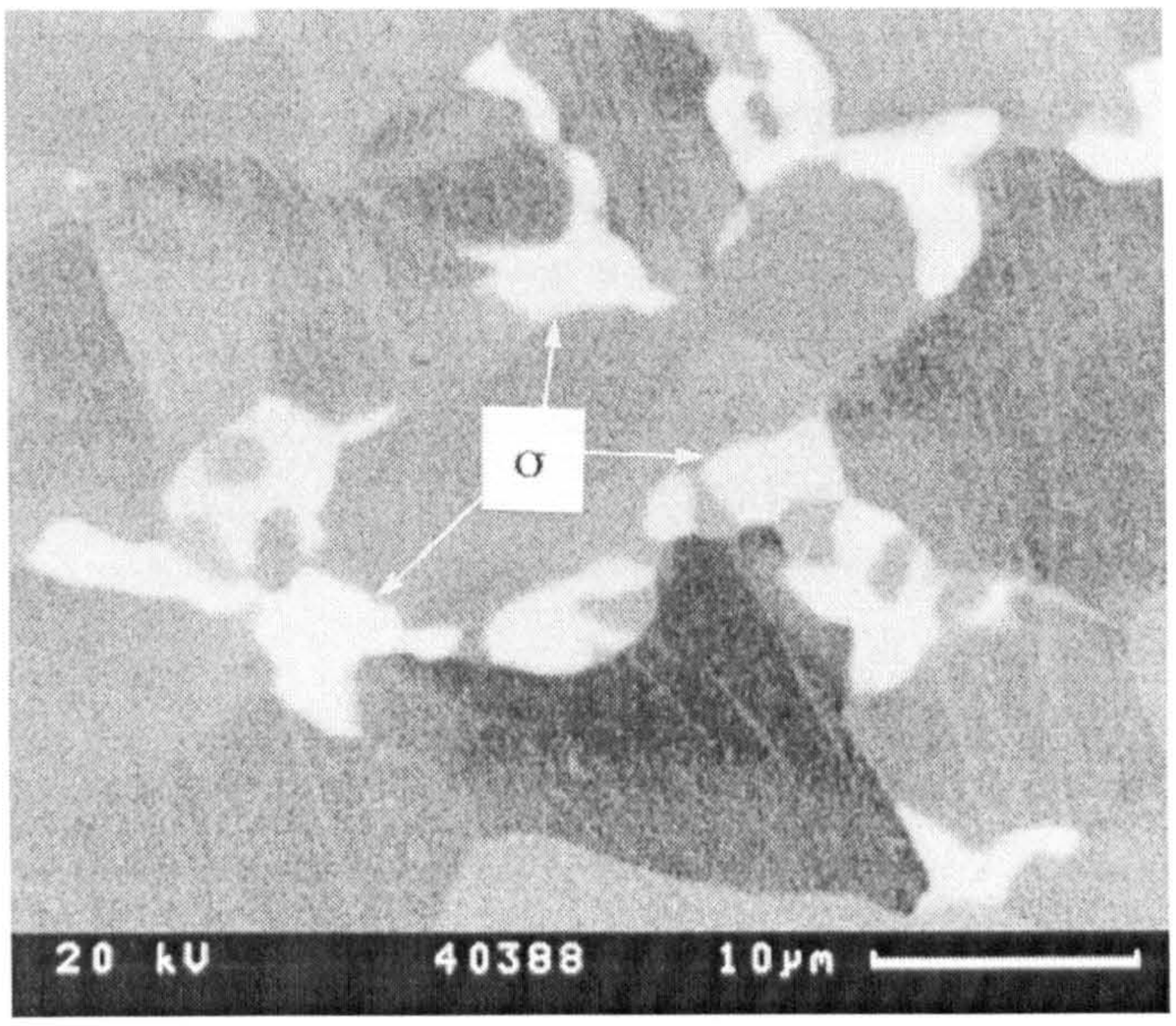


Fig.4-13 Back scattered SEM images of steel S32750/1 heat treated at 1000°C for about 10 minutes. [x2000]

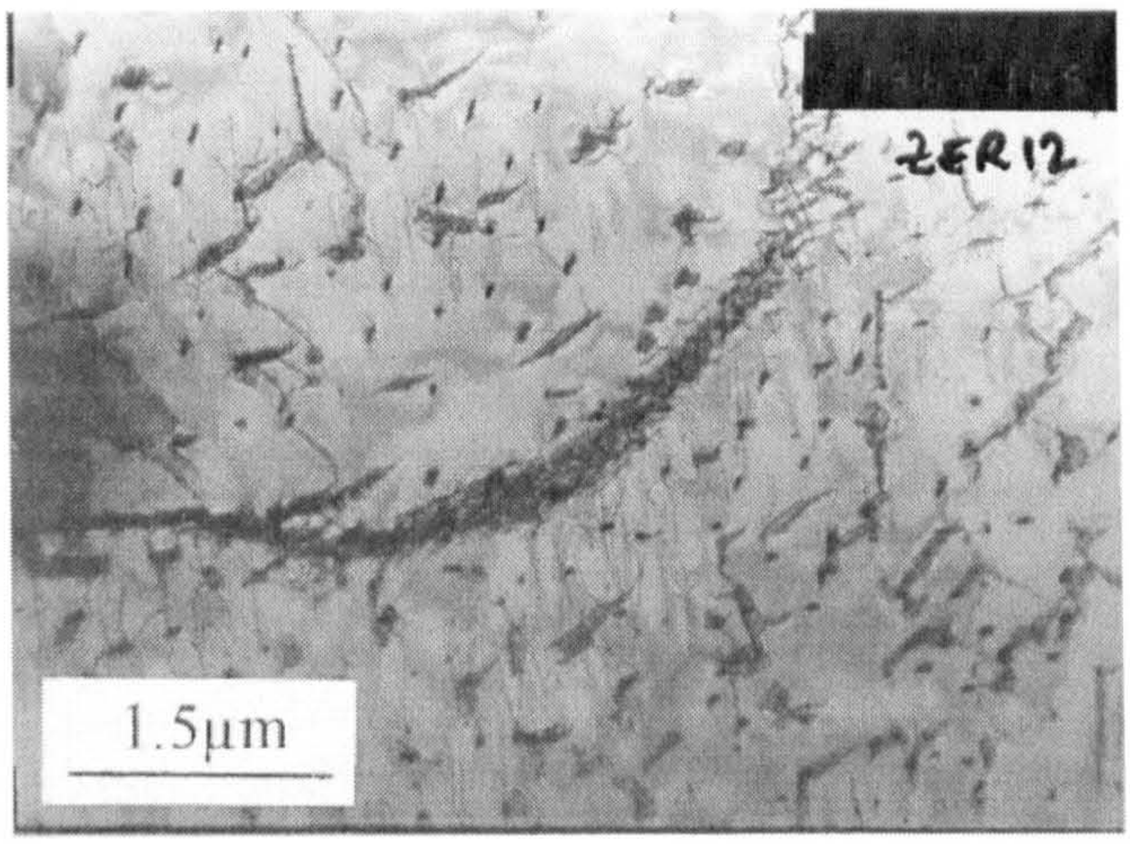
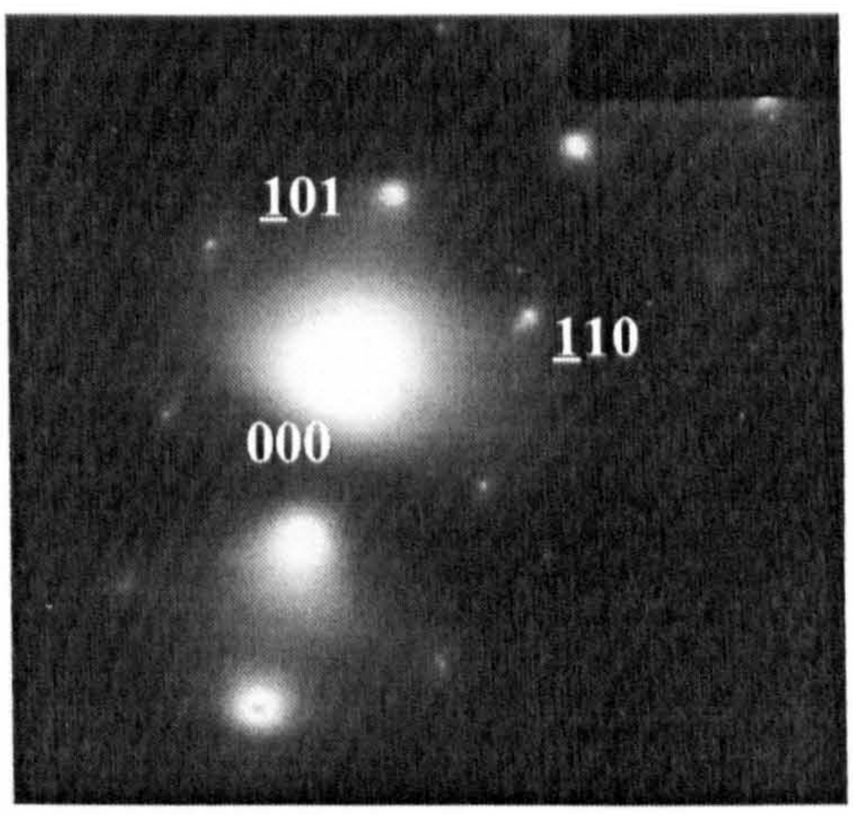


Fig.4-14 Bright field TEM micrograph from steel S32760/7 after 1200°C for about 10 minutes. Note Cr_2N forming along the δ/δ sub-grain boundaries [x13k, 62165].



SADP for Fig.4-14 demonstrating that Cr_2N is present in ferrite <111> [62166]. Note: α' 'particles' were too small to produce characteristic SADP

4.4.2. Effect of Intermetallic Formation on Toughness

In the as-received (solution annealed) condition, both steels showed good toughness at -40°C (Fig.4-15), associated with predominantly ductile behaviour, with some cleavage in steel S32760/7 (Fig.4-16a). Intermetallic precipitation occurred in both steels and caused loss of impact toughness over the temperature range 700 to 1000°C (Fig.4-15). The fracture face became more irregular (Fig.4-16b) with the crack crossing the ferrite phase and following the precipitate lined δ/γ boundaries, leaving the austenite islands intact (Fig.4-16c).

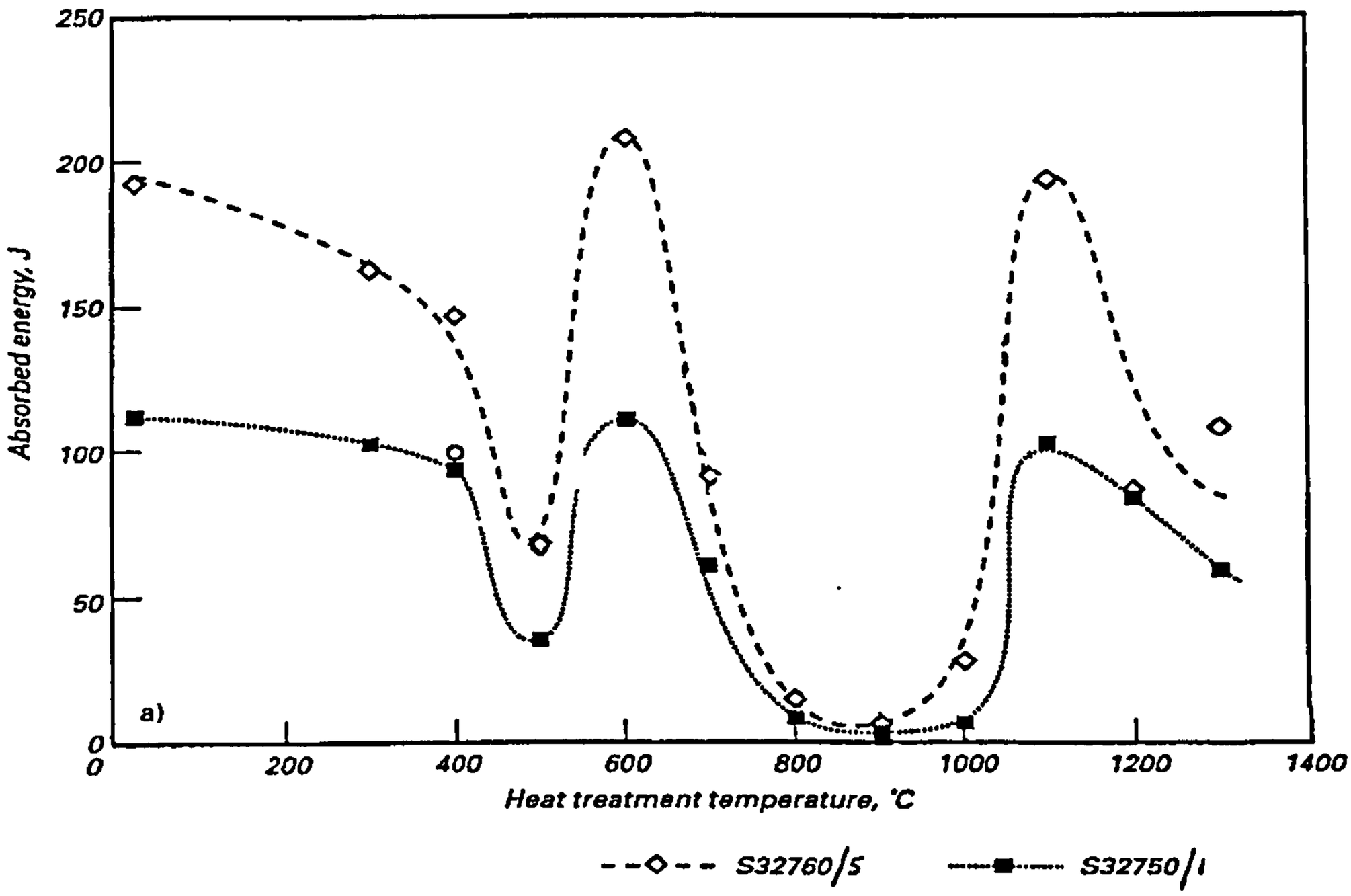


Fig.4-15 Effect of heat treatment on impact properties at -40°C

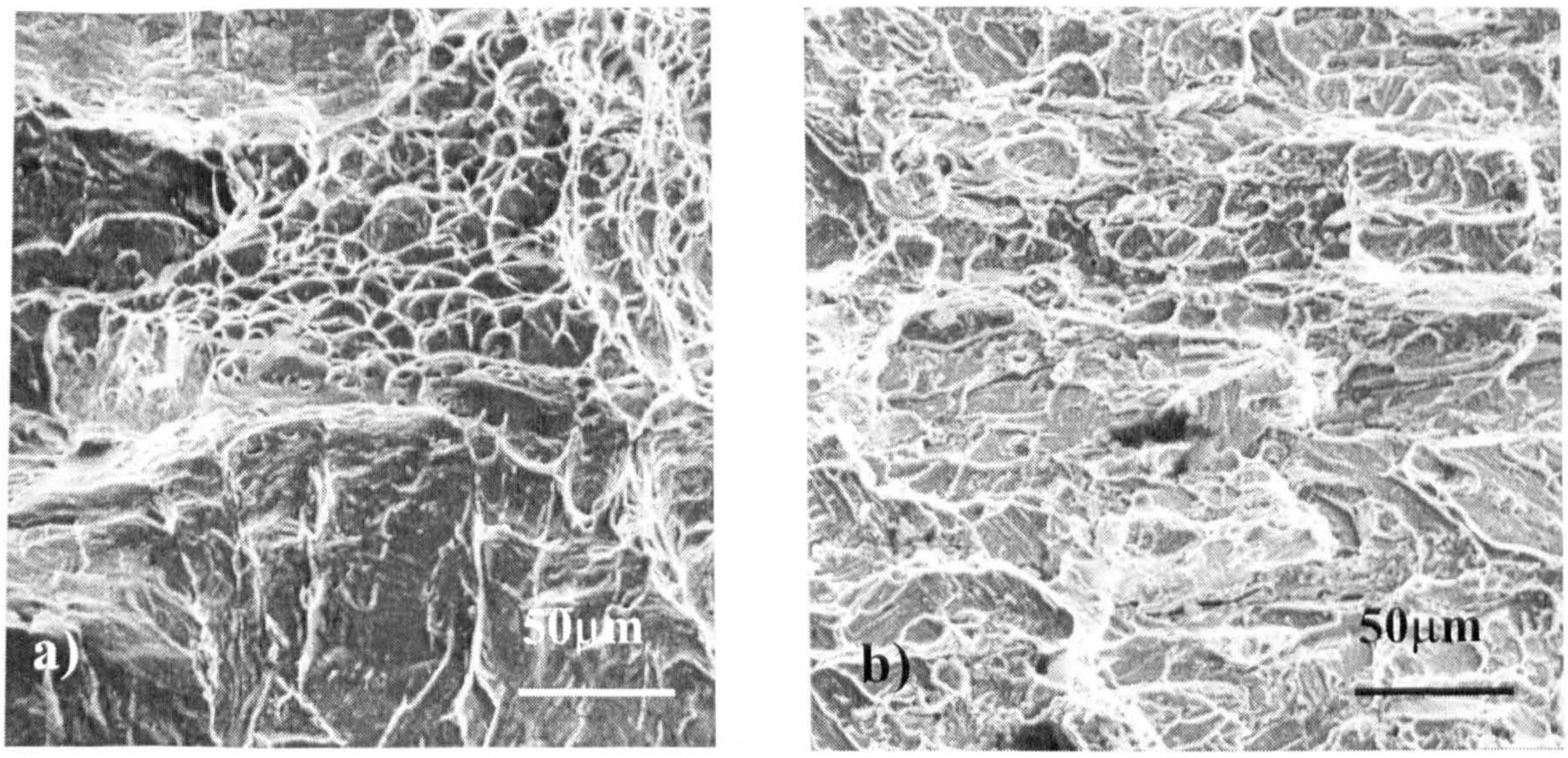
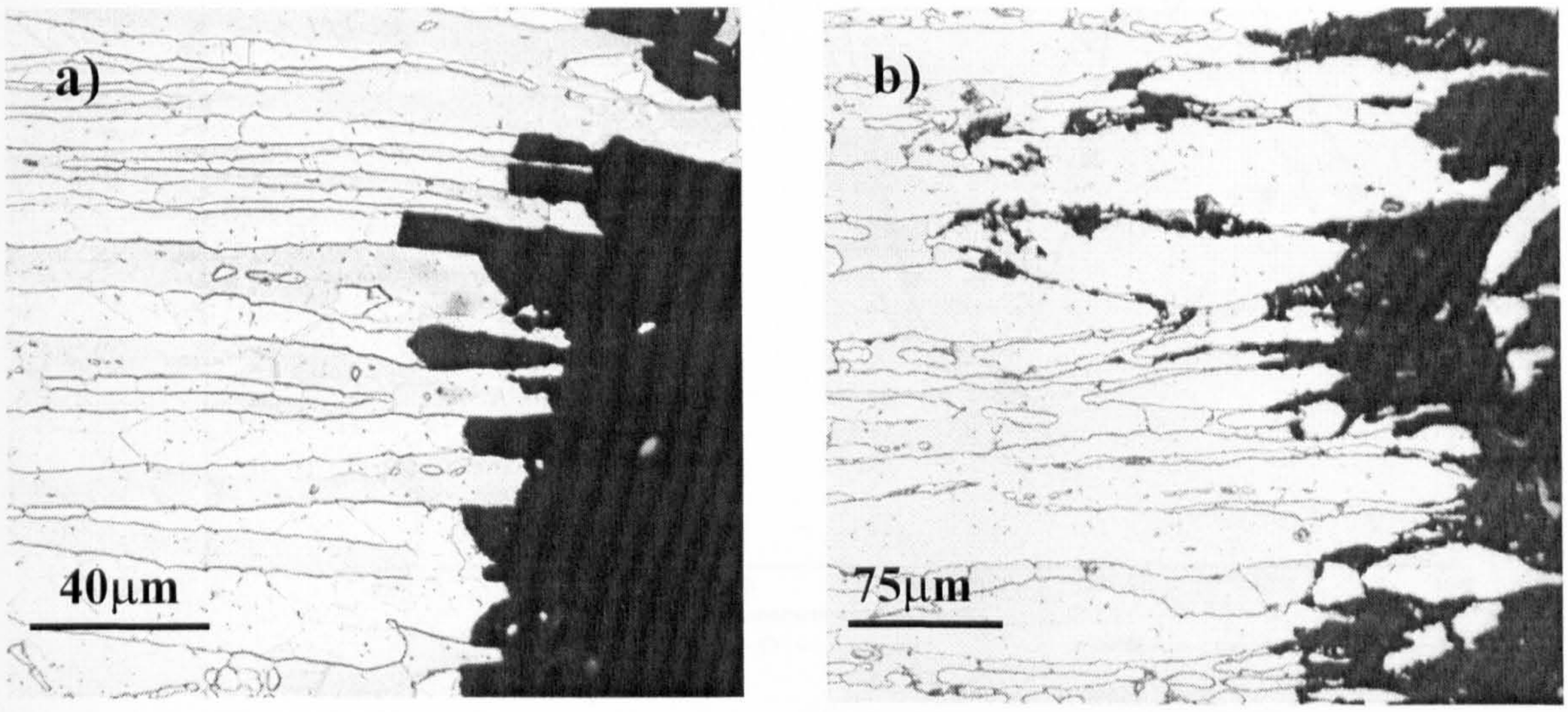


Fig.4-16 Effect of intermetallic precipitates on fracture mode (steel S32760/7).
a) Evidence of cleavage in as-received steel. [x300, 92/4954.]
b) Predominant cleavage after exposure to 900°C for about 10 mins. [x300, 92/4967.]
c) Crack path beneath notch after exposure to 900°C for about 10 mins. The white phase is austenite and the darker phase is ferrite. The dark precipitates on the δ/γ boundaries are intermetallic phases [x100, AF146.]



4.4.3. Effect of Heat Treatment on Pitting Resistance

For the lower heat treatment temperatures (say, below 600°C), the δ-phase was more resistant to pitting attack than γ (Fig.4-17a). This observation is consistent with the literature (Section 2.2.7), as, in solution annealed products, substitutional element partitioning between the ferrite and austenite has time to occur which provides the ferrite with higher levels of Cr and Mo than the austenite and so renders the ferrite more resistant to localised attack.



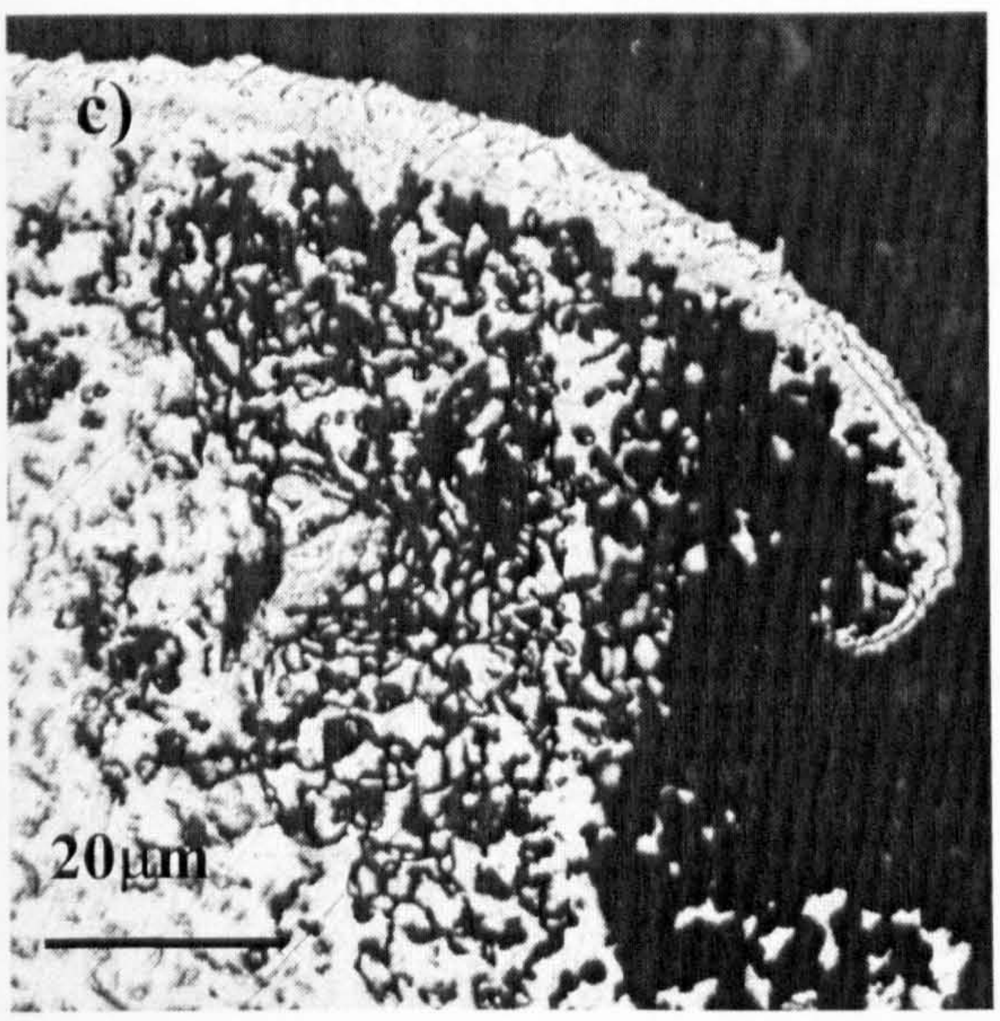


Fig.4-17 Sites of preferential attack after exposure to ferric chloride solution.
a) Attack of austenite. Steel S32760/7 in as-received condition. [x400, AE2861]
b) Attack along phase boundaries decorated with precipitates. Steel S32750/1 after exposure to 800°C for about 10 mins. [x200, AE2853]
c) Attack of ferrite decorated with Cr_2N precipitates. Steel S32550 after exposure to 1300°C for 10 mins. [AE2857, x800]

As the heat treatment temperature was increased above 700°C, the corrosion sites tended to move to the δ-phase and the CPT dropped by about 40°C (Figs.4-17b and 4-18). Again, this is consistent with the literature as the formation of Mo, Cr -rich intermetallic phases denudes the surrounding microstructure of these elements and reduces the bulk CPT. At more elevated temperatures, e.g. 1300°C, there was also a drop in CPT, due to element redistribution and Cr_2N formation (Fig.4-17c).

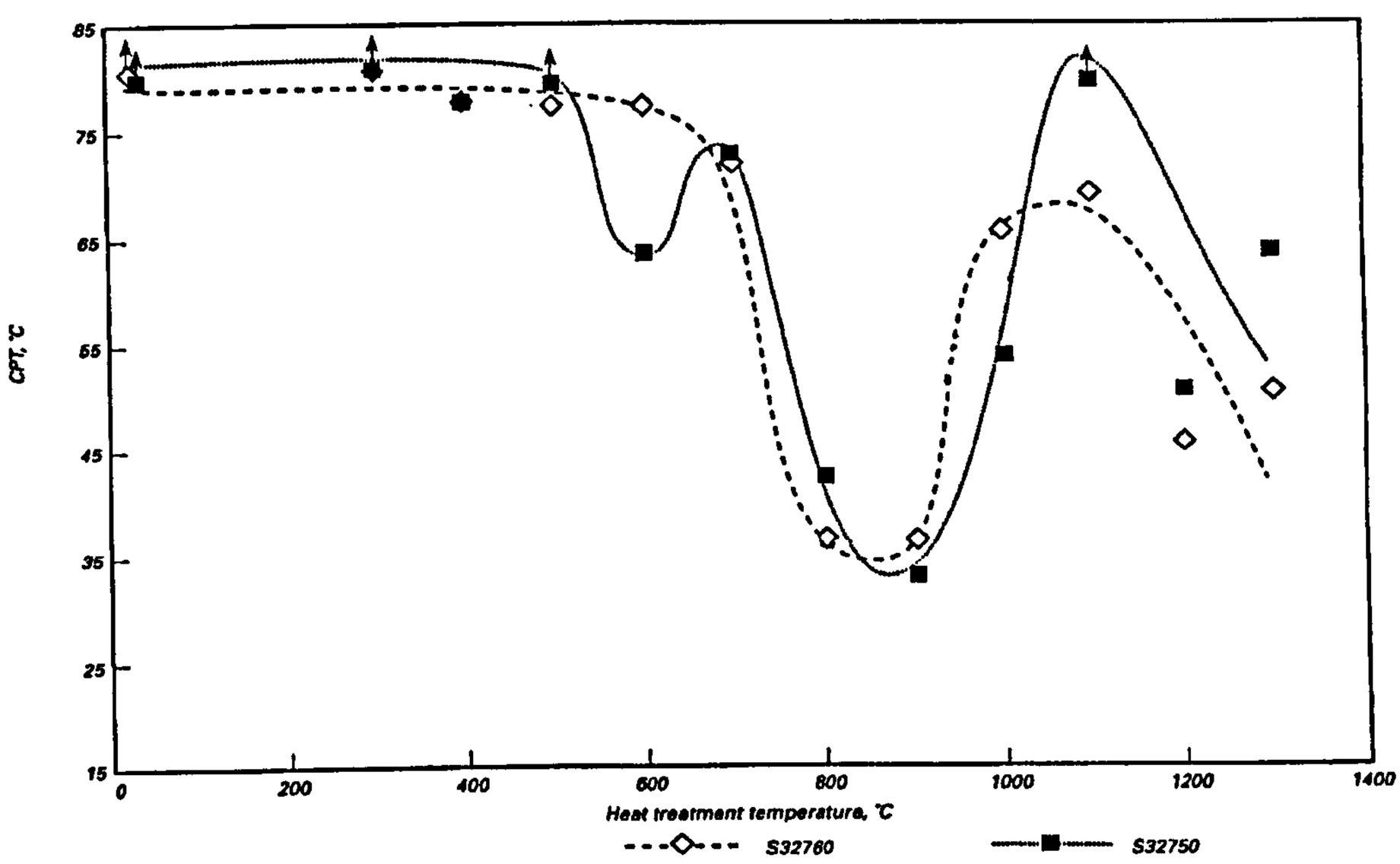


Fig.4-18 Effect of heat treatment on critical pitting temperature (CPT) in ferric chloride solution. Each data point represents results from an individual sample and so some scatter exists, eg. steel S32750 at 600°C

The drop in CPT with intermetallic content is shown in Fig.4-19. Clearly, high intermetallic contents reduce pitting resistance, but it is noted that samples heat treated at 1000°C did not show such as marked a reduction in CPT as samples heat treated at 800 or 900°C with similar precipitation levels. The difference in intermetallic phase morphology between these samples is noted (Figs. 4-11 & 4-13) and it is suggested that a corresponding difference in alloy depletion around precipitates exists. Therefore, It would seem that there is no direct correlation between intermetallic content and drop in CPT for isothermally heat treated samples exposed to ferric chloride solution. This subject shall be further discussed in Section 6.7.

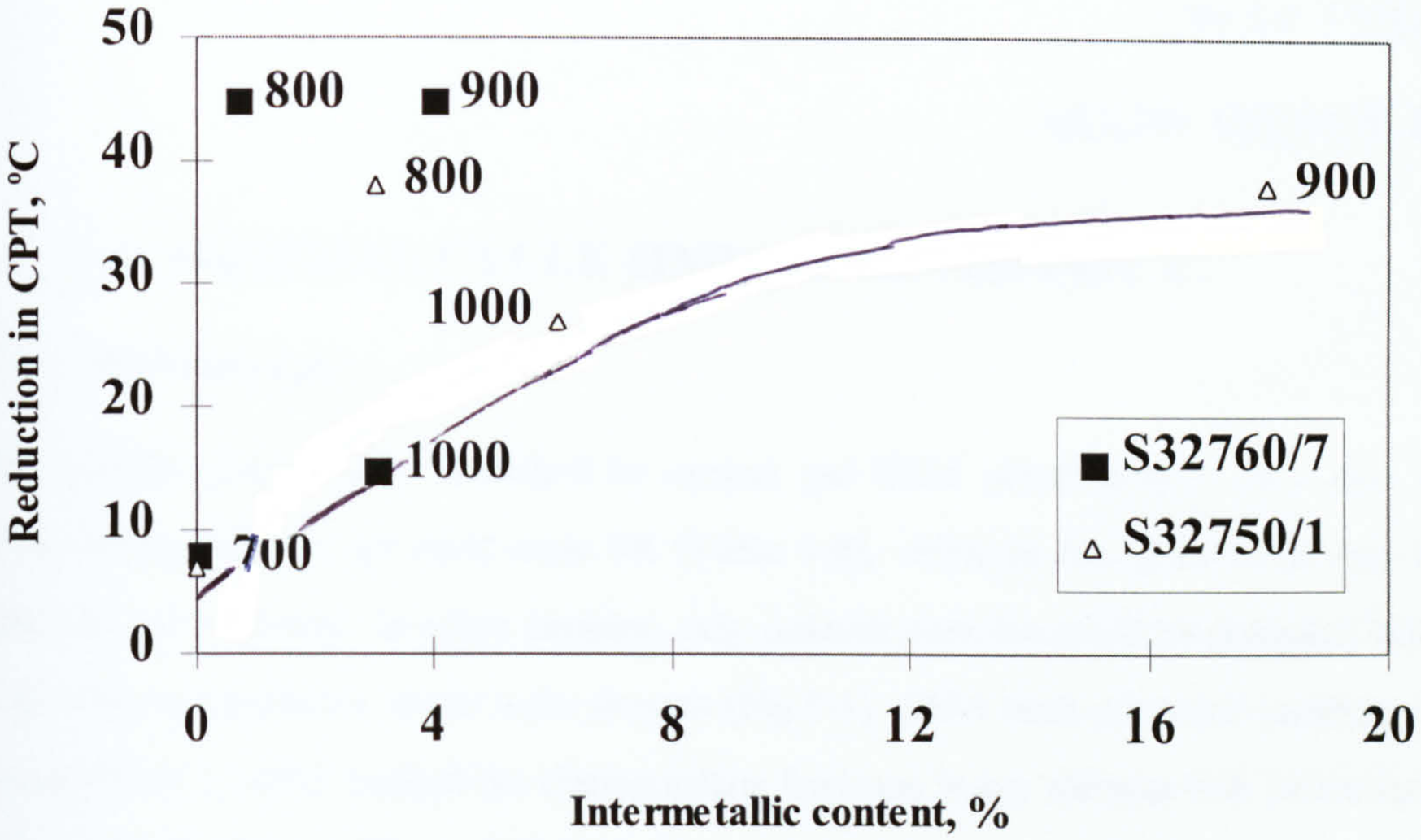


Fig.4-19 Relationship between intermetallic content and reduction in CPT. The values next to each data point indicate the heat treatment temperature.
The line denotes the lower bound curve.

CHAPTER 5
MAIN RESULTS

5.1. THERMAL CYCLE SIMULATION (STUDY V)

5.1.1. Metallography

Intermetallic phases were identified by optical and SEM metallography only after the most prolonged thermal cycle code 3R (Table 3-6), although the distribution was not uniform, i.e. clustered. In some samples, only isolated particles could be detected, but in others more significant levels were present (Fig.5-1). SEM back-scattered imaging was found to be a useful method for distinguishing between heavy element rich intermetallic phases (i.e. containing Mo and W) and other precipitates.

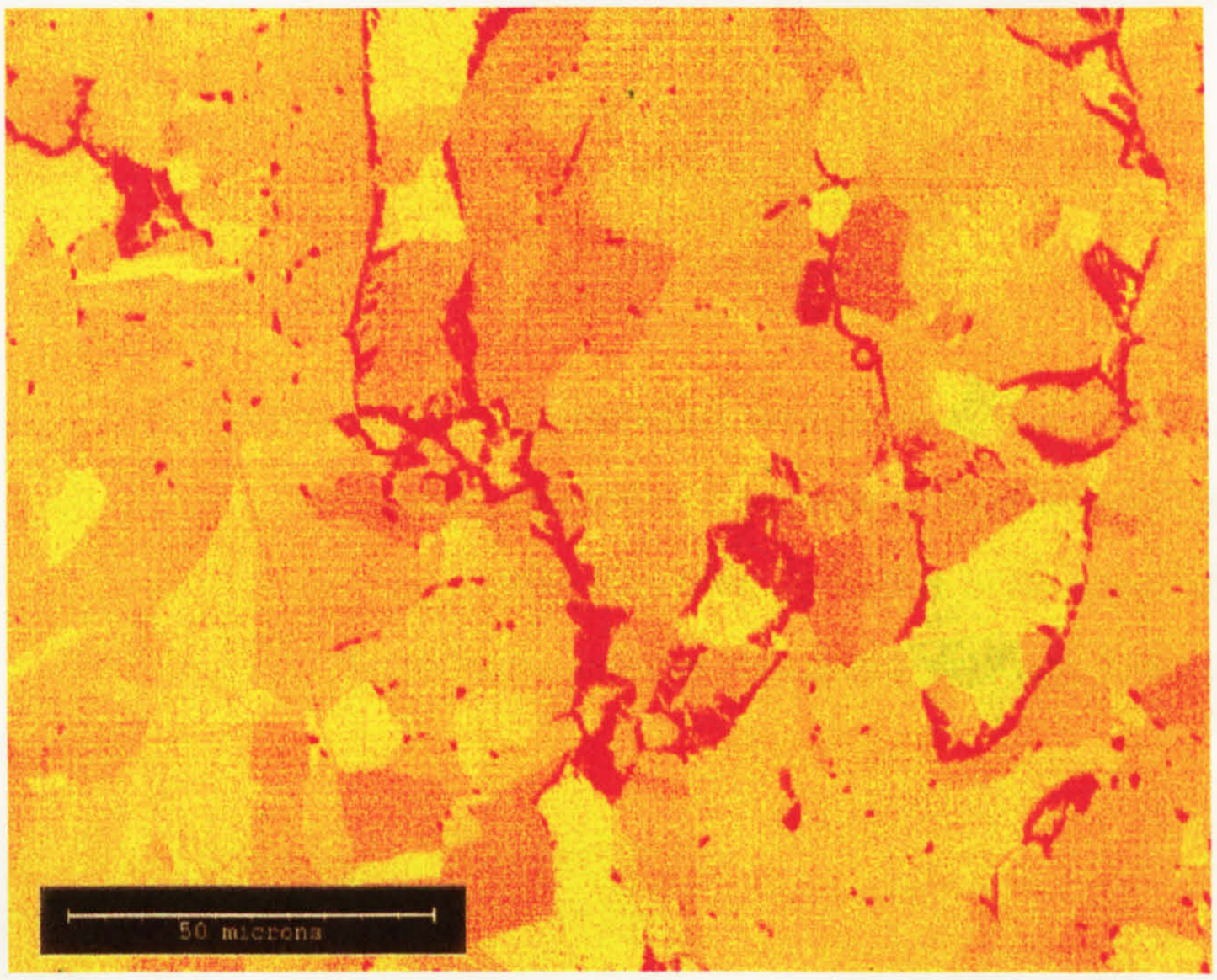


Fig.5-1 SEM back scattered image of steel S32760/7 after thermal cycle code 3R. NB Intermetallic phases in red, i.e. high atomic number. [x620]

The highest level of precipitation was measured at 1.60 ± 0.81% (Fig.5-2). In all the other specimens, including thermal cycle code 2D+ with an applied tensile strain of 3.1%, no intermetallic phases were recorded by optical or SEM techniques even at magnifications up to x1000. These techniques provide a particle size detection "limit" of about 0.1μm.

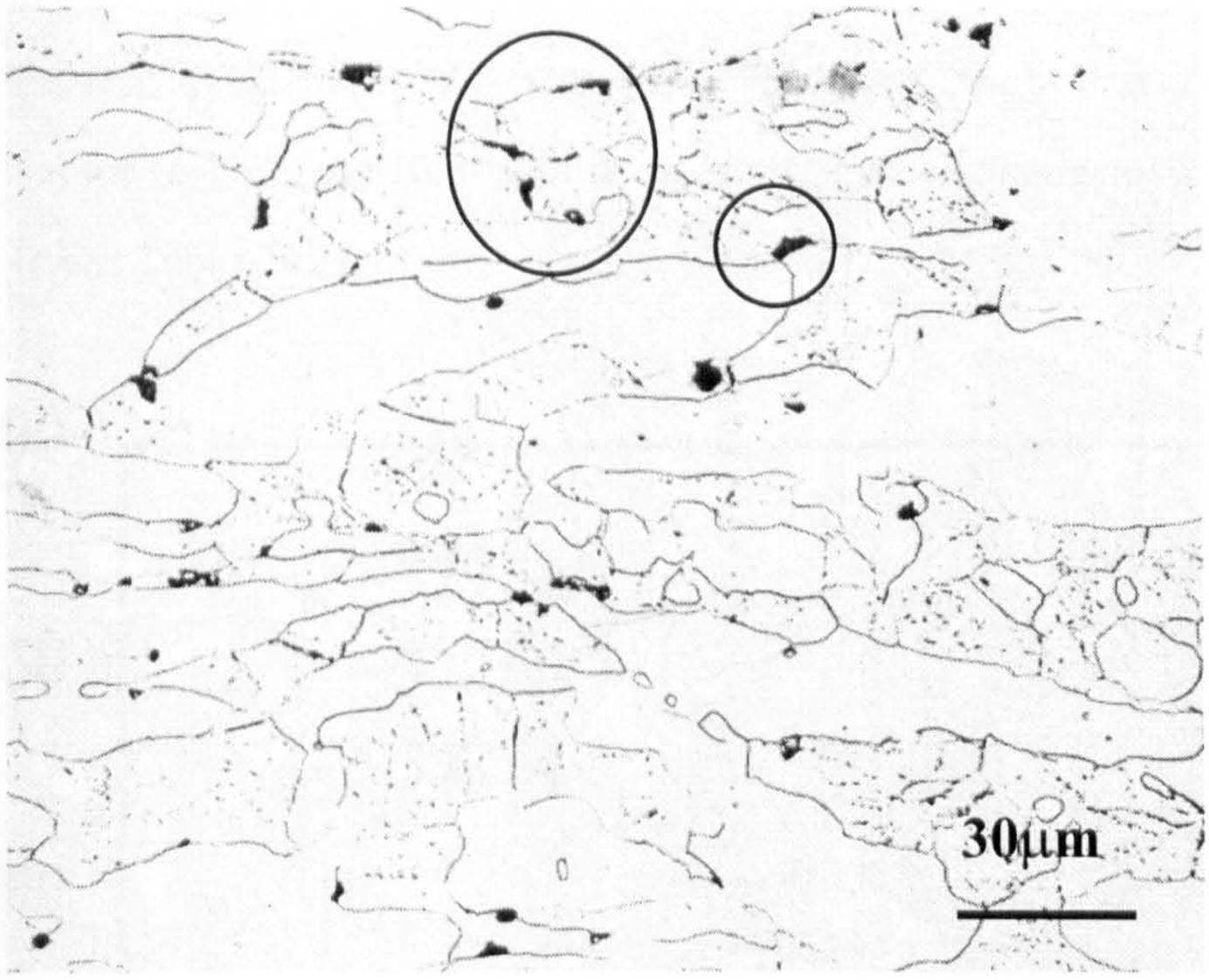


Fig.5-2 Greatest density of intermetallic phases detected in all thermal simulated samples. 1.6±0.8%I. Steel S32750/1, code 3R. NB The larger more spherical particles are REM inclusions. [x500, AH2518]

In order to establish whether finer precipitation was present, than could be detected using optical and SEM techniques, thin foils were prepared from selected samples and examined at magnifications up to x40k. However, no further evidence of intermetallic precipitation on the ferrite:austenite boundaries was found, although dislocations were present (Fig.5-3).

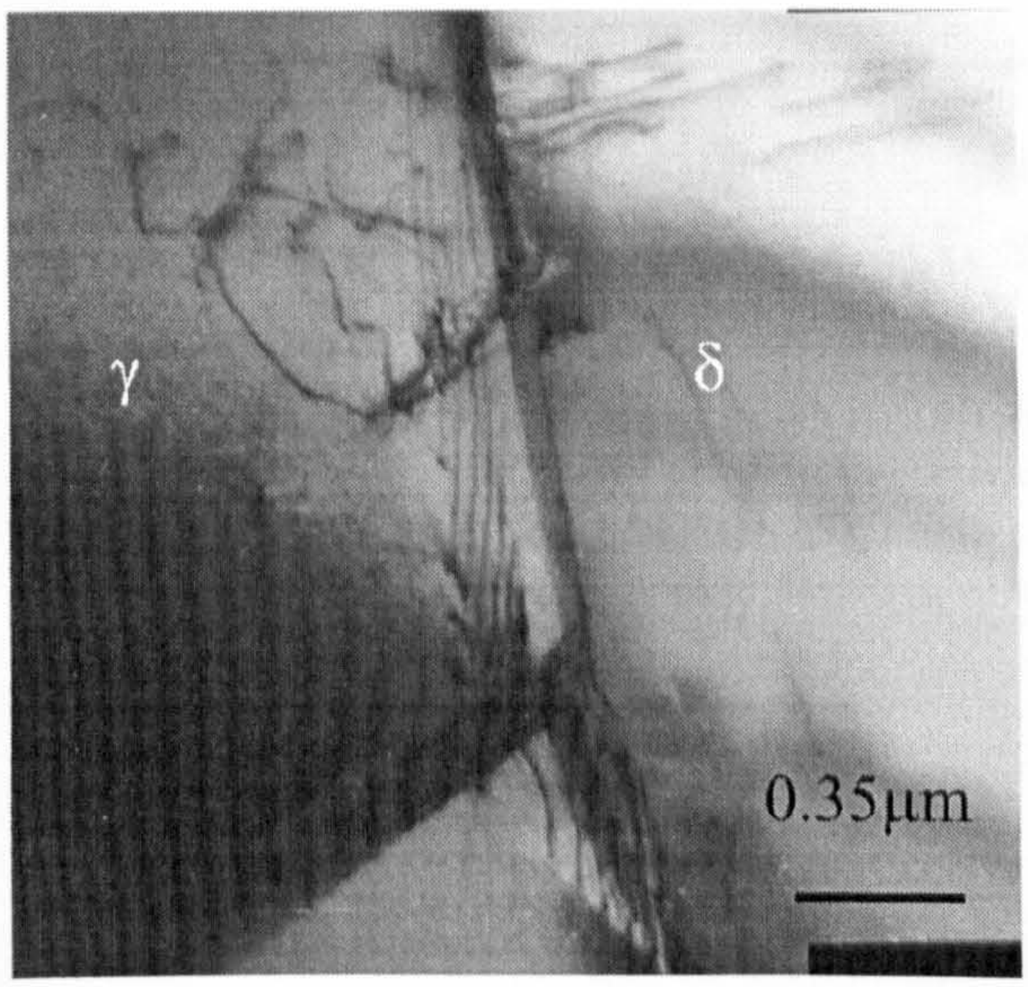


Fig.5-3 Bright field TEM micrograph of steel S32760/7 after thermal cycle 1T5. Note the presence of dislocations and absence of precipitates on the δ/γ phase boundaries [x40k, BA0003965]

5.1.2. Impact Tests

The results of the impact tests are presented in Fig.5-4. For the Set 1 specimens, plates S32750/1 and S32760/7 exhibited a drop in the absorbed energy compared to the as-received plates, when subjected to one or more thermal cycles. However, steel S39274 showed a small increase in absorbed energy after thermal simulation. Nevertheless, for thermal cycle Set 1 (Δt from 19 to 79 sec), there was a trend for lower toughness values to be associated with more prolonged exposure to temperatures above 600°C (Δt in Table 3- 7).

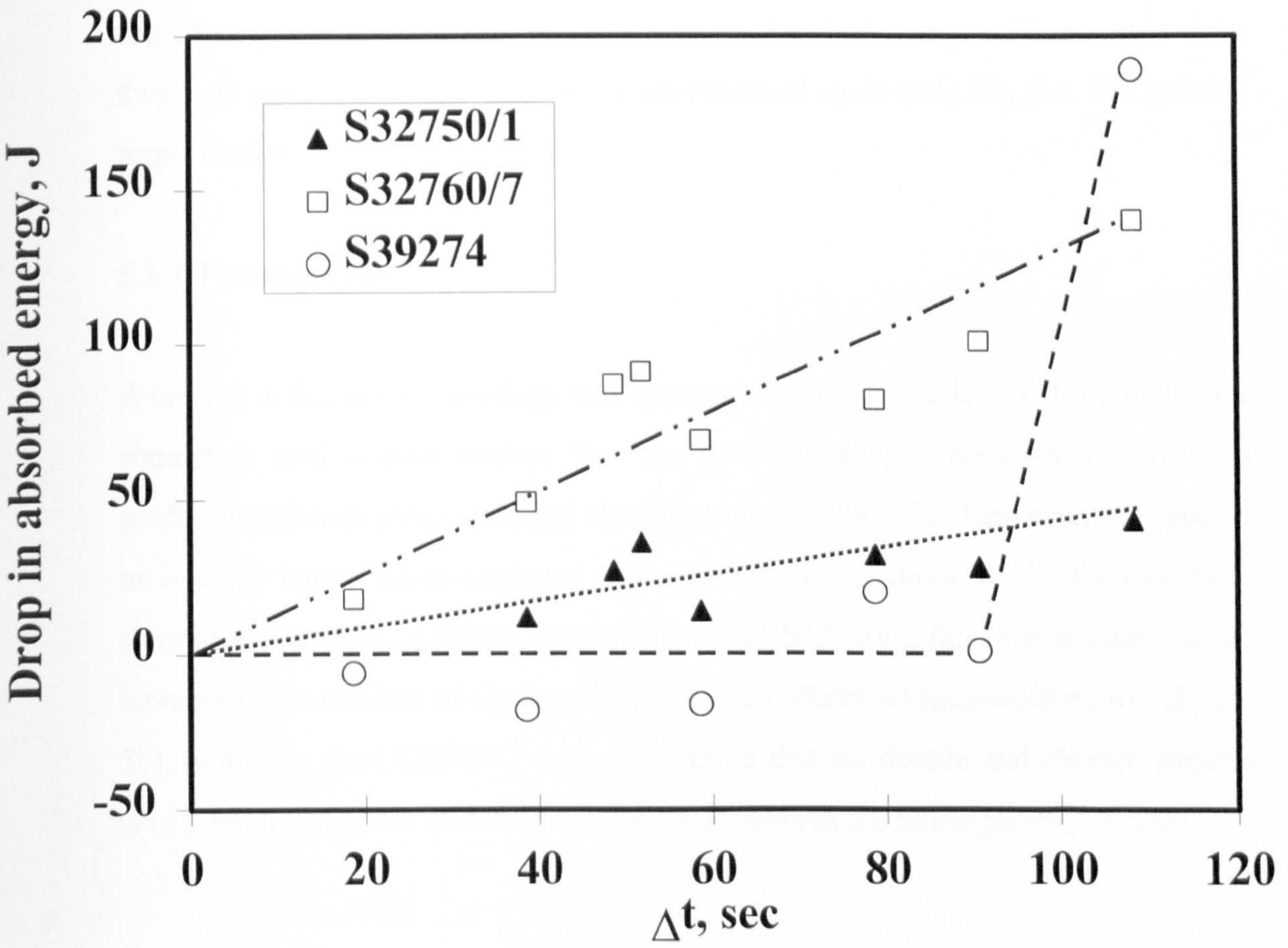


Fig.5-4 Effect of exposure time (Δt) on the absorbed energy at -40°C for different superduplex grades. As-received results (i.e. $\Delta t = 0$): S32750/1 = 119J, S32760/7 = 217J & S39274 = 257J.

Δt = time between 1050°C and 600°C.

Similar trends were apparent after thermal cycle Sets 2 and 3, although the absorbed energy values were lower than after Set 1. This is in keeping with the longer exposure times to elevated temperatures (Δt in Table 3-7).

The drop in toughness with Δt was more marked for steel S32760/7 than for steel S32750/1 (Fig.5-4). However, steel S32760/7 was also noted to produce high absorbed energy values in the as-received condition (217J) and so had more "potential" for a reduction in toughness. On the other hand, steel S32750/1 gave a relatively low absorbed energy in the as-received condition (119J), possibly reflected by the presence of REM inclusions in this steel (Fig.5-2). On balance, even though these two grades showed varying reductions in absorbed energy with exposure time, they both gave similar absolute values after thermal cycle code 3R, [i.e. 77J and 79J respectively].

5.1.3. Fractography

A change in fracture morphology was apparent for all steels after weld thermal cycle simulation and impact testing. For the as-received specimens, ductile features predominated with some voids and cleavage pockets (Fig.5-5a). However, as exposure to elevated temperatures increased and absorbed energy dropped, the fracture faces showed an increase in brittle features. For steel S32750/1, this was manifest as an increase in the number of cleavage pockets in an otherwise microvoid matrix (Fig.5-5b), while for steel S32760/7 there were more distinct ductile and cleaved regions (Fig.5-6a). In addition, steel S32760/7 showed splits in the ferrite phase (Fig.5-6b).

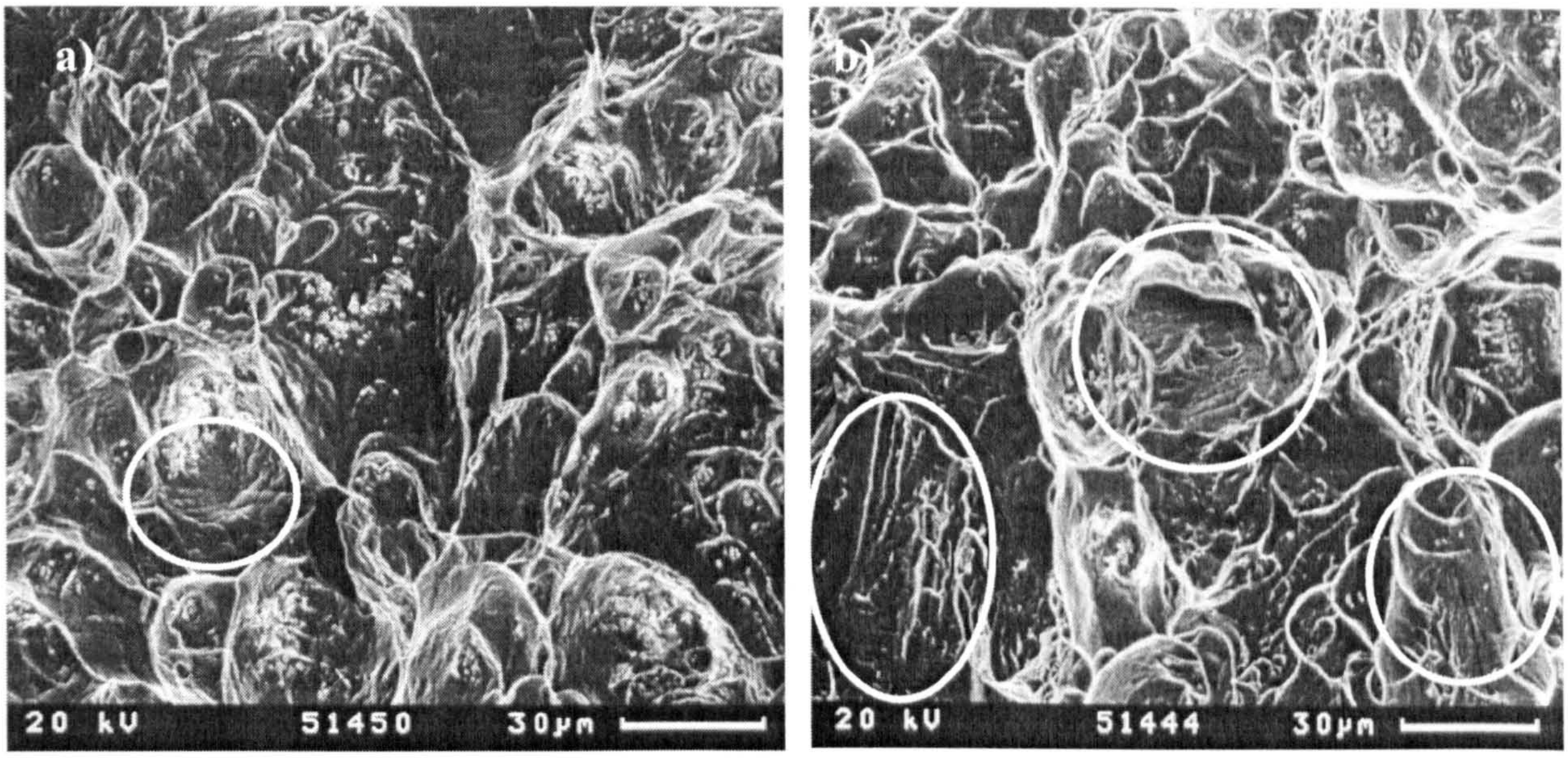


Fig.5-5 Fracture faces of steel S32750/1 with cleavage facets circled [x500]
a) in 'as-received' condition. 119J
b) after thermal cycle 3R. 77J.

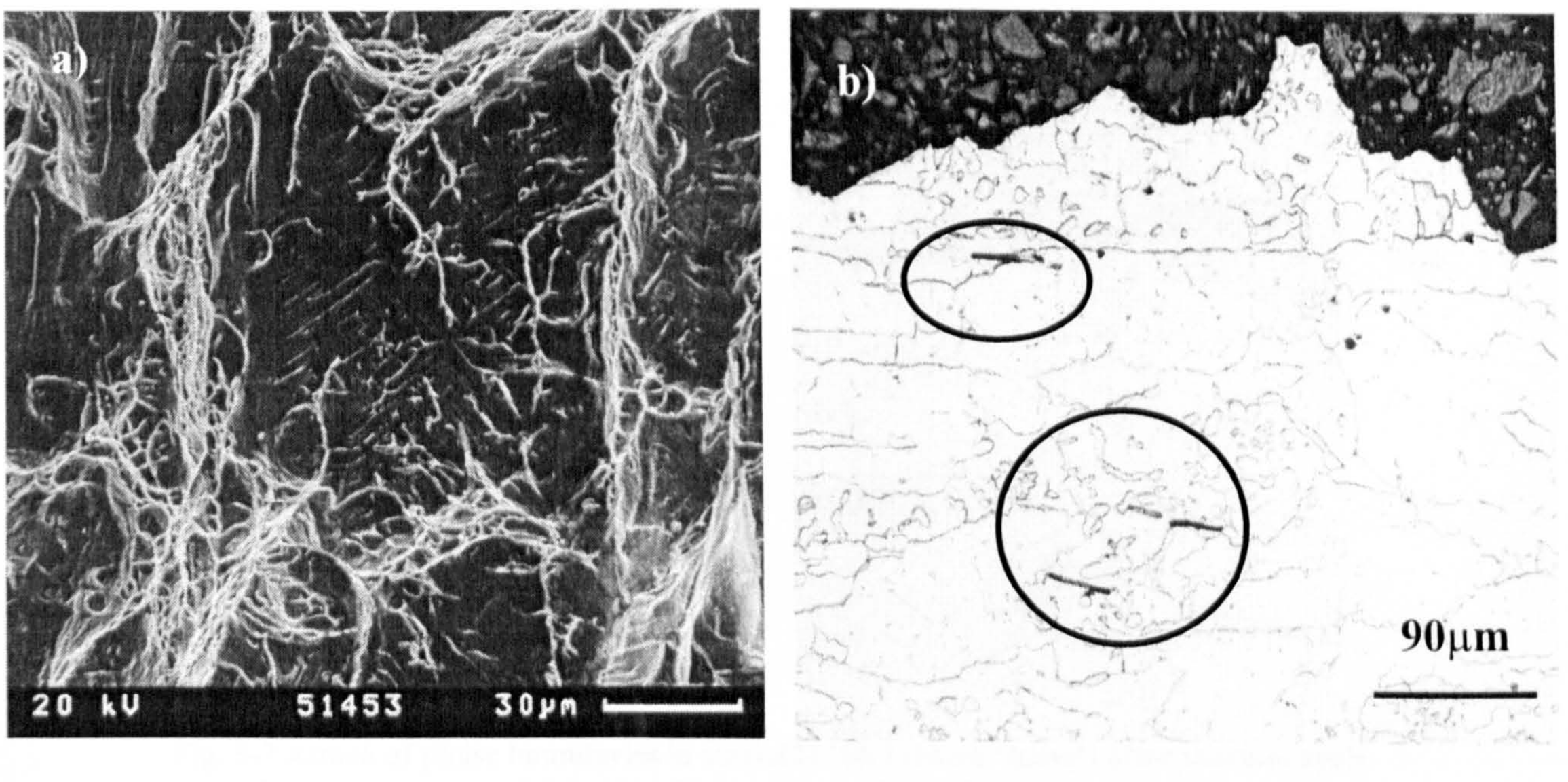


Fig.5-6 Steel S32760/7 after thermal cycle 3R.
a) Predominantly cleavage region. [x500]
b) Subsidiary cracks beneath fracture surface. [x200, AH2022]

5.1.4. Pitting Tests

For steel S32750/1, the as-received specimens and those subject to thermal cycle code 3R reached 72°C without any signs of pitting or significant weight loss (<1mg). Notwithstanding this, small isolated intermetallic phases (about 2μm across) were identified in the simulated sample (Fig.5-2). In contrast, the as-received S32760/7 material pitted after exposure to 72°C (1mg weight loss) and the specimen that had been subject to thermal cycle code 3R, developed a pit after exposure to 53°C (4.4mg). Preferential attack occurred along the phase boundaries, where a network of intermetallic phases was present (Fig.5-7).

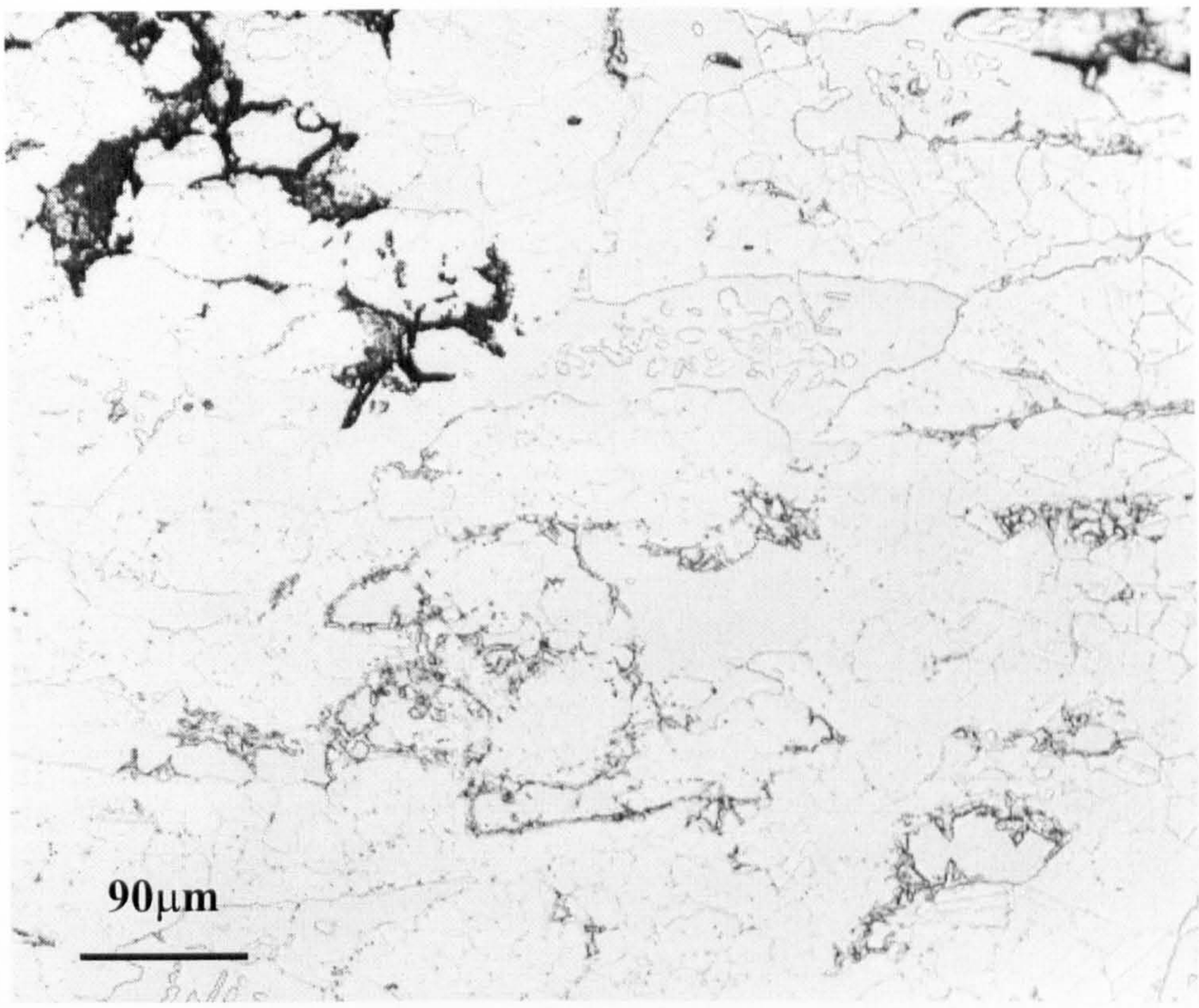


Fig. 5-7 Attack of phase boundaries in steel S32760/7 (black 'holes') after thermal cycle code 3R and exposure to ferric chloride solution at 53°C. Note the network of intermetallic phases that remain unattacked in the bottom half of the micrograph [x200, AH1994]

5.2. HEAT TREATMENT TRIALS (STUDY VI)

5.2.1 Laboratory Heat Treatments

For pipe S32760/3 examined in the laboratory, a significant level of intermetallic phases were present in the HAZ after welding (Fig.5-8a), whilst none were detectable in similar pipe HAZs which had been given a prior solution annealed (Fig.5-8b). Further, no intermetallic phases were found in the HAZ of the as-received solid extrusion pipe S32760/4.

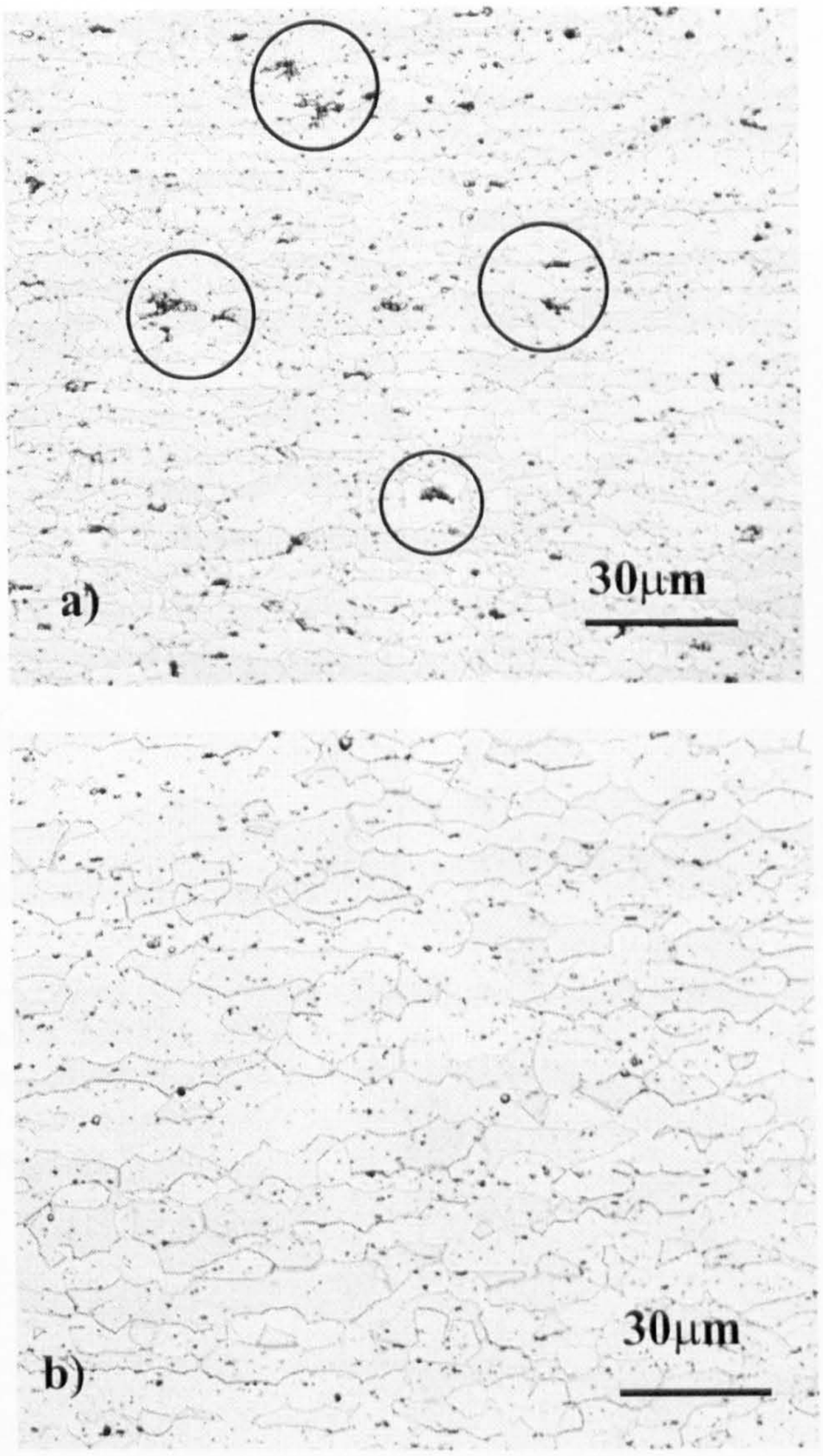


Fig.5-8 HAZs of pipe S32760/3 [x500]
a) pipe in as-received condition prior to welding. [Weld VI-1, AJ688]
b) pipe re-solution annealed prior to welding. [Weld VI-2, AJ689]
Note that intermetallic phases show as black particles against the background of ferrite, austenite and fine non-metallic inclusions (a feature of powder metallurgy pipe).

5.2.2 Production Heat Treatments

No intermetallic phases could be seen using optical techniques in the as-received pipes S32760/5 (as-manufactured) and S32760/6 (reheat treated) at x500 magnification. However, closer examination using SEM techniques revealed that both pipes contained small precipitates (about 0.5μm in diameter) in both parent material and HAZ (Figs.5-9). In addition, the as-manufactured pipe (S32760/5) also contained a few larger HAZ precipitates (about 2x5μm with a peak volume fraction of about 0.1%), Fig.5-9a, which were analysed by EDX and found to have a composition consistent with sigma phase, i.e. Cr, Mo-rich and Ni-lean (Pipe S32760/5 in Table 5-1). Overall, there was a tendency for more HAZ precipitation at the 12 o'clock welding position rather than the 6 o'clock.

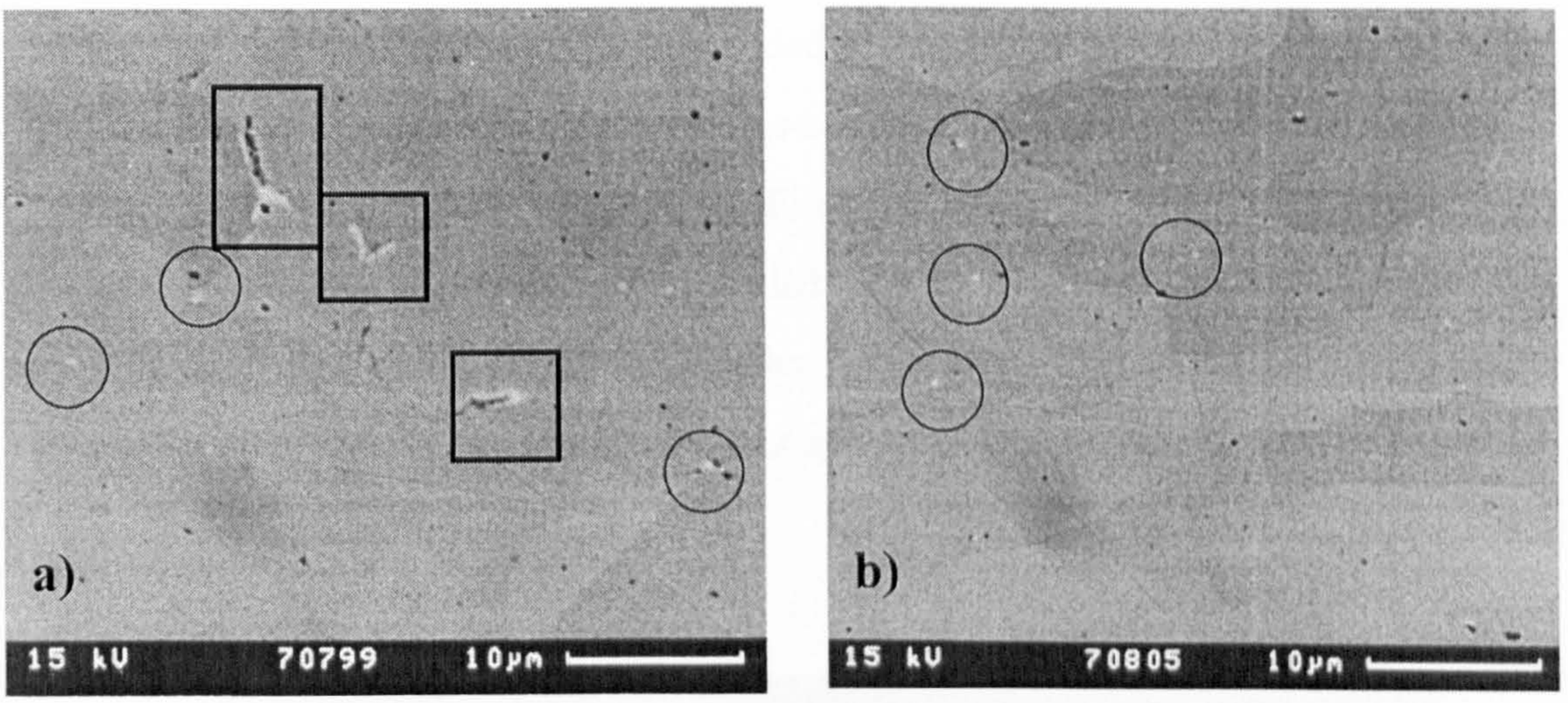


Fig.5-9 SEM back scattered micrographs of HAZs in thin walled pipes. [x2000]
a) As-received pipe S32760/5 (weld VI-4, 12 o'clock)
b) Re-solution annealed pipe S32760/6 (weld VI-5, 6 o'clock)
Note the small grey circled precipitates in both figures and the larger boxed 'sigma' phase (grey) particles in Fig.5-9a.

Table 5-1 Results of semi-quantitative SEM/EDX analysis

Phase	Element, wt% (EDX analysis)				
analysed	Cr	Ni	Mo	Si	Mn
Pipe S32760/5					
Bulk	25.3	7.7	3.1	0.5	0.5
Precipitate	28.8	5.0	5.5	0.8	0.7
Ferrite	27.0	5.3	4.0	0.7	0.7
Austenite	24.4	8.4	2.5	0.6	0.9
K	1.11	0.63	1.60	1.17	0.78
Pipe S32760/6					
Bulk	25.0	7.9	2.9	0.7	0.5
Ferrite	27.2	6.0	3.4	0.7	0.4
Austenite	22.8	9.9	2.2	0.6	0.5
K	1.19	0.61	1.55	1.17	0.80

$$\text{K, partition coefficient} = \frac{composition\ of\ ferrite}{composition\ of\ austenite}$$

Results are an average of four readings

Both weld samples VI-4 and VI-5 recorded a weight loss of less than 10mg after exposure at 50°C, while at 52.5°C the as-manufactured pipe weld VI-4 exhibited extensive attack in the root weld metal, Fig.5-10, i.e. a CPT of 52.5°C. Even after exposure to 52.5°C, the re-solution annealed pipe weld VI-5 showed no weight loss or evidence of pit initiation. These results demonstrate that the small precipitates present in both pipes (Figs.5-9a&b) do not appear to have a significant effect on the CPT.

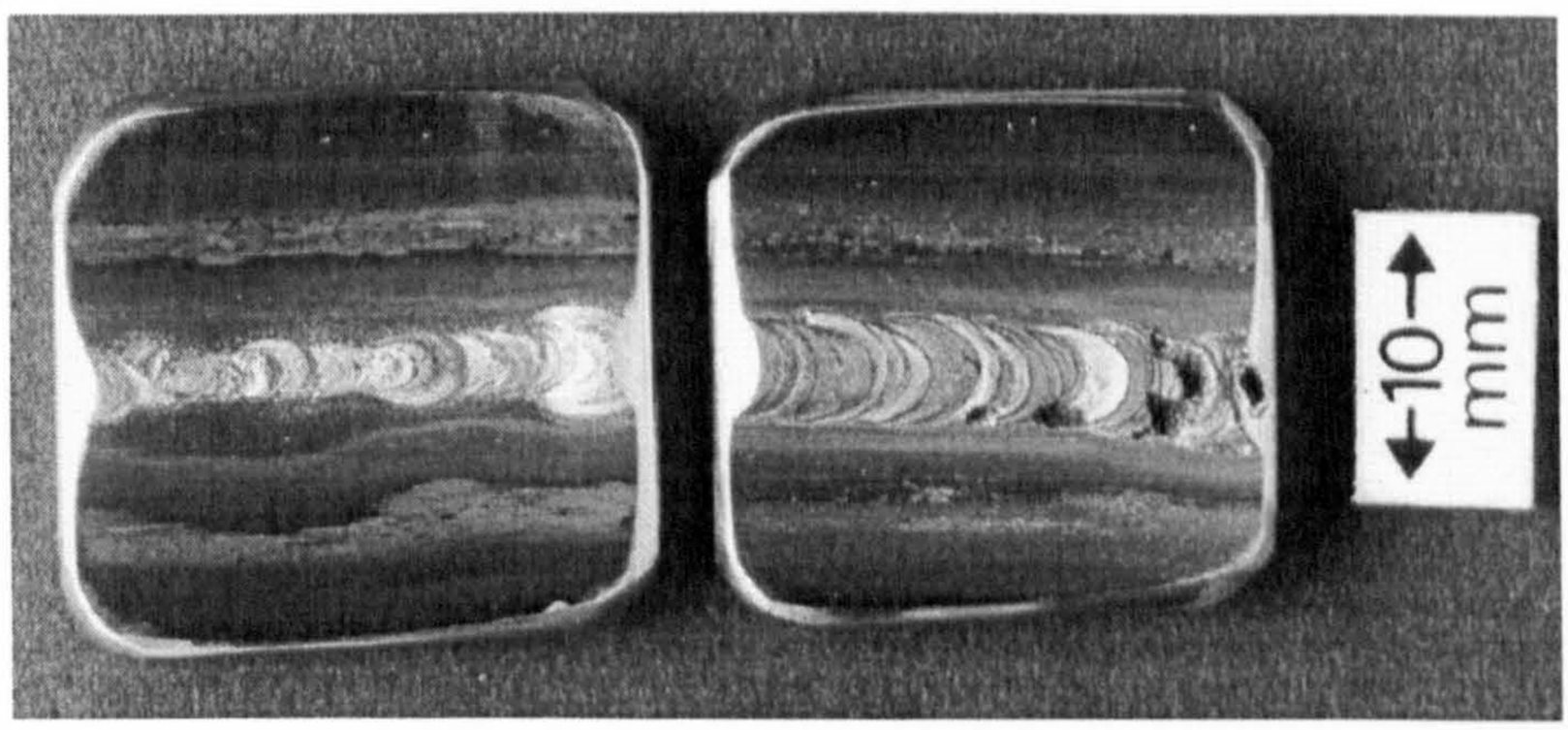


Fig.5-10 Appearance of weldment roots after exposure to ferric chloride solution at 52.3°C (66381).
LHS: Re-heat treated pipe S32760/6 (Weld VI-5). No attack or weight loss.
RHS: As-manufactured pipe S32760/5 (Weld VI-4). Weld metal attack.

5.3. FRACTURE BEHAVIOUR (STUDY VII)

5.3.1. Metallography

A few isolated precipitates were observed in the as-received pipe (Fig.5-11a), which were analysed by EDX to be enriched in Cr and Mo, and thus intermetallic phases (Table 5-2). The volume fraction of such phases was estimated to be below 0.01%.

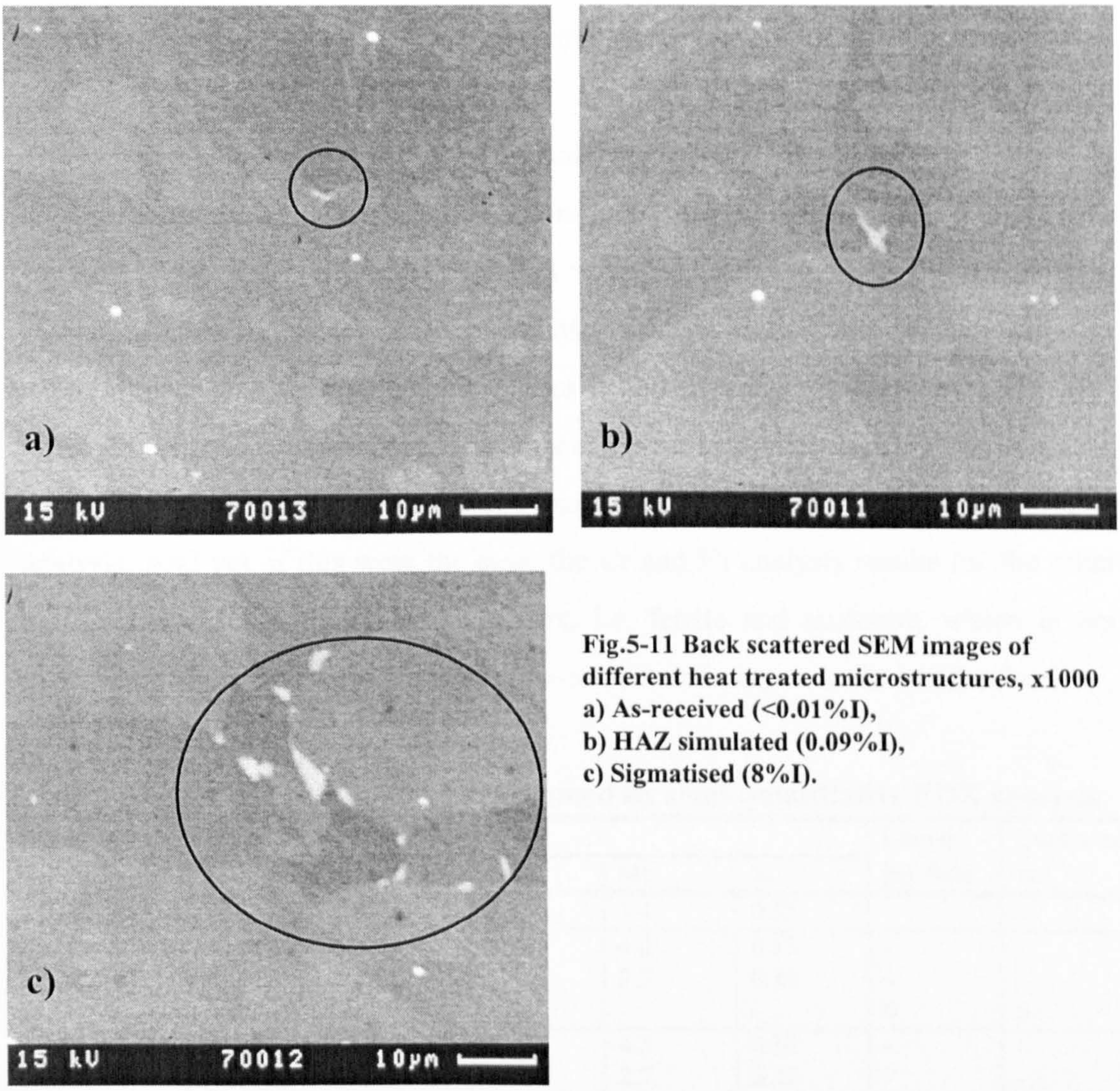


Fig.5-11 Back scattered SEM images of different heat treated microstructures, x1000
a) As-received (<0.01%I),
b) HAZ simulated (0.09%I),
c) Sigmatised (8%I).

Following re-solution annealing, no intermetallic phases were found. However, after the thermal simulation, a small increase in such phases was observed (Fig.5-11b), i.e. 0.09% intermetallic phase, as compared to the as-received microstructure (<0.01%I). The 'sigmatised' heat treatment (refer to Section 3.10) produced the highest intermetallic contents, i.e. 8.1%I ± 0.7% as measured by optical point counting or about 5% estimated from the SEM examination, Fig.5-11c. The somewhat lower value obtained by the SEM examination is a reflection of the different methods. Nevertheless, as the optical point count technique is more typical of that used in practice, the value of 8%I will be used forthwith.

The compositions (wt%) of the intermetallic precipitates are shown in Table 5-2, together with the associated ferrite and austenite matrix. In each case, the ferrite is Cr- and Mo-rich and Ni-lean compared with the austenite, with the precipitates containing even higher levels of Cr and Mo and less Ni than the ferrite. Further, it would appear that the intermetallic phases in the sigmatised sample are more Mo-rich than the precipitates analysed in other samples. This observation may reflect the larger particle size of the sigmatised particles allowing for more reliable EDX analysis. And yet, if this were the case, the Cr and Ni analysis results for the other particles would be similar to the matrix, i.e. ferrite and austenite, which is not demonstrated. Thus, the difference in Mo-content does appear to be a real effect.

Table 5-2 Composition of phases determined by semi-quantitative EDX analysis.

Sample type	Phase analysed	Element, wt%				Counts per field	Estimated vol. %I
		Cr	Ni	Mo	Si		
Pipe	Bulk	24.4	7.2	3.4	0.35	-	-
Solution annealed	Ferrite	25.4	6.1	4.0	0.35	-	-
	Austenite	23.1	8.7	2.7	0.34	-	-
	Precipitate	-	-	-	-	0	0
As-received	Ferrite	26.2	5.2	4.3	0.38	-	-
	Austenite	22.9	8.9	2.7	0.32	-	-
	Precipitate	28.2	4.6	6.5	0.40	0.2	0.007
HAZ simulation	Ferrite	26.4	5.4	4.3	0.34	-	-
	Austenite	23.2	8.5	2.7	0.36	-	-
	Precipitate	28.5	5.1	6.9	0.40	0.9	0.9
Sigmatised	Ferrite	25.9	5.3	4.2	0.30	-	-
	Austenite	23.1	8.9	2.7	0.33	-	-
	Precipitate	29.0	4.6	9.0	0.50	24.9	(5)*

Results for ferrite, austenite and bulk are an average of at least 4 readings.

- = not applicable

* = A more precise value of 8.1 ± 0.7% was obtained by optical point counting

5.3.2. Charpy and CTOD Toughness

The results of the Charpy tests are presented in Fig.5-12a. The solution annealed specimens exhibited an upper shelf energy of about 220J above -20°C and gave an impact energy value in excess of 80J at -80°C. On the other hand, the as-received and HAZ simulated samples did not reach upper shelf behaviour at the highest temperature tested, i.e. 0°C, while the absorbed energy dropped to about 20J at -90°C. The HAZ simulated samples gave consistently lower absorbed energies than the as-received material (by about 20J). The sigmatised specimens gave values of 30J or less for temperatures up to 0°C.

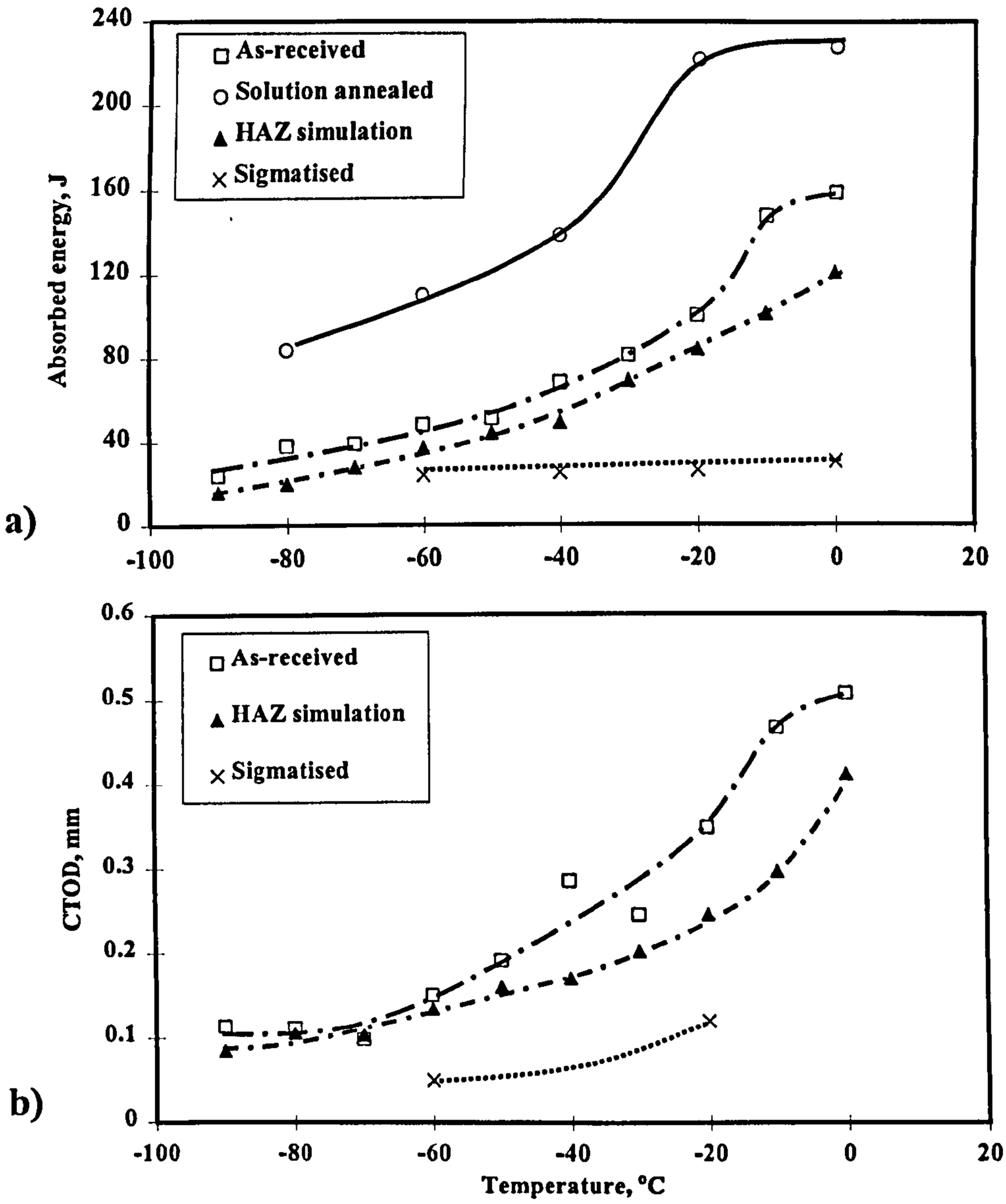


Fig.5-12 Transition curves for different heat treatments.
a) Charpy energy, and b) CTOD fracture toughness.

The CTOD values are presented in Fig.5-12b. The CTOD transition curves are very similar to the Charpy results (Fig.5-12a) with neither the HAZ simulated or 'sigmatised' samples clearly reaching the upper shelf level within the temperature range studied. Again, there is a small but consistent shift between these two data sets, with the simulated samples recording CTOD values up to 0.1mm lower than the as-received specimens. This difference diminishes below approximately -60°C, and at CTOD values below 0.15mm. The sigmatised samples gave relatively low CTOD values with 0.12mm achieved at -20°C.

All CTOD samples reached maximum load during the test (δ_m-type results), even though CTOD values as low as 0.052mm were obtained. A comparison of the load versus crack mouth opening plots of as-received, sigmatised and HAZ simulated specimens at -20° and -60°C is shown in Fig.5-13. It can be seen that both the load bearing capacity of the nominally identical specimens and the peaky/serrated nature of the maximum load plateau increases with higher intermetallic contents. These features imply that intermetallic particles initiate multiple crack events which subsequently arrest, lowering the overall tearing resistance. However, none of the cracks appear to lead to significant cleavage events.

5.3.3 Fracture Face and Crack Propagation Path Examination

The fracture faces of two Charpy/CTOD pairs were examined i.e. i) as-received and tested at -90°C and ii) 'sigmatised' and tested at -60°C. The aim was to compare samples which exhibited fairly low toughness with and without sigma phase. Both of these sample types gave 24J at their respective test temperatures. For one specimen half, this involved removal of a metallographic section perpendicular to the notch, while the fracture face of the other half was viewed in an SEM.

Charpy specimens

For both Charpy specimens, the fracture path tended to pass through the ferrite and around the austenite, where possible, Fig.5-14. Further, subsidiary cracking in the ferrite was noted.

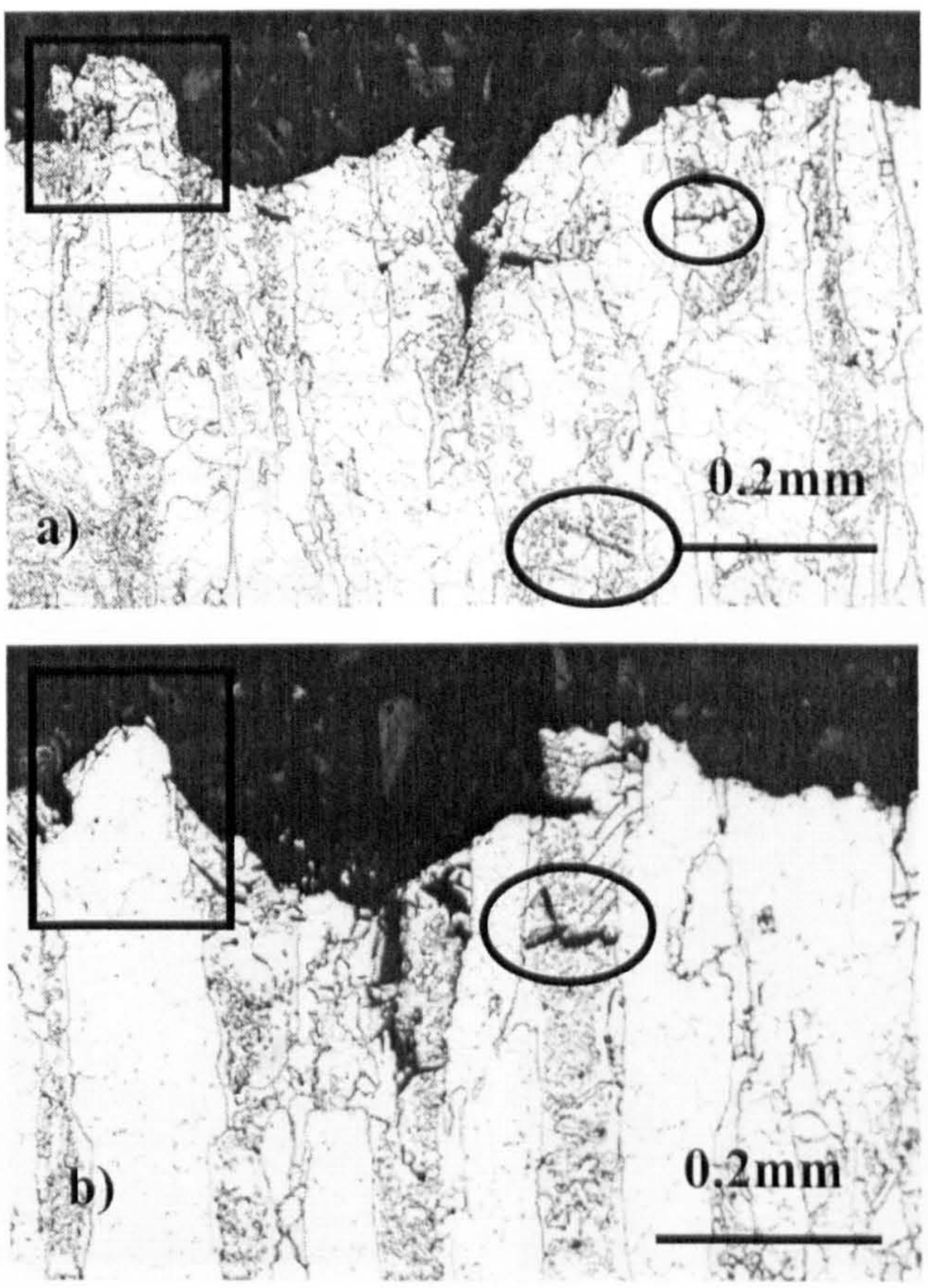


Fig.5-14 Optical micrographs illustrating the fracture path beneath the notch:
a) As-received specimen tested at -90°C, 24J [x100, AK688]
b) Sigmatised specimen tested at -60°C, 24J [x100, AK687]
Note: Boxed areas illustrate where the crack path deviates around austenite. Circled areas show subsidiary cracking in the ferrite.

On the fracture face of the as-received Charpy specimen (24J), there was a 100μm wide ductile region just below the notch, which consisted of microvoid coalescence (Fig.5-15a), while the majority of the fracture face showed mainly cleavage features (Fig.5-15b), presumably within the ferrite phase as in Fig.5-14a.

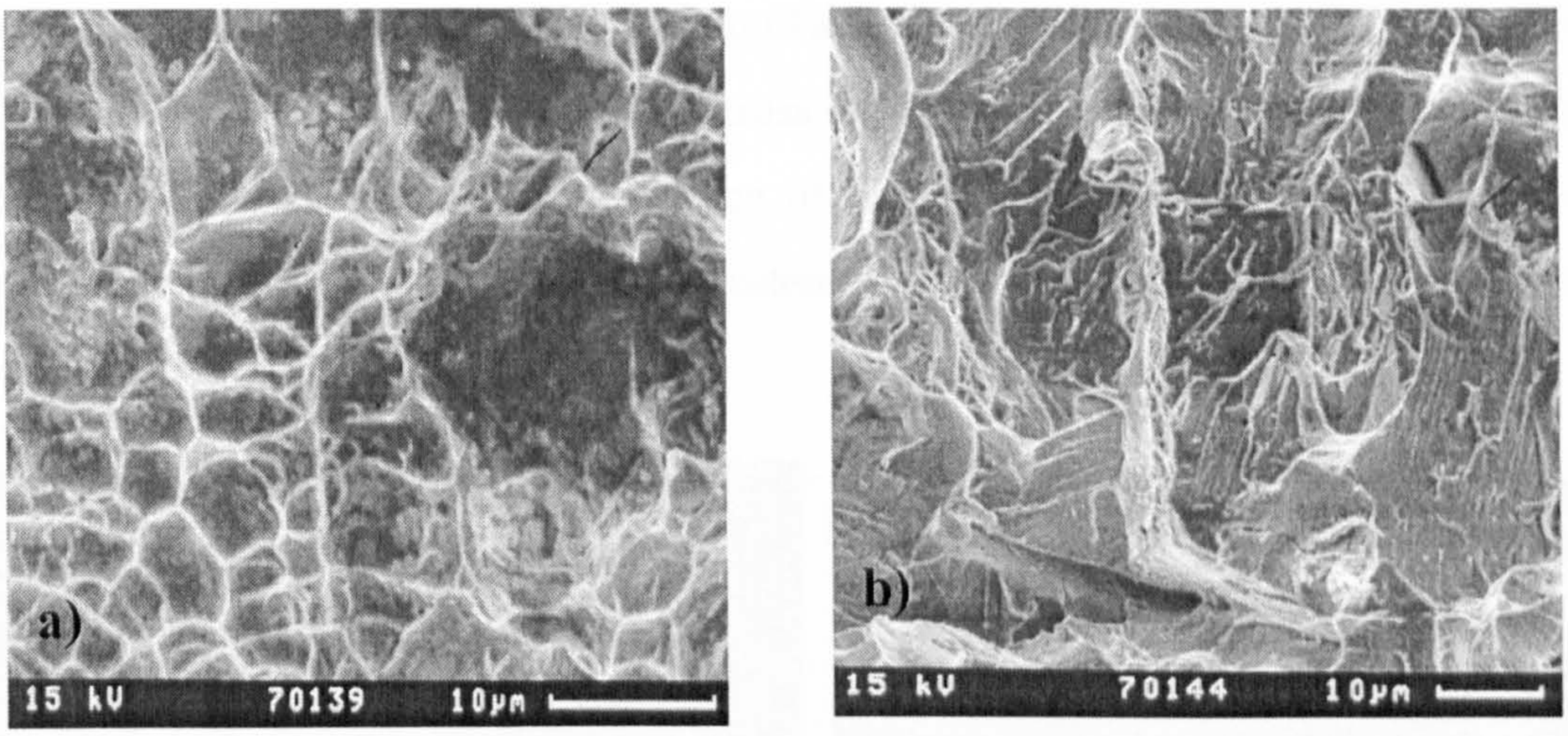


Fig.5-15 Charpy fracture face on as-received sample tested at -90°C (24J).
a) Ductile features just below notch. [x2000]
b) Typical region of fracture face with predominant cleavage. [x1000]

The sigmatised Charpy sample tested at -60°C (24J) also contained a ductile band beneath the notch (200μm wide) (Fig.5-16a), with predominant cleavage on the rest of the fracture face (Fig.5-16b).

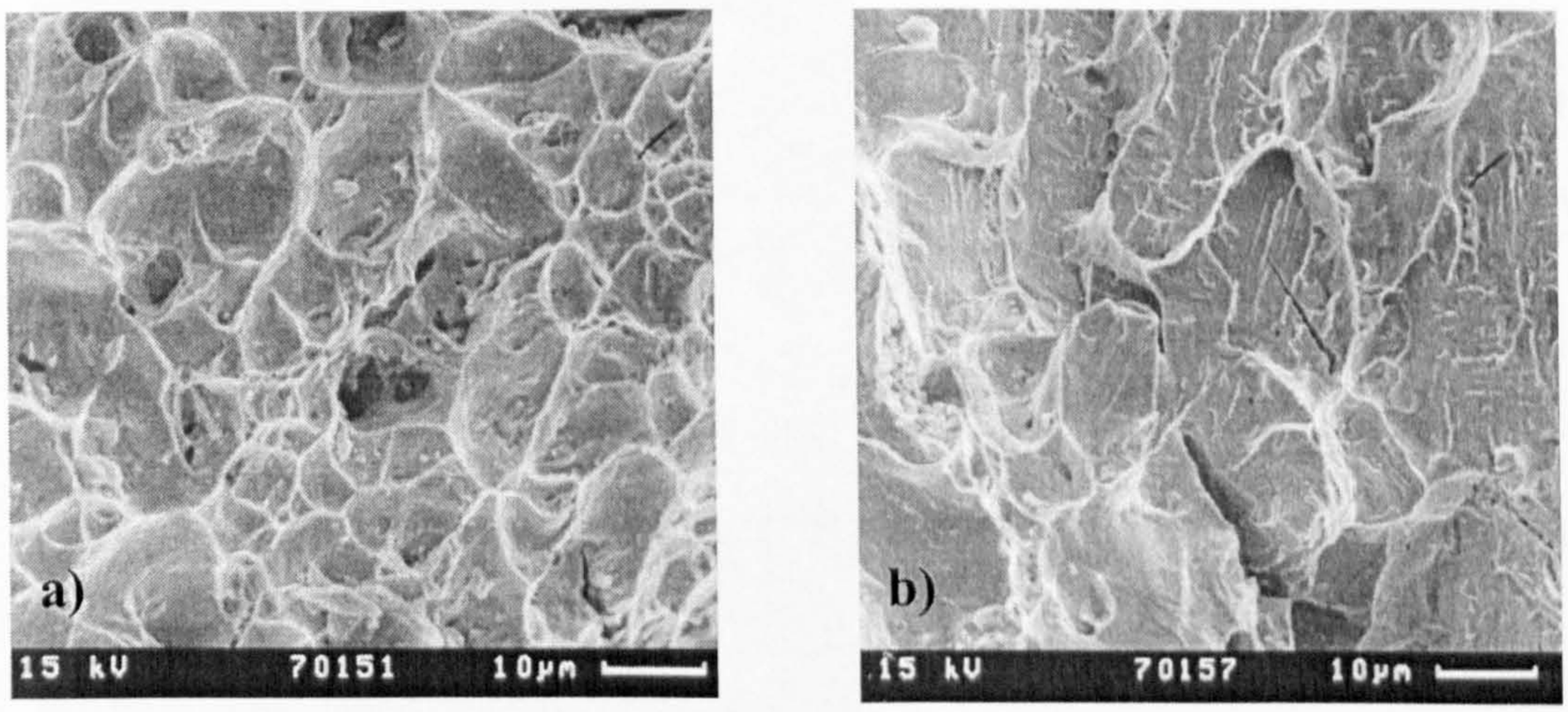


Fig-5-16 Charpy fracture face on sigmatised sample tested at -60°C (24J). [x1000].
a) Ductile features just below notch.
b) Typical region of fracture face with predominant cleavage.

CTOD specimens

The as-received CTOD sample tested at -90°C (0.11mm) appeared ductile at the notch tip (Fig.5-17a), although the majority of the fracture face showed cleavage features (Fig.5-17b). The cleaved areas varied from 10-50μm across, which is less tha the lamellar spacing of about 120μm (Table 3-3 and Fig.5-14). This implies that cleavage did not pass completely across a ferrite grain, but was arrested by intragranular austenite. Further evidence of this behaviour is shown in Fig.5-17c, where ductile tearing of intragranular austenite has occurred within a cleaved ferrite grain.

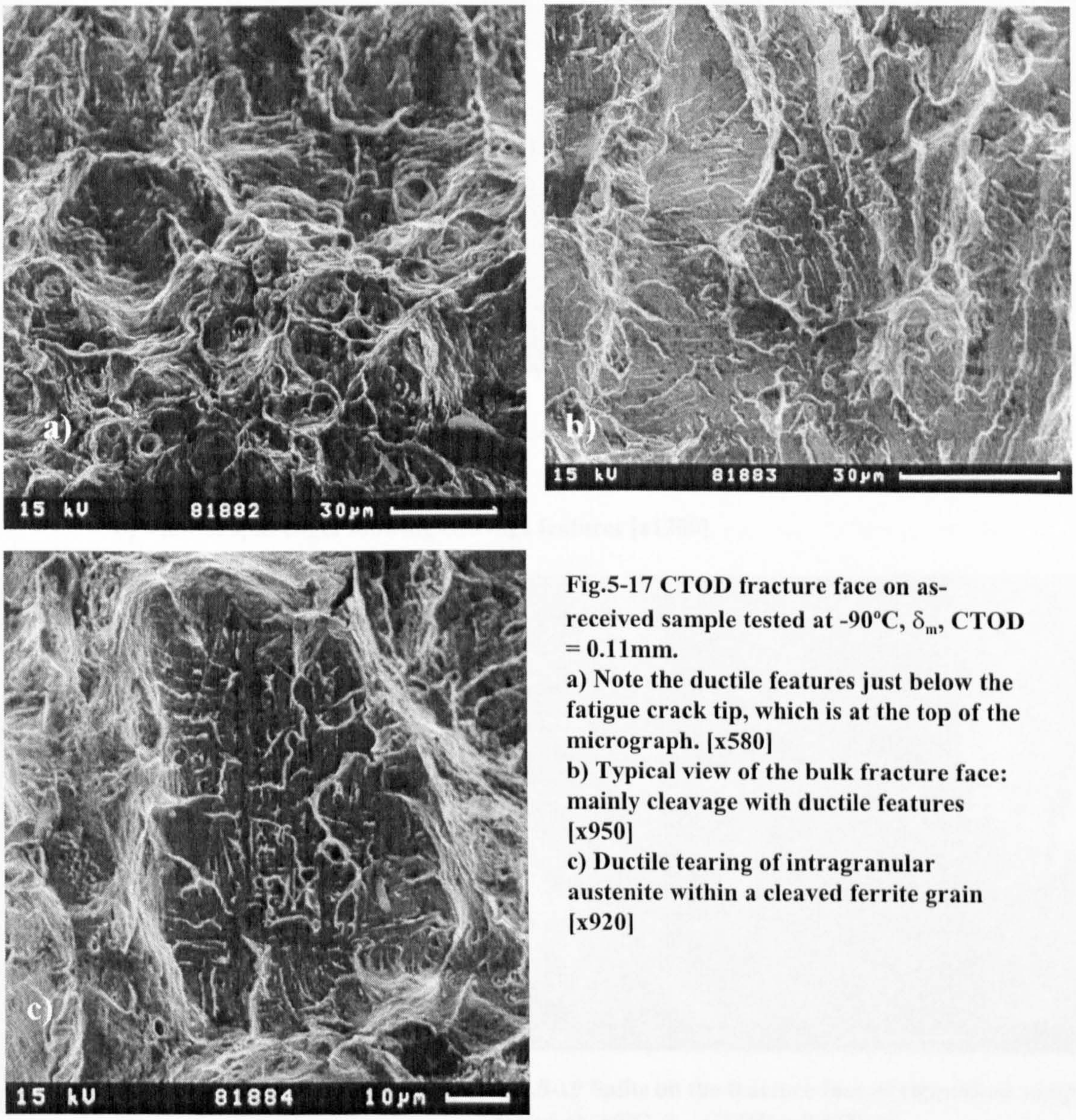


Fig.5-17 CTOD fracture face on as-received sample tested at -90°C, δ_m, CTOD = 0.11mm.
a) Note the ductile features just below the fatigue crack tip, which is at the top of the micrograph. [x580]
b) Typical view of the bulk fracture face: mainly cleavage with ductile features [x950]
c) Ductile tearing of intragranular austenite within a cleaved ferrite grain [x920]

Large splits were present across the whole of the 'as-received' specimen fracture face, running perpendicular to the crack path (Fig.5-18a), and so passing along the ferrite grains. Examination of the fracture face within a split revealed cleaved edges (Fig.5-18b). Similar features were present on the 'sigmatised' sample, although less pronounced (Fig.5-19). These observations are in keeping with the literature [Rob91] [Era92].

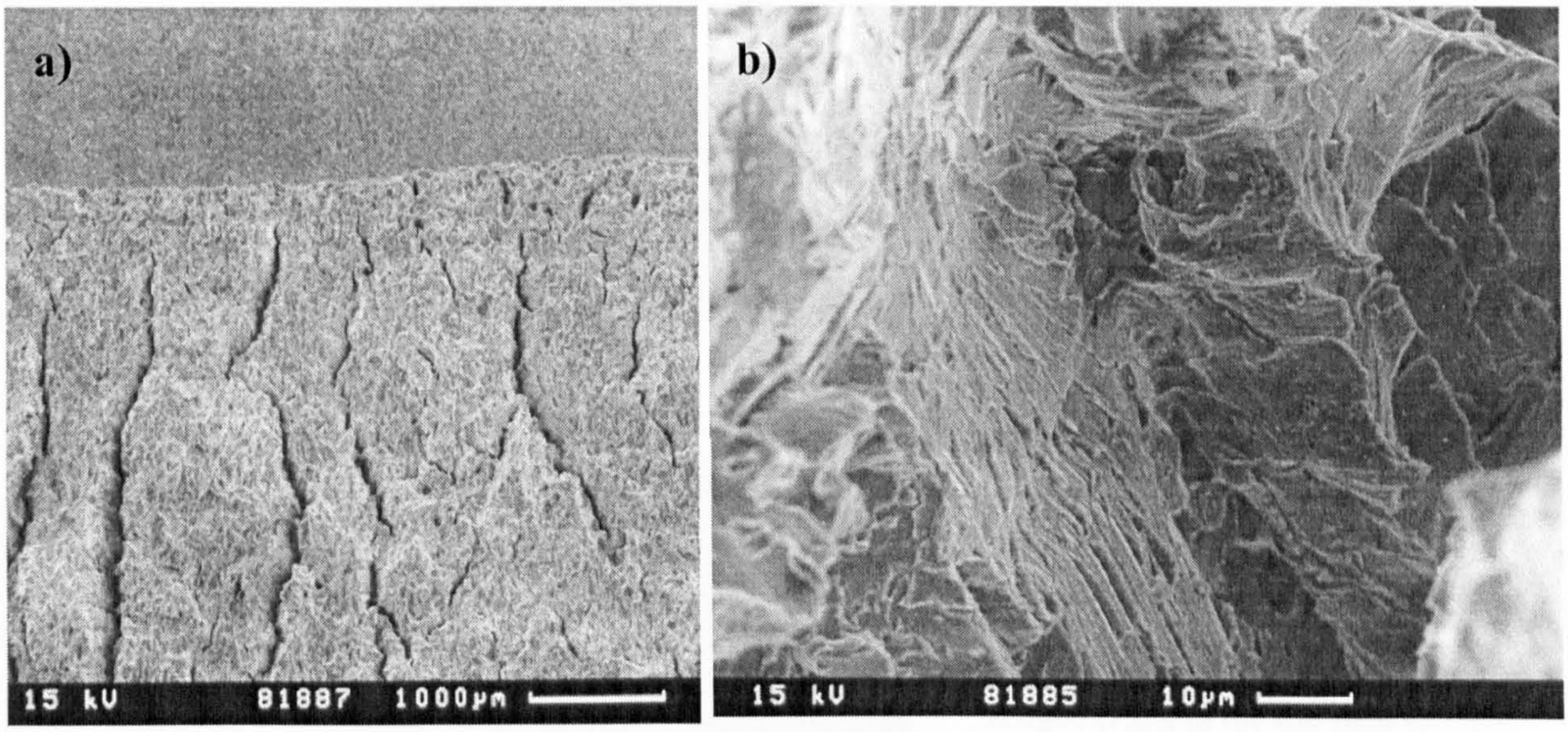


Fig.5-18 Splits on the CTOD fracture face of as-received sample tested at -90°C, δ_m, CTOD = 0.11mm.
a) General view [x16]
b) View of split edges showing cleavage features [x1200]

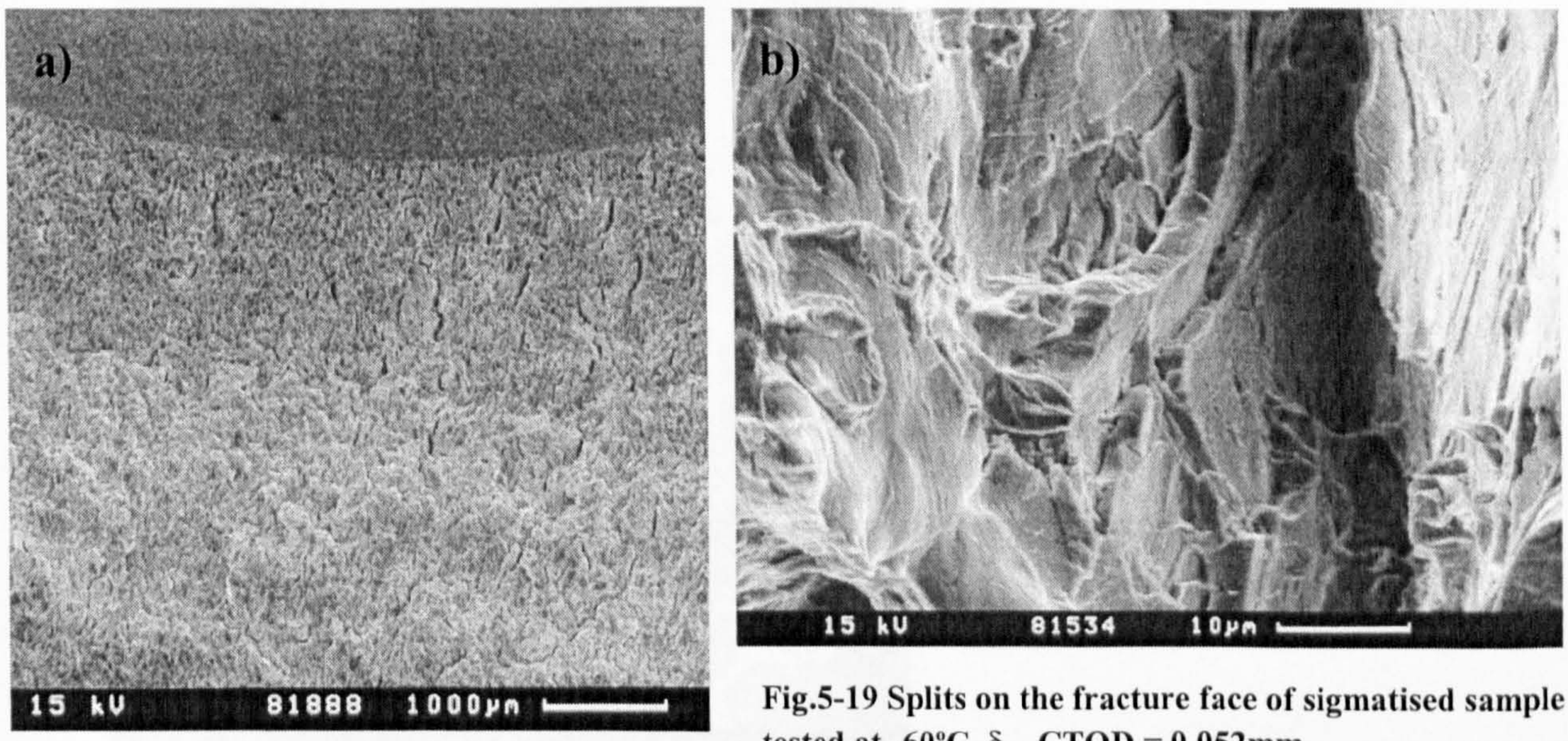
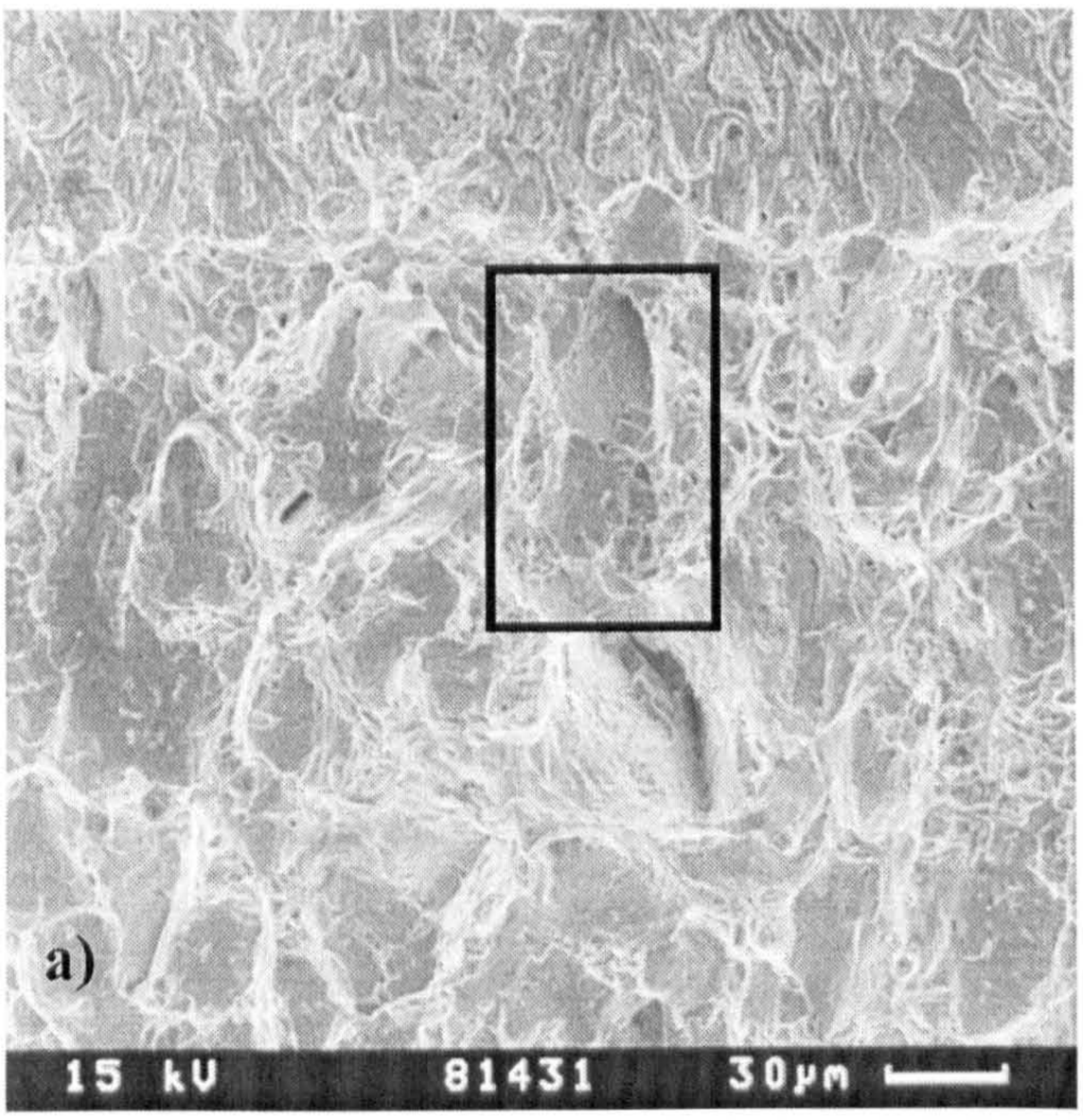


Fig.5-19 Splits on the fracture face of sigmatised sample tested at -60°C, δ_m, CTOD = 0.052mm.
a) Overall view [x16]
b) View of split edges showing cleavage features [x1810]

In the low temperature sigmatised CTOD sample (0.052mm), cleavage initiated from the fatigue crack tip (Fig.5-20a) with evidence that this was encouraged by the presence of particles (Fig.5-20b). In some cases the particles were absent leaving a void and in other cases had fractured (Fig.5-20c). Nevertheless, some particles were still present and could be analysed qualitatively by EDX (Fig.5-20d). The particles were enriched in Mo and depleted in Ni, compared to the ferrite, which is in keeping with the composition of sigma phase (see Table 5-2).



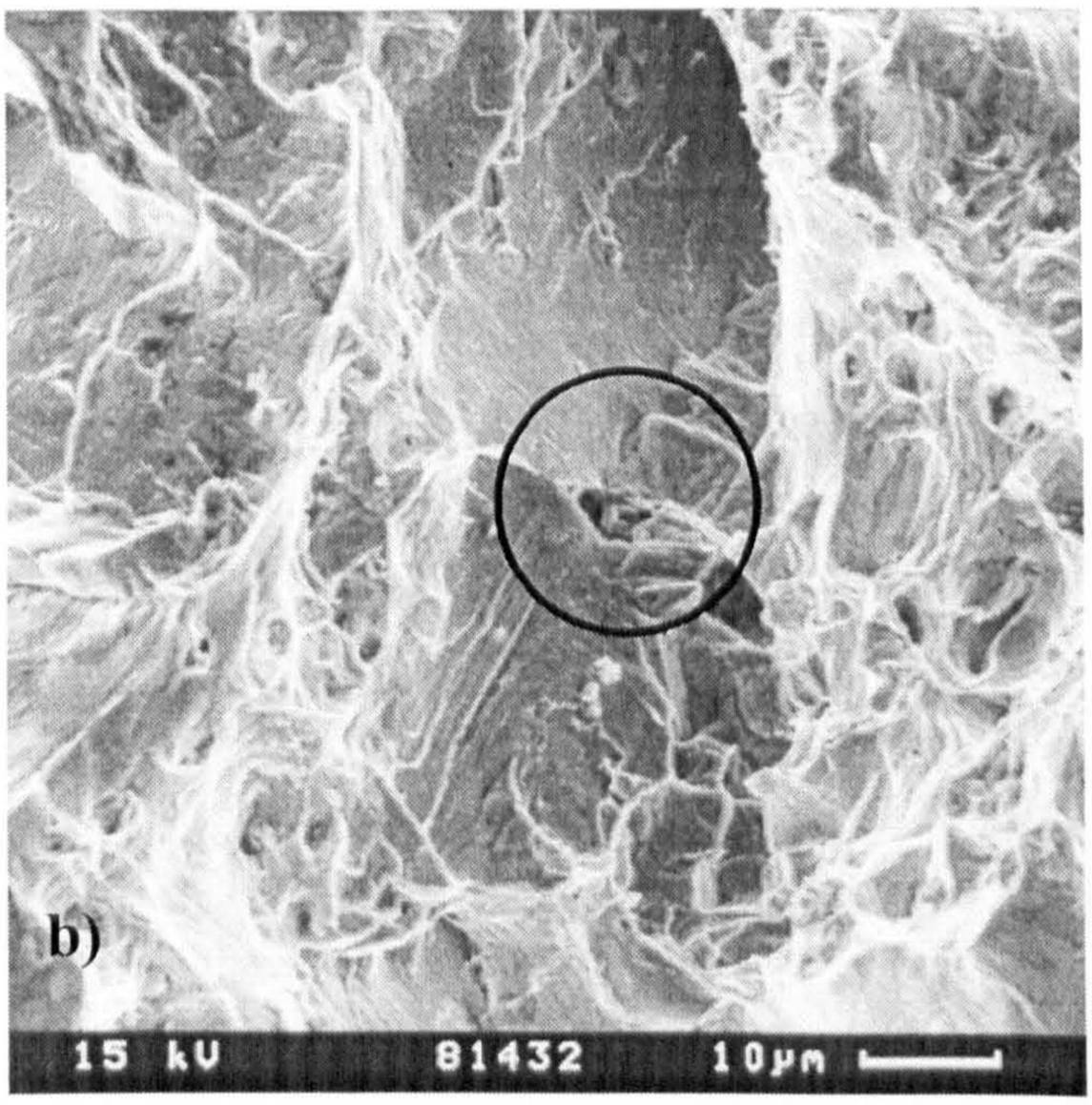
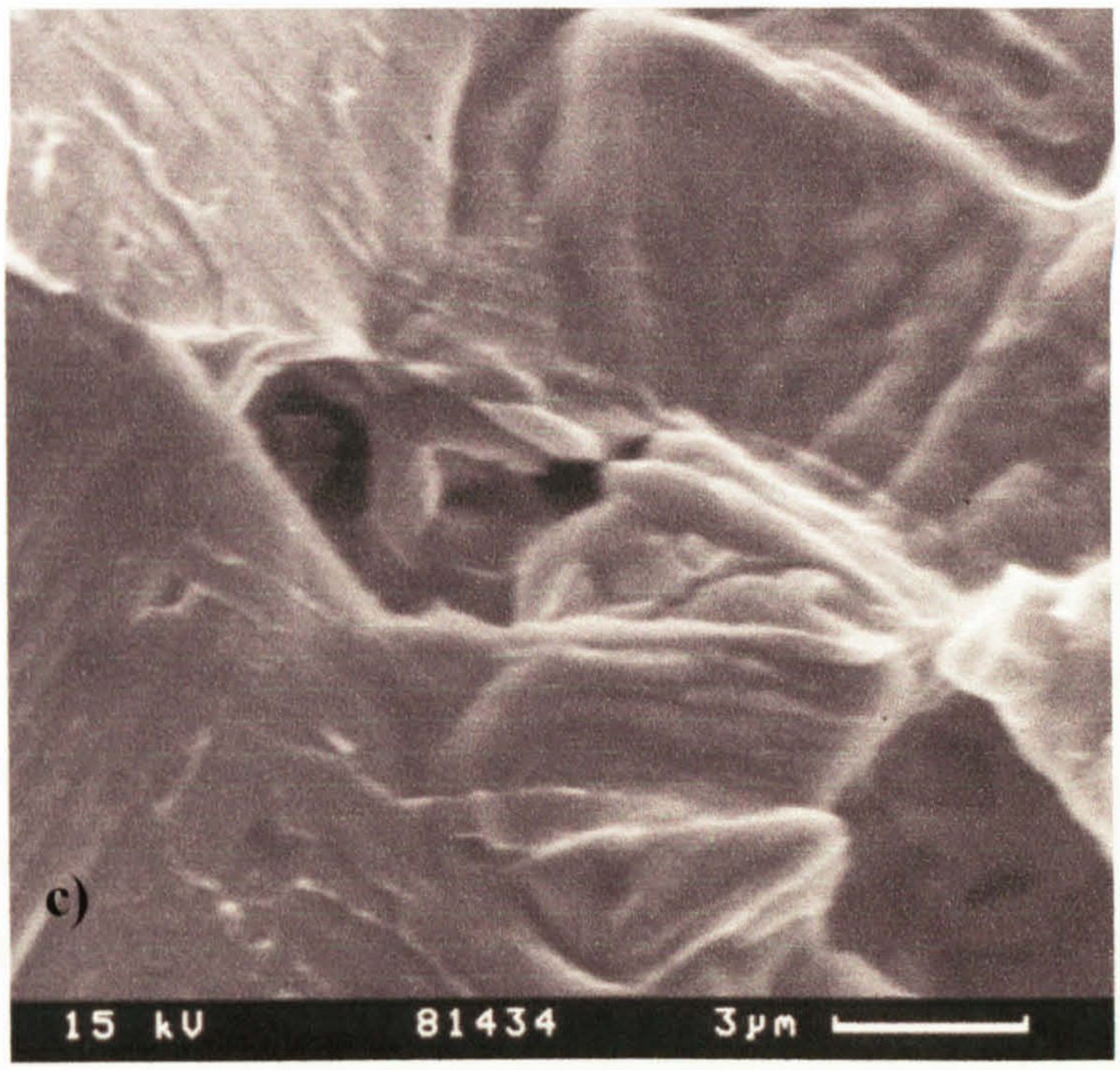


Fig.5-20 CTOD fracture face on sigmatised sample tested at -60°C, δ_m, CTOD = 0.052mm.
a) Predominant cleavage with the fatigue crack in the top field of view. [x800]
b) Cleavage facets boxed in Fig.5-20a. The circled area indicates where the cleavage appeared to initiate, which coincides with a particle. [x1000]



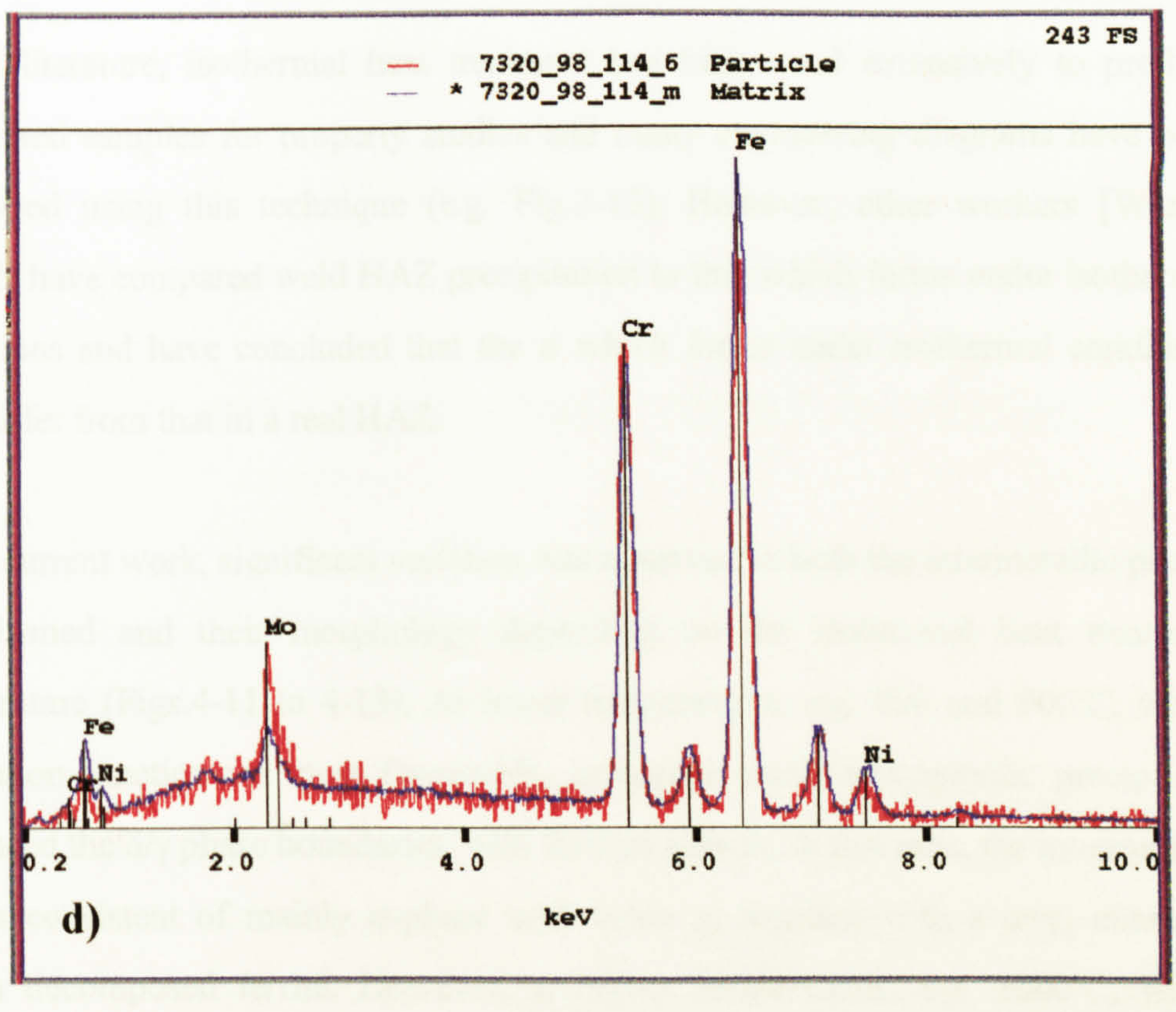


Fig.5-20 contd
c) Close-up of fractured particle circled in Fig.5-20b that triggered cleavage in adjacent ferrite [x5200]
d) Qualitative EDX spectrum for particle in Fig.5-20c and adjacent ferrite matrix. Note the higher Mo and lower Ni contents of the particle.

CHAPTER 6
DISCUSSION

6.1. EXPERIMENTAL TECHNIQUES

The isothermal heat treatment results (Study IV) were consistent with those of other workers [Ros84] [Sol82] [Jos91], illustrating the different precipitation processes that can take place in duplex steels and the marked effect that precipitation can have on resultant properties. The response of the steels to heat treatment varied between the alloys, and with the particular temperature range experienced, as summarised in Table 4-1.

In the literature, isothermal heat treatment has been used extensively to produce sigmatised samples for property studies and many engineering diagrams have been developed using this technique (e.g. Fig.2-15). However, other workers [Wie93] [Fra92] have compared weld HAZ precipitation to that which forms under isothermal conditions and have concluded that the σ which forms under isothermal conditions may differ from that in a real HAZ.

In the current work, significant variation was observed in both the intermetallic phases that formed and their morphology depending on the isothermal heat treatment temperature (Figs.4-11 to 4-13). At lower temperatures, e.g. 800 and 900°C, where nucleation kinetics are most favourable, numerous small intermetallic precipitates necklaced the δ/γ phase boundaries, with limited growth. In this case, the intermetallic phases consistent of mainly σ-phase with some χ, together with a $\sigma+\gamma_2$ eutectoid within decomposed ferrite. However, at higher temperatures, e.g. 1000°C, where nucleation is less favourable, far fewer, but much larger precipitates were present. At this temperature, all the precipitates appeared to be σ-phase.

Given the range of isothermal conditions explored and the finer microstructure of the welded pipes studied, it is difficult to make direct comparison of precipitate morphology. However, it is proposed that the intermetallic precipitate morphology in real weld HAZs is most similar to that found at lower isothermal heat treatment temperatures, and it would seem that thermal simulation induced precipitation (Fig.5-2) of a similar nature to that found in real welds (Fig.4-1). In Study V, a Δt of about 100 seconds was required to form observable intermetallic phases which is consistent with isothermal or TTT diagrams for superduplex alloys (Fig.2-15).

The significance of intermetallic phase morphology on properties was not directly examined in the current studies. However, as considered in later sections (6.4. and 6.7.), numerous fine precipitates will have a different effect on properties than a few coarser particles and so the thermal cycle experienced by the steel is an important experimental parameter [Hoc73]. Moreover, precipitate distribution and size will influence toughness and corrosion resistance and so it is recommended that, in order to study the influence of weld precipitation processes on properties, either real welds are made or that thermal simulation is undertaken of realistic welding parameters.

6.2. PREDICTION OF WELD THERMAL CYCLES

In Study II, weld thermal cycles were measured using thermocouples during the welding of thin walled pipe (pipe S32760/3, weld II). This weld was sectioned through the thermocouple, so that the exact location could be determined. In addition, the presence of intermetallic phases was confirmed and their distribution was mapped (Fig.4-5). The same weld was examined in Study III, where the welding conditions at the thermocouple location were used to produce a 2D finite element mesh. Thermal cycles were predicted for the thermocouple location and were compared with those measured by the thermocouple (Figs.4-4a&b). The key parameters are summarised in Table 6-1, which shows that the model predicted higher peak temperatures and more prolonged exposure to elevated temperatures than measured values.

Table 6-1 Comparison of measured and predicted thermal cycle data from Studies II and III

Weld run	Source of values	Peak temperature	Time above 600°C	Δt (Time between 600 and 1050°C)
1-4	Measured	825°C	15 sec	15 sec
	Predicted	1028°C	47 sec	47 sec
2-2	Measured	1065°C	26 sec	10 sec
	Predicted	1260°C	44 sec	32 sec
3-2	Measured	750°C	11 sec	11 sec
	Predicted	994°C	58 sec	58 sec

The 2D model produced for Study III, over predicted peak temperatures by about 200°C and overestimated Δt (Section 4.3.). There are several possible reasons for these differences. First, as the thermocouple was relatively large, the precise location from where the thermal cycles emanated was difficult to ascertain. So the effect of location on thermal cycle was examined using the model and it was demonstrated that Δt is hardly affected by small distance variations from the fusion boundary (Table 4-1) and that there is little difference between thermal cycles predicted at the outer and mid-wall. However, peak temperature was found to vary by about 100°C per mm along the outer wall (for the temperatures of interest). These results indicate that, although errors in the estimated position of the thermocouple may explain some of the error in the peak temperature, it cannot explain the significant overestimation of Δt.

Second, it was noted that the modelled thermocouple TC51C was located towards the beginning of a weld run, whereas the 2D model assumed steady state conditions (Section 3.6.). These two conditions differ, as, in the modelled situation (mid-way between start and stop in Fig.6-1), the surrounding material is not only heated by the molten pool, but also by the forward travelling heat of the previously solidified bead. In contrast, at the start of the weld, there is no previous bead and so, not only is the material not preheated, but also there is a mass of cold metal behind the initial molten pool which will remove the heat more rapidly. The difference between these two situations was shown to effect Δt, with faster cooling rates present at the beginning of the weld (Fig.4-7).

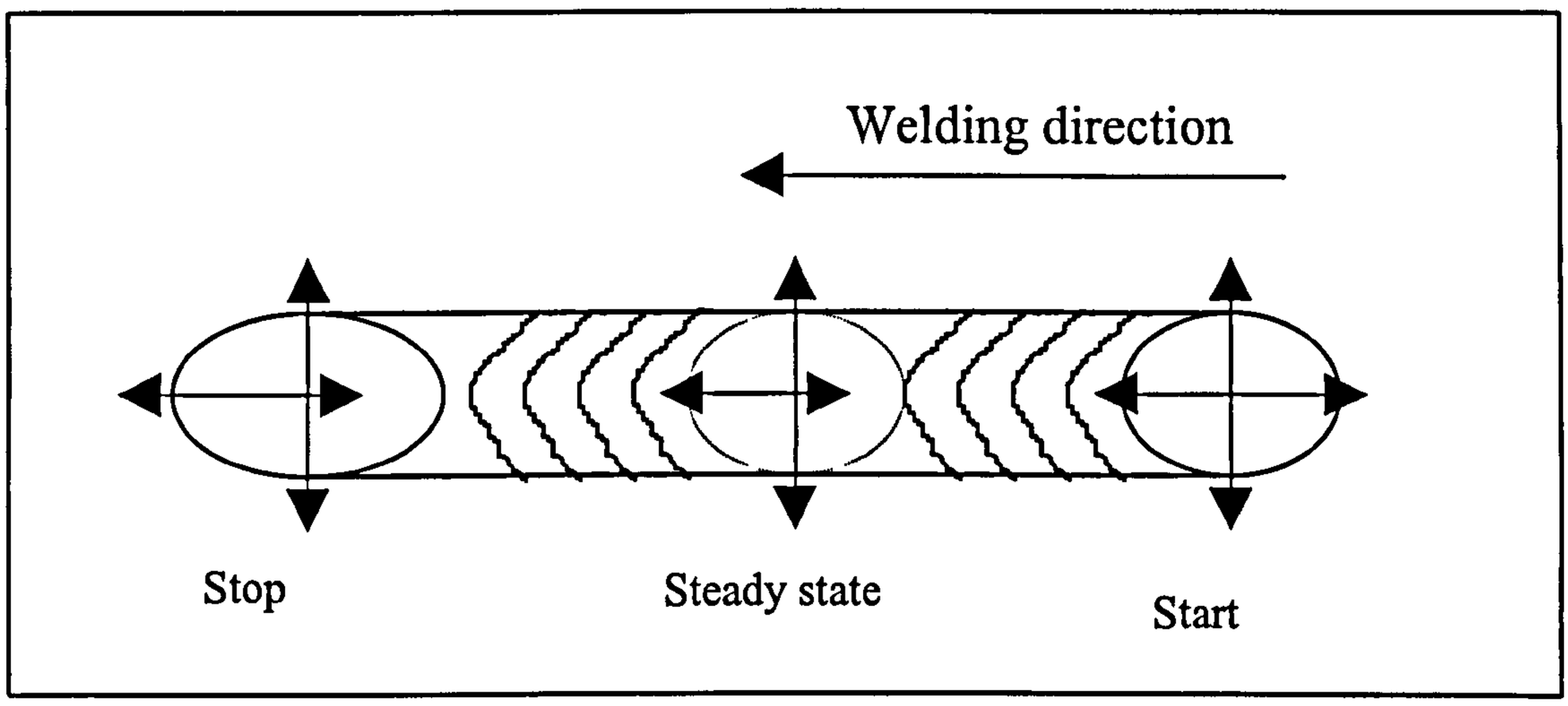


Fig.6-1 Schematic illustration of the variation of heat flow from the weld bead as the weld progresses. Note: At the start of the weld, heat is removed in all directions while during steady state conditions, the pipe ahead and behind the pool are preheated.

In summary, the overestimation of peak temperatures and Δt would appear to be combination of factors. First, thermocouple TC51C happened to be near the beginning of a weld pass, which produces a faster cooling rate than predicted under steady state conditions. And second, as the thermocouple is relatively large, it is difficult to define precisely its location. These experiments have shown the limitations of the 2D model and indicate that such models should only be used during steady state welding conditions. Where models are required for the beginning and end of weld runs, then a 3D FEA will be required, although the more complex nature of these methods should be noted.

The results of the 2D model were used in thermal simulation Studies V and VII. The aims of these studies were to establish the time (i.e. Δt) at which intermetallic phases form and to measure the effect of low intermetallic phase contents on properties. Given these aims, the use of the simplified 2D model to simulate real welds is justifiable. Further, as the 2D model overestimates Δt, the thermal simulation undertaken could be seen as more severe than real welds and, in terms of the conclusions drawn, conservative in nature.

6.3. INTERMETALLIC PRECIPITATION IN PRODUCTION WELDS

Comparison of results from Studies II and III (Sections 4.2. and 4.3.) showed that finite element mapping of production welds overestimated both peak temperature and Δt. Nevertheless, in Study V (Section 5.1.), samples were subjected to thermal cycle simulation (based on finite element models), which can be considered to exacerbate intermetallic formation (Section 6.2.). And yet the level of intermetallic phases that formed was significantly lower than seen in practical weld HAZs. For instance, none of the specimens subject to thermal cycle Set 2 contained detectable intermetallic phases, while in the practical situation 1.2% (±0.3%) was measured (Fig.4-1a).

Furthermore, thermal cycle code 3R covered the "worst case" welding conditions, that is a repair procedure in thin walled superduplex pipe. Under these circumstances, intermetallic phases were nucleated, but in relatively low quantities, reaching a maximum in one steel at 1.6% (±0.8%), as in Fig.5-2. Thermal cycle code 3R equated to a Δt (1050 to 600°C) of about 100 seconds and thus the observation of resulting precipitation is consistent with the literature [Cha91] [Jos91] [Cha94] [Her94] [Huh94] [Oka94]. Nevertheless, in real welds, made under the same nominal conditions, 9.5% (±1.7%) of intermetallic phases were recorded (Fig.4-1b).

In Study V, attempts were made to explore other effects that might accelerate precipitation, such as the application of a tensile load during thermal simulation to emulate thermal stresses. Nonetheless, no effect on precipitation was noted (Section 5.1.1.). Another possible cause of the disparate behaviour might have been compositional differences. Comparison of the pipes and plates in Table 3-2 reveals that the thin walled pipes used in production (S32760/1 and /2) contain higher Cr, W, Si, Mn and Cu, and lower Mo than plate S32760/7 used for thermal simulation [Ni and N are similar]. In the context of the current steels, these differences could be considered significant, but if comparison is expanded to the range of pipe and plate compositions available from suppliers, it would not explain why the practical problem with HAZ intermetallic formation was a phenomenon largely restricted to thin walled pipes.

Another difference between thin walled pipes and plates is the thermo-mechanical processing, which can be broken down into its two components: mechanical (i.e. solid extrusion or powder metallurgy) and thermal history (i.e. intermediary and final solution anneal). As described in Section 2.2.3., the production of wrought duplex stainless steels is a multiple step process, with each step having an influence on the final properties. For the steels studied, comparison can be drawn for similar products made by two different mechanical process routes (Table 3-4). In Study VI, the HAZ of as-received thin walled pipes were compared for steels manufactured by solid extrusion (welds VI-3 in steel S32760/4) and by powder metallurgy (welds VI-1 and VI-4 in pipes S32760/3 and /5 respectively). Both of the powder metallurgy pipes were susceptible to HAZ precipitation, when welded in the received condition, while the HAZ in the extruded pipe appeared to be free of precipitates (Section 5.2.1.). Although this result did not clarify whether aspects of mechanical processing or thermal history were responsible for the different behaviour, it did show that the problem was not necessarily associated with thin walled products. This prompted a further series of experiments undertaken in Study VI.

In the first of these experiments, two comparable welds were made in lengths of pipe S32760/3. In one length, the pipe was re-solution annealed prior to welding, while in the other, the pipe was welded in the as-received condition (Section 3.9.1.). Intermetallic phases were identified in the HAZ of the as-received pipe weld (Figs.5-8a), whereas the HAZ in the re-solution annealed pipe was free of significant precipitation (Figs.5-8b). These results prompted a second experiment employing a pipe that had undergone a solution anneal in an industrial continuous furnace (Section 3.9.2.). Again, two welds were made in pipe lengths after re-solution anneal and in the as-received condition. Again, only the as-received pipe HAZ showed significant intermetallic formation.

However, in this experiment, the welds were made in two different heats of pipe, due to problems with availability. As shown in Table 3-2, small differences in composition between the two pipes can be discerned (pipes S32760/5 and /6), with the main difference being in the nitrogen contents (0.22% and 0.27%N). However, the lower nitrogen content was in the re-heat treated pipe S32760/6. As nitrogen has been shown to retard intermetallic formation [Cha90] by reducing Cr-partitioning [Liz81], the effect of compositional differences between the two pipes can not explain the observed results. Given this evidence, it is concluded that the cause of intermetallic formation in thin walled pipe HAZs was an inadequate heat treatment in production tube dating from 1990 [Gun97b].

The major implication of this work is that some of the restrictive welding practices currently specified for superduplex alloys were based on thin walled pipes from the early 1990s, which had not been subject to the optimum solution heat treatment. Therefore, it is considered that, provided pipe is selected from more recent production or has been re-heat treated, the current limits [Goo94] on interpass temperature and arc energy could be reset at higher levels.

In this regard, control of thermal cycle may be more critical with thin wall material than with the other products. The former can often be welded in only one or two passes, so that heat flow during arc welding approaches the two dimensional situation, and cooling rate is slow. With thicker material, heat flow will be nearer the 3D case, and cooling more rapid, so that greater latitude will exist in selection of welding conditions. At the same time, caution is necessary, and excessive arc energy must be avoided: arc energy and interpass temperature must be carefully selected in formulating a welding procedure, recognising the specific thickness and joint geometry concerned. A further caveat is that the HAZ thermal cycle experienced will depend on the exact welding procedure, as well as on the calculated arc energy. Certainly, if root runs in pipe are made using the GTAW process, the amount of filler addition will affect the situation, HAZ cooling rates tending to be faster with greater rate of filler addition, thereby minimising the risk of intermetallic precipitation [Gun91].

6.4. EFFECT OF INTERMETALLIC PHASES ON TOUGHNESS

For the isothermal heat treatment samples (Study IV), where heavy precipitation was recorded, low Charpy impact values were obtained and the fracture path was largely determined by the location and continuity of the intermetallic precipitation. In Study VII, Charpy impact specimens with a range of intermetallic contents were produced (0 to 8.1%) by heat treatment and thermal simulation. When these results are compared with other Charpy toughness data, the marked influence of intermetallic content becomes apparent (Fig.6-2). Figure 6-2 also demonstrates that the results of the present work lie within the data range established for heat treated parent steel and actual HAZs [Wie93].

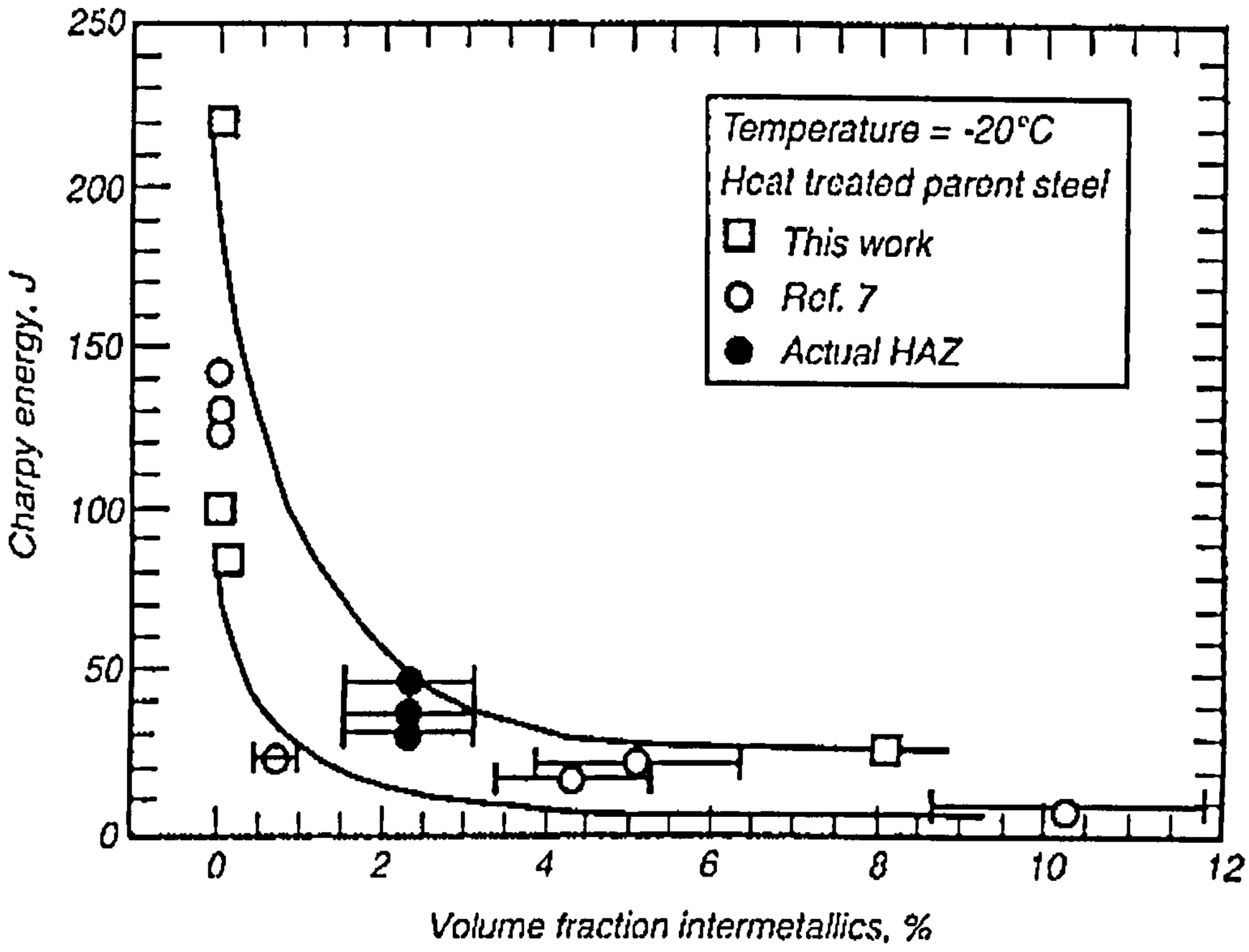


Fig.6-2 Charpy toughness versus measured intermetallic content at -20°C: Ref.7 refers to [Wie93].

Two of the Charpy specimens from Study VII both gave 24J (Table 6-2). The first was sigmatised and impact tested at –60°C, while the second was as-received and tested at –90°C. Both samples contained a ductile region beneath the notch (Figs.5-15a and 5-16a) and cleavage over the majority of the fracture face (Figs.5-15b and 5-16b). This would imply that most of the energy was absorbed in initiating the cracks.

Table 6-2 Summary of results for specimen pairs subject to detailed fractography in Study VII

Specimen	Test	Result	Appearance	
			Below notch	Fracture face
As-received (0.007%I), tested at –90°C	Charpy	24J	Ductile	Cleavage pockets with ductile features
	CTOD	0.11mm, δ_m	Ductile	
Sigmatised (8.1%I), tested at –60°C	Charpy	24J	Ductile	
	CTOD	0.052mm*, δ_m	Cleavage	

* Serrated load versus crack mouth opening plot (Fig.5-13)

Comparison of CTOD data generated in Study VII with other workers (Fig.6-3) reveals that, as for Charpy impact data, there is a marked influence of intermetallic content. Further, all compiled CTOD data were maximum load, i.e. δ_m, except one side-grooved sample containing 15.4±1.8% intermetallic phase (heat treated parent steel), which behaved in a brittle manner (0.0lmm, δ_c) [Wie93]. Otherwise, the highest intermetallic content that still produced a δ_m result was 8%I from Study VII. However, this sample recorded relatively low CTOD values, e.g. 0.052mm at –60°C and its load versus crack mouth opening plot (Fig.5-13) had a serrated appearance, consistent with multiple crack initiation and arrests without leading to significant cleavage events. Further, Fig.5-13 indicates that there is an increase in the peaky nature of the maximum load plateau with higher intermetallic contents.

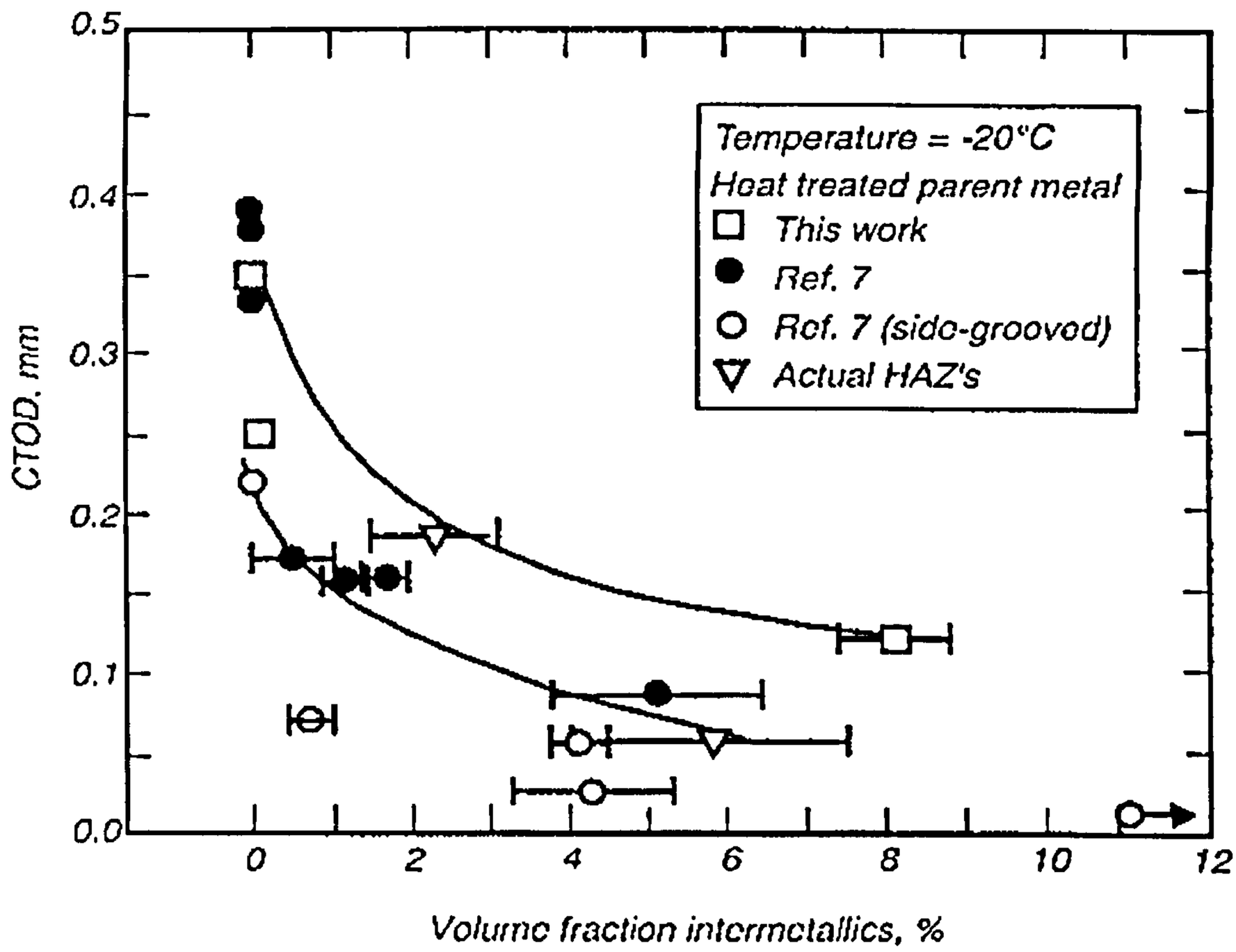


Fig.6-3 Fracture toughness in terms of CTOD versus measured intermetallic content at -20°C:
Ref.7 refers to [Wie93].

The fracture faces of the CTOD specimens for which the comparable Charpy specimens both gave 24J were examined (summarised in Table 6-2). Even though the same Charpy energy was recorded in these samples, a significant difference in the CTOD values is noted. Further, there was a marked difference in the fracture behaviour just below the fatigue crack tip. The sigmatised sample showed cleavage pockets, of which some were initiated at sigma particles (Fig.5-20a&b), while the same region in the as-received sample was ductile (Fig.5-17a). In both cases, the remainder of the fracture face was mixed mode with cleavage pockets and ductile regions (Fig.5-17b), with the sigmatised sample showing more evidence of cleavage pockets.

The implication of the CTOD results is that, at the 8% sigma level, cleavage in the ferrite was assisted by the presence of intermetallic particles, most significantly at the notch tip. In all evidence, the austenite remained ductile, sometimes arresting cleavage in the ferrite, evidenced by the cleavage pocket size compared to the lamellar spacing (Section 5.3.3.). However, where the austenite islands were smaller and could not restrain the crack, the austenite was torn and the crack continued, to be arrested at a larger austenite island (Fig.5-17c). These observations are in keeping with the serrated nature of the load versus crack mouth opening plot (Fig.5-13), as each 'tooth' can be related to a cleavage event within a ferrite grain, which is subsequently arrested by austenite before a significant drop in load occurs.

The mechanism of sigma particles triggering cleavage in the ferrite is consistent with the Charpy data, where a comparable reduction in absorbed energy was not apparent in Study VII. The Charpy test involves very fast strain rates, which may not allow time for the brittle sigma at the phase boundary particle to fracture or disbond from the surrounding δ and γ and initiate a cleavage event. However, as the sigma content increases, the opportunity for cleavage events also increases, as illustrated in Fig.6-2, although this will depend on the test temperature. For instance, if the temperature is above the DBTT for ferrite (e.g. Fig.2-15), then cleavage is considered less likely.

A common feature of duplex fracture faces is the presence of splits (e.g. Fig.5-18a & 5-19a). These splits run perpendicular to the crack path and pass through the ferrite in a brittle manner (Fig.5-18b & 5-19b). Further, subsidiary cracking in the ferrite is commonplace (Fig.5-14), with some energy absorption. All of these features do not appear to have a significant effect on fracture properties, except that, in the sigmatised sample, smaller splits were present than the comparable as-received sample. This may imply that for the sigmatised sample, where cleavage was easier in the plane of the crack, there was a relatively reduced tendency for cleavage to run perpendicularly. These events have been observed previously in duplex CTOD samples, where the cause of pop-ins has been investigated. It was concluded that such out of plane cracks can be categorised as Class 2 pop-ins [Wie97] and, as such, are not reportable. These was justified, as, in essence, the splits would run parallel to a pipe/plate surface (with the possible exclusion of set-through nozzles), and so are of less concern than through thickness cracks.

6.5. OTHER FACTORS THAT INFLUENCE TOUGHNESS

In Study V, intermetallic phases were positively identified (i.e. cycle code 3R), preferentially forming on δ/γ boundaries (Fig.5-1 and Fig. 5-2), and leading to a reduction in the absorbed energy (Fig.5-4). However, there also appeared to be a drop in toughness with shorter exposure times and yet no intermetallic phases were observed in these specimens, using optical or SEM techniques (0.1μm detection limit). The presence of finer particles was explored using TEM thin foils, but again no precipitation was detected on the δ/γ phase boundaries (Fig.5-3). The presence of dislocations is noted (Fig.5-3), reflecting that the boundaries are regions of high energy following thermomechanical processing [Sma85]. However, it is unlikely that the presence of dislocations alone would significantly effect fracture toughness. Alternatively, the exposure to elevated temperatures will lead to element redistribution across the δ/γ boundaries and limited growth of ferrite into the austenite. Although this may reduce the localised corrosion resistance, it is unlikely to affect toughness.

In summary, none of the findings of the present study explain the reduction of toughness prior to the observation of intermetallic phases by optical and SEM techniques. It would seem that fine intermetallic phases are present at Δt exposure times less than 100 seconds and are the cause of the toughness reduction (i.e. <0.1μm), but their detection requires examination of a larger number of thin foils. In order to confirm this conclusion, it is recommended that future work includes a more thorough TEM thin foil exercise.

In Study V, steel S39274 behaved slightly differently to the other grades (Fig.5-4). The relatively high tensile properties of this steels are noted (R_m in Table 3-4), and it may be that this pipe was supplied with some prior cold work. As the effect of cold work is to introduce dislocations and restrict deformation by slip, short term thermal cycling may have induced a measure of recovery. Nevertheless, prolonged thermal cycles caused appreciable reduction in impact toughness, due to intermetallic precipitation.

Similarly in Study VII, the as-received pipe S32750/2 would appear to have been delivered with some degree of cold work (Table 3-4), which was relieved by the solution anneal. This induced a marked increase in toughness (Fig.5-12a), although an effect from the small differences in precipitation level between the two specimens cannot be dismissed. Further, both batches of steel S32750 contained REM inclusions (Fig.5-2), originating either as trace residuals from scrap or as additions to aid hot workability. In Study IV, the REM added steel (S32750/1) showed lower overall toughness than a comparable 'clean' steel (Figs.4-14).

In Study IV, chromium nitrides were located within the ferrite and along δ/δ boundaries (Fig. 4-14), especially after heat treatments between 1100 and 1300°C (Table 4-2). With reference to the impact results for these specimens (Fig.4-15), the toughness was found to drop as the heat treatment temperature increased, although this was also associated with austenite dissolution, high ferrite contents and grain growth. As there is no evidence for Cr_2N reducing toughness (presumably a function of their small size), it is suggested that the current results reflect the presence of coarse ferrite grains and low austenite contents.

6.6. CORRELATION BETWEEN IMPACT AND FRACTURE TOUGHNESS

Previous work [Wie96] [Dho94] has aimed to establish appropriate Charpy toughness requirements for this type of steel. The procedure adopted [Wie96] was to carry out fracture mechanics (CTOD) and Charpy toughness tests to achieve a correlation. Fitness for purpose calculations were used to determine required CTOD values for typical weld flaw dimensions which could be missed by usual inspection procedures. The Charpy-CTOD correlation was then used to translate the required CTOD value into a Charpy energy. The question was whether the correlation established would also be valid for material containing intermetallic precipitates. Although some results on sigmatised weld metal tended to indicate that the correlation remained valid [Wie96], there was little information for parent steel and HAZ microstructures. The correlation of the Charpy versus CTOD results from Study VII is shown in Fig.6-4. There is a good correlation (R^2 value 0.95) between the results of Charpy and CTOD tests (i.e. same heat treatment and test temperature) despite the variation in intermetallic content and morphology.

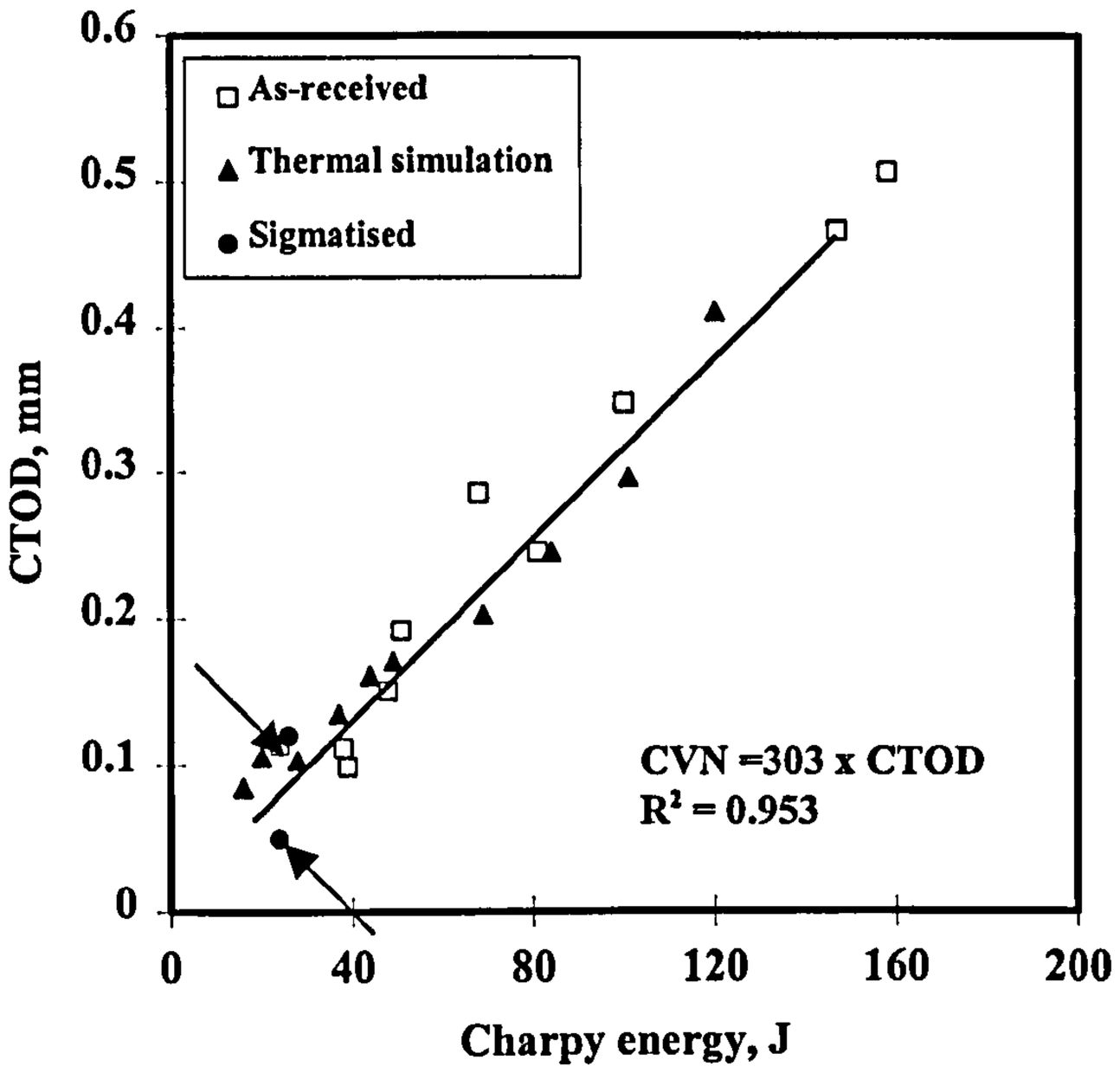


Fig.6-4 Comparison of Charpy energy and CTOD results for identical heat treatment conditions. All samples were 10x10mm in cross section. The two arrowed data points represent the two specimen pairs subject to detailed fractography.

The significance of Fig.6-4 is that, irrespective of intermetallic content and test temperature, the relationship between CVN and CTOD appears to hold (for the given specimen thickness studied, i.e. 10mm). Comparison of current with other data [Wie96] [Wie97] in Fig.6-5 shows that the correlation developed in this work is consistent with a wide range of data for parent steel, weld metal and HAZ, with and without intermetallic precipitation. (Within the thickness 7 to 15mm range no clear effect of thickness on CTOD can be discerned.) This has practical significance for material/weld quality control tests where toughness requirements are, in general, expressed by Charpy V-notch tests, and for which existing fabrication codes do not normally allow for the presence of any intermetallic phases.

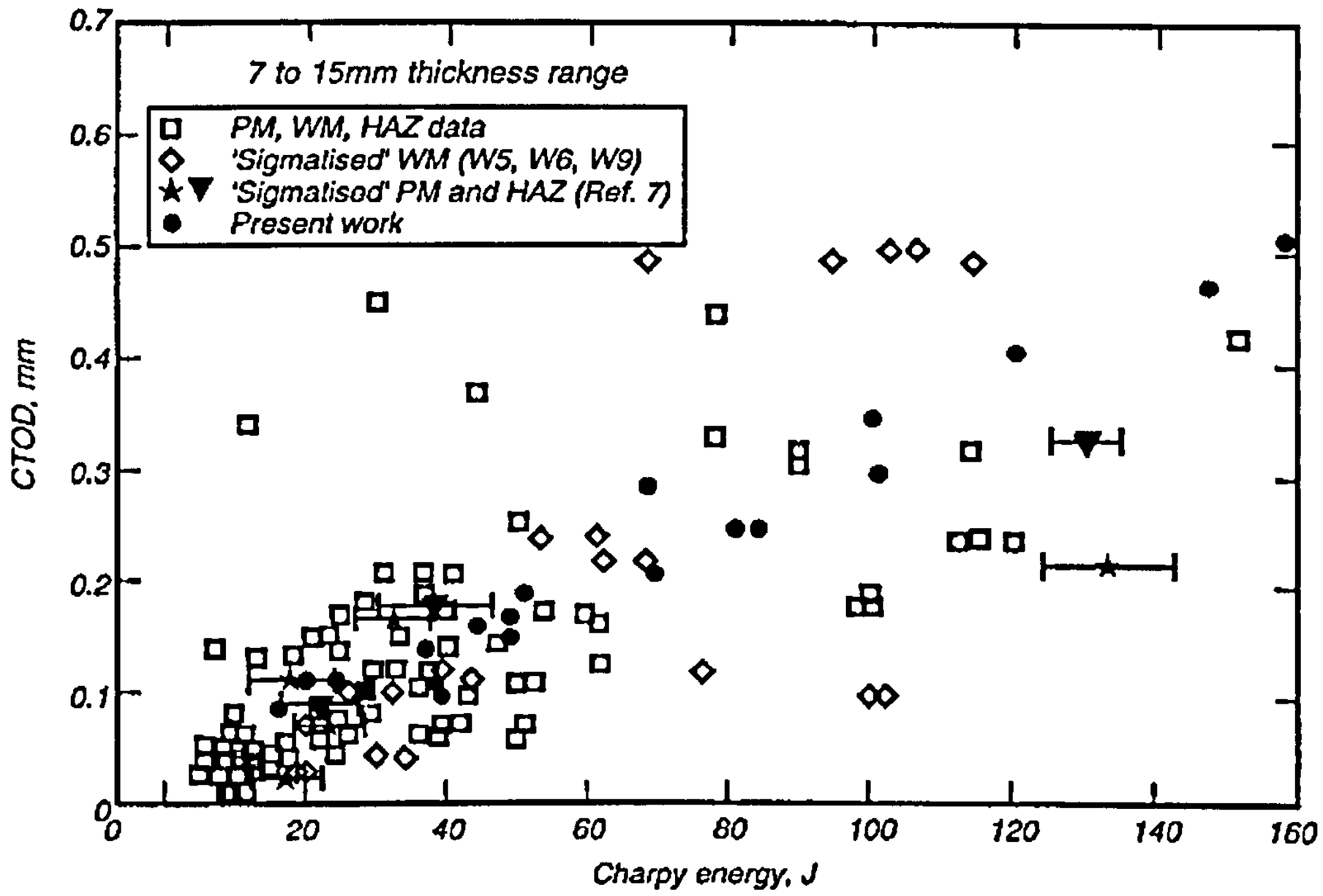


Fig. 6-5 Comparison of present data with previous results [Wie97]: Charpy energy versus CTOD values for parent steels, weld metals and HAZs with and without intermetallic precipitates. Ref. 7 refers to ref [Wie93]

In Section 6.5, it was concluded that intermetallic phases facilitate cleavage events in the ferrite at –60°C and so, for comparable intermetallic-containing CTOD and Charpy samples, the CTOD results is expected to be proportionally lower. Nevertheless, the correlation between Charpy and CTOD toughness appears to hold with or without the presence of intermetallic phase (Fig.6-4). It is noted that the 'sigmatised' data point at 24J and 0.052mm (arrowed in Fig.6-4) does lie a little below the best fit line, but could be said to be within the general scatter of the rest of the data. This implies that for low Charpy values, say below 30J in 10x10mm specimens, the line of best fit may not be appropriate and additional CTOD tests are recommended. However, for other specimens that do contain some intermetallic particles, but give higher absorbed energy values, the Charpy versus CTOD correlation can be employed. The advantage of this last comment, is that as long as the Charpy requirements are appropriate and are met, the presence of intermetallic phase can be considered as not significant in terms of the prevention of fracture initiation.

6.7. EFFECT OF INTERMETALLIC PHASES ON PITTING RESISTANCE

For the superduplex steels in Study IV, the preference for γ-phase attack, after heat treatments which did not result in precipitation, was not so marked as for earlier 25%Cr duplex grades [Gun95]. In earlier grades, which have been solution annealed, the δ-phase is enriched in Cr and Mo, whilst the γ contains higher Ni contents [Bae88]. As Cr and Mo are the elements primarily responsible for enhancing pitting resistance, see Eqn {1-1}, the δ-phase is more resistant to attack. However, as superduplex steels contain high bulk nitrogen levels, e.g. >0.20%N from Table 3-2, the γ can be assumed to contain around 0.5%N, given that the nitrogen solubility in high chromium ferrite at ambient temperatures is only 0.03% [Lil86]. This local nitrogen level is equivalent to 8%Cr from Eqn {1-1}, which gives the γ similar pitting resistance to δ in the solution annealed condition.

As the isothermal heat treatment temperature was increased above 700°C, intermetallic phases formed; the corrosion sites tended to move to the δ-phase and the CPT dropped by about 40°C (Figs.4-16b and 4-17). From Fig.2-36, this equates to a local reduction in the PRE by about 5 points. Given that sigma is enriched proportionally more in Mo than Cr (Table 5-2) and that diffusion rates are much faster in ferrite than in austenite [Smi83], the drop in CPT can be equated to localised depletion in the ferrite adjacent to the sigma of about 0.67%Cr and 1.33%Mo. (As sigma phase is not known to contain nitrogen, the nitrogen term in Eqn {1-1} is not considered influential in this context).

As $PRE_N = \%Cr + 3.3x\%Mo + 16x\%N$ Eqn {1-1}

Then $\Delta PRE_N = (1 \times 0.67) + (3.3 \times 1.33) + (16 \times 0) = 5.0$

To further demonstrate this, the mean diffusion distances (x) for Cr and Mo in both ferrite and austenite can be calculated [Por92] from the relationship:-

$$x = 2\sqrt{Dt} \qquad \text{Eqn \{6-1\}}$$

where D is the diffusion coefficient and t is the time at temperature. The results are given in Table 6-3, which show that diffusion is limited in the austenite and so the formation of sigma phase is governed by diffusion of Cr and Mo from the ferrite.

Table 6-3 Calculated diffusion distances for Cr and Mo in ferrite and austenite after 10 minutes

Element	Phase	Distance, μm		
		800°C	900°C	1000°C
Cr	Ferrite	1.56	4.81	12.4
	Austenite	0.08	0.23	0.59
Mo	Ferrite	1.19	4.38	11.6
	Austenite	0.14	0.45	1.19

The values used for D [Smi83], should not be regarded as exact for the present alloy type.

The expected depletion of Mo in ferrite is shown schematically in Fig.6-6a, assuming a typical sigma particle width of 1μm and Mo-content of 9% (Fig.4-11 and Table 5-2), and simplifying the depletion profile from parabolic to linear form [Por92]. To maintain conservation of solute from ferrite to intermetallic, the minimum Mo content predicted at the interface is about 2.4% or a drop of 1.8% compared to the Mo content of the ferrite. This is consistent with the estimate from Eqn {1-1}, i.e. 1.33%Mo, considering the dependence of the result on D-values and on the particle size.

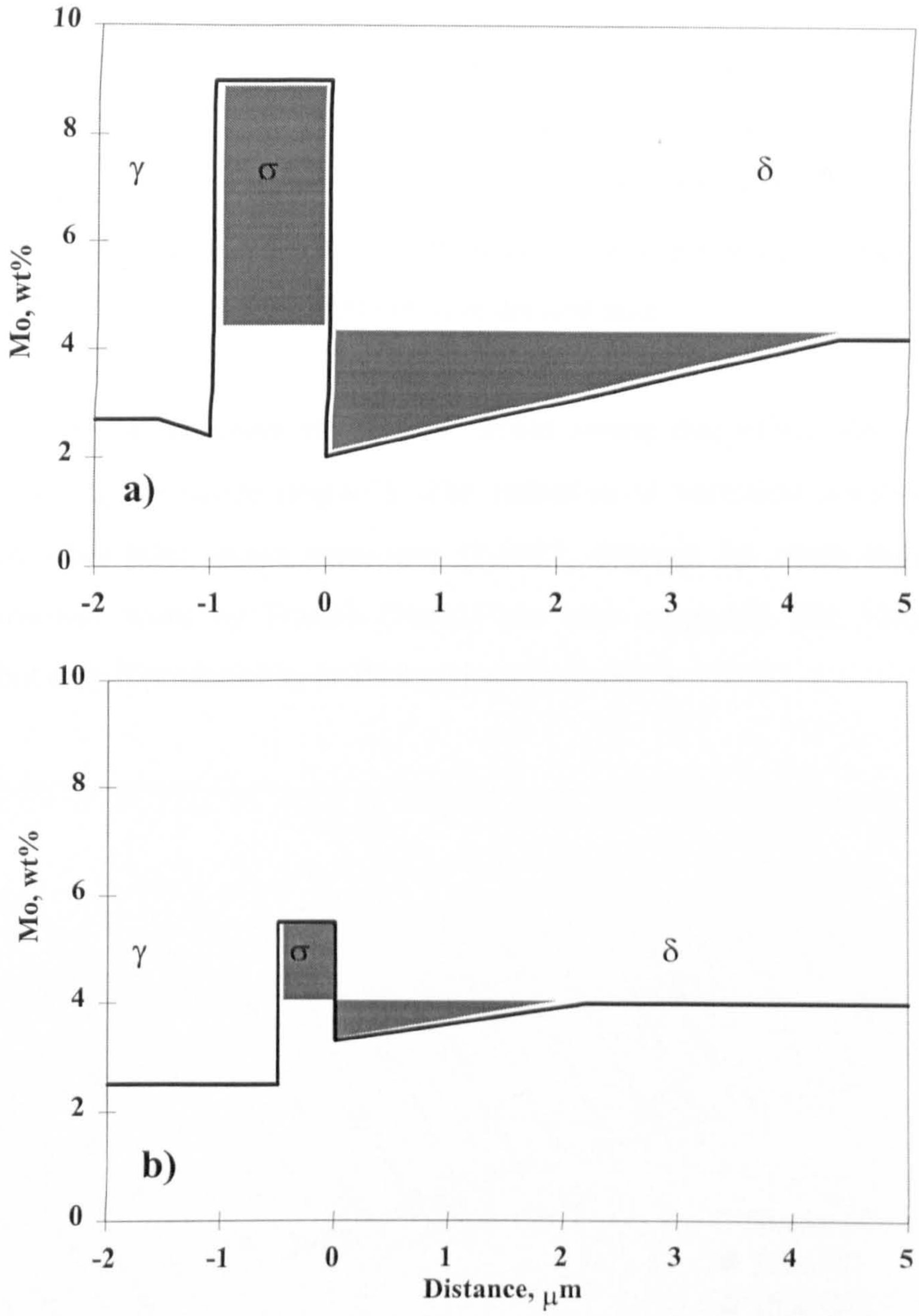


Fig.6-6 Simplified Mo concentration profiles across austenite/sigma/ferrite:
a) sigma particle formed after 900°C for 10 minutes,
b) sigma particle formed in a real weld HAZ (Weld II).
Note that the shaded areas are equal on either side of the interface

It is also worth noting from Fig.6-6a that the Mo-content of the austenite is only just above that of the alloy depleted zone. Even though the austenite will contain significantly higher nitrogen than this zone, its Cr-content will be lower and so attack in the austenite will depend on small variations in these elements. In fact, some workers [Gin98] have witnessed pit initiation in the austenite.

In the isothermal heat treatment study IV, it would appear that <1%σ significantly reduced the pitting resistance (Fig.6-7). The reduction in corrosion resistance in chloride media has been shown previously *[Pot92]*, although for much higher σ-contents. However work by Francis [Fra92] has also suggested that 1%σ was influential, but only if produced by isothermal heat treatment at 750°C.

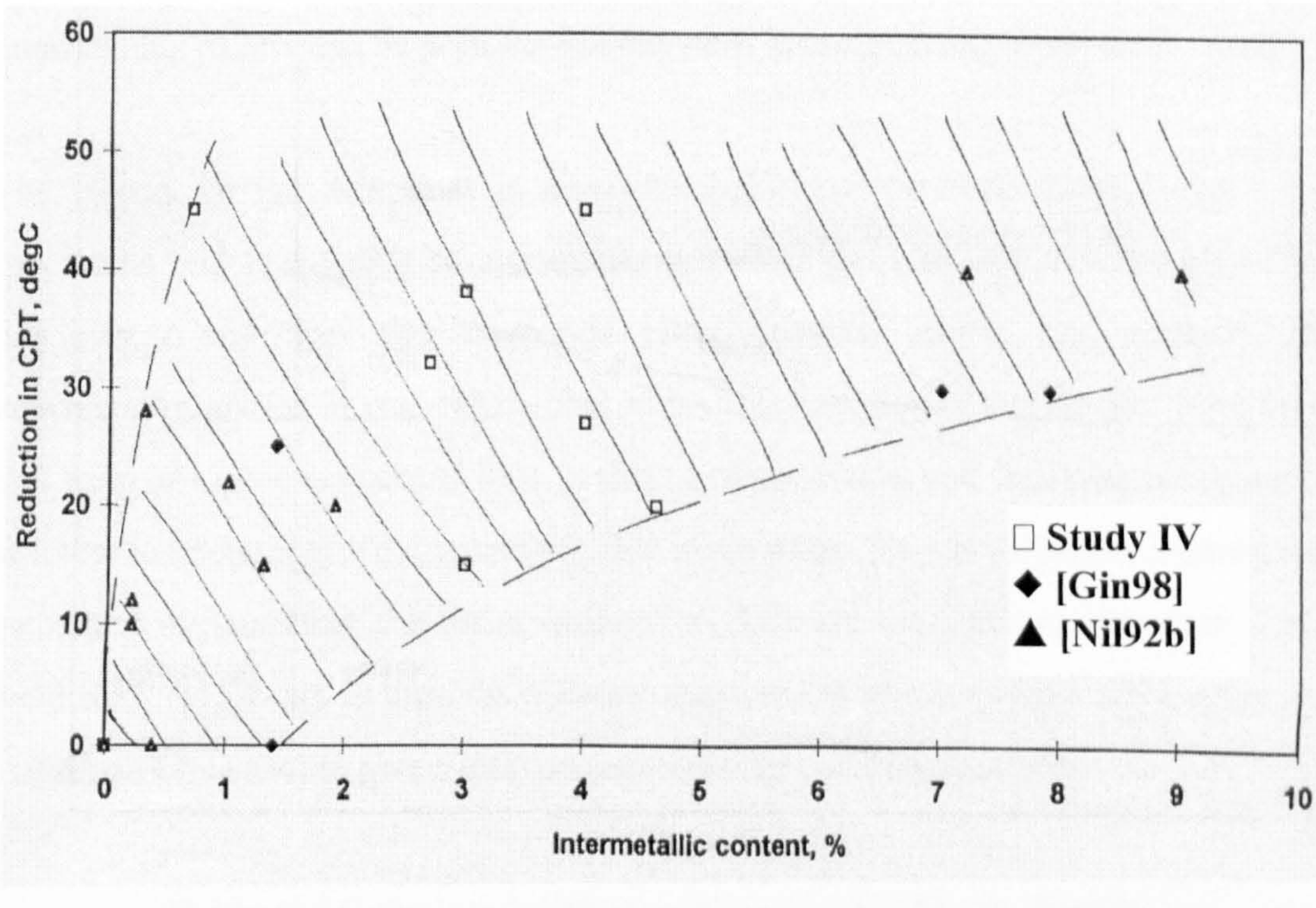


Fig.6-7 Effect of intermetallic content on the drop in critical pitting temperature (CPT) using isothermal heat treated samples

The thermal simulation Study V confirmed that intermetallic phases can lead to pit initiation (Fig.5-9). However, as the onset of weight loss did not occur until 53°C (associated with a cluster of intermetallic phases, Fig.5-7), and it is normal to screen superduplex weldments at 35°C, this is not of practical significance. Furthermore, steel S32750/1 contained intermetallic phases after a simulated repair operation (with 1.6 ± 0.8%I, Fig.5-2) and yet this did not lead to attack even at 72°C.

Clearly, there is some discrepancy between corrosion tests performed on thermal simulation specimens and real welds. For real welds, significant attack occurred at 35°C in weld I-2 (Fig.4-2), albeit with about 10%I (Fig.4-1b), and at 52.5°C in weld VI-4 (Fig.5-10). However, in this last case attack occurred in the weld metal, even though 0.1%I was present in the HAZ. These results indicate that in real welds, some intermetallic phases can be present with the weak link remaining in the weld metal.

The reason for the difference in corrosion behaviour between thermal simulation specimens and real welds would appear to reflect the size and distribution of the precipitates and thus the associated alloy depleted zones. For instance, the intermetallic phases in real HAZs tend to be more numerous but smaller than those that form at higher isothermal heat treatment temperatures and emulates precipitation at lower temperatures. To demonstrate this assumption, the Mo diffusion distance was estimated by summing the times exposed to different temperature ranges in a real weld HAZ (Fig.4-4a). In turn, the distance associated with each temperature range was summed (Table 6-4) to give a total diffusion distance of Mo as 2.2μm.

Table 6-4 Calculated diffusion distances for Mo in ferrite over various temperature ranges in the HAZ of weld II

Temperature range, °C	Total time within temperature range, sec	Distance of Mo diffusion in ferrite, μm
1150-1050	0.6	0.11
1050-950	3	0.31
950-850	2.4	0.27
850-750	14	0.75
750-650	26.5	0.78

Further, as indicated by Table 5-1, the composition of sigma phase after thermal simulation is not as Cr and Mo-rich as after higher isothermal heat treatments. (Although this may reflect some contribution to the X-ray signal from the matrix, due to the small particle size and spatial resolution of the probe.) These results are shown in Fig.6-6b, which indicates that the sigma phase that precipitates in HAZs will have a narrower and less . alloy-lean depleted zone. Pit initiation studies have indicated that pits can grow from nuclei as small as 10nm to perhaps 1μm, depending on the severity of the corrosive medium [Pis92] [Mat94], which would imply that HAZ depleted zones are sufficiently wide to enough to start a pit. However, as the level of depletion is not so marked, nor will be the reduction in pitting resistance, and in the context of weldments with inferior weld metal (Fig.2-36), this explains why the depleted zones around HAZ precipitates are not the weak link.

The precipitation of Cr_2N, which was found also to initiate pits in the isothermal specimens (Fig. 4-17c), is commonly found in weld HAZs. It is understood that the formation of Cr_2N leaves a Cr-depleted zone that is prone to attack. In the current work, Cr_2N precipitation was induced by extended exposure times to elevated temperatures (above 1000°C for 10 minutes), which is unrepresentative of the thermal cycles in a weld. Other workers [Rum98] have applied more realistic thermal cycles to induce precipitation and concluded that a maximum drop in CPT from 80°C to 65°C was attributable to Cr_2N precipitation. Even though this may seem quite significant, in the context of weld metal, which is only expected to reach 35 to 40°C, and the more influential intermetallic phases, the effect of Cr_2N precipitation is only considered of secondary importance. This comment is compounded by practical experience whereby there have been no reported cases of Cr_2N initiating failure in service.

CHAPTER 7

SUMMARY AND CONCLUSIONS

The present work comprised seven studies that can be broken down into data collection for thick walled products and investigation into intermetallic formation in thin walled pipe. The data collection exercises covered Studies IV, V and VII. In these studies, superduplex pipes and plates (10 to 20mm thick) were subject to both isothermal and thermal simulation heat treatments and the resultant microstructures, pitting resistance, impact and fracture toughness were evaluated. In parallel to the thick walled studies, the effect of welding thin walled pipes was examined in Studies I, II, III and VI. In the first part, the thermal cycles in production welds were estimated, as well as their influence on HAZ precipitation and properties. Finally, several thin walled pipes underwent both laboratory and production solution heat treatments to establish the cause of HAZ intermetallic formation and identify remedial measures. As a result of all these studies, the following overall conclusions can be drawn:

1. Laboratory and production solution annealing of thin walled pipes restored the resistance to intermetallic formation and so demonstrated that the original problems with such pipe was due to an inadequate heat treatment in the first instance.

2. 2D finite element models of the thermal cycles within heat affected zones (HAZs) provide reasonable agreement with measured thermal cycles, given the practical inaccuracies of thermocouple placement. However, for more precise prediction, especially when examining locations towards the beginning and end of weld runs, 3D models should be explored.

3. Thermal simulation induced intermetallic phases after about 100 seconds exposure to the 600 to 1050°C temperature range (Δt), which is keeping with isothermal heat treatment data published in the open literature. Nevertheless, precipitate morphology can vary from numerous fine particles necklacing the δ/γ boundaries to fewer large particles growing into the ferrite. Thermal simulation produced the former particle morphology, consistent with heat treatment at lower temperatures, say 800-900°C, and representative of the particle morphology found in real HAZs. Thus, thermal simulation is preferred to isothermal heat treatment for producing HAZ specimens if real welds can not be sampled.

4. Brittle intermetallic precipitates can either fracture or disbond from the surrounding δ and γ, act as local stress raisers, and encourage cleavage through the ferrite phase. This implies that intermetallic precipitates assist crack initiation and produce proportionally lower CTOD results than comparable Charpy V notch results might suggest.

5. A drop in toughness was observed, prior to the detection of intermetallic phases by optical, SEM or TEM techniques. Alternative mechanisms for a reduction in toughness have been discussed and dismissed. It is believed that fine intermetallic phases are the cause, which, as yet, have not been detected in TEM thin foils.

6. Notwithstanding conclusion 4 above, a correlation between Charpy and CTOD toughness was found to hold in the presence of up to 8% intermetallic phases. This allows for the presence of moderate intermetallic contents to be ignored when determining Charpy impact test requirements in procedure codes. However, this correlation should be used with caution, especially if the temperature of interest is below the ferrite DBTT. In such instances, intermetallic precipitates may encourage crack initiation and cleavage of the ferrite, which would not necessarily be highlighted by a fast strain rate test such as Charpy V notch.

7. Pitting corrosion resistance was reduced in the presence of intermetallic precipitates. The extent of the reduction depended on the precipitate morphology and thus the type of heat treatment employed. In the case of HAZ precipitation induced during real GTA welds, the reduction was not so marked (weld metal remained the critical region), as the precipitates were fine and, presumably, the associated depleted zone was not as alloy lean.

CHAPTER 8
FURTHER RESEARCH

During the course of the present study many avenues were explored, not of all of which are reported herein. Nevertheless, there are three main topics which stand out as worthy candidates for future work.

1. The present study and current literature report that detectable intermetallic precipitates form after about 100 seconds exposure to elevated temperatures and yet a drop in toughness has been observed for shorter exposure periods. It is believed that fine precipitates do indeed form during shorter exposures, which are beyond industrial metallographic techniques. It is recommended that the presence of fine precipitates is further explored using suitable TEM thin foils.

2. It has been shown that intermetallic particles can initiate cleavage in the ferrite, which is subsequently arrested at significant austenite islands. This observation is dependent on the fracture toughness test temperature, as the above comment refers to tests undertaken below the ductile to brittle transition temperature (DBTT) of ferrite. Further work should establish the ferrite DBTT, so that tests/service above this temperature would be free of intermetallic induced cleavage.

3. In the current work, the limitations of a 2D finite element mesh to model HAZ thermal cycles was demonstrated. It is suggested that similar 3D meshes are examined to establish whether a more precise technique is feasible.

A

[Ann84] de Anna P L, Bassoli M, Cerisola G, Bonova P L, Magzoldi P: *Passivity of Metals and Semiconductors*, Elsevier Science Publishers BV, Amsterdam, (1984) p591.

[Ata91a] Atamert S and King J E: *Z. Metallkd* **82** (3) (1991) p230.

[Ata91b] Atamert S and King J E: *Acta Metall Mater* **39** (3) (1991) p273.

[Aug90] Auger P, Danoix F, Manand A, Bonnet S, Bourgoin J, Guttmann M: *Mater. Sci. Technol.* **6** (1990) p301.

B

[Bae88] Baeslack W A and Lippold J C: *Met Con*, 1988, 20 (1), 26R-31R.

[Bai27] Bain E C and Griffiths W E: *Trans A.I.M.E.* **75** (1927) p166.

[Bax93] Baxter C: Conf proc *Third International Offshore and Polar Engineering*, Singapore, ISOPE (1993).

[Bec69] Beckitt F R: *J. Iron Steel Inst.* **207** (1969) p632.

[Ber80] Bernhardsson S O, Oredsson J and Tynell M: *Corrosion 80*, NACE, (1980) paper 14.

[Ber82] Bernhardsson S, Oredsson J and Martenson C: Conf proc *Duplex Stainless Steels '82*, St.Louis, ASM, (1982) p267-276.

[Ber90] Bernhardsson S: *Corrosion 90*, NACE, (1990) paper 164.

[Ber91] Bernhardsson S: Conf proc *Duplex Stainless Steels '91*, Beaune, Les editions de physique, (1991) Vol.1, p185-210 and p137-150.

[Bin46] Binder W D and Brown C M: Proc ASTM **46** (1946) p593.

[Bla64] Blackburn M J and Nutling J: *J.I.S.I.* **202** (1964) p610-613.

[Ble67] Blenkinsop P A and Nutting J: *J.I.S.I.* **205** (1967) p953.

[Bon91a] Bonnefois B, Charles J, Dupoiron F, Soulignac P: Conf proc *Duplex Stainless Steels '91*, Beaune, Les editions de physique, (1991) Vol.1, p347-362.

[Bon91b] Bonnefois B, Soulignac P, Charles J: Conf proc *Duplex Stainless Steels '91*, Beaune, Les editions de physique, (1991) Vol.1, p469-478.

[Bow72] Bowman A L, Arnold G P, Storms E K, Nereson N G: *Acta. Cryst. B* **28** (1972) p3102.

[Bow86] Bower E N, Fielder J W, King K J: *25emes Journees des Aciers Speciaux*, St Etienne, TWI, (1986) paper 51.

[Bui83] Bui N, Irhzo A, Dabosi F, Limouzin-Maire Y: *Corrosion* **39** (1983) p491.

C

[Cah68] Cahn J W: *Trans A.I.M.E.* **242** (1968) p166.

[Cah82] Cahn J W and Kalonji G: Conf proc *Solid State Transformations*, Warendale, TMS-AIME, (1982) p3.

[Car70] Carlen J C: *Werkstoffe und Korrosion* **21** 8 (1970) p654-650.

[Cas74] Castro R J and de Cadenet J J: *Welding metallurgy of stainless and heat resistant steels*, Cambridge University Press, 1975.

[Cha82] Chance J, Coop W, Gradwell K J, Roscoe C V: Conf proc *Duplex Stainless Steels '82*, St.Louis, ASM, (1982) p371-398.

[Cha90] Charles J and Bonnefois B: Sem proc *Weldability of New Ferritic & Stainless Steels*, Cambridge, TWI (1990).

[Cha91] Charles J: Conf proc *Duplex Stainless Steels '91*, Beaune, Les editions de physique, (1991) Vol.1, p3-48 and p151-168.

[Cha94] Charles J: Conf proc *Duplex Stainless Steels '94*, Glasgow, Scotland, 13-16 November 1994, TWI, Vol.1, Paper KI.

[Chr91] Christianus D: Conf proc *Duplex Stainless Steels '91*, Beaune, Les editions de physique, (1991) Vol.2, p1353-1361.

[Cig91] Cigada A, DeMartiis S, Rondelli G, Vicentini B, Giacomazzi M, Roos A: Conf proc *Stainless Steels 91*, Chiba, ISIJ, Vol.1, p716-723.

[Cla81] Clark G A and Guha P: *Metal Construction* and *British Welding Journal* **13** 5 (1981) p269-273.

[Cla89] Clayton C R and Martin K G: Conf proc *High Nitrogen steels 88*, Lille, The Institute of Metals (1989).

[Col55] Colombier L and Hochmann J: *Aciers inoxydable, aciers refractaire*, Dunod, Paris (1955 and 1957).

[Com82] Combrade P, Desestret A, Jolly P, Mayoud R: Conf proc *Predictive methods for assessing corrosion damage to BWR piping and PWR steam generators*, Fuji, May-June 1978, NACE (1982) p153.

[Cot75] Cottrell A: *An introduction to metallurgy: Second edition*, Publ E Arnold, London (1975).

[Coz94] Cozar R, Lardon J M, Mayonobe B, Morixot C: Conf proc *Duplex Stainless Steels '94*, Glasgow, TWI (1994), Vol.1, paper 84.

D

[DeL56] DeLong W T: *Welding Journal* **35** (1956) p521-528.

[DeL74] DeLong W T: *Welding Journal* **53** (7) (1974) p273s.

[Den76] Denny A K and Shuttlewood J R: Conf proc *Welding of Castings*, Bradford, TWI, (1976).

[Des84] Desestret A and Mayoud R: *Revue de Metallurgie* **81** (4) (1984) p321-333. Also *in Stress Corrosion cracking and Embrittlement*, John Wiley & Sons, New York (1956).

[Dho94] Dhooge A and Deleu E: Proc. conf. '*Duplex Stainless Steels 94*', Glasgow, 13-16 November 1994, TWI, Vol 1, Paper 77.

[Dru90] Drugli J M, Rogne T, Valen S, Johnsen R, Olsen S: *Corrosion 90*, NACE, (1990) paper 270.

E

[Ede53] Edeleanu C: *J.I.S.I.*, 173 (1953) p140.

[Era92] Erauzkin E and Irisarri A M: *Fatigue Fract. Engng. Mater. Struct.* **15 2** (1992) p129-137.

[Eri34] Eriksson S: *Jernkontorets Annaler* **118** (1934) p530.

[Eva57] Evans D A and Jack K H: *Acta Cryst.* **10** (1957) p769.

F

[Fag91] Fager S-A: Conf proc *Duplex Stainless Steels '91*, Beaune, Les editions de physique, (1991) Vol.1, p403-412.

[Fau91] Faucheur D and Gilbert D: Conf proc *Duplex Stainless Steels '86*, The Hague, Nederlands Instituut voor Lastechniek (1986) p83-89.

[Fek86] Fekken U, van Nassau L, Vewey M: Conf proc *Duplex Stainless Steels '86*, The Hague, Nederlands Instituut voor Lastechniek (1986) Paper 26, p268-279.

[Fis53] Fisher R M, Dulis E J and Carroll K G: *Trans A.I.M.E.* **197** (1953) p690.

[Flo68] Floreen S and Hayden H W: *Trans ASM* **61** (1968) p489.

[Fon64] Fontana and Beck: ACI Project 44, Report 49, (1964).

[Fon65] Fontana and Beck: ACI Project 44, Report 52, (1965).

[Fra92] Francis R: Letter to *British Corrosion Journal*, 1992, Vol. 27, No.4, 319-320.

[Fra97] Francis R: Weir Materials Limited, Private communication 13 January 1997.

[Fuk80] Fukuzaka T et al: *Trans I.S.I.J.* **20** (1980) 9B 403.

G

[Gar82] Garner A: *Materials Performance* **21** 8 (1982) p9-14.

[Gin98] Ginn B J and Gooch T G: TWI draft Research Report 7320.03/98/1000.02, June 1998.

[Gla60] Gladman T and Woodhead J H: *J.I.S.I.* 194 (1960) p184-193.

[Gol51] Goldschmidt H: Sym proc *High temperature steels and alloys for gas turbines*, Iron and Steel Institute, Report No.43, (1951) p249.

[Gol67] Goldsmith H J: *Interstitial Alloys*, Plenum Press (1967) p167.

[Goo82] Gooch T G: Conf proc *Duplex Stainless Steels '82*, St.Louis, ASM, (1982) p573-602.

[Goo86] Gooch T G: *Welding in the World* **24** (1986) p148.

[Goo90] Gooch T G: Conf proc *Weldability of Materials*, Detroit, ASM Materials Week (1990).

[Goo92] Gooch T G and Gunn R N: TWI internal report 5607/1/92, June 1992.

[Goo94] Gooch T G and Gunn R N: *Corrosion 94*, Baltimore, NACE (1984) paper 385 and *Materials Performance* **34 3** (1995) p58-61.

[Gre87] Gretoft B, Rigdal S, Karlsson L, Svesson L E: Conf proc *Stainless Steels '87*, York (1987), Institute of Metals, p105-112.

[Gru88] Grundmann R, Gumpel P, Ortmann R, Roth P: *Thyssen Edelst Techn* Ber 14, Band 1988 Heft, 1, p57-58.

[Guh82] Guha P and Clark C A: Conf proc *Duplex Stainless Steels '82*, St.Louis, ASM (1982), p355-369.

[Gui67] Guiraldenq P: *Memoires Scientifiques Rev. Metall. LXIV* **11** (1967) p907.

[Gun91] Gunn R N: TWI confidential report 29335/1/91, August 1991.

[Gun92] Gunn R N: Conf proc *Recent Developments in the Joining of Stainless steels and High Alloys*,Columbus, EWI/TWI/AWS (1992).

[Gun93a] Gunn R N, Atamert S, Gooch T G: Conf proc *Innovation Stainless Steel*, Florence, Italy (1993) p3.53-3.58.

[Gun93b] Gunn R N: Conf proc *Third International Offshore and Polar Engineering*, Singapore, ISOPE (1993), Vol.IV, p228-233.

[Gun94a] Gunn R N: Conf proc *Duplex Stainless Steels '94*, Glasgow, TWI, (1994), paper 32.

[Gun94b] Gunn R N and Anderson P C J: Conf proc *Duplex Stainless Steels '94*, Glasgow, TWI, (1994), paper 30.

[Gun95] Gunn R N: TWI Research Report 505/1995, April 1995. Also in *TWI Journal* 7 (1) January 1998, p5-45.

[Gun96] Gunn R N: TWI unpublished work ref. 5669 (1996).

[Gun97a] Gunn R N: *Duplex Stainless Steels: Microstructure, properties and applications*, Abington Publishing (1997).

[Gun97b] Gunn R N: Bulletin, TWI, (1997) Vol. 38, No. 6, p111-113.

[Gut91] Guttmann M: Conf proc *Duplex Stainless Steels '91*, Beaune, Les editions de physique, (1991) Vol.1, p79-92.

H

[Hal66] Hall E O and Algie S H: *Met. Rev.* **11** (1966) p61.

[Hal95] Halada G P, Clayton C R, Fritz J D, Kim D: *Corrosion 95*, NACE, (1995) paper 95531.

[Has79] Hashimoto K, Asami K, Teramoto K: *Corrosion Science* **19** (1979) p3-14.

[Hay68] Hayden H W and Floreen H W: *Trans ASM* **61** (1968) p474-488.

[Hen75] Henriksson S and Knutsson L: *British Corrosion Journal* (1975) **10** 3 p128.

[Her80] Herbsleb G and Poepperling R K: *Corrosion* **36** 11 (1980) p611.

[Her82] Herbsleb G and Schwaab P: Conf proc *Duplex Stainless Steels '82*, St.Louis, ASM (1982), p15-40.

[Her86] Hertzman S, Roberts W, Lindenmo M: Conf proc *Duplex Stainless Steels '86*, The Hague, Nederlands Instituut voor Lastechniek (1986) p257-267.

[Her91] Hertzman S and Symniotis E: Conf proc *Stainless Steels 91*, Chiba, ISIJ, Vol.2, p1085-1092.

[Her92] Hertzman S, Lehtinen B, Symniotis-Barrdahl E: Conf proc *Applications of Stainless Steel '92* Stockholm, Jernkontoret (1992) Vol.1, p345-359.

[Her93] Hertzman S, Ferreira P J, Brolund B: Conf proc *Innovation Stainless Steel*, Florence, Italy (1993) p3.243.

[Her94] Hertzman S, Nilsson M and Jargelius-Pettersson R: Conf proc *Duplex Stainless Steels '94*, Glasgow, TWI, (1994), paper 1.

[Heu83] Heubner U, Rockel M B, Wallis E: Conf proc *Copper in Steel*, Luxemburg, (1983).

[Hil61] Hillert M: Acta Metall, 9 (1961) p525.

[Hil87] Hilkes J and Bekkers K: Conf proc *Stainless Steels '87*, York (1987), Institute of Metals, p87.

[Hoc50] Hochmann J: *Revue du Nickel*, (1950), **7, 8, 9**, p53-60.

[Hoc73] Hochmann J, Desestret A, Jolly P, Mayoud R: Conf proc *Stress corrosion cracking and hydrogen embittlement of iron base alloys*, Firminy, NACE (1973) p965-1002. Published in English in 1977.

[Hoc91] Hochortler G and Jager H: Conf proc *Duplex Stainless Steels '91*, Beaune, Les editions de physique, (1991) Vol.2, p813-818.

[Hof78] Hoffmeister H and Mundt R: *SchweiBen und Schneiden* **30** (6) (1978) p214.

[Hof81] Hoffmeister H and Mundt R: *Arch. Eisenh* (1981) **52** (4) p159.

[Hof82] Hoffmeister H and Mundt R: WRA **28** 5 (1982) p22.

[Hon76] Honeycombe J and Gooch T G: WRA **22** 9 (1976) p2-29.

[Hon78] Honeycombe J and Gooch T G: Conf proc Trends in *Steels and Consumables*, London, TWI, (1978) paper 24, p383-450.

[Hon79] Honeycombe J and Gooch T G: *Welding Research Journal*, 9, 5, (1979) p25-52.

[Hos78] Hoshino A, Nakano N, Kanao M: *Trans. Natl. Res. Inst. Met. Japan* **20** (1978) p346.

[How77] Howard R D: *Welding Research International* 7 6 (1977) p482-502.

[Huh94] Huhtala T, Nilsson J-O, Wilson A and Jonsson P: Conf proc *Duplex Stainless Steels '94*, Glasgow, TWI, (1994), paper 43.

[Hus79] Husen C and Samans C H: *Chem Eng* (1979) p178.

[Hut86] Hutchinson W B, Schlippenbach U V, Jonsson J: Conf proc *Duplex Stainless Steels '86*, The Hague, Nederlands Instituut voor Lastechniek (1986) paper 32, p326-330.

I

[Irv61] Irvine K J, Llewellyn D T, Pickering F B: *J. Iron Steel Inst.* **199** (1961) p153.

[Irv63] Irvine K J and Pickering F B: *J. Iron Steel Inst.* **201** (1963) p944.

[Ish86] Ishizawa Y and Inazumi T: Conf proc *Duplex Stainless Steels '86*, The Hague, Nederlands Instituut voor Lastechniek (1986) paper 23, p392-398.

[Ish92] Ishizawa Y, Miniami Y, Hashizume S, TakaokaT: *NKK Technical Review* 64 (1992), p15-20.

[Itu91] Iturgoyen L and Anglada M: Conf proc *Stainless Steels 91*, Chiba, ISIJ, Vol.1, p746-753.

J

[Jac91] Jackson E M L E M and matthew L M: Conf proc *Stainless Steels 91*, Chiba, ISIJ, Vol.1, p730-737.

[Jar91] Jargelius R F A and Fan Cun-Gan: Conf proc *Stainless Steels 91*, Chiba, ISIJ, Vol.1, p692-699.

[Jon91] Jonsson O, Liljas M, Stenvall P: Conf proc *Duplex Stainless Steels '91*, Beaune, Les editions de physique, (1991) Vol.1, p461-468.

[Jos91] Jossefson B, Nilsson J-O, Wilson A: Conf proc *Duplex Stainless Steels '91*, Beaune, Les editions de physique, (1991) Vol.1, p67-78.

K

[Kaj91] Kajimura H, Ogawa K, Nagano H: *Trans I.S.I.J.* 31 2 (1991) p216.

[Kas54] Kasper J S: *Acta Metallurgica* 2 (1954) p456-461.

[Kit86] Kitada T, Ishihara T, Ume K, Tsuji T, Itoh M, Uma K: Conf proc *Duplex Stainless Steels '86*, The Hague, Nederlands Instituut voor Lastechniek (1986) paper 19, p69-76.

[Kob88] Kobayashi K, Motoda K, Kurisu T: *Kawasaki Steel Tech. Rep.* 19 (1988) p3-9.

[Koh78] Kohno A and Jones S B: *TWI Research Report*, 81/1978/PE, (1978).

[Kol81] Kolts J and Asphahani A I: *Corrosion 81*, NACE (1981) paper 99.

[Kol82] Kolts J, Flasche L H, Agarwal D C, Tawancy H M: *Corrosion 82*, NACE (1982) paper 190.

[Kol83] Kolts J, Sridhar N, Zeller M V: Conf *Symposium of Metallurgy and Corrosion*, ASM-NACE-IMS, Calgary, (1983).

[Kom91] Komi J I, Kyrolainen A J, Karjalainen L P, Suutala N J: Conf proc *Stainless Steels 91*, Chiba, ISIJ, Vol.2, p807-814.

[Kot82] Kotecki D J: Conf proc *Duplex Stainless Steels '82*, St.Louis, ASM, (1982) p415-430.

[Kot89] Kotecki D J: *Welding Research Supplement*, Nov. 1989, p431s-441s.

[Kot92] Kotecki D J and Siewert T A: *Welding Research Supplement*, May 1992, p171-178.

[Kot97] Kotecki D J: *Welding Research Supplement*, January 1997, p24s.

[Kuj79] Kujanpaa V, Suutala H, Takalo T, Moisio T: *Welding Research Interntaional*, 9 (2) (1979) p55-75.

[Kur30] Kurdjumov G V and Sachs G: *Z.Physik* 64 (1930) p325-343.

L

[Lag67] Lagneborg R: *ASM Trans Quart* **60** (1967) p17.

[Lang] Langley Alloys Ltd: Trade literature for Ferralium 255.

[Lar87] Lardon J M, Charles J, Dupoiron F, Pugeault P, Catelin D: Conf proc *Stainless Steels '87*, York (1987), Institute of Metals, p422-431.

[Lef97] Leffler B: Avesta-Sheffield AB, Private communication, 3 January 1997.

[Len54] Lena A: *Metals Progress* **66** (1954) p86.

[Lil86] Liljas M and Qvarfort R: Conf proc *Duplex Stainless Steels '86*, The Hague, Nederlands Instituut voor Lastechniek (1986) paper 2, p244-256.

[Lin91] Lindblom B E S, Lundqvist B, Hannerz N-E: Conf proc *Duplex Stainless Steels '91*, Beaune, Les editions de physique, (1991) Vol.1, p373-381.

[Lip91] Lippold J C, Varol I, Baesla ck III W A: Conf proc *Duplex Stainless Steels '91*, Beaune, Les editions de physique, (1991) Vol.1, p383-402.

[Liz81] Lizlovs E A: Climax Report RP-33-08-08, (1981).

[Lu83] Lu Y C, Bandy R, Clayton C R, Newman R C: *J. Electrochem. Soc.* **130** (1983) 1774.

[Lun87] Lundqvist B, Norberg P, Nystrom R: Conf proc *ASM Materials Week '87*, Cincinatti, ASM (1987).

[Lun92] Lundin C D, Kikuchi Y, Khan K K: *WRC Progress Reports*, **47** (1/2) 1992, p41-62.

M

[Mae83a] Maehara Y, Ohmori Y, Murayama J, Fujino N, Kunitake T: *Metal Science* **17** (1983) p541.

[Mae83b] Maehara Y, Fujino N, Kunitake T: *Trans I.S.I.J.* **23** (1983) p247.

[Mae87] Maehara Y: *Trans I.S.I.J.* **27** (1987) p705.

[Mar64] Marcinkowski M J, Fisher R M, Zirmae A S: *Trans. TMS-AIME* **230** (1964) p676.

[MARC90] MARC K4.1: Reference manuals volumes A-E, Palo Alto, USA, 1990.

[Mat86] Matsuda F, Nakagawa H, Kato I, Murata Y: *Trans JWRI* **15** (1) (1986) p99-112.

[Mat94] Mattin S P: *Nucleation of corrosion pits on stainless steel*, PhD dissertation, Cambridge University (1994).

[Miy82] Miyuki F, Kudo T, Koso M, Miura M, Moroishi T: Conf proc *Duplex Stainless Steels '82*, St.Louis, ASM, (1982) p95-112.

[Mun83] Mundt R and Hoffmeister H: *Arch Eisenh* **54** (8) (1983) p333.

[Mun85] Mundt R and Hoffmeister H: Conf proc *Stainless Steels '84*, Goteborg, The Institute of Metals, (1985) p315.

[Mye67] Myers P S, Uyehara O A, Boreman G L: *WRC Bulletin* **123** July (1967).

N

[Nag81] Nagano H, Kudo T, Inaba Y, Harada M: *Metaux Corrosion Industrie* 667 (1981) p23.1.

[Nas82] van Nassau L: *Welding in the World* **20** 1/2 (1982) p23-30.

[Nas91] van Nassau L, Meelker H, Hilkes J: Conf proc *Duplex Stainless Steels '91*, Beaune, Les editions de physique, (1991) Vol.1, p303-323.

[Nel87] Nelson D E, Baeslack III W A, Lippold J C: *Welding Journal* **66** (1987) p241s.

[Neu94] Neubert V: Conf proc *Duplex Stainless Steels '94*, Glasgow, TWI, (1994), paper KII.

[New84] Newman R C and Franz E: *Journal Electrochem. Soc.* (1984) p223.

[New87] Newman R C and Shahrabi T: *Corrosion Science* **27** 8 (1987) p827-838.

[Nic94] Nicholls J M: Conf proc *Duplex Stainless Steels '94*, Glasgow, TWI, (1994), paper KIII.

[Nie91] Niederau H and Overbeck G W: Conf proc *Duplex Stainless Steels '91*, Beaune, Les editions de physique, (1991) Vol.1, p641-648.

[Nil88] Nilsson J-O and Liu P: Sandvik Internal Report No. 5603 (1988).

[Nil91a] Nilsson J-O and Liu P: *Mater Sci Technol* **7** (1991) p853.

[Nil91b] Nilsson J-O and Liu P: Conf proc *Stainless Steels 91*, Chiba, ISIJ, p1109-1116.

[Nil92a] Nilsson J-O: *Materials Science and Technology* **8** (1992) p685-700.

[Nil92b] Nilsson J-O, Wilson A, Josefsson B, Thorvaldsson T: Conf proc *Applications of Stainless Steel '92* Stockholm, Jernkontoret (1992) p280-289.

[Nil94] Nilsson J-O, Jonsson P, Wilson A: Conf proc *Duplex Stainless Steels '94*, Glasgow, TWI (1994), paper 39.

[Nis87] Niset M, Doyen R, van Bemst A: Conf proc *Stainless Steels '87*, York (1987), Institute of Metals, p96-104.

[Nob86] Noble D N and Gooch T G: TWI Research Report 321/1986 (1986). Also in [Gun92].

[Nob92] Noble D N and Gunn R N: *Stainless Steel Europe* 4 19-20 (1992) p32-39 and 24-29.

[Nys91] Nystrom M, Karlsson B, Wasen J: Conf proc *Stainless Steels 91*, Chiba, ISIJ, Vol.1, p738-745.

O

[Ode91] Odegard L and Fager S-A: Conf proc *Duplex Stainless Steels '91*, Beaune, Les editions de physique, (1991) Vol.1, p451.

[Oga82] Ogawa T, Aoki S, Sakamoto T, Zaizen T: *Welding Journal* **61** 5 (1982) p139-148.

[Oga86] Ogawa T and Koseki T: IIW Doc IX 1416.86 (1986).

[Oga89] Ogawa T and Koseki T: *Welding Journal* May 1989, p181s.

[Oga90] Ogawa T, Koseki T, Hiroshige T: Conf proc *Weldability of Materials*, Detroit, ASM, (1990) p135.

[Ohm84] Ohmori Y and Maehara Y: *Trans I.S.I.J.* **24** (1984) p61.

[Oka92] Okamoto H: Conf proc *Applications of Stainless Steel '92* Stockholm, Jernkontoret (1992) p360-369.

[Oka93] Okazawa T, Kobayashi T, Ueda M, Kushida T: *Corrosion '93*, Houston, NACE, (1993), p2464-2481.

[Oka94] Okamoto H, Tsuda K, Azuma S, Ueda M, Ogawa K, Igarashi M: Conf proc *Duplex Stainless Steels '94*, Glasgow, TWI, (1994), Vol.1, paper 91.

[Old91] Oldfield J W and Todd B: *British Corrosion Journal*, **26** (3) (1991) p173.

[Ole84] Oleford I and Brox B: *Passivity of Metals and Semiconductors*, Elsevier Science Publishers BV, Amsterdam, (1984) p561.

[Ols86] Olsson J and Nordin S: Conf proc *Duplex Stainless Steels '86*, The Hague, Nederlands Instituut voor Lastechniek (1986) paper 48, p219-225.

[Ols94] Olsson J and Liljas M: Conf *Corrosion '94*, NACE, Baltimore (1994) paper 395.

[Ono82] Onoyama M, Hayashi N, Shitani K, Suehiro T: Conf proc *Duplex Stainless Steels '82*, St.Louis, ASM, (1982), p191-209.

[Ore82] Oredsson J and Berhardsson S: *Corrosion 82*, NACE (1982) paper 126 and *Materials Performance* **22** 1 (1983) p35-42.

[Ono92] Ono M et al: *Tetsu to Hagne* **78** (1) (1992) p178-185.

[Oso86] Osozawa and Okato: *Corrosion 86*, Houston, NACE (1986).

P

[Pak90] Pak S and Karlsson L: *Scand J Metall* **19** (1990) p9.

[Pat35] French patent 803-361 (1935), J. Holtzer Co.

[Pat37] French patent 49-211 (1937), J. Holtzer Co.

[Pat72] German patent DT 2 225 673 (1972) Sudwestfalen (Krupp).

[PatUSa] US patent 3,337,331, AB Sandvik Steel.

[PatUSb] US patent 4,765,953, AB Sandvik Steel.

[Pay32] Payson: *Nickel Trans. Ame. Inst. Min. Met. - Eng.*, (1932) **100**, p306.

[Per86] Perteneder E, Tosch J, Reiterer P, Rabensteiner G: Conf proc *Duplex Stainless Steels '86*, The Hague, Nederlands Instituut voor Lastechniek (1986) paper 21, p48-56.

[Pic78] Pickering F B: *Physical Metallurgy and the Design of Steels*, Applied Science Publishers, London, (1978) p233.

[Pin79] Pini G and Weber J: *Sulzer Technical Review* No.2, (1979).

[Pis92] Pistorius P and Burnstein T: *Phil Trans Roy Soc*, A341 (1992) p531-559.

[Ple82] Pleva J and Nordin S: Conf proc *Duplex Stainless Steels '82*, St.Louis, ASM (1982) p603-629.

[Ple84] Pleva J: Conf proc *Stainless Steels '84*, Goteborg, The Institute of Metals, (1984) p343-352.

[Por92] Porter D A and Easterling K E: *Phase transformations in metals and alloys*, 2nd edition, Chapman and Hall (1992).

[Pot92] Potgeiter J H: *British Corrosion Journal*, 1992, Vol. 27, No.3, 219-223.

Q

[Qui94] Quik J M A and Guedeke M: Conf *Corrosion '94*, NACE, Baltimore (1994) paper 393.

R

[Red91] Redjaimia A, Metauer G, Gantois M: Conf proc *Duplex Stainless Steels '91*, Beaune, Les editions de physique (1991) Vol.1, p119-126.

[Ren86] Renner M, Heubner U, Rockel M B, Wallis E: *Werkstoffe und Korrosion* **37** (1986) p183-190.

[Rho82] Rhodes P R, Welch G A, Abrego L: Conf proc *Duplex Stainless Steels '82*, St.Louis, ASM, (1982) p757-803.

[Rid51] Rideout S, Manly W D, Kamen E L, Lement B S, Beck P A: *Trans A.I.M.E.* (1951) p872.

[Rob91] Roberti R, Nocodemi W, La Vecchia G M, Basha Sh: Conf proc *Stainless Steels 91*, Chiba, ISIJ, p700-707.

[Roc84] Rockel M B and Renner M: *Werkstoffe und Korrosion* **35** (1984) p537.

[Ros84] Roscoe C V, Gradwell K J, Lorimer G W: Conf proc *Stainless Steels '84*, Goteborg, The Institute of Metals (1984) p563-577.

[Ros86] Roscoe C V and Gradwell K J: Conf proc *Duplex Stainless Steels '86*, The Hague, Nederlands Instituut voor Lastechniek (1986) paper 34, p126-135.

[Rou70] Rouault A, Herpin P, Fruchart R: *Ann. Chim.* **5** (1970) p461.

[Rum98] Rumaih A M Al- and Lippold J C: *8th Middle East Corrosion Conference*, NACE (1998) p212-223.

S

[Sak82] Sakai J, Matsushima I, Kamemura Y, Tanimura M and Osuka T: Conf proc *Duplex Stainless Steels '82*, St.Louis, ASM (1982) p211-232.

[Sand] Sandvik Steel: Private communication.

[Sch38] Scherer R: *Journee de la lutte contre corrosion*, Paris, (1938), p363-370.

[Sch49] Schaeffler A L: *Metal Progress* **56** (1949), p680-680B.

[Sco93] Scoppio L, Cumino G, Frizzi A: Conf proc *Processes & Materials Innovation-Stainless Steel*, Florence, **3** (1993) p373-379.

[Sed79] Sedriks A J: *Corrosion of Stainless Steels*, John Wiley & Sons, (1979).

[Sed84] Sedriks A J: Conf proc *Stainless Steels '84*, Goteborg, Institute of Metals, (1984) p125-133.

[Sku78] Skuin K and Kreyssing T: *Neue Hutte* **23** (1) (1978) p22.

[Sma68] Small W M and Pehlke R D: *Trans AIME* **242** (1968) p2501-2505.

[Sma85] Smallman R E: *Modern Physical Metallurgy*, 4th edition, Butterworths (1985)

[Smi83] Smithells Reference Book, 6th edition, Butterworth & Co (1983).

[Smi92] Smith S D and Gunn R N: *TWI Bulletin*, Vol.33, No.4, July/August 1992, p84-88.

[Sol78] Solomon H D and Levinson L M: *Acta Metallurgica* **26** (1978) p429-442.

[Sol79] Solomon H D and Devine T M Jr: STP 672 (1979) p430-461.

[Sol82] Solomon H D and Devine T M Jr: Conf proc *Duplex Stainless Steels '82*, St.Louis, ASM, (1982) p693-756.

[Sou80] Southwick P D and Honeycombe R W K: *Metal Science* **14** 7 (1980), p253.

[Sou90] Soulignac P and Dupoiron F: *Stainless Steel Europe* **2** (1990) p18-21.

[Sri84] Sridhar N, Flasche L H, Kolts J: *Advances in Stainless Steel Technology*, Detroit, ASM (1984).

[Ste91] Steindecker N: Conf proc *Duplex Stainless Steels '91*, Beaune, Les editions de physique (1991) Vol.2, p1393-1396.

[Ste92] Stevenson A W, Gough P G, Farrar J C M: Conf proc *Applications of Stainless Steel '92* Stockholm, Jernkontoret (1992) p290-306.

[Str86] Strutt A J, Lorimer G W, Roscoe C V, Gradwell K J: Conf proc *Duplex Stainless Steels '86*, The Hague, Nederlands Instituut voor Lastechniek (1986) paper 3, p310-318.

[Sug91] Suga M: *Tube International* **10** 45 (1991) p285-289.

T

[Tek87] Tekriwal P, Stitt M and Mazumder J: *Metal Construction*, 1987, Vol. 19, No. 10, 599R-606R.

[Tho84] Thorvaldsson T, Eriksson H, Kutka J and Salwen A: Conf proc *Stainless Steels '84*, Goteborg, Institute of Metals (1984), p101-105.

[Tru65] Trueman J E and Crawshaw B: ISI Publication 117 (1965) p195.

[Tru77] Trueman J E, Coleman M J , Pirt K R: *British Corrosion Journal* **12** (1977) p236.

[Tru82] Trueman J E and Pirt K R: Conf proc *Duplex Stainless Steels '82*, St.Louis, ASM, (1982) p113.

[Tsu86] Tsuge H, Tarutani Y, Kudo T: *Corrosion '86*, Houston, NACE (1986), paper 156. Also in *Corrosion* 44 (5) (1988) p305-314.

[Tsu91] Tsuge S: Proc conf *Stainless steels '91*, Chiba, ISIJ (1991) Vol.2, p799-806.

[TWI93a] TWI document 5632/19/93: 'Recommended practice for pitting corrosion testing of duplex stainless steel weldments by the use of ferric chloride solution', TWI, June 1993.

[TWI93b] TWI document 5632/18/93: 'Recommended practice for systematic point count of duplex stainless steel weldments', TWI, June 1993. Also IIW document codes II-C-942-93 and IX-H-291-93.

U

[Ued93] Ueda M, Okamoto H, Kobayashi T, Kondo K, Ogawa K, Kudo T: *Corrosion '93,* NACE, (1993) Paper 125.

[Uhl67] Uhlig H H: *Corrosion Science* **7** (1967) p325.

[Ume86] Ume K, Seki N, Naganawa Y, Satoh K, Kuriki Y: *Corrosion '86,* NACE, (1993) Paper 155.

W

[Wah87] Wahlberg G and Dunlop G L: Conf proc *Stainless Steels '87*, York (1987), Institute of Metals, p291-299.

[Wal90] Walker R A and Noble D N: Conf proc *Weldability of Materials*, Detroit, ASM Materials Week (1990) p117-126.

[Wal91] Walker R A and Gooch T G: *British Corrosion Journal* **26** 1 (1991) p51-59.

[Wan91] Wang X G, Dumortier D, Riquier Y: Conf proc *Duplex Stainless Steels '91*, Beaune, Les editions de physique (1991) Vol.1, p127-134.

[Wei72] Weiss B and Stickler R: *Met Trans* (1972) p851.

[Wie93] Wiesner C S, Garwood S J and Bowden P L: Conf proc *12th International Conference on Offshore Mechanics and Arctic Engineering*, Glasgow OMAE (1993).

[Wie96] Wiesner C S: TWI GSP Report 5661/10a/96, November 1996.

[Wie97] Wiesner C S: Proc. conf. *'Duplex stainless steels 97'*, Maastricht, 21-23 October 1997, Stainless Steel World, Paper 107.

[Wil58] Williams R D: *Trans A.I.M.E.* **212** (1958) p497-502.

Y

[Yas86] Yasuda K, Tamaki K, Nagano S, Kobayashi K, Nishiyama N: Conf proc *Duplex Stainless Steels '86*, The Hague, Nederlands Instituut voor Lastechniek (1986) paper 24, p201-212.

[Yas94] Yasuda K, Gunn R N and Gooch T G: Conf proc *Duplex Stainless Steels '94*, Glasgow, TWI (1994), paper 26.

[Yus93] Yushchenko K A and Avdeeva A K: Conf proc *Welding Technology Paton Institute*, Cambridge, TWI, October 1993, paper 1.

Z

[Zap49] Zapffe C A: *Stainless Steels,* ASM (1949) p106.

[Zha96] Zhang Z, Marshall A W, Farrar J C M: IIW docs II-1295-96 and II-C-070-96.

Easterling K: 'Introduction to the physical metallurgy of welds', Butterworths, 1985.

Edington J W: '2. Electron diffraction in the electron microscope', Philips Technical Library.

Gunn R N: 'Duplex stainless steels: Microstructure, properties and applications', Abington Publishing, 1998.

Knott J F: 'Fundamentals of fracture mechanics' Butterworths, 1973.

Loretto M H: Electron beam analysis of materials', Chapman and Hall, 1984.

Sedriks A J: 'Corrosion of stainless steels', John Wiley & Sons, 1979.

2D	Two dimensional
3D	Three dimensional
AOD	Argon-oxygen decarburisation
ASTM	American Society for Testing and Materials (USA)
BCC	Body centered cubic (lattice structure)
BS	British Standard (UK)
CCT	Continuous cooling transformation diagrams (when used in a heat treatment context)
CCT	Critical crevice temperature (when used in a corrosion context)
CI	Confidence interval
Cr_{eq}	Chromium equivalent (Cr_{eq} = %Cr + %Mo + 0.7x %Nb): Eqn{2-2}
Cr/Ni	Ratio of Cr_{eq}/ Ni_{eq}
CPT	Critical pitting temperature
CTOD	Crack tip opening displacement (fracture toughness)
CVN	Charpy V notch
Δt	Cumulative time spent between 600 and 1050°C
DBTT	Ductile to brittle transition temperature
FCC	Face centered cubic (lattice structure)
FL	Fusion line of a weld
EAF	Electric arc furnace
EDX	Energy dispersive X-ray analysis
EN	Euronorm
E_p	Pitting or breakdown potential
FEA	Finite element analysis
FCA	Flux cored arc welding
FN	Ferrite Number
GMA	Gas metal arc welding, otherwise known as MIG/MAG (metal inert/active gas)
GTA	Gas tungsten arc welding, otherwise known as TIG (tungsten inert gas)
HAZ	Heat affected zone (of a weld)
HRC	Rockwell hardness on the C-scale
HTHAZ	High temperature HAZ (adjacent to the weld fusion boundary)
HV	Vickers hardness
I	Intermetallic, e.g. σ, χ
IGC	Intergranular corrosion
i_{max}	Maximum corrosion current
i_{pass}	Corrosion current in the passive range
K	Element partition coefficient
LTHAZ	Low Temperature HAZ (remote from weld fusion boundary)
Ni_{eq}	Nickel equivalent (Ni_{eq} = %Ni + 35x %C + 20x %N + 0.25x %Cu): Eqn {2-3}
OD	Outer diameter of a pipe
PAW	Plasma arc welding
PRE_N	Pitting resistance equivalent number: (PRE_N = %Cr + 3.3x%Mo + 16x %N): Eqn {1-1}
PREw	Pitting resistance equivalent number: (PRE_W = %Cr + 3.3x(%Mo + 0.5%W) + 16x %N): Eqn {2-1}
PWHT	Postweld heat treatment
REM	Rare earth metals (Lanthanide group of the Periodic Table)

R_m	ISO/EN shorthand for UTS (ultimate tensile strength or stress)
$Rp_{0.2}$	0.2% proof stress (similar to yield stress for BCC steels)
SADP	Selected area diffraction pattern
SAW	Submerged arc welding
SCC	Stress corrosion cracking (in chloride media)
SCE	Saturated calomel electrode
SEM	Scanning electron microscope
SMAW	Shielded metal arc welding, otherwise known as MMA (manual metal arc)
SSCC	Sulphide stress corrosion cracking (in H_2S bearing media)
$t_{8/5}$	Cooling time between 800 and 500°C
$t_{12/8}$	Cooling time between 1200 and 800°C
TEM	Transmission electron microscope
TL	Transverse longitudinal orientation
TTT	Time-temperature transformation (diagrams produced by isothermal heat treatment)
UNS	Unified Numbering System (USA)
VARP	Vacuum arc remelting process
VOD	Vacuum oxygen decarburisation
WRC	Welding Research Council (USA)
wt	Wall thickness

Greek letters act as shorthand for the following:

α	Ferrite (see also δ)
$\alpha`$	Alpha prime phase
χ	Chi phase
δ	Ferrite (see also α)
δ_c	CTOD test result where failure occurs after maximum load
δ_m	CTOD test result where failure occurs at maximum load
Δt	Cumulative time spent between 600 and 1050°C
ε	Epsilon phase
γ	Austenite
γ_2	Secondary austenite
π	Pi-nitride
σ	Sigma
τ	Tau-phase

EQUATIONS

Eqn {1-1} $PRE_N = \%Cr + 3.3 \times (\%Mo) + 16 \times (\%N)$

Eqn {2-1} $PRE_W = \%Cr + 3.3 \times (\%Mo + 0.5 \times \%W) + 16 \times (\%N)$

Eqn {2-2} $Cr_{eq} = \%Cr + \%Mo + 0.7 \times \%Nb$

Eqn {2-3} $Ni_{eq} = \%Ni + 35 \times \%C + 20 \times \%N + 0.25 \times \%Cu$

Eqn {6-1} $x = 2\sqrt{Dt}$